



**FRIEDRICH-SCHILLER-
UNIVERSITÄT
JENA**

Relativistic Electron-Cyclotron Resonances in Laser Wakefield Acceleration

Dissertation

Zur Erlangung des akademischen Grades

Doctor rerum naturalium (Dr. rer. nat.)

Vorgelegt dem Rat der
Physikalisch-Astronomischen Fakultät
Friedrich-Schiller-Universität Jena

von **M.Sc. Matthew Bradley Schwab**
Geboren am 02. März 1986 in Tucson, AZ, USA

Gutachter:

1. Prof. Dr. Malte Kaluza
2. Prof. Dr. Alexander Thomas
3. Dr. Andreas Döpp

Tag der Disputation: 24. Mai 2022

Abstract

Laser plasma accelerators (LPAs) have the potential to revolutionize research fields that rely on relativistic particle beams and secondary radiation sources thanks to their 10-100 GV/m accelerating fields. In the Laser Wakefield Acceleration (LWFA) scheme, a relativistically intense pump or driver laser is focused into a low-Z gas target, ionizing the gas and driving a relativistic, electron plasma wave. Under the proper conditions, such a plasma wave can be used to accelerate electrons to GeV kinetic energies in only centimeters of plasma propagation. As LPAs continue to be tested and refined, nondestructive measurement techniques must be developed to further investigate and understand the dynamic laser-plasma interaction as well as to help ensure reliable operation and measurement of future accelerator facilities based on plasma technology.

In this thesis, experiment, theory and simulation are combined to investigate the magnetized, relativistic plasma coinciding with the pump laser at the front of the plasma wave. Experimentally, the Jeti 40 TW laser system was used at the Institute of Optics and Quantum Electronics in Jena, Germany to drive a LWFA in tenuous plasma. The plasma wave was then shadowgraphically imaged using a transverse, few-cycle probe pulse in the visible to near-infrared spectrum and an achromatic microscope using various polarizers and spectral interference filters. The resulting shadowgrams were sorted depending on the properties of the LWFA's accelerated electron bunches, and subsequently stitched together based on the timing delay between the pump and probe beams. This allowed for the detailed investigation of the laser-plasma interaction's propagation and evolution as imaged in different polarizations and spectral bands.

The resulting data showed two primary signatures unique to the relativistic, magnetized plasma near the pump pulse. Firstly, a significant change in the brightness modulation of the shadowgrams, coinciding with the location of the pump pulse, is seen to have a strong dependence on the pump's propagation length and the probe's spectrum. Secondly, after ~ 1.5 mm of propagation through the plasma, diffraction rings, whose appearance is polarization dependent, appear in front of the plasma wave. A mathematical model using relativistic corrections to the Appleton-Hartree equation was developed to explain these signals. By combining the model with data from 2D PIC simulations using the VSim code, the plasma's birefringent refractive index distribution was investigated. Furthermore, simulated shadowgrams of a 3D PIC simulation using the EPOCH code were analyzed with respect to the aforementioned signals from magnetized, relativistic plasma near the pump pulse.

The results of the study present a compelling description of the pump-plasma interaction. The previously unknown signals arise from relativistic, electron-cyclotron motion originating in the 10s of kilotesla strong magnetic fields of the pump pulse. Advantageously, a VIS-NIR probe is resonant with the cyclotron frequencies at the peak of the pump. With further refinement, the measurement of this phenomenon could allow for the non-invasive experimental visualization of the pump laser's spatio-temporal energy distribution and evolution during propagation through the plasma.

Zusammenfassung

Laserplasmabeschleuniger (LPAs) haben dank ihrer beschleunigenden Felder von 10-100 GV/m das Potenzial Forschungsbereiche zu revolutionieren, die auf relativistische Teilchenstrahlen und sekundäre Strahlungsquellen angewiesen sind. Bei der Laser-Wakefield-Beschleunigung (LWFA) wird ein relativistisch intensiver Laserpuls (Pumpuls) auf ein Gastarget fokussiert, wodurch das Gas ionisiert wird. Durch die Interaktion des Pumpulaser mit diesem Plasma kann eine relativistische Elektronenplasmawelle erzeugt werden, mit der Elektronen innerhalb weniger Zentimeter auf kinetische Energien im GeV-Bereich beschleunigt werden. Für die Weiterentwicklung dieser LPAs müssen zerstörungsfreie Messverfahren entwickelt werden, um die Interaktion besser zu verstehen und damit den zuverlässigen Betrieb künftiger plasma-basierter Beschleunigeranlagen zu gewährleisten.

Im Rahmen dieser Dissertation wurde mithilfe von Experimenten, Theorie und Simulationen das Plasma an der Position des Pumpulses untersucht. Im Experiment wurde das Jeti-40 Lasersystem am Institut für Optik und Quantenelektronik in Jena verwendet. Mit diesem wurde ein LWFA angetrieben, der mit einem ultrakurzen Beobachtungspuls (Probepuls) bei seiner Propagation durch das Plasma untersucht wurde. Dabei wurden Schattenbilder der Interaktion mit einem hochauflösenden Abbildungssystem mit verschiedenen Polarisations- und Interferenzfiltern abgebildet, und der zeitlichen Verzögerung zwischen Pump- und Probepuls entsprechend, zusammengefügt. Dies ermöglichte die detaillierte Untersuchung der Ausbreitung und Entwicklung der in verschiedenen Polarisationszuständen und Spektralbereichen abgebildeten Laser-Plasma Wechselwirkung.

Die resultierenden Daten zeigten zwei Signaturen, die einzigartig für das relativistische und magnetisierte Plasma nahe des Pumpulaser sind. Erstens, eine signifikante Veränderung der Helligkeitsmodulationen im Schattenbild, die mit der Position des Pumpulaser zusammenfällt und eine starke Abhängigkeit von der Propagationsdistanz des Pumpulaser und der Wellenlänge des Probestrahls aufweist. Zweitens, wurden nach ca. 1,5 mm Propagation des Pumpulaser im Plasma Beugungsringe am Anfang der Plasmawelle sichtbar, deren Aussehen von der Polarisation des Probestrahls abhängig ist. Zur Erklärung dieser Signale wurde ein mathematisches Modell, das relativistische Korrekturen der Appleton-Hartree-Gleichung enthält, entwickelt. Durch die Kombination dieses Modells mit Daten aus 2D-PIC-Simulationen (VSim-Code) wurde die Brechungsindexverteilung des Plasmas untersucht. Darüber hinaus wurden simulierte Schattenbilder einer 3D-PIC-Simulation (EPOCH-Code) im Hinblick auf diese Signaturen analysiert.

Die Ergebnisse dieser Untersuchungen liefern eine überzeugende Beschreibung der Wechselwirkung zwischen Pumpuls, Probepuls und Plasma. Die bisher unbekannt Signale entstehen durch relativistische Zyklotronbewegungen der Elektronen, verursacht durch die mehrere Kilotesla starken Magnetfelder des Pumpulses. Günstigerweise ist eine VIS-NIR-Probepuls in Resonanz mit diesen Zyklotronfrequenzen. Durch weitere Verbesserungen könnte die Messung dieses Phänomens die nichtinvasive experimentelle Visualisierung der räumlich-zeitlichen Energieverteilung und Entwicklung des Pumpulaser durch das Plasma ermöglichen.

Table of Contents

1. Introduction	4
2. Theory	7
2.1 Basic Properties of Plasma	7
2.1.1 Temperature.....	8
2.1.2 Debye Shielding and Debye Length.....	9
2.1.3 Electron Plasma Frequency	10
2.1.4 Electron Cyclotron Frequency.....	11
2.2 Magnetoionic Theory	12
2.2.1 Cold, Unmagnetized Plasma	12
2.2.2 Cold, Magnetized Plasma.....	15
2.2.3 Resonance and Reflection Points of the Appleton-Hartree Equation.....	16
2.3 Few-Cycle Laser Pulses	18
2.3.1 Linearly Polarized Plane Waves.....	18
2.3.2 Few-Cycle Laser Pulses and Dispersion	19
2.3.3 Spatial Distribution of Gaussian Beams.....	23
2.3.4 Shadowgraphic Imaging Theory	24
2.3.5 Coherent Imaging Theory.....	25
2.4 Electron Motion in an Electro-Magnetic Field.....	29
2.4.1 Single Electron Motion in a Plane Wave	29
2.4.2 The Ponderomotive Force	32
2.5 Laser Wakefield Acceleration	33
2.5.1 Self-Compression of the Laser Driver.....	33
2.5.2 Excitation of a Plasma wave.....	35
2.5.3 Injection Mechanisms.....	37
2.5.4 Dephasing, Pump Depletion and Energy Gain.....	38
2.5.5 Particle-in-Cell Simulations	39
3. Experimental Setup	41
3.1 Jeti 40 Laser System.....	41
3.2 Laser Wakefield Acceleration Setup.....	42
3.2.1 Gas-Cell Target for LWFA	44
3.2.2 Electron Diagnostics.....	45
3.3 Few-Cycle Probe System	46
3.3.1 Setup and Characterization.....	46

3.3.2	Microscope, Filters, Polarizers, CCDs	48
3.3.3	Temporal Resolution of Few-Cycle Microscopy in LWFA.....	50
4.	Experimental Data.....	51
4.1	Introduction to Few-Cycle Shadowgrams	51
4.2	Electron Spectra as a Sorting Criteria	52
4.3	H-pol and V-pol Shadowgrams with Full Spectrum	54
4.4	Comparison of Spectrally Filtered H-pol Images.....	55
5	Methods of Analysis.....	57
5.1	Relativistic Appleton-Hartree Equation	57
5.1.1	Cartesian Coordinate System	58
5.1.2	Relativistic Modifications to the AH Equation	59
5.1.3	From the RAH Equation and η_{\pm} to the Effective Refractive Index η_{eff}	62
5.1.4	Example Behavior of the RAH Equation	64
5.1.5	Lorentz Transformation of Vector Orientations.....	66
5.1.6	Resonance Points, Reflection Points and Shadowgraphy	68
5.2	2D PIC Simulations with VSim Code	69
5.2.1	Setup of the 2D VSim Simulations	69
5.2.2	Calculating the Drift Velocity and Residual Quiver Velocity.....	70
5.2.3	Numerically Solving the RAH Equation with Results from VSim	73
5.2.4	Testing Physical Solutions	74
5.3	3D PIC Simulation with the EPOCH Code.....	76
5.3.1	Setup of the 3D EPOCH Simulation	76
5.3.2	Simulating Shadowgrams with Results from EPOCH	77
6	Analysis of Experimental Results	77
6.1	Asymmetric Signal.....	78
6.1.1	2D PIC Simulation Results.....	79
6.1.2	3D PIC Simulation Results.....	81
6.2	Half-Ring Signal.....	83
6.2.1	2D PIC Simulation Results.....	84
6.2.2	3D PIC Simulation Results.....	86
6.2.3	Coherent Imaging Model for Relativistic Objects.....	87
6.2.4	Coherent Imaging Model and the Half-Ring Signal.....	89
7.	Summary and Conclusion	98
Appendix A	– Plasma Physics.....	101
A.1	Collisional Processes	101
A.2	Phase Space Distribution Function.....	102

A.3 Ionization Mechanisms.....	104
Photoelectric Effect.....	104
Multi-Photon Ionization (MPI)	104
Above Threshold Ionization (ATI).....	105
Tunnel Ionization	106
Barrier Suppression Ionization.....	106
Appendix B – Laser Physics	108
B.1 Creation of Few-Cycle Pulses	108
B.2 Single-Shot Characterization of Few-Cycle Pulses	110
SPIDER.....	110
SRSI	111
CEPM/SATI.....	112
Third-Order Autocorrelation	113
Appendix C – Lorentz Transformations.....	114
C.1 Vector Orientations in Oblique Planes	114
Appendix D – Cited Figures.....	116
9. References	121
10. Ehrenwörtliche Erklärung	130
11. Chronological List of Publications.....	131
12. Chronological List of Presentations and Posters.....	131

1. Introduction

In roughly 100 years of development, testing and implementation, particle accelerators have become indispensable tools for a wide range of markets including industry, medicine, materials science and general physics [1]. The discovery of new particles and interactions in the Standard Model, production of radioisotopes for medical use, sterilization of medical and food equipment, and the processing of heat shrink tubing for electronics are only some of the many applications born from the increase in availability and decrease in cost of particle accelerators. In the fields of particle and accelerator physics, scaling laws can be used to motivate the continued development of next generation technology such as laser plasma accelerators (LPAs) [2], [3]. Current state-of-the-art particle colliders operate with accelerating fields ranging from a few hundred kV/m to tens of MV/m, which requires facilities spanning from a few to tens of kilometers in length to achieve GeV and TeV particle energies [4]–[6]. With the ability to produce 10-100 GV/m accelerating fields, plasma-based accelerators have the general potential to help “miniaturize” high-energy particle sources [7]–[10]. The possible cost and size reduction of future accelerators using plasma as an accelerating medium not only allows for higher particle energies for a given facility size, but also provides smaller, university-level laboratories access to high-energy beams and secondary emission sources that were previously too costly and complex to manage. Just as the advent and widespread use of lasers drastically shifted the research landscape near the turn of the 21st century, enabling widespread use of high-energy particle beams in the laboratory will also facilitate new and exciting research in several fields [11].

Due to the current availability of Terawatt (TW), and more recently Petawatt (PW) lasers, laser-plasma accelerators (LPAs) using the laser wakefield acceleration (LWFA) mechanism to accelerate electrons are at the forefront of plasma-based accelerator research. In brief, a high-intensity laser pulse drives a propagating charge separation in ionized plasma, known as a plasma wave, in which electrons can be accelerated to GeV energies [12]. Less widespread, but increasing in its appeal due to easier hybridization with existing accelerators, is PWFA or plasma wakefield acceleration, where an electron or proton bunch drives the plasma wave, in which a second “witness” bunch is further accelerated [13], [14]. While improvements have been made over the past twenty years concerning the maximum energy, energy spread, beam divergence, and stability of the produced electron beams, further improvement must be achieved in order to realize certain applications such as “table-top” FEL operation [15]–[17], x-ray tomographic imaging [18], cancer therapy [19], or LPA staging for a purely plasma-based particle collider [10], [20]. A roadmap for plasma accelerators beyond 2020, including applications, by *Albert et al.* can be found in [11]. Improvements in theory, simulation and experiment are ongoing and to this effect the work presented in this dissertation follows the adage, “your accelerator is only as good as your diagnostics”. The better you can measure what is occurring in your accelerator, the better you can understand and holistically improve the system.

1. Introduction

Methods for measuring the accelerated particles are well established thanks to a long history of development at existing accelerator facilities [21]. Conversely, recording the laser-plasma interaction in an LPA itself is no small feat. The driver laser and the excited plasma wave have micrometer-sized dimensions and move essentially at the speed of light through the background plasma. Scattered laser light from the driver and emitted light from the plasma have their own diagnostic usefulness, but they can complicate matters when the goal is to directly image the plasma distribution and its interaction with the drive laser. Luckily, many groups have found successful ways of gleaning information from the laser-plasma interaction in the laboratory. *Matlis* et al. used Fourier Domain Holography in a co-propagating geometry to measure the plasma wave's induced phase shift on the probe beam [22]. This allowed for measurement of the plasma wave's period as a function of the background plasma density and visualization of plasma wave curvature with increasing distance behind the pump laser. *Kaluza* et al. used a transverse probing geometry to conduct polarimetry measurements on the magnetic fields generated in the LWFA interaction, but were unable to resolve the plasma wave itself due to the long temporal duration of the probe beam [23]. *Buck* et al. improved on the transverse probing method by reducing the probe pulse's duration by using a pick-off of the pump pulse already having an 8.5 fs full-width at half-maximum (FWHM) duration [24]. Both polarimetric and shadowgraphic methods were used to visualize structures of the plasma wave and the change in plasma wavelength with varying background plasma density. By switching to a probe pulse broadened via self-phase modulation and temporally compressed with chirped mirrors, we combined a 35 fs pump pulse with a 6 fs probe pulse in transverse geometry and obtained detailed shadowgraphic images of the plasma wave in underdense plasma [25]. Post-interaction spectral filtering was also tested and shown not to fundamentally degrade the resulting temporal resolution of the images. *Sävert* et al. continued using the few-cycle (fc-), transverse, VIS-NIR probe and investigated changes in the plasma wave before, during and after self-injection of the accelerated electron bunch [26]. Their work showed the lengthening of the plasma wave's first oscillation directly before self-injection as well as an increase in the plasma wave's amplitude correlating with an increase in the accelerated bunch's electron charge as seen from a relativistically corrected 2nd oscillation period of the plasma wave. In support of Dr. Sävert's work, *Siminos* et al. developed a method of simulating transverse, ultrafast shadowgraphy of LWFA using output from the EPOCH Particle-in-Cell code (PIC) [27]. The ability to scan several parameters of the transverse probe and visualize their effects on the shadowgraphic image of the plasma wave significantly reduces the effort in both understanding previous experiments as well as designing new experiments. Optical probes are not the only tool to visualize the plasma wave. *Zhang* et al. used a femtosecond, relativistic electron bunch from one LWFA to probe the plasma wave of a second LWFA [28]. This method was successful in reconstructing the electric fields and electron density distribution in the plasmwave in the linear regime. Extension to the nonlinear regime has yet to be published but will no doubt be a powerful diagnostic tool considering the quantitative

1. Introduction

reconstruction of fields and densities. Finally, returning to optical probing techniques, *Gilljohann et al.* and *Kurz et al.* used the transverse probing geometry with a sub-10 fs probe pulse duration to record shadowgrams of a PWFA plasma wave. This allowed for the investigation of the formation of an ion channel in the plasma due to the higher ponderomotive gradient of the particle driver as compared to the typical laser drivers used in LWFA [29]. In the case of *Kurz et al.*, the transverse shadowgrams were used to verify the differences between the self-ionized and pre-ionized plasma interaction with the drive bunch, showing more efficient plasma wave creation using pre-ionized plasma [10].

With the technical aspects of optically imaging the plasma wave having been achieved, the majority of future research will be in understanding what physics are recorded in the images, depending on a specific configuration of pump, probe, plasma and imaging system. How do the known parameters of the system interact to produce a certain image of the plasma wave and surrounding area, and what does that reveal about the interaction and the generated particle beam? Thanks to the ultra-broadband spectrum of a few-cycle probe beam, several interesting research avenues can be pursued. The single-shot temporal evolution of the plasma wave using a linearly chirped probe beam that maps wavelength to time could be implemented as was performed with different experimental parameters in [30]. Fourier-domain interferometry could be tested to attempt the quantitative measurement of the plasma wave's density distribution which could also produce quantitative information about the driver itself [31], [32]. Furthermore, the few-cycle, transverse probing method could also be developed at longer wavelengths in order to probe the driver-plasma interaction at lower plasma densities such as those used in PW-class LWFA experiments and PWFA experiments coupled to rf-accelerators [8], [9]. The fundamental interest in this dissertation will be; however, how can one exploit the broadband spectrum and polarization of a few-cycle, transverse, VIS-NIR probe beam to visualize and investigate the evolution of the pump laser in LWFA. The ability to measure the position and distribution of the pump laser as it propagates through the plasma would not only facilitate the refinement of laser-plasma simulations and the understanding of the interaction itself, it could also act as a new method for measuring the spatio-temporal distribution of the pump laser.

Previous work using different methods to record the plasma wave of LWFA, as described in a previous paragraph, could only infer the location and approximate size of the laser driver being used via the visualized distribution of the plasma's density. While simulations can exquisitely model laser-plasma interactions depending on the available computational resources, they should always be complemented with real laboratory experiments, which are intrinsically devoid of approximations and assumptions. This dissertation proposes, tests and explains the use of a well-known plasma phenomenon, electron-cyclotron motion, to visualize the location and distribution of the pump laser as it propagates through the plasma and drives the plasma wave. The main objectives were as follows:

1. Build and characterize the necessary pump-probe-plasma experiment in the context of LWFA with the potential to measure, via the probe beam, electron-cyclotron motion in the plasma.

2. Theory

2. Perform a LWFA campaign with the above-mentioned experimental setup and record the necessary parameter scans to evaluate the usefulness of the electron-cyclotron phenomenon in the context of LWFA diagnostics.
3. Establish and assess a mathematical representation of pump-probe-plasma system in the context of the transverse, probe beam imaging setup.
4. Combine the experimental data, mathematical model and available simulation data to investigate the role of electron-cyclotron motion in LWFA.
5. Assess and present the feasibility of developing an LPA diagnostic based on the intended work and findings listed above.

Ultimately, the ability to resolve the laser-driver's full intensity distribution during the length of the laser-plasma interaction would be comparable to having first imaged the plasma wave itself. It would allow for detailed comparisons to simulations and improved understanding of the laser-plasma interaction. Practically; however, it would be a significant first step to be able to track the peak or FWHM of the laser-driver. This would allow, for example, for further investigation of pulse self-compression and self-focusing, the change in spatio-temporal couplings with propagation, changes in the laser-driver during density transitions in the plasma and soliton formation in the plasma [33]–[36]. The overall value of being able to visualize and measure the laser's field distribution in plasma will only be realized if a practical and robust measurement method can be developed.

2. Theory

This chapter presents most of the basic concepts, already found in text books, that are necessary to understand the content in the remaining chapters. **Section 2.1** covers the properties of plasma and **Section 2.2** goes into more details about electromagnetic (EM) waves in both unmagnetized and magnetized plasmas. **Section 2.3** then describes the mathematics behind ultra-short or few-cycle laser pulses followed by examples of using said pulses in a coherent imaging system. The two main concepts, plasma and laser pulses, are then combined in **Sections 2.4** and **2.5** to describe the motion of electrons in EM waves and by extension the basic physics underlying the LWFA mechanism. Finally, **Section 2.5** concludes with a short description of simulations used to model LWFA experiments.

2.1 Basic Properties of Plasma

To begin piecing together all of the necessary background information concerning LWFA and few-cycle transverse probing, the basic properties of plasma will be first introduced. A material is defined as plasma based on four criteria: the plasma has a spatial extent larger than a Debye length (see **Section 2.1.2**), it has an inter-particle distance less than the Debye length, it possesses macroscopic charge neutrality, and it exhibits an electron-to-neutral particle collision rate that is lower than the characteristic electron plasma frequency (see **Appendix A.1** and **Sections 2.1.3**). These criteria are

2. Theory

discussed at length in any introductory text book on plasma physics [37]–[39]. In the sections to follow, emphasis is placed on describing a plasma’s temperature, the Debye length and Debye shielding, and basic characteristic frequencies of plasma.

2.1.1 Temperature

The temperature of plasma is a measure of the average kinetic energy of the plasma’s constituents given by $E_{kin} = \frac{1}{2}m_s\langle v_s^2 \rangle = \frac{3}{2}k_B T_s$, with mass of the particle of species m_s , speed v_s , Boltzmann constant k_B , and temperature of the particles of species T_s . Different species, denoted by the subscript s of particles can have different temperatures and different groups of a species can also vary in their temperatures. The plasma used in typical LWFA experiments include particles such as electrons, protons and light ions such as He^{1+} and He^{2+} . In thermal equilibrium, particles take on a Maxwell-Boltzmann velocity distribution with a temperature T_s and number density n_s [39]. Assuming the motion of the particles is isotropic, the speed distribution function, **Eq. 1**, can be calculated from the velocity distribution. **Figures 1** and **2** show the speed distributions for protons and He ions as well as for electrons.

$$F(v) = 4\pi n_s \left(\frac{m_s}{2\pi k_B T_s} \right)^{3/2} v^2 \exp \left[-\frac{m_s v^2}{2k_B T_s} \right] \quad (1)$$

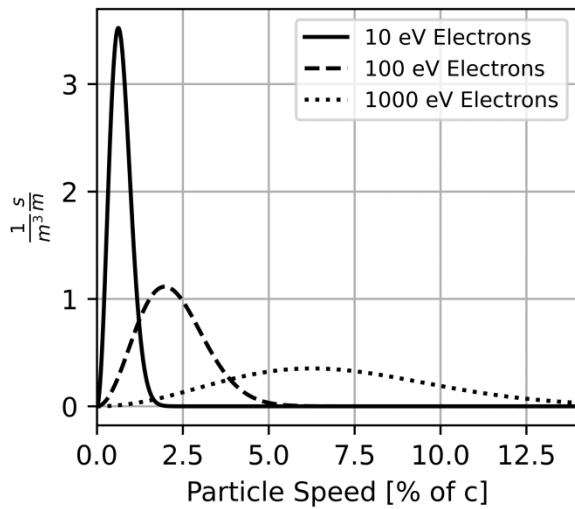


Figure 2: Maxwellian speed distribution of electrons assuming isotropic motion. Integration over all speeds results in the number density of electrons.

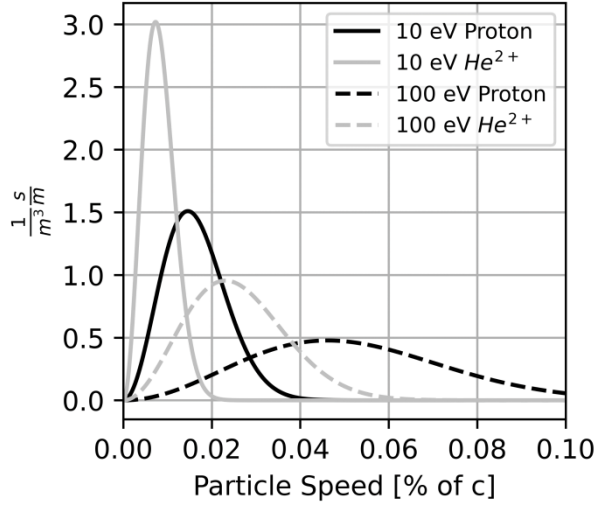


Figure 1: Maxwellian speed distribution assuming isotropic motion of the particles. Integration over all speeds results in the number density of particles.

Assuming the same force acts on particles of different masses, the resulting accelerations experienced by those particles differ by the square root of the ratio of the particles’ masses, for example $\sqrt{m_p}/\sqrt{m_e}$ for the proton and electron. This results in the electron gaining a speed 43 times higher than a proton when acted on by the same force, even though their thermal energies are the same. Due to their smaller masses, electrons reach relativistic speeds at much lower thermal temperatures compared to more massive particles. This is the primary

2. Theory

reason as to why protons and heavier ions are considered immobile in most LWFA experiments when considering the movement of plasma electrons on the femtosecond- to picosecond-timescale.

While basic theory often assumes cold plasma for mathematical convenience, the plasma's behavior can change significantly as it diverges away from the cold plasma description. Of importance in LWFA is the role the plasma temperature takes in amplifying or suppressing nonlinear instabilities. These instabilities, such as Raman scattering, lie outside the immediate purview of this dissertation; however, there are many excellent references for the interested reader [33]. The different temperatures of the various particle species depend highly on the ionization mechanisms that create the plasma (see **Appendix A.3**). Transverse probing of LWFA experiments typically observes the plasma within femtoseconds or picoseconds of its creation (ionization). Within this time span, neither the plasma as a whole, nor its constituent species have had sufficient time to thermally equilibrate. The mass difference between the electrons and ions and the low collision frequency in low-density plasma (see **Appendix A.1**) are the primary reasons for the plasma's slow return to thermal equilibrium. Whether the plasma is in thermal equilibrium or not, the concept of temperature is necessary for presenting the Debye length and its connection to collective behavior of the plasma.

2.1.2 Debye Shielding and Debye Length

The primary force acting between charged particles in plasma is the Coulomb force having an r^{-2} dependence with r being the distance between two particles. Any non-neutral charge distribution in plasma will become modified over time due to the mobility of the electrons, and, over longer time-scales, the mobility of the ions, until neutrality is reached barring any influence from external forces. The reduction in the Coulomb force between charged particles due to particle mobility is known as Debye shielding. It has a characteristic length, the Debye length λ_D , which for immobile ions depends only on the electron temperature and electron-plasma density as seen in **Eq. 2** with the electric permittivity of vacuum ϵ_0 , elementary charge e , and the plasma's electron number density n_e . The Coulomb potential between two particles will be reduced by a factor e^{-1} over one Debye length. The higher the electron temperature and lower the electron density is, the longer the Debye length will become and any Coulomb potential present will be more weakly shielded.

$$\lambda_D = \sqrt{\frac{\epsilon_0 k_B T_e}{n_e e^2}} = 6.9 \cdot 10^9 \sqrt{\frac{T_e \cdot \text{Kelvin}^{-1}}{n_e \cdot \text{cm}^3}} \mu\text{m} \quad (2)$$

Knowing that only charged particles separated by less than a Debye length interact strongly with each other leads to calculating how many particles are within a Debye sphere given by $N_D = n_e \lambda_D^3$. **Figure 3** shows the Debye length calculated for three different electron plasma densities versus thermal energy in eV as well as the number of electrons per Debye cube vs. electron density for three different Debye lengths. The more electrons there are in a Debye cube the more fluid-like or collective the behavior of the plasma. As per definition, the plasma itself must have a larger extent than the

2. Theory

Debye length and there must be more than one charged particle per Debye length, $N_D \gg 1$, otherwise there would be no collective behavior and also no macroscopic charge neutrality.

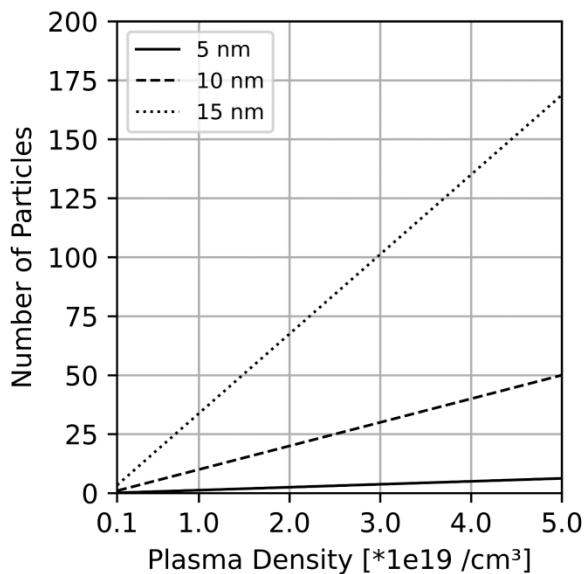
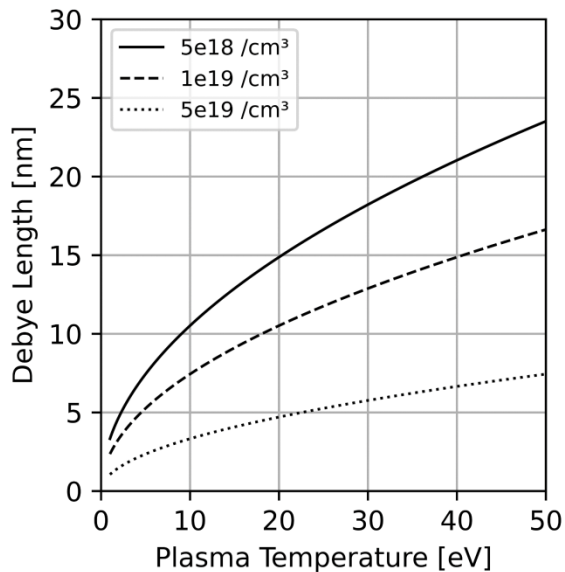


Figure 3: (Upper) Debye length vs. plasma temperature for three different plasma densities. (Lower) Number of particles in a Debye cube vs. plasma density for three different Debye lengths.

Luckily for LWFA, the electron response of low-density plasma is still too slow to shield the potentials created in the plasma by a laser driver. Whether or not a laser field can penetrate the plasma can be determined by calculating the electron plasma frequency as discussed in the next section.

2.1.3 Electron Plasma Frequency

The electron plasma frequency ω_p describes a characteristic longitudinal, electrostatic and collective oscillation of plasma electrons in a cold plasma. Due to neglecting the ion motion in the plasma, this thesis will use “electron plasma frequency” and “plasma frequency” synonymously. The

As a small note of interest one can investigate the electron temperature and density necessary to force a treatment of the plasma based on quantum physics instead of classical physics. This occurs when the interparticle spacing of the plasma electrons approaches their de Broglie wavelength [37] which is fulfilled for a thermal energy of 1 eV and a plasma density of $5 \cdot 10^{19} \text{ cm}^{-3}$. While that density is not uncommon for LWFA, the thermal energy of the laser-ionized gas is much higher than 1 eV, and a quantum mechanical treatment of the plasma is unnecessary.

One can now consider the time-scales under which charged particles are moving in the system compared to the Debye length. After an outside driver creates an electric potential in the plasma, it will take a certain amount of time for the charged particles to move in response to the potential. Going back to **Fig. 2** and **Fig. 3**, one can take the average thermal speed of an electron and a proton at 10 eV and compare the travel times across a Debye length of 10 nm. The inertial mass difference between proton and electron causes the electrons to undergo a higher acceleration in response to an electric potential. The electrons cover this distance in 5 fs, whereas the protons need 200 fs, or a factor of 43 slower.

2. Theory

derivation of ω_p begins by displacing a large group of plasma electrons from their equilibrium position by a distance Δx in a plasma with background electron density n_e . This creates three distinct regions: one with excess negative charge, a second region with local charge neutrality and a third with excess positive charge. The resulting restoring force on the displaced electrons is directly proportional to their displacement and because the electrons have inertia they will overshoot their equilibrium positions creating a longitudinal oscillation. The electric field due to the charge displacement can be written as $E = n_e e \Delta x / \epsilon_0$. Inserting this field into the classical equation of motion (without magnetic fields) gives the equation of a harmonic oscillator with the characteristic frequency given by **Eq. 3** below. For comparison, the VIS-NIR spectral range from roughly 400 nm to 1000 nm covers the angular frequency range of 4.71 PHz to 1.88 PHz, while the plasma frequency for plasmas with an electron density between $5 \cdot 10^{18} \text{ cm}^{-3}$ to $5 \cdot 10^{19} \text{ cm}^{-3}$ is in the range of 0.13 PHz to 0.4 PHz.

$$\omega_p = \sqrt{\frac{n_e e^2}{m_e \epsilon_0}} \quad (3)$$

A fully relativistic derivation of the electron plasma frequency is found in the literature [40] and results in replacing m_e with γm_e , where γ is the Lorentz factor of the relativistic plasma electrons. The displacement of the electrons via an external driver can cause their velocity to become relativistic, and the electrons' motion in the electric field from any charge distributions can also be relativistic. While the correction is typically small for situations where the electron plasma is still considered a fluid (compared to say an accelerated beam of electrons), the difference is measurable and relevant for understanding plasma-based accelerators [26]. The use of the relativistic plasma frequency will be described later, see **Section 5.1**, when dealing with the drift-frame of relativistic plasma electrons.

2.1.4 Electron Cyclotron Frequency

Another characteristic frequency in cold plasma arises when the plasma is magnetized by a uniform and static magnetic field. As seen using the equation of motion, $\mathbf{F} = q(\mathbf{E} + \mathbf{v} \times \mathbf{B})$ with no electric field ($\mathbf{E} = 0$), the force \mathbf{F} acting on a charged particle with charge q in a magnetic field \mathbf{B} is always perpendicular to its velocity \mathbf{v} , causing circular orbits with a frequency given by **Eq. 4**. Note, bold variables such as \mathbf{F} will be used to denote 3-dimensional vectors whereas non-bolded variables are their equivalent magnitude, $F = \sqrt{F_x^2 + F_y^2 + F_z^2}$. The cyclotron frequency is always taken to be positive despite the difference in the direction of gyration for positively and negatively charged particles.

$$\Omega_c = \frac{|q|B}{m_e} \quad (4)$$

Cyclotron motion exhibits one of the fundamental aspects of the motion of charged particles under the influence of an external magnetic field, specifically diamagnetism. The resulting motion of the charged particle in reaction to the externally applied magnetic field will be such that the induced magnetic field opposes the externally applied field. In the case of cyclotron motion, negatively

2. Theory

charged particles will gyrate around the magnetic field lines in a right-handed sense. This motion of negatively charged particles induces a ring current and therefore a magnetic field that points oppositely to the externally applied magnetic field inside the particle's orbit.

An iron magnet used in conventional particle accelerators achieving a magnet field of 1 Tesla would cause an electron to gyrate at a frequency of 176 GHz. This frequency is well within the microwave spectrum of 300 MHz to 300 GHz. Magnetic fields in the kT (kilotesla) range are required to create cyclotron frequencies in the VIS-NIR spectral range. Specifically, a magnetic field of 13.4 kT would cause an electron to gyrate at a frequency corresponding to an 800 nm wavelength.

More complex motion of charged particles in spatially and temporally varying EM fields are described in several text books [37]–[39]. The mathematics quickly become quite complicated for non-simplified systems and is often investigated using numerical simulations. **Sections 2.4** and **5.1** will describe the interaction of plasma electrons with the EM fields of focused laser pulses.

2.2 Magnetoionic Theory

With the basic characteristics of plasma having been described, the emphasis moves toward mathematically describing laser-plasma interactions and more specifically in describing the dispersion relationships for EM waves in cold plasma. As the title of the section suggests, the derivation will assume magnetized plasma as well as the simpler case of wave propagation in free space to prepare for a later description of fc-pulses in vacuum (see **Section 2.3**).

2.2.1 Cold, Unmagnetized Plasma

Starting from the phase space distribution function (see **Appendix A.2**) of the particle species s in plasma, $f_s(\mathbf{r}, \mathbf{v}, t)$, two important variables can be derived. **Equation 5** shows the number density or number of particles of type s inside the volume d^3r in phase space regardless of velocity at time t and **Eq. 6** shows the average velocity of particles in the area near \mathbf{r} at time t . Both will be written in the following without subscript s and will refer to the plasma electrons.

$$n_s(\mathbf{r}, t) = \int f_s(\mathbf{r}, \mathbf{v}, t) d^3v = \frac{1}{d^3r} \int d^6N(\mathbf{r}, \mathbf{v}, t) d^3v \quad (5)$$

$$\mathbf{u}_s(\mathbf{r}, t) = \frac{1}{n_s(\mathbf{r}, t)} \int \mathbf{v} f_s(\mathbf{r}, \mathbf{v}, t) d^3v \quad (6)$$

Another six equations will be needed, including the continuity equation (**Eq. 7**), the Langevin equation of motion (**Eq. 8**) with collision frequency ν , and Maxwell's equations (**Eq. 9-12**) with the total electric charge density $\rho = -en + q_i n_i$, and electric current density $\mathbf{J} = -e\mathbf{nu}$ assuming immobile ions $\mathbf{u}_i = 0$, of number density n_i and charge q_i .

$$\frac{\partial n}{\partial t} + \nabla \cdot (n\mathbf{u}) = 0 \quad (7)$$

$$m \frac{\partial \mathbf{u}}{\partial t} = q(\mathbf{E} + \mathbf{u} \times \mathbf{B}) - m\nu\mathbf{u} \quad (8)$$

2. Theory

$$\nabla \cdot \mathbf{E} = \frac{\rho}{\varepsilon_0} \quad (9)$$

$$\nabla \cdot \mathbf{B} = 0 \quad (10)$$

$$\nabla \times \mathbf{E} = -\frac{\partial \mathbf{B}}{\partial t} \quad (11)$$

$$\nabla \times \mathbf{B} = \mu_0 \left(\mathbf{J} + \varepsilon_0 \frac{\partial \mathbf{E}}{\partial t} \right) \quad (12)$$

The standard derivation proceeds by linearizing the magnetic field and electron number density into a zero-order component, \mathbf{B}_0 being the constant uniform field and n_0 an undisturbed background electron density, and harmonic plane wave components: $\mathbf{B}_1(\mathbf{r}, t)$ and $n_1(\mathbf{r}, t)$. The variables \mathbf{E} , \mathbf{B}_1 , \mathbf{u} , and n_1 are written in terms of harmonic planes wave of the form $\psi(\mathbf{r}, t) = \psi_0 \exp(i\mathbf{k} \cdot \mathbf{r} - i\omega t)$ and any second order terms or products of two first order terms are neglected assuming that the average velocity of the plasma electrons remains small compared to the phase velocity of the wave, i.e. $|\mathbf{u}| \ll \frac{\omega}{k}$. Using harmonic plane wave solutions allows the nabla operator to be replaced as $\nabla = i\mathbf{k}$, and the partial temporal derivative to be replaced as $\partial/\partial t = -i\omega$.

In the case of unmagnetized plasma, $\mathbf{B}_0 = 0$ causes the cross-product in the equation of motion, **Eq. 8**, to be zero, resulting in an expression relating the average particle velocity to the electric field: $\mathbf{u} = -e\mathbf{E}/(m(\nu - i\omega))$. This result is combined with Faraday's law of induction, **Eq. 11**, and Ampere's law, **Eq. 12**, along with substitutions for the electron plasma frequency and speed of light in terms of the electric permittivity ε_0 and magnetic permeability of free space μ_0 , i.e., $1/c^2 = \varepsilon_0\mu_0$. The resulting equation, **Eq. 13**, captures the behavior of transverse and longitudinal waves propagating through a cold and unmagnetized plasma characterized by ω_p and ν , with the latter variable typically representing the collision frequency involving electrons.

$$\mathbf{k} \times [\mathbf{k} \times \mathbf{E}] = \frac{\omega_p^2}{c^2 \left(1 + i\frac{\nu}{\omega}\right)} \mathbf{E} - \frac{\omega^2}{c^2} \mathbf{E} \quad (13)$$

By further splitting the electric field vector into components parallel and transverse to \mathbf{k} , i.e., $\mathbf{E} = \mathbf{E}_l + \mathbf{E}_t$, using $\mathbf{k} \times \mathbf{E}_l = 0$ and $\mathbf{k} \times [\mathbf{k} \times \mathbf{E}_t] = -k^2 \mathbf{E}_t$ and assuming that collisions do not play a significant role, i.e., $\nu \ll \omega$, dispersion relations for a longitudinal, stationary, electrostatic wave and a transverse propagating wave can be identified. The longitudinal electrostatic wave oscillates at the electron plasma frequency and has no associated magnetic field since $\mathbf{k} \times \mathbf{E}_l = 0 = \omega \mathbf{B}_1$. The transverse mode, whose dispersion relation is shown by **Eq. 14**, shows propagation of the wave (real wave number k) for $\omega > \omega_p$ and reflection of the wave (imaginary wave number k) for $\omega < \omega_p$. This corresponds to underdense and overdense plasma, respectively. The phase and group velocities of the wave are further defined by **Eqs. 15** and **16** while introducing the refractive index of cold plasma η in **Eq. 17** and the critical plasma density $n_c = m_e \varepsilon_0 \omega^2 / e^2$. With a bit of rearranging one sees that the

2. Theory

under- and overdense cases correspond to $n_0 < n_c$ and $n_0 > n_c$, respectively. **Figure 4** below shows the refractive index, phase and group velocities for an electron density of 10^{19} cm^{-3} .

$$k^2 c^2 = \omega^2 - \omega_p^2 \quad (14)$$

$$v_{ph} = \frac{\omega}{\text{Re}(k)} = \frac{c}{\sqrt{1 - \frac{\omega_p^2}{\omega^2}}} = \frac{c}{\eta} \quad (15)$$

$$v_g = \frac{\partial \omega}{\partial k} = \frac{c^2}{v_{ph}} = c\eta \quad (16)$$

$$\eta = \sqrt{1 - \frac{\omega_p^2}{\omega^2}} = \sqrt{1 - \frac{n_0}{n_c}} \quad (17)$$

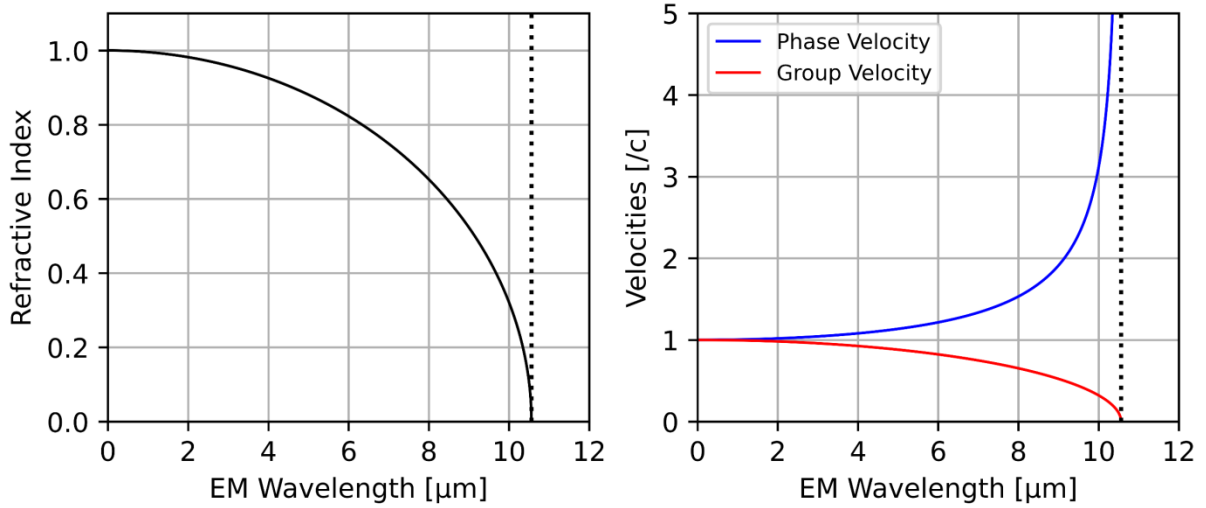


Figure 4: Refractive index of cold plasma (left) and phase and group velocities (right) as functions of EM wavelength. Dotted line depicts the wavelength corresponding to the electron plasma frequency that marks the boundary between underdense and overdense plasma.

Before moving on to the case of cold, magnetized plasma it is worthwhile to note that by setting the electron-plasma density in **Eq. 13** to zero one retrieves the wave equation for transverse EM waves in free space shown below by **Eq. 18**. The corresponding dispersion relation takes the form $k^2 c^2 = \omega^2$ with which $v_{ph} = c$ and $v_g = c$ can be calculated. The plane wave solutions to this wave equation will be used in **Section 2.3** to describe the properties of fc-pulses.

$$\mathbf{k} \times [\mathbf{k} \times \mathbf{E}] = -\frac{\omega^2}{c^2} \mathbf{E} \quad (18)$$

The behavior of transverse waves in cold plasma mimics that of free space propagation in the high frequency limit, i.e., $\omega \gg \omega_p$. Here, the value of the refractive index tends to one causing both phase and group velocities to approach c as in free space propagation. However, as seen in **Fig. 4**, the plasma response will vary considerably as the EM frequency approaches the value of the plasma frequency.

2. Theory

2.2.2 Cold, Magnetized Plasma

Without setting the background magnetic field in the plasma to zero, the plasma exhibits anisotropic behavior due to the cyclotron motion of the plasma electrons around the magnetic field lines. Returning to the Langevin equation of motion, **Eq. 8**, with $\mathbf{B}_0 \neq 0$, **Eq. 19** can be formulated.

$$\left(1 + i\frac{\nu}{\omega}\right)\mathbf{u} + \frac{ie}{m\omega}(\mathbf{u} \times \mathbf{B}_0) = \frac{-ie}{m\omega}\mathbf{E} \quad (19)$$

A Cartesian coordinate system is used with \mathbf{B}_0 along \hat{z} such that $\mathbf{u} \times \mathbf{B}_0 = B_0(u_y\hat{x} - u_x\hat{y})$. After substitution into the equation of motion, using $\mathbf{E} = E_x\hat{x} + E_y\hat{y} + E_z\hat{z}$ for the electric field and simplifying for Ω_c , the following matrix expression can be derived shown in **Eq. 20**:

$$\begin{pmatrix} \left(1 + i\frac{\nu}{\omega}\right) & i\frac{\Omega_c}{\omega} & 0 \\ -i\frac{\Omega_c}{\omega} & \left(1 + i\frac{\nu}{\omega}\right) & 0 \\ 0 & 0 & \left(1 + i\frac{\nu}{\omega}\right) \end{pmatrix} \begin{pmatrix} u_x \\ u_y \\ u_z \end{pmatrix} = \frac{-ie}{m\omega} \begin{pmatrix} E_x \\ E_y \\ E_z \end{pmatrix} \quad (20)$$

This equation is then inverted to obtain an expression for the column vector \mathbf{u} which can then be combined with results from manipulating Maxwell's equations as follows. By defining the angle θ between the EM wave's propagation vector \mathbf{k} and the local magnetic field \mathbf{B}_0 the wave number can be rewritten as components perpendicular, k_\perp , or parallel, k_\parallel , to the magnetic field or with sines and cosines as $\mathbf{k} = k_\perp\hat{x} + k_\parallel\hat{z} = k \sin\theta \hat{x} + k \cos\theta \hat{z}$. This definition of \mathbf{k} and the use of $\mathbf{E} = E_x\hat{x} + E_y\hat{y} + E_z\hat{z}$ are substituted into the $\mathbf{k} \times \mathbf{k} \times \mathbf{E}$ term from combining Faraday and Ampere's laws. Here, $\eta = kc/\omega$ has been used to further simplify the equation.

$$\begin{pmatrix} 1 - \eta^2 \cos^2\theta & 0 & \eta^2 \sin\theta \cos\theta \\ 0 & 1 - \eta^2 & 0 \\ \eta^2 \sin\theta \cos\theta & 0 & 1 - \eta^2 \sin^2\theta \end{pmatrix} \begin{pmatrix} E_x \\ E_y \\ E_z \end{pmatrix} = \frac{ien_0}{\epsilon_0\omega} \begin{pmatrix} u_x \\ u_y \\ u_z \end{pmatrix} \quad (21)$$

The inverted form of **Eq. 20** is combined with **Eq. 21** along with several substitutions to simplify the expression. These substitutions include $U = 1 + i\nu/\omega$, $X = \omega_p^2/\omega^2$, $Y = \Omega_c/\omega$, $S = 1 - XU/(U^2 - Y^2)$, $D = -XY/(U^2 - Y^2)$, $P = 1 - X/U$, and finally $R = S + D$, and $L = S - D$. This results in **Eq. 22** for which the determinant of the 3x3 matrix must equal zero for non-trivial solutions of the electric field, i.e., $\mathbf{E} \neq 0$. Setting the determinant to zero and solving results in a quadratic equation in η^2 given by **Eq. 23**. There are generally two solutions or roots to this equation, denoted as η_+ and η_- , associated with two orthogonal polarization states of the EM wave. Each state can propagate in forward or backwards direction as $\sqrt{\eta_\pm^2} = \pm\eta_\pm$.

$$\begin{pmatrix} S - \eta^2 \cos^2\theta & -iD & \eta^2 \sin\theta \cos\theta \\ iD & S - \eta^2 & 0 \\ \eta^2 \sin\theta \cos\theta & 0 & P - \eta^2 \sin^2\theta \end{pmatrix} \begin{pmatrix} E_x \\ E_y \\ E_z \end{pmatrix} = 0 \quad (22)$$

$$(S\sin^2\theta + P\cos^2\theta)\eta^4 - [RL\sin^2\theta + SP(1 + \cos^2\theta)]\eta^2 + PRL = 0 \quad (23)$$

2. Theory

Solving **Eq. 23** for η^2 results in the Appleton-Hartree equation shown in **Eq. 24** for collisionless plasma. Historically, the Appleton-Hartree equation [37]–[39], [41] has been used in the study of the propagation of radio waves through the Earth’s ionosphere, a layer of magnetized plasma between 75 km and several hundred kilometers above the surface of the Earth. While the scientists who developed this equation and the theory behind it almost 100 years ago might not have imagined it being applied to laser-plasma accelerators, with a few modifications, it will prove useful in investigating relativistic plasma effects found in the vicinity of a laser driver in a LWFA setup.

$$\eta_{\pm}^2 = 1 - \frac{\left(\frac{\omega_p}{\omega}\right)^2}{1 - \frac{\left(\frac{\Omega_c}{\omega}\right)^2 \sin^2 \theta}{2\left(1 - \left(\frac{\omega_p}{\omega}\right)^2\right)} \pm \sqrt{\frac{\left(\frac{\Omega_c}{\omega}\right)^4 \sin^4 \theta}{4\left(1 - \left(\frac{\omega_p}{\omega}\right)^2\right)^2} + \left(\frac{\Omega_c}{\omega}\right)^2 \cos^2 \theta}} \quad (24)$$

2.2.3 Resonance and Reflection Points of the Appleton-Hartree Equation

In most text books on plasma physics, the Appleton-Hartree equation is described first in two cases: parallel ($\theta = 0^\circ$) and perpendicular ($\theta = 90^\circ$) propagation of the EM wave relative to the magnetic field vector. Subsequently, the case of arbitrary angle of propagation is handled. Of primary interest in this thesis is in identifying cases where the refractive index tends towards an extreme value of zero or infinity as will become clear later. Such values of the plasma’s refractive index are seen at resonance and reflection points. A resonance point in plasma is ascribed to the case where the phase velocity of the EM wave is zero and the refractive index of the plasma infinite ($v_{ph} = 0$ and $\eta = \infty$). Classically, the wave is strongly absorbed in this condition. In contrast, a reflection point is defined when the phase velocity approaches infinity and the refractive index approaches zero ($v_{ph} = \infty$ and $\eta = 0$). In this case the EM wave is reflected from such a plasma, and an evanescent component of the wave penetrates a short distance into the overdense plasma.

Due to the number of free parameters (e.g. angle of propagation, polarization state, plasma and cyclotron frequencies), it can be difficult to keep track of the various resonance and reflection frequencies and when they play a role for a specific EM wave in the plasma. For the sake of brevity, the relevant frequencies will be listed here for the three propagation cases mentioned above.

For parallel propagation, ($\theta = 0^\circ$), the eigenstates of the EM wave are circularly polarized. The left-handed circularly polarized mode (LCP) has a resonance frequency at the ion-cyclotron frequency Ω_{ci} as any ions in the plasma will rotate in the same direction as an LCP wave. Since this work considers ions to be immobile, this resonance frequency will be ignored. The reflection frequency for the LCP wave ω_{01} is given by **Eq. 25** below.

$$\omega_{01} = \frac{1}{2} \left[-\Omega_c + \left(\Omega_c^2 + 4\omega_p^2 \right)^{1/2} \right] \quad (25)$$

2. Theory

The right-handed circularly polarized mode (RCP) rotates in the same orientation as the plasma electrons' cyclotron motion around the magnetic field and so the RCP mode exhibits a resonance frequency at the electron-cyclotron frequency Ω_c . The RCP's reflection point is at the frequency ω_{02} given by **Eq. 26** below. The difference in refractive index between the LCP and RCP modes can lead to a rotation of a linearly polarized EM wave, which is the basis for Faraday rotation measurements used often in plasma physics both in the lab and in astrophysics [42]–[44].

$$\omega_{02} = \frac{1}{2} \left[\Omega_c + (\Omega_c^2 + 4\omega_p^2)^{1/2} \right] \quad (26)$$

For perpendicular propagation, ($\theta = 90^\circ$), the eigenstates of the system are linearly polarized and the two orthogonal states are typically named *ordinary* and *extraordinary*. The ordinary- or O-wave lies in the plane parallel to \mathbf{B} (perpendicular to the plane of electron-cyclotron motion). Accordingly, the O-wave exhibits the same behavior as it would in non-magnetized plasma. It has a reflection point at the electron-plasma frequency ω_p , but no resonance points. The extraordinary- or X-wave encounters very different plasma. The X-wave's polarization lies in the plane of electron-cyclotron motion, has a resonance at the upper-hybrid frequency ω_{uh} given by **Eq. 27** and two reflection points given by ω_{01} and ω_{02} . This will be of considerable interest later on due to the fact that for frequencies $\omega_{uh} < \omega < \omega_{02}$ the X-wave is evanescent which can be exploited experimentally in the LWFA setup.

$$\omega_{uh} = \sqrt{\Omega_c^2 + \omega_p^2} \quad (27)$$

$$\omega_{0\pm}^2 = \frac{1}{2} (\omega_p^2 + \Omega_c^2) \pm \left[\frac{1}{4} (\omega_p^2 + \Omega_c^2)^2 - \omega_p^2 \Omega_c^2 \cos^2 \theta_{kB} \right]^{1/2} \quad (28)$$

In the general case, the EM wave travels with an arbitrary angle θ , here renamed θ_{kB} for clarity, to the local magnetic field. Two resonance frequencies can be defined using this angle following **Eq. 28**. The sum of the square of these two frequencies gives the value of the squared upper-hybrid frequency ω_{uh} . **Figure 5** shows how the ω_{0+} resonance frequency varies between Ω_c and ω_{uh} for changing propagation angle and how resonance frequency ω_{0-} falls from a value of ω_p to zero for increasing angle θ_{kB} . The figures have been plotted here for the case $\Omega_c > \omega_p$ due to the fact that for tenuous plasma the EM wave's angular frequency is also significantly larger than the plasma frequency.

$$\eta_{\theta_{EB}} = \left(\frac{\cos^2 \theta_{EB}}{\eta_+^2} + \frac{\sin^2 \theta_{EB}}{\eta_-^2} \right)^{-1/2} \quad (29)$$

Returning to the Appleton-Hartree equation itself, an analogy to optics in anisotropic crystals is made. The AH equation can be used to calculate the refractive indices of orthogonal polarization states (η_+ and η_-) for any propagation angle θ_{kB} of the EM wave. These indices represent the extrema indices analogous to the extraordinary and ordinary indices in a crystal. For the case of perpendicular

2. Theory

or near-perpendicular propagation ($\theta_{kB} \approx 90^\circ$), the question arises as to what refractive index a linearly polarized EM wave experiences in the plasma if its electric field is not aligned perfectly to the

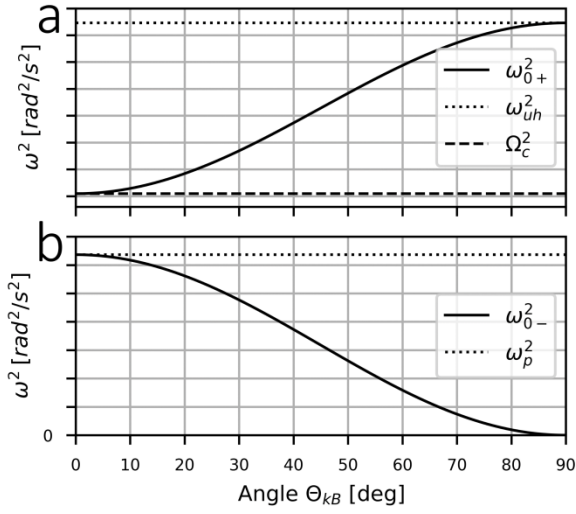


Figure 5: $B = 15.3$ kT, $n_e = 1 \cdot 10^{19}$ cm⁻³. (a) shows ω_{0+}^2 between Ω_c^2 and ω_{uh}^2 for varying propagation angle of the EM wave to the local magnetic field. (b) shows relative value of ω_{0-}^2 between ω_p^2 and zero.

magnetic field, **Eq. 29** is used to define an effective refractive index $\eta_{\theta_{EB}}$ of a linearly polarized wave with an electric field at an angle θ_{EB} to the local magnetic field in the plasma.

In lieu of using an effective refractive index for a linearly polarized wave oriented obliquely to the system's primary axes, it is also accurate to decompose the EM waves electric field onto the fast and slow axes of the system and to calculate the accumulated phase difference between the decomposed components. As described later in **Section 5.1**, this approach will not be necessary in the current work.

2.3 Few-Cycle Laser Pulses

Following the descriptions found in [46]–[49], the mathematics for representing fc-pulses will be presented. These equations are the foundation for understanding and modeling electromagnetic waves in vacuum as well as in various media found in the laboratory such as glass and cold plasma. The topics covered will progress from linearly polarized plane waves, to the temporal and spatial descriptions of fc-pulses and finally the use of fc-pulses in imaging systems.

2.3.1 Linearly Polarized Plane Waves

The free-space wave equation for EM waves, **Eq. 18**, was derived in **Section 2.2.1** after setting the charge density and current densities in Maxwell's equations to zero. These assumptions correspond to propagation in vacuum at low electric field amplitudes where solutions to the wave equation can be written as monochromatic plane waves. Such a wave can be described with an electric field oscillating in \hat{x} with angular frequency $\omega = 2\pi\nu$ and propagating in \hat{z} with wave vector $\mathbf{k} = k_z\hat{z}$ and wave

O-wave or X-wave case. By defining the angle θ_{EB} as the angle between the EM wave's electric field and the local magnetic field in the plasma, one can define the resulting refractive index as seen in **Eq. 29**. This equation is used for calculating the refractive index experienced by an EM wave in a uniaxial crystal with refractive indices defined for the fast and slow waves [45]. Strictly speaking, angle θ_{EB} in **Eq. 29** is the angle between the uniaxial crystal's optical axis and the k-vector of the EM wave. Since the AH equation already gives the two possible extrema of refractive indices for an EM wave with a wave vector propagating with θ_{kB} relative to the local

2. Theory

number $k_z = 2\pi\eta/\lambda_0$ where the refractive index of vacuum is one, i.e., $\eta = 1$. The wavelength λ_0 and linear frequency ν are related as $c = \lambda_0\nu$ and the electric field can be written as in **Eq. 30**.

$$\mathbf{E}(z, t) = E_x \exp[i(\omega t - k_z z)] \hat{x} \quad (30)$$

For propagation through a medium, the refractive index describes the material response to the EM wave. $\eta = \sqrt{\varepsilon/\varepsilon_0}$ shows the relationship between a non-magnetic material's refractive index η , its complex and frequency dependent electric permittivity ε , and the permittivity of vacuum ε_0 . Generally, the electric permittivity of a material is written as a tensor, but for a linear, isotropic, dielectric medium like glass, or cold, unmagnetized plasma, the electric permittivity tensor is diagonal and each element is the same function of frequency and wave vector, $\varepsilon(\omega, \mathbf{k})$. In contrast, an anisotropic material response, such as in magnetized plasma, is described by an electric permittivity tensor where each element might be a different function of ω and \mathbf{k} , resulting in different refractive indices depending on the direction, polarization and frequency of the propagating wave. For the purposes of describing fc-pulses and material dispersion, the medium of interest will be limited to a linear, isotropic, dielectric such as normal fused silica or BK7 glass.

2.3.2 Few-Cycle Laser Pulses and Dispersion

Equation 30 represents a solution to the wave equation describing a linearly polarized plane wave that exists for all time and space. While mathematically useful, a more physical representation of the EM field used in laboratory experiments is necessary. While not the most typical pulse shape found in the laboratory, the Gaussian profile is most often used to present the basic features of pulsed lasers. An electric field following a Gaussian temporal profile is given in **Eq. 31** and its corresponding Gaussian spectral profile in **Eq. 32**. The two are related via the Fourier transform pair described in several text books on optics or signals processing [50].

$$E_G(t) = E_0 \exp\left(-2\ln 2 \frac{(t - t_0)^2}{\Delta t^2}\right) \exp(-i\omega_0 t) \exp(i\phi(t)) \exp(i\phi_{CEP}) \quad (31)$$

$$\tilde{E}_G(\omega) = \tilde{E}_0 \exp\left(-2\ln 2 \frac{(\omega - \omega_0)^2}{\Delta\omega^2}\right) \exp(i\phi(\omega)) \quad (32)$$

E_0 and \tilde{E}_0 are the temporal and spectral field amplitudes, respectively. Δt and $\Delta\omega$ are the full width at half maximum (FWHM) temporal duration and spectral width of the corresponding temporal intensity profile and spectral intensity profiles. The temporal field distribution is centered at t_0 and is sinusoidally modulated at the carrier frequency ω_0 which is typically the central frequency in the spectral distribution but is better defined via a weighted average for spectral profiles that do not follow a smooth distribution. The temporal phase is characterized by two other terms. First, the Carrier-Envelope-Phase ϕ_{CEP} , which determines the phase shift between the peak of the Gaussian envelope and the underlying sinusoidal modulation, and second, a temporal phase function $\phi(t)$, whose

2. Theory

temporal derivative shows the shift in the carrier frequency over the duration of the pulse. Finally, the spectral phase function $\phi(\omega)$, gives the phase of each spectral component in the spectral distribution.

$$\Delta\omega \geq \frac{2\pi\kappa}{\Delta t} \quad (33) \quad \Delta\lambda \geq \frac{\lambda_0^2\kappa}{c\Delta t} \quad (34)$$

The Fourier relationship between the spectral and temporal domains presents certain challenges to creating and controlling fc-pulses. From this relationship, it follows that pulses in the visible and near-infrared spectra with few-cycle duration (~3-10 fs) must have in their spectral domains considerable spectral bandwidth. This can be characterized via the Time-Bandwidth-Product (TBP) κ and **Eqs. 33** and **34** that show the relationships between temporal duration and bandwidth expressed in frequency and wavelength. Here, Δt is again the intensity FWHM pulse duration, $\Delta\omega$ the spectral intensity's FWHM angular frequency bandwidth, λ_0 the spectral distribution's central wavelength, and $\Delta\lambda$ spectral intensity's FWHM bandwidth in wavelength. Lower-case kappa κ is the TBP for a given temporal intensity distribution. For example, a Gaussian pulse envelope ($\kappa = 0.441$) with an intensity FWHM duration of 4 fs centered at 750 nm wavelength requires a spectral intensity FWHM bandwidth of 207 nm, and a bandwidth of almost 534 nm if spectral amplitudes down to 1% of the maximum are considered. Real laser pulses do not exactly follow Gaussian distributions in frequency and time; however, the Fourier relationship remains valid and spectral intensity bandwidths of over an octave (doubling of frequency) are to be expected when working with fc-pulses.

$$I(t) = \varepsilon_0 c \cdot \text{Re}[E(t)]^2 = \varepsilon_0 c E_0^2 \exp\left(-4\ln 2 \frac{(t-t_0)^2}{\Delta t^2}\right) \cos^2(\phi_{CEP} + \phi(t) - \omega_0 t) \quad (35)$$

$$\langle I(t) \rangle = \frac{\varepsilon_0 c}{T} \int_{t-T/2}^{t+T/2} E^2(t') dt' = \frac{\varepsilon_0 c}{2} E(t) E^*(t) = \frac{\varepsilon_0 c}{2} E_0^2 \exp\left(-4\ln 2 \frac{(t-t_0)^2}{\Delta t^2}\right) \quad (36)$$

Methods exist to gain direct information about the electric field of fc-pulses **[51]**, **[52]**; however, for most applications concerning LWFA, the cycle-averaged temporal intensity distribution of the pulse is of primary interest. **Eq. 35** and **36** show the relationship between the complex electric field $E(t)$, its complex conjugate $E^*(t)$, and the temporal intensity distribution, with **Eq. 35** giving the instantaneous temporal intensity $I(t)$ and **Eq. 36** the cycle-averaged, temporal intensity envelope of the pulse $\langle I(t) \rangle$. The results for the previous Gaussian temporal distribution have also been given as the right-most terms in the equations. **Figure 6** below shows the resulting electric field and intensity distributions for a 10 fs FWHM laser pulse centered at 800 nm.

It is important to keep in mind, as is also described in **Section 2.3.3**, that linear plots of field amplitude or intensity versus time or space can be misleading when dealing with laser intensities in the 10^{19} W/cm² range as in LWFA. Due to the finite spectral bandwidth of the pulse, the intensity distribution cannot follow a step-like function but instead has a rise and fall time characterized by the Temporal Intensity Contrast or TIC. A Gaussian pulse with 30 fs FWHM pulse duration and 10^{19} W/

2. Theory

cm² peak intensity, rises to an intensity of 10¹¹ W/cm² already 77 fs before the peak of the laser pulse. Several effects in the laser system can cause such intensities, capable of ionizing material, to be achieved even up to several 100 femtoseconds from the laser's peak intensity [53], [54].

$$\phi(\omega) = - \int_0^L \beta(\omega, l) dl = - \frac{\omega}{c} \int_0^L \eta(\omega, l) dl \quad (37)$$

Looking again at the pulse's spectral phase, one sees more precisely why such bandwidths are, at least experimentally, problematic. The spectral phase $\phi(\omega)$ consists of the propagation constant $\beta(\omega)$ integrated along the propagation path l of the laser pulse, see **Eq. 37**. For homogeneous media in space and time, the integration becomes a product but the heart of the matter lies in the dispersive properties of the medium being traversed. Materials can be designed to have a refractive index independent of frequency over a relatively small bandwidth [55], but in the visible and near-infrared (VIS-NIR) spectrum, and more problematic over an octave of bandwidth, materials will inevitably exhibit a non-negligible amount of dispersion, and the non-zero spectral phase accumulated during propagation through the medium will begin to temporally distort the fc-pulse to longer pulse durations.

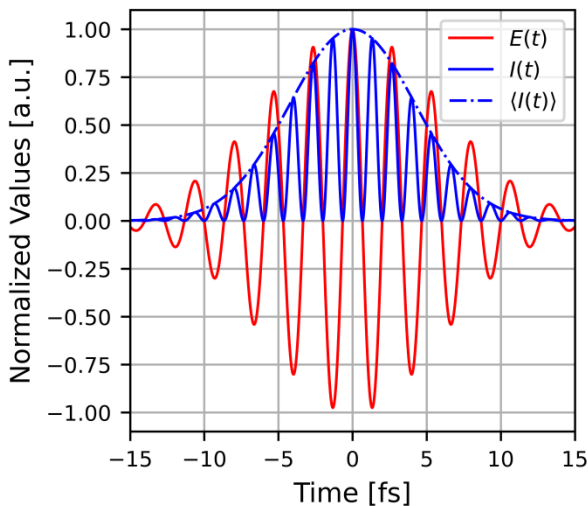


Figure 6: Electric field (red), temporal intensity (blue) and intensity envelope (blue dot-dashed) of a 10 fs FWHM duration Gaussian pulse.

The propagation constant $\beta(\omega)$ is can be expressed as a Taylor expansion centered on the pulse's central wavelength or frequency. The Taylor expansion model is broken down into orders of dispersion. **Equation 38** shows the expansion of the spectral phase up to fifth order dispersion β_5 . When investigating the FWHM of the pulse's temporal intensity profile I_{FWHM} the first two orders, β_0 and β_1 , can be ignored as they represent the absolute phase and the group velocity of the pulse, neither of which change the shape of the temporal intensity profile. Removing these two orders is the same as fitting a line through the spectral phase at the central

laser frequency and subtracting it from the spectral phase profile. In the temporal domain, this amounts to removing any non-zero carrier envelope phase and any temporal shift of the pulse. Group velocity dispersion (GVD), given by β_2 , represents the quadratic dispersion around the laser's central frequency and results in a symmetric broadening of the pulse's temporal shape. The third (TOD), fourth (FOD), and fifth order (FiOD) terms (β_3 , β_4 , and β_5 , respectively) are typically ignored for pulses longer than few-cycle, but will cause a pulse distortion for ultra-short pulse durations. **Equations 39-43** show the analytical forms of the dispersion terms and their units as a function of angular frequency and wavelength.

2. Theory

$$\phi(\omega) = -L \left[\beta_0 + \beta_1(\omega - \omega_0) + \frac{\beta_2}{2}(\omega - \omega_0)^2 + \frac{\beta_3}{6}(\omega - \omega_0)^3 + \frac{\beta_4}{24}(\omega - \omega_0)^4 + \frac{\beta_5}{120}(\omega - \omega_0)^5 \right] \quad (38)$$

$$\beta_1 = \frac{1}{c} \left(n(\omega) + \omega \frac{dn}{d\omega} \right) = \frac{1}{c} \left(n(\lambda) - \lambda \frac{dn}{d\lambda} \right) \left[\frac{fs}{mm} \right] \quad (39)$$

$$\beta_2 = \frac{1}{c} \left(2 \frac{dn}{d\omega} + \omega \frac{d^2n}{d\omega^2} \right) = \frac{\lambda^3}{2\pi c^2} \frac{d^2n}{d\lambda^2} \left[\frac{fs^2}{mm} \right] \quad (40)$$

$$\beta_3 = \frac{1}{c} \left(3 \frac{d^2n}{d\omega^2} + \omega \frac{d^3n}{d\omega^3} \right) = \frac{-\lambda^4}{4\pi^2 c^3} \left(3 \frac{d^2n}{d\lambda^2} + \lambda \frac{d^3n}{d\lambda^3} \right) \left[\frac{fs^3}{mm} \right] \quad (41)$$

$$\beta_4 = \frac{1}{c} \left(4 \frac{d^3n}{d\omega^3} + \omega \frac{d^4n}{d\omega^4} \right) = \frac{\lambda^5}{2\pi^3 c^4} \left(\frac{\lambda^2}{4} \frac{d^4n}{d\lambda^4} + 2\lambda \frac{d^3n}{d\lambda^3} + 3 \frac{d^2n}{d\lambda^2} \right) \left[\frac{fs^4}{mm} \right] \quad (42)$$

$$\beta_5 = \frac{1}{c} \left(5 \frac{d^4n}{d\omega^4} + \omega \frac{d^5n}{d\omega^5} \right) = \frac{-\lambda^6}{16\pi^4 c^5} \left(\lambda^3 \frac{d^5n}{d\lambda^5} + 15\lambda^2 \frac{d^4n}{d\lambda^4} + 60\lambda \frac{d^3n}{d\lambda^3} + 60 \frac{d^2n}{d\lambda^2} \right) \left[\frac{fs^5}{mm} \right] \quad (43)$$

Starting with an initial Gaussian pulse centered at 750 nm with an I_{FWHM} pulse duration of 4 fs, **Fig. 7** shows both the initial pulse as well as the pulse after propagation through 1 mm of fused silica glass. The Sellmeier equation was used to calculate the refractive index and its derivatives as a function of wavelength [56]. One sees that the 4 fs FWHM pulse duration has been stretched to 28 fs, the pulse's temporal distribution is no longer symmetric and the instantaneous carrier frequency is red-shifted earlier in the pulse and blue-shifted later in the pulse; known as temporal up-chirp.

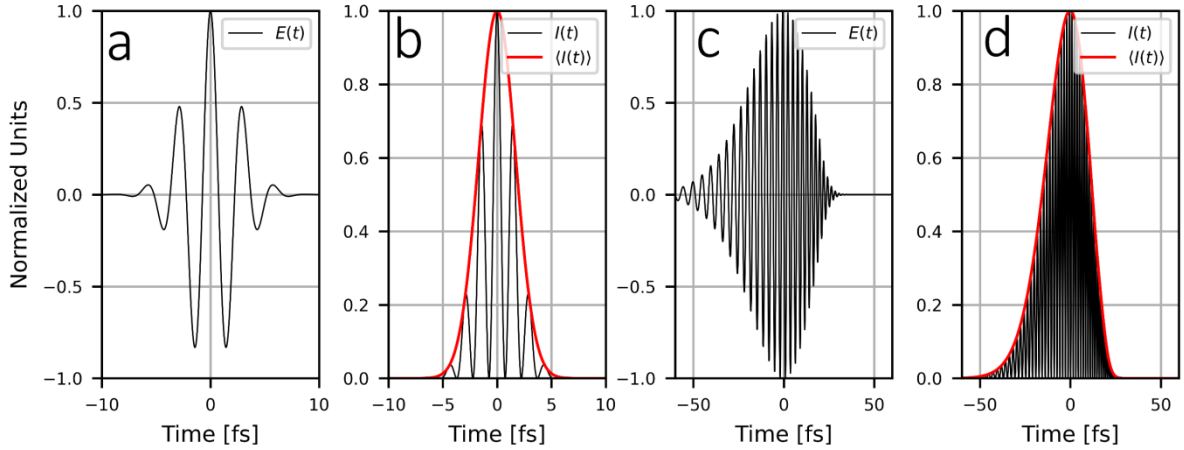


Figure 7: Plots (a) and (b) show the electric field and intensity distributions of a Fourier-limited 4 fs FWHM Gaussian pulse. Plots (c) and (d) show the same pulse after having propagated through 1 mm fused silica. The resulting FWHM pulse duration is approximately 28 fs.

As the fc-pulse propagates through a medium, it is of interest for several applications to look at the mapping between the pulse's instantaneous carrier frequency and time. This property of the pulse, mentioned before as temporal chirp, arises due to the varying group velocity across the pulse's spectral bandwidth in a given medium. Defined by **Eq. 44**, group velocity represents the speed at which the intensity envelope of a pulse centered at a specific frequency travels through a medium. As an example, the group velocity in fused silica varies by about 3% over the spectral range of 400 nm to 1000 nm. The longer wavelength components of the pulse will travel faster through the medium than the shorter wavelengths, causing the central wavelength or frequency of the pulse to vary across the pulse's temporal width. The instantaneous carrier frequency, **Eq. 45**, can be calculated from the

2. Theory

pulse's temporal phase which must be extracted from the complex temporal electric field. Pulses with a "well-behaved" or linear temporal chirp are quite useful for plasma diagnostics such as in Frequency Domain Interferometry and STAMP [30], [31].

$$v_g = \beta_1^{-1} = \frac{c}{n - \lambda \frac{dn}{d\lambda}} \quad (44)$$

$$\omega(t) = \omega_0 + \frac{d\phi(t)}{dt} \quad (45)$$

2.3.3 Spatial Distribution of Gaussian Beams

The basics of an fc-pulse's temporal properties were described in **Section 2.3.2**. Building on that topic, the matter of focusing and spatial propagation of Gaussian pulses can be addressed. Ignoring higher Hermite-Gaussian modes and concentrating on a spherical Gaussian wave in the paraxial approximation; the monochromatic electric field can be expressed as shown in **Eq. 46**.

$$E(x, y, z, t) = E_0 \frac{w_0}{w(z)} \exp \left[ik \left(\frac{x^2 + y^2}{2R(z)} \right) \right] \exp \left[\frac{-(x^2 + y^2)}{w^2(z)} \right] \exp \left[i \left(kz - \omega t - \arctan \left(\frac{\lambda z}{\pi w_0^2} \right) \right) \right] \quad (46)$$

The first exponential term gives the phase attributed to a spherical wavefront approximated by a parabolic surface with x and y being the transverse directions and z being the direction of propagation. $R(z) = z[1 + (\pi w_0^2/\lambda z)^2]$ is the radius of curvature of the spherical wavefronts at a distance z from the plane of minimum beam waist w_0 . Diverging wavefronts have a positive R and converging wavefronts a negative R . The beam waist squared, $w^2(z) = w_0^2[1 + (\lambda z/\pi w_0^2)^2]$, represents the transverse beam radius at which the electric field falls to $e^{-1} \approx 0.368$ of its maximum, or where the intensity falls to $e^{-2} \approx 0.135$ of its maximum. Use of the paraxial approximation to investigate the properties of the wave is valid in the limit where $(x^2 + y^2) \ll R^2$. The second exponential term in **Eq. 46** defines the transverse Gaussian profile of the beam while the final exponential term modifies the plane wave's phase with that of the zero order Hermite-Gaussian phase given by the arctangent term. Both expressions for $R(z)$ and $w(z)$ can be simplified by defining the Rayleigh range $z_R = \pi w_0^2/\lambda$. A Gaussian beam is said to be collimated for $-z_R \leq z \leq z_R$ and at $z = \pm z_R$ the transverse area of the beam is doubled compared to its area at the plane of minimum beam waist. This corresponds to an increase in the beam waist as $w(\pm z_R) = \sqrt{2}w_0$. Moving to distances $z \gg z_R$, one speaks of far-field propagation with a half-angle divergence of $\theta_{FF} = \lambda/\pi w_0$ of the beam. In this space, the beam size increases linearly and all wavefront-radii of curvature are centered on the location of the minimum beam waist.

Equation 46 can be rewritten as **Eq. 47** to represent the transverse intensity profile of the Gaussian wave as it propagates along the z -direction. The minimum beam waist can be rewritten to represent the spatial I_{FWHM} measurement (FWHM spot diameter in intensity D_{FWHM}) using $w_0 = D_{FWHM}/\sqrt{2 \ln 2}$ which is more typical for laboratory work.

2. Theory

$$I(z, r) = \frac{\varepsilon_0 c}{2} E_0^2 \left(\frac{w_0}{w(z)} \right)^2 \exp\left(\frac{-2r^2}{w^2(z)} \right) = I_0 \left(\frac{w_0}{w(z)} \right)^2 \exp\left(\frac{-2r^2}{w^2(z)} \right) \quad (47)$$

Figure 8 uses **Eq. 47** to plot the intensity profile of a $D_{FWHM} = 10 \mu\text{m}$ focused Gaussian beam with 800 nm wavelength. The Rayleigh range is $283 \mu\text{m}$ indicated by the dashed black lines. The solid black contours show the I_{FWHM} spot size at each plane of propagation while black/white color scale presents the beam's intensity in a logarithmic scale. If ionization is expected above 10^{11} W/cm^2 , as delineated by the dotted lines corresponding to -80 dB for a peak intensity of 10^{19} W/cm^2 , then the created plasma column is approximately $200 \mu\text{m}$ in diameter at the vacuum focal position, $z = 0 \mu\text{m}$ (see **Section 4.1**). Note that the divergence of the FWHM spot size is smaller than the -80 dB contour lines, increasing from $10 \mu\text{m}$ at the focal plane to $14.14 \mu\text{m}$ at one Rayleigh length away (doubling of FWHM area). Similar to considering the temporal distribution of the laser pulse, relying on the pulse's FWHM spatial measurement can be misleading depending on the physics being investigated.

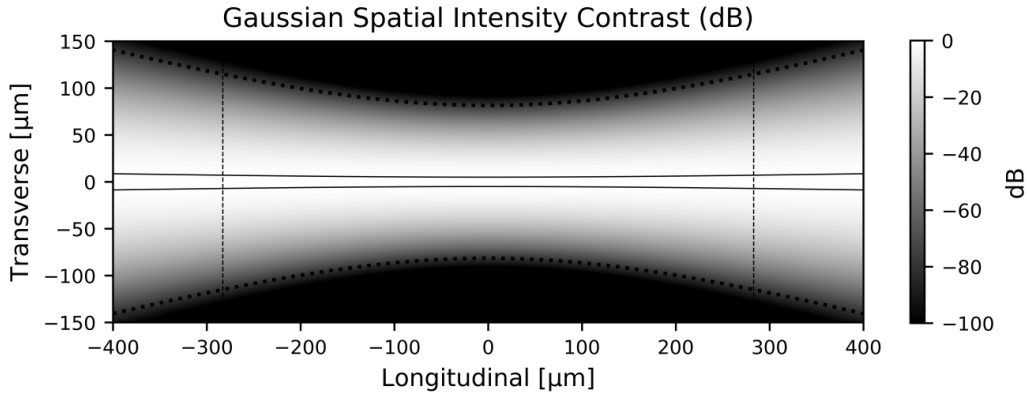


Figure 8: Spatial intensity contrast of a Gaussian beam. Longitudinal solid lines show the contour of the FWHM intensity. Transverse vertical dashed lines are show the Rayleigh Range as measured from the $0 \mu\text{m}$ longitudinal position. Curved dashed contour lines mark the -80 dB intensity boundary.

For the purposes of achieving relativistic laser intensities, a term which was described in Section 2.5, it is necessary to focus the laser pulse down from its beam diameter exiting the laser system of a few to several centimeters to a spot size of a few micrometers. Focusing in LWFA experiments is performed by a single optic such that the focused minimum beam waist w_{02} is significantly smaller than the minimum beam waist before the optic w_{01} , i.e., $w_{01} \gg w_{02}$. It follows that the focused minimum beam waist is then given by $w_{02} \cong f\lambda/\pi w_{01} = f\theta_{FF}$, with central wavelength λ of the pulse and focal length f of the focusing optic. This can be further simplified to $w_{02} \cong 2\lambda \cdot F_{\#}/\pi$ if the F-number ($F_{\#}$) is known, with $F_{\#} = \frac{\text{Focal Length}}{\text{Beam Diameter on Optic}}$. More useful is perhaps the equation $D_{FWHM} = \sqrt{8 \ln 2} \lambda F_{\#}/\pi$ giving the FWHM measurement of the focal spot after the focusing optic.

2.3.4 Shadowgraphic Imaging Theory

The necessity for generating and characterizing (see **Appendices B.1** and **B.2**) an fc-pulse becomes evident when the goal is to image the plasma wave created in a plasma-based accelerator. Described

2. Theory

further in **Section 3.3.3**, the plasma wave has a characteristic scale-length λ_p that is inversely proportional to the square root of the plasma density n_e and moves through the plasma with v_g of the laser driver. For densities between $5 \cdot 10^{18} \text{ cm}^{-3}$ and $5 \cdot 10^{19} \text{ cm}^{-3}$, λ_p is in the range of $5 \text{ }\mu\text{m}$ to $15 \text{ }\mu\text{m}$ and $v_g \approx c$. For a simple sinusoidal density variation of the plasma wave with $\lambda_p = 10 \text{ }\mu\text{m}$, the recorded image of the plasma wave would appear blurred for an exposure time longer than $\approx \lambda_p/2c$ giving an upper limit to the fc-pulse duration of $\sim 15 \text{ fs}$, with shorter pulses allowing for higher detail.

The fc-pulses themselves are used to illuminate the volume of plasma being measured similar to how a camera flash illuminates a scene to be photographed. The setup of the imaging system is that of a shadowgraph in which a collimated light source, i.e., fc-pulse, enters the medium of interest, i.e., the plasma. The fields of the fc-pulse primarily gain phase components during propagation through the refractive index distribution of the plasma, while its amplitude remains mostly unchanged in the case of unmagnetized tenuous plasma. After exiting the plasma and propagating a distance the resulting distorted far-field intensity distribution of the fc-pulse can be viewed on a screen or imaged to a camera [57], [58]. The results give qualitative information about the refractive index distribution in the medium; however, quantitative methods have also been developed for certain cases [59]–[62].

The governing equations behind shadowgraphy will not be presented here as they are readily found with ample derivation in the previously cited literature. Though shadowgraphy lies at the core of the experimental setup described in this dissertation, the results and analysis that will be presented made no direct use of the omitted equations. Instead, comparisons between experimental results, numerical simulations and predictions given by magnetoionic theory were sufficient in explaining the features of interest found in the recorded shadowgrams. Nonetheless, the underlying equation describing shadowgraphy is given below by **Eq. 48** to give the reader a better understanding of how the variations in refractive index of the plasma translate to variations in intensity seen in the recorded shadowgram.

$$I_s = \frac{I_0}{1 + L \cdot D \cdot \nabla^2[\log(\bar{\eta})]} \quad (48)$$

Assuming no transverse displacement of the light rays propagating through the medium, no ray displacement between the medium and the observing screen, and a linear Jacobian in the derivation, the variation of the incident light's intensity I_0 seen at the observing plane I_s is given by **Eq. 48**. Here, D is the length of the medium along the propagation direction and L is the distance from the medium to the observation screen. $\bar{\eta}$ is the refractive index averaged over the length of the medium for a given ray and ∇^2 represents the second spatial derivative in the plane transverse to the ray's propagation direction. Shadowgraphy's sensitivity to $\nabla^2[\log(\bar{\eta})]$ makes it useful for imaging areas of plasma where the rate of change of the refractive index is large and varies over the transverse plane.

2.3.5 Coherent Imaging Theory

Use of an fc-pulse as the illumination source in shadowgraphy necessitates the understanding of coherent imaging theory because the resulting interference effects can be both beneficial and

2. Theory

burdensome to the recorded data. The following discussion on coherent imaging theory will assume a paraxial, aberration-free imaging system as the interference effects of coherent imaging are of primary concern. More information can be found in [50].

Using the subscripts *obj* for the object plane and *img* for the image plane one can define an electric field at either plane in terms of its transverse and temporal coordinates. Starting in the spatial domain $E_{obj}(x, z, t) = E_0(x, z, t)\exp[i\phi(x, z, t)]$ describes the electric field at the plane of the object (a specific plane along the $-y$ -axis) with transverse coordinates (x, z) at time t . The field amplitude E_0 can later be replaced by an envelope function, e.g., a Gaussian from **Eq. 31**, and the temporal dependence of the phase term $\phi(x, z, t)$ can be replaced by a carrier frequency term $\omega_0 t$. The field at the image plane is likewise described by $E_{img}(x, z, t)$ where the relationship between the two fields depends on the properties of the imaging system being used.

The properties of an aberration-free imaging system that play a primary role in the resulting resolution of the image are given by the Abbe diffraction limit $d = \lambda/2NA$, where d is the minimum distance between two points being resolved, λ is the illumination wavelength and NA is the numerical aperture of the imaging system. The NA defines the cone of light entering (in object space) and exiting (in image space) the imaging system, and is important because it defines the spatial frequencies of the object that can be collected by the imaging system and transferred to the image. The larger the NA of the system, the higher the spatial frequencies collected and the higher the spatial resolution of the image. Physically, a cone of light can be defined in image space by the radius of the exit pupil w_{XP} and the distance between the exit pupil and the image plane d_{XP} . As the electric field propagates from the object to the image, it is inevitably truncated in its transverse extent by a physical aperture in the imaging system, known as the aperture stop. The exit pupil is the aperture stop having been imaged into image-space. In the case of cylindrically symmetric optics, the entrance pupil, exit pupil and aperture stop is defined by using the circ function [50]. A circular exit pupil can be described by $P(x, z) = \text{circ}(\sqrt{x^2 + z^2}/w_{XP})$.

Knowing the system's NA from its exit pupil function $P(x, z)$ and the imaging distance d_{XP} brings the discussion back to transforming the fields from the object plane to the image plane. Mathematically, this can be performed in the spatial domain with the coherent impulse response of the system $h(x, z)$, or in the frequency domain with the coherent transfer function of the system $H(f_x, f_z)$ with spatial frequency coordinates (f_x, f_z) . Both functions are related to the exit pupil function. The impulse response function $h(x, z)$ is the inverse Fourier transform of the transfer function and will not be presented here. **Equation 49** shows the relationship between object and image electric fields as the convolution of the scaled object field with the coherent impulse response function. The \otimes symbol is the convolution operator and M_t is the transverse magnification of the imaging system. In a perfect imaging system the coherent impulse response function would be a delta function resulting in the

2. Theory

image field being the object field scaled by the transverse magnification. Every imaging system; however, has a non-ideal response function that inevitably limits the spatial resolution of the image.

$$E_{img}(x, z, t) = \frac{1}{|M_t|} h(x, z) \odot E_{obj}\left(\frac{x}{M_t}, \frac{z}{M_t}, t\right) \quad (49)$$

By transforming into the frequency domain, one can avoid the use of convolutions because the convolution of two functions in the spatial domain is equivalent to the product of their Fourier transforms in the frequency domain. With this approach, one rewrites the resulting image field as **Eq. 50** where \mathcal{F} and \mathcal{F}^{-1} denote the Fourier and inverse Fourier transforms, respectively.

$$E_{img}(x, z, t) = \mathcal{F}^{-1}\left\{\mathcal{F}\{h(x, z)\}\mathcal{F}\left\{\frac{1}{|M_t|}E_{obj}\left(\frac{x}{M_t}, \frac{z}{M_t}, t\right)\right\}\right\} \quad (50)$$

The coherent transfer function is the Fourier transform of the coherent impulse response function, i.e., $H(f_x, f_z) = \mathcal{F}\{h(x, z)\}$, and can be written directly in frequency-space using the pupil function where each spatial coordinate is scaled via λ and d_{XP} to represent a spatial frequency coordinate, i.e. $H(f_x, f_z) = P(-\lambda d_{XP} f_x, -\lambda d_{XP} f_z)$. By defining the cutoff frequency $f_0 = w_{XP}/(\lambda d_{XP})$ and using a circular exit pupil, the coherent transfer function can be expressed as $H(f_x, f_z) = \text{circ}\left[\sqrt{f_x^2 + f_z^2}/f_0\right]$. The cutoff frequency is the highest spatial frequency of the electric field (not intensity!) passed from the object plane to the image plane.

This description of imaging theory has barely scratched the surface of what can be found in the literature; however, it will help to later explain certain effects seen in the experimental data. For the time being, a simple example will be used for illustration. An aberration-free imaging system with $M_t = 1$ and a NA = 0.26 is assumed. The electric field at the plane of the object is modelled for two different cases of a Gaussian temporal laser pulse. The first, **Fig. 9a**, is centered at 750 nm with 6 fs FWHM pulse duration in intensity giving it a FWHM spectrum $\Delta\lambda$ of 138 nm. The second pulse, **Fig. 9b**, is centered at 900 nm, has a 3 fs FWHM duration and a $\Delta\lambda$ of almost 400 nm. The electric field amplitude over the transverse extent of the object plane is assumed to be constant.

A 20 μm diameter sphere centered in the object plane is used as a phase or amplitude object. The complex electric field at the object plane is multiplied by the term $\exp(i\omega_0 OPL/c)$ with ω_0 the central laser frequency of the illumination pulse and OPL being the optical path length, described as follows. The 20 μm sphere is assumed to be surrounded by vacuum with a refractive index $n_0 = 1$. The refractive index of the sphere, η , is allowed to be complex allowing for flexibility in choosing the optical properties of the sphere. For example, a water droplet as a pure phase object would use $\eta = 1.333 + 0i$, an underdense plasma as a pure phase object would use something like $\eta = 0.996 + 0i$, and an overdense plasma as a pure amplitude object would use something like $\eta = 0.0 + 3i$. The purely real refractive indices only affect the phase of the illumination pulse, while the purely imaginary indices only affect the amplitude of the illumination pulse. Refraction through the sphere/vacuum geometry as well as the dispersive properties of the sphere's refractive index are,

2. Theory

for this simplified model, ignored. Consequently, $OPL = 2Rn_0 + (\eta - n_0)L_s(x, z)$ with R the radius of the sphere and $L_s(x, z)$ is the straight-line path length of a ray traveling through the sphere/vacuum geometry parallel to the y-axis.

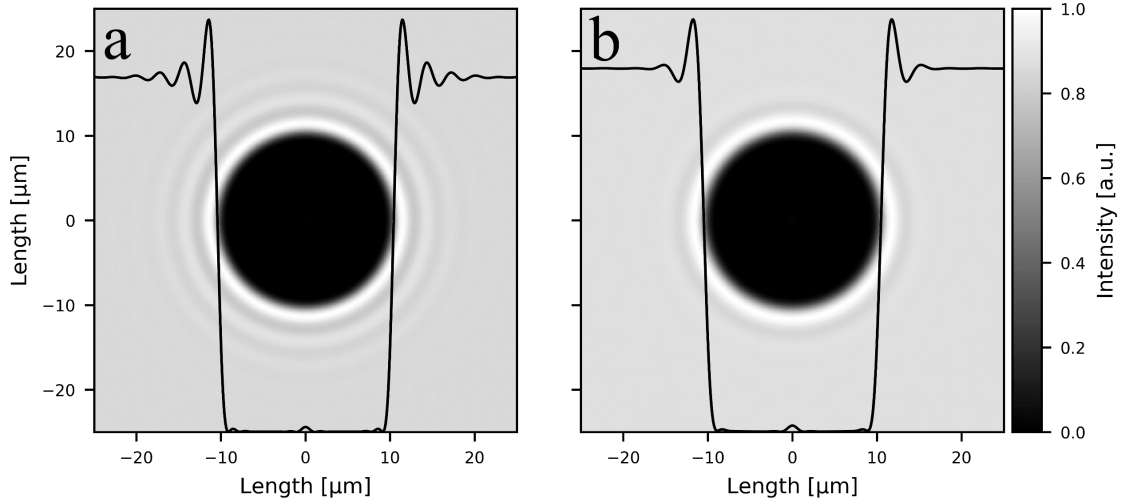


Figure 9: Simulated images of a 20 μm diameter opaque sphere illuminated by two different Gaussian laser pulses and imaged with an $M_t = 1$ and $\text{NA}=0.26$ imaging system. (a) results using a $\Delta t = 6$ fs at $\lambda_0 = 750$ nm, with 2.90 μm fringe period. (b) $\Delta t = 3$ fs at $\lambda_0 = 900$ nm, with 3.45 μm fringe period. Solid lines show the cross-sectional intensity distribution in each image to highlight the periodic interference rings.

Due to the coherent nature of the illuminating laser pulse and the diffraction limited imaging system, diffraction rings around the imaged object are expected. The number of visible rings will depend on the spectral bandwidth of the illuminating laser pulse, and the period of the rings will depend on the central wavelength of the spectrum. After illuminating the sphere as an opaque, 10x overcritical plasma, i.e., $\eta = \sqrt{1 - 10n_c/n_c} = 0.0 + 3i$, with a 6 fs pulse centered at 750 nm, **Fig. 9a** shows the resulting image with about four visible diffraction rings with constant period of 2.9 μm . Changing the illuminating pulse to a central wavelength of 900 nm and FWHM pulse duration of 3 fs, **Fig. 9b** shows an increase in the ring period to 3.45 μm (proportional to the increase in central wavelength) but the number of visible rings is significantly reduced. The drastic increase in bandwidth for a 3 fs FWHM pulse to almost 400 nm FWHM significantly reduces the coherence length [46] of the laser pulse resulting in fewer visible diffraction rings.

After changing the sphere to a phase object with $\eta = 0.5$, **Fig. 10a** and **d**, $\eta = 0.996$, **Fig. 10b** and **e**, and $\eta = 1.333$, **Fig. 10c** and **f**, the two FTL pulses (6 fs at 750 nm and 3 fs at 900 nm) were once again used. The resulting interference rings show the same general results as with the opaque sphere, i.e., larger ring period for longer central wavelength and fewer visible rings for shorter pulses due to the pulse's shorter coherence length, as well as a generally constant ring period for rings outside of the objects' ± 10 μm extent. It is important to remember that this coherent imaging model only uses the accumulated phase through the object. The model's primary goal is to recreate the diffraction rings surrounding the imaged object as will be further described in **Section 6.2**.

2. Theory

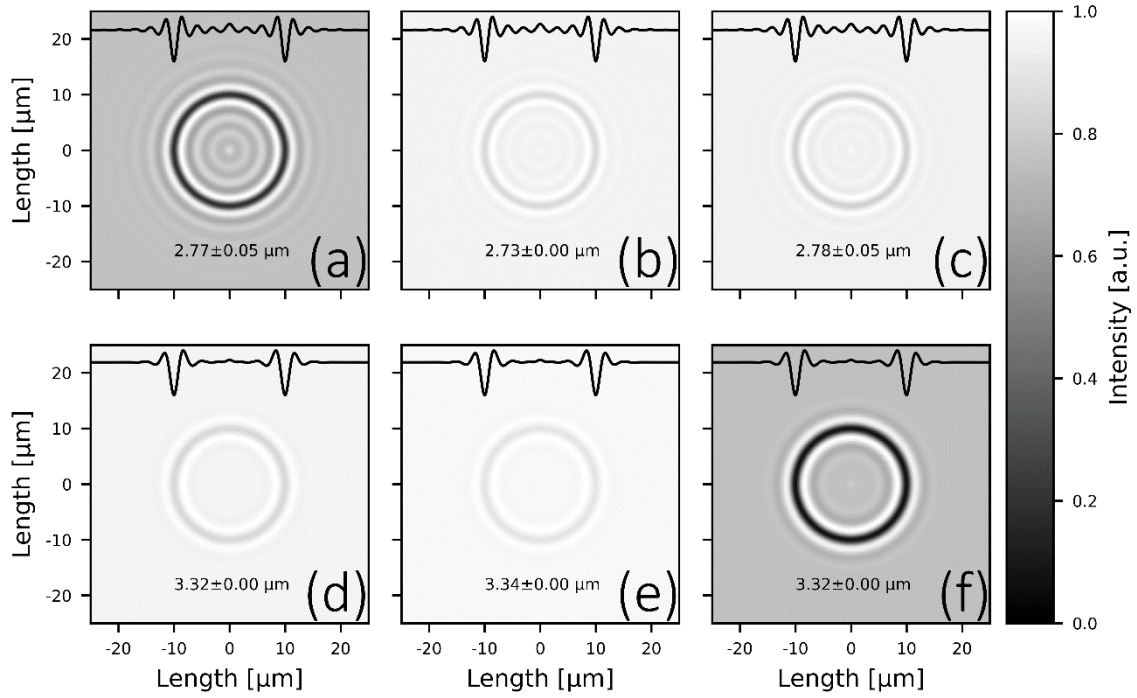


Figure 10: Simulated images of a 20 μm diameter transparent sphere illuminated by two different Gaussian laser pulses and imaged with an $M_t = 1$ and $\text{NA}=0.26$ imaging system. (a-c) show results using a 6 fs FWHM Gaussian pulse centered at 750 nm while (d-f) shows the results for a 3 fs FWHM pulse centered at 900 nm. The refractive index of the sphere is $\eta = 0.5$ in a and d, $\eta = 0.996$ in b and e, and $\eta = 1.333$ in c and f. The solid line in each plot shows the cross-sectional intensity distribution in each image to highlight the periodic interference rings. The cross-sections have been scaled to show the general form of the rings, while the grayscale colormaps have been normalized to show the difference in contrast of each image. Each subplot is also labelled with the mean \pm standard deviation of the rings' period.

2.4 Electron Motion in an Electro-Magnetic Field

As in all complex systems it is advantageous to analytically study a simplified version of the system. In this sub-chapter, the motion of a single electron in both a plane wave and a focused laser pulse will be investigated. The results will help to later understand the interaction between the driving laser and the plasma electrons in the LWFA experiments and as modelled via numerical simulations.

2.4.1 Single Electron Motion in a Plane Wave

Starting from an elliptically polarized plane wave propagating in \hat{z} given by its electric field (**Eq. 51**) and its magnetic field (**Eq. 52**), the trajectory of a single electron can be calculated. E_1 and E_2 are electric field amplitudes and ϕ is the phase of the wave given by $\phi = kz - \omega t$. The motion of the single electron is governed by the relativistic equation of motion (EoM), seen in **Eq. 53**, with the relativistic momentum of the electron \mathbf{p} , velocity \mathbf{u} , rest mass m , and charge q [63]. For simplicity, m and ω will be used instead of m_e and ω_L , respectively.

$$\mathbf{E} = E_1 \cos(\phi) \hat{\mathbf{x}} - E_2 \sin(\phi) \hat{\mathbf{y}} \quad (51)$$

$$\mathbf{B} = \frac{E_2}{c} \sin(\phi) \hat{\mathbf{x}} + \frac{E_1}{c} \cos(\phi) \hat{\mathbf{y}} \quad (52)$$

2. Theory

$$\frac{d\mathbf{p}}{dt} = \frac{d}{dt} \left[\frac{m\mathbf{u}}{\sqrt{1 - u^2/c^2}} \right] = q(\mathbf{E} + \mathbf{u} \times \mathbf{B}) \quad (53)$$

The transverse momentum of the electron can be derived by substituting both the expressions for \mathbf{E} and \mathbf{B} into the relativistic EoM. Furthermore, the temporal derivative of the wave's phase $d\phi/dt = (u_z/c - 1)\omega$ is substituted and integrated over the phase. This results in the relativistic momentum of the electron in $\hat{\mathbf{x}}$ and $\hat{\mathbf{y}}$ as shown in **Eqs. 54** and **55** with initial momentum in the x- and y-directions of p_{x0} and p_{y0} , respectively.

$$p_x = \frac{-qE_1}{\omega} \sin(\phi) + p_{x0} \quad (54)$$

$$p_y = \frac{qE_2}{\omega} [1 - \cos(\phi)] + p_{y0} \quad (55)$$

Coming to an expression for the relativistic momentum in $\hat{\mathbf{z}}$ is a little more involved. The resulting differential form for p_z from the steps listed above is given by $dp_z/dt = q\mathbf{u} \cdot \mathbf{E}/c$. From the conservation of power one can equate the change in electron's energy \mathcal{E} with time to the work done on the particle by the Coulomb force $d\mathcal{E}/dt = q\mathbf{u} \cdot \mathbf{E}$. By comparison to the differential form for p_z one sees the relationship $c \cdot dp_z/dt = d\mathcal{E}/dt$, which when integrated from the electron's rest energy $\mathcal{E}_0 = mc^2$ to \mathcal{E} gives the result shown in **Eq. 56**.

$$cp_z = \mathcal{E} - mc^2 \quad (56)$$

It is desirable to write p_z in terms of p_x and p_y . To this end the total energy of the electron given by $\mathcal{E} = \sqrt{c^2 p^2 + m^2 c^4}$ is needed as well as a few mathematical manipulations, ultimately resulting in the electron's relativistic momentum in $\hat{\mathbf{z}}$ given by **Eq. 57**.

$$p_z = \frac{p_x^2 + p_y^2}{2mc} = \frac{1}{2mc} \left\{ \left[\frac{qE_1}{\omega} \sin(\phi) + p_{x0} \right]^2 + \left[\frac{qE_2}{\omega} [1 - \cos(\phi)] + p_{y0} \right]^2 \right\} \quad (57)$$

A few final tricks are necessary to move from the relativistic momentum $\mathbf{p} = \gamma m\mathbf{u}$ to the electron's trajectory in Cartesian coordinates as a function of the plane wave's phase ϕ . To this end one rewrites **Eq. 58** as **Eq. 59** by recognizing that $d\mathbf{r}/dt = \mathbf{u}$ and once again using $d\phi/dt = (u_z/c - 1)\omega$. u_z is replaced by p_z via **Eq. 56** and \mathcal{E} is replaced by $\mathcal{E} = \mathbf{p}c^2/\mathbf{u}$ which is found by combining $\mathbf{p} = \gamma m\mathbf{u}$ with $\mathcal{E} = \gamma mc^2$, the total energy of the electron.

$$\frac{d\mathbf{r}}{d\phi} = \frac{d\mathbf{r}}{dt} \frac{dt}{d\phi} \quad (58)$$

$$\frac{d\mathbf{r}}{d\phi} = \frac{-\mathbf{p}}{\omega m} \quad (59)$$

Integrating each component of **Eq. 59** using **Eqs. 54, 55** and **57** gives the electron's trajectory in Cartesian coordinates with initial position (x_0, y_0, z_0) and as a function of the plane wave's phase as shown in **Eqs. 60-62**.

2. Theory

$$x = \frac{qE_1}{m\omega^2} [1 - \cos(\phi)] - \frac{p_{x0}\phi}{m\omega} + x_0 \quad (60)$$

$$y = \frac{qE_2}{m\omega^2} [\sin(\phi) - \phi] - \frac{p_{y0}\phi}{m\omega} + y_0 \quad (61)$$

$$z = \frac{-1}{2\omega cm^2} \left[\frac{q^2 E_1^2}{\omega^2} \left(\frac{\phi}{2} - \frac{1}{4} \sin 2\phi \right) + \frac{q^2 E_2^2}{\omega^2} \left(\frac{3\phi}{2} - 2 \sin \phi + \frac{1}{4} \sin 2\phi \right) \right. \\ \left. + \frac{2qE_1 p_{x0}}{\omega} (1 + \cos \phi) + \frac{2qE_2 p_{y0}}{\omega} (\phi - \sin \phi) + \phi (p_{x0}^2 + p_{y0}^2) \right] \\ + z_0 \quad (62)$$

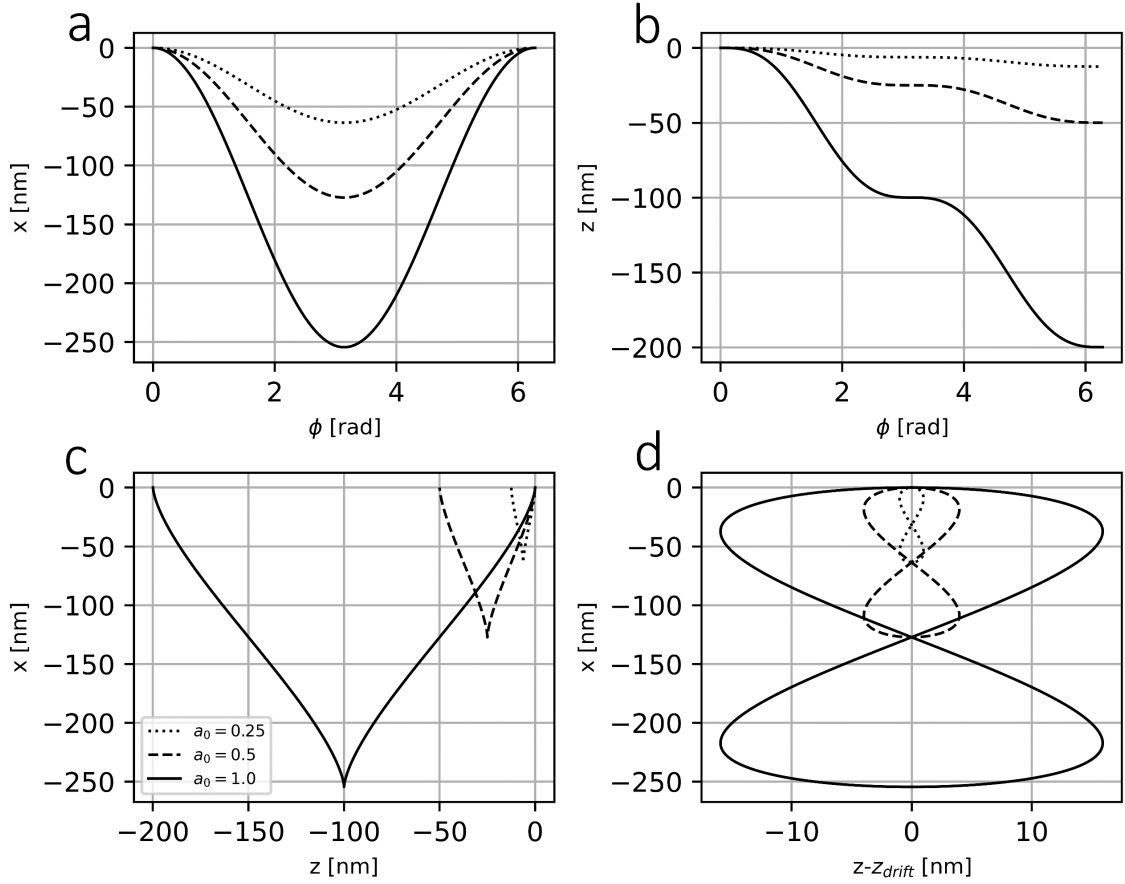


Figure 11: Electron trajectory in a linearly polarized plane wave for an a_0 of 0.25 (dotted), 0.5 (dashed), and 1.0 (solid), legend in subplot (c). The electron is driven by a linearly polarized plane wave given by **Eqs. 51** and **52** with $E_2 = 0$ V/m. (a) and (b) show the electron's transverse (x) and longitudinal (z) positions as a function of the laser's phase, respectively. (c) depicts the electron's motion in the xz -plane and (d) shows the electron's "Figure-of-Eight" motion in the drift-frame of its guiding center.

Typically, LWFA experiments are performed using linearly polarized laser pulses. By setting $E_2 = 0$ V/m the trajectory of an electron in a linearly polarized plane wave can be investigated for an electron starting at the origin with no initial momentum, as shown in **Fig. 11**. Additionally, the normalized vector potential $a_0 = eE_1/(\omega mc)$ of the laser pulse can be used to help qualify whether or not the motion of the electron is relativistic. $a_0 \ll 1$ is considered the classical regime while $a_0 \gtrsim 1$ causes relativistic motion of the electron. For moderately relativistic and relativistic intensities of

2. Theory

$a_0 = 0.25, 0.5$ and 1.0 the motion of the electron in \hat{x} and \hat{z} is plotted against the phase of the plane wave (**Fig. 11a,b**). **Fig. 11c** shows the xz-trajectory in the “lab”-frame and **Fig. 11d** shows the particle’s trajectory in the co-moving “drift”-frame of its guiding center.

Although not directly apparent from the trajectory equations, after taking the second temporal derivative of **Eqs. 60-62** and calculating their temporal average, one finds that no net acceleration is imparted to the electron in a plane EM wave. This is in agreement with the Lawson-Woodward theorem described in [64], [65]. The “Figure-of-Eight” motion seen in **Fig. 11d** will be of interest later when considering anisotropy of plasma under the influence of a relativistically intense laser field due to the motion of its constituent electrons. It is show in [66] that only electrons that are initially counter-propagating to the plane wave at a the speed of light will perform strict Figure-of-Eight orbits in the lab-frame. Since those initial conditions are unphysical and since LWFA experiments used focused laser pulses, one will expect any electron under the influence of an EM field too also exhibit a drift velocity in addition to any faster oscillating motion as described above.

2.4.2 The Ponderomotive Force

Although infinite plane waves are useful for first approximations in understanding the interaction between EM waves and electrons, the more realistic yet complicated case of an electron moving in the focus of a laser pulse more accurately models the motion of plasma electrons near the laser driver of the LWFA setup [66], [67]. The primary difference arises in considering the drift motion of the electron due to the ponderomotive force (PMF) of the spatially inhomogeneous laser distribution. Qualitatively, as the electron completes a transverse oscillation in the focused EM pulse it varies from its trajectory in the case of the plane wave due to the spatially varying wave amplitudes in the laser pulse. The net energy gained by the electron while interacting with the laser pulse results in a radial scattering of the particle from the laser’s focus.

Assuming a time-harmonic electromagnetic wave with low intensity such that the resulting motion of a charged particle remains non-relativistic, one can approximate the magnetic contribution to the Lorentz force on a charged particle as a perturbation to the Coulomb force. As shown in [63], for small radial displacements \mathbf{r} of the charged particle from the laser pulse’s propagation axis, one can write the electric field as $\mathbf{E}(\mathbf{r}, t) \approx \mathbf{E}_0 + (\mathbf{r} \cdot \nabla)\mathbf{E}_0$ and magnetic field $\mathbf{B}(\mathbf{r}, t) \approx \mathbf{B}_0$ with $\mathbf{E}_0 = \mathbf{E}(\mathbf{r})\exp(-i\omega t)$ and $\mathbf{B}_0 = \mathbf{B}(\mathbf{r})\exp(-i\omega t)$. Investigating only the particle’s displacement due to the Coulomb force assuming initial conditions of $\mathbf{r} = 0$ and $d\mathbf{r}/dt = 0$ produces the expression $\mathbf{r} = -q\mathbf{E}/m\omega^2$ with m the mass of the particle. Substituting the electric and magnetic fields from above into the Lorentz force and using the vector identity $(\mathbf{E} \cdot \nabla)\mathbf{E} = \frac{1}{2}\nabla(\mathbf{E} \cdot \mathbf{E}) - \mathbf{E} \times (\nabla \times \mathbf{E})$ and Faraday’s law of induction **Eq. 11** results in **Eq. 63**.

$$\mathbf{F} = q\mathbf{E}_0 - \frac{q^2}{m\omega^2} \left[\frac{1}{2}\nabla(\mathbf{E}_0 \cdot \mathbf{E}_0) + \frac{\partial}{\partial t}(\mathbf{E}_0 \times \mathbf{B}_0) \right] \quad (63)$$

2. Theory

Eq. 63 can be further simplified by taking only the real parts the electric and magnetic fields and by temporally averaging over one oscillation. This results in the final form of the classical ponderomotive force as shown in **Eq. 64**. Note that the PMF is independent of the sign of the particle's charge and independent of the laser's polarization. The overall motion of the charged particle is a scattering away from regions of high laser intensity. Depending on the gradient of the laser's intensity, the scattering velocity of the charged particle can reach relativistic values.

$$\langle \mathbf{F}(\mathbf{r}) \rangle = -\frac{q^2}{4m\omega^2} \nabla |\mathbf{E}(\mathbf{r})|^2 \quad (64)$$

More detailed analysis of ponderomotive scattering including derivations of the relativistic PMF can be found in the literature [66], [67]. These studies consider relativistic motion of the charged particles, quickly varying field gradients, longitudinal field components of the laser pulse near focus, short pulse durations, etc. and must be numerically solved due to their complexity. Of importance for the current work is the realization that the motion of the charged particles, in this case electrons, under the influence of a high-intensity laser pulse can be decomposed into a fast oscillating or quiver motion at the time-scale of the laser's period, similar to the previously described "Figure-of-Eight" motion, and a scattering or drift of the electron away from the laser pulse at time-scales on the laser pulse's duration. This motion will be further modified when considering populations of plasma electrons moving in inhomogeneous plasma distributions.

2.5 Laser Wakefield Acceleration

The original idea of the laser-plasma accelerator (LPA) was proposed in 1979 by Tajima and Dawson [12], but early attempts to realize one resulted in electron beams with parameters unsuitable for most applications [68]–[71]. A significant improvement in the energy spectrum, bunch charge and beam divergence was achieved by three different groups in 2004 due to operation of the respective LPA setups in a new nonlinear regime [72]–[74]. Further refinement over the past 15 years of the LWFA process has led to electron beams in the few-GeV energy range, with sub-mrad divergence and few to tens of pC beam charges [7]. The following sub-sections will give an overview of the most important LWFA topics concerning the work done in the thesis. For more information, the interested reader can find many relevant papers including [33], [75]–[78].

2.5.1 Self-Compression of the Laser Driver

During propagation of a high-intensity laser pulse ($a_0 \gtrsim 1$) through plasma, an interplay between the laser's intensity distribution and the plasma's electron density distribution via the ponderomotive force can act to self-compress the laser pulse relative to the characteristic length of the plasma. Self-compression in the transverse direction, i.e., self-focusing, allows for guided propagation over lengths greater than the Rayleigh length. This effect, combined with longitudinal self-compression, enables the laser's peak intensity to reach values higher than those achievable through focusing in free-space.

2. Theory

Self-Focusing and Guiding

Much like a gradient index fiber, for example see chapter 1.3 of [79], a radial distribution of the plasma's refractive index with $\partial\eta/\partial r < 0$ will cause focusing of the laser driver that can counteract natural diffraction. Assuming a driver laser with a Gaussian-like transverse intensity profile, the two main mechanisms that cause a radial change in refractive index of the plasma are ponderomotive self-focusing (PSF) and relativistic self-focusing (RSF). PSF arises from the ponderomotive force ejecting plasma electrons out of the laser's focus, which causes an on-axis depletion of plasma electrons and leads to a radial distribution of the electron density $\delta n_e(r)$ relative to the background density n_e . RSF stems from the radial dependence of the electrons' quiver velocity due to the laser driver's radial field distribution. The transverse, relativistic motion of the electrons is characterized by the transverse gamma factor $\gamma_t(r) = \sqrt{1 + a(r)^2}$ where $a(r)$ is the amplitude of the laser driver's vector potential. These modifications to the refractive index of the plasma can be approximated by Eq. 65 below [33].

$$\eta(r) \approx 1 - \frac{\omega_p^2}{2\omega_L^2} \left(1 - \frac{a^2(r)}{2} + \frac{\delta n_e(r)}{n_e} \right) \quad (65)$$

Guiding becomes possible when the focusing effects mentioned above cancel out the natural diffraction of the laser driver. The evolution of the beam waist, as described in Section 2.3.3, must be modified using Eq. 66. One sees that the ratio of the laser driver's power P to the critical power P_c determines whether the beam waist diffracts, remains constant, or focuses. While the beam's behavior is more complicated than this simple Gaussian model, guiding of a laser in plasma over several Rayleigh lengths has been measured and presented experimentally [80]. The critical power can be approximated as $P_c = 17.4 \omega_L^2 / \omega_p^2$ [GW], which, using a laser centered at 800 nm and a plasma density at 10^{19} cm^{-3} , results in a critical power of 3 TW, much less than the operating power of modern, high-intensity Ti:Sapphire lasers.

$$w(z) = w_0 \sqrt{1 + \left(1 - \frac{P}{P_c}\right) \frac{z^2}{z_R^2}} \quad (66)$$

Temporal Pulse Modification

Longitudinally, the modification to the plasma's refractive index looks quite similar to the transverse modification. Moving to a co-moving frame with longitudinal coordinate $\xi = z - ct$, the longitudinal intensity distribution of the laser driver alters both the electron-plasma density $\delta n_e(\xi)$ and the relativistically-corrected mass of the electrons via the term $a(\xi)$. Furthermore, the change in refractive index itself induces a longitudinal chirp to the laser pulse due to the pulse's temporal phase being index-dependent. In a process known as self-phase modulation (SPM) (see Appendix B.1) the front of the pulse is red-shifted and the back of the pulse becomes blue-shifted. Taking the longitudinal refractive index as given in Eq. 67 below, and knowing that the group velocity in plasma

2. Theory

is $v_g = c\eta$, one sees that the front portion of the laser driver will slow down and the trailing portion of the laser will speed up, causing the longitudinal extent of the pulse to compress.

$$\eta(\xi) \approx 1 - \frac{\omega_p^2}{2\omega_L^2} \left(1 - \frac{a^2(\xi)}{2} + \frac{\delta n_e(\xi)}{n_e} - 2 \frac{\delta\omega(\xi)}{\omega_L} \right) \quad (67)$$

The resulting compressed pulse duration Δt_{comp} after a propagation distance l in the plasma is approximated with the equation $\Delta t_{comp} = \Delta t - n_e l / (2cn_c)$. A compression factor of 2-3 was found experimentally, but depends on the initial laser pulse, plasma density and propagation length [81], [82]. Assuming that the laser pulse self-focuses and -compresses to match the characteristic length of the plasma wave, then a further increase in pulse intensity can drive the system from the linear to the non-linear regime in which self-injection and acceleration of electrons is possible.

2.5.2 Excitation of a Plasma wave

The mathematics behind linear and nonlinear wakefield formation can be found in several publications [33], [83]–[87]. In the next few paragraphs the major results from the linear and nonlinear theory of LWFA will be presented with the goal of summarizing the important aspects of LWFA relevant to this thesis, e.g., the relative magnitude and distribution of the laser's fields, wakefields and electron-plasma density.

Linear Regime

By assuming a non-relativistic laser intensity, i.e., $a_0 \ll 1$, and a weakly perturbed plasma, i.e., $\delta n_e \ll n_e$, an analytical description of the scalar potential $\phi(r, \xi)$, see Eq. 68, and thus the longitudinal field E_z , radial field E_r and electron density perturbation δn_e can be described using Eqs. 69-71, respectively [76]. Here, k_p is the wave number of the plasma wave, i.e., $2\pi/\lambda_p$ and E_{wb} is the cold, nonrelativistic wave breaking field given by $E_{wb} = m_e c \omega_p / e$.

$$\phi(r, \xi) = -a_0^2 \omega_p \tau_0 \sqrt{\frac{\pi}{32}} \sin(k_p \xi) \exp\left(-\frac{2r^2}{w_0^2}\right) \exp\left(-\frac{(\omega_p \tau_0)^2}{8}\right) \quad (68)$$

$$E_z = -\frac{E_{wb}}{k_p} \frac{\partial \phi}{\partial \xi} \quad (69) \quad E_r = -\frac{E_{wb}}{k_p} \frac{\partial \phi}{\partial r} \quad (70) \quad \delta n_e = \frac{n_e}{k_p^2} \frac{\partial^2 \phi}{\partial \xi^2} \quad (71)$$

Using an a_0 of 0.5, a FWHM pulse duration $\Delta t = \tau_0 \sqrt{2 \ln 2}$ of 17.7 fs, a FWHM spot diameter $D_{FWHM} = w_0 \sqrt{2 \ln 2}$ of 11.8 μm and a background electron density of $5 \cdot 10^{18} \text{ cm}^{-3}$ (corresponding to a 14.9 μm plasma wavelength), Fig. 12 was plotted. The wakefield's radial extent matches the diameter of the Gaussian laser pulse and the wakefield's longitudinal period, i.e., plasma wave's period, corresponds to the background density's plasma frequency. It follows that a laser pulse short enough to fit into roughly one-half of the plasma wavelength, i.e., $c\Delta t = 0.37\lambda_p$, will efficiently drive

2. Theory

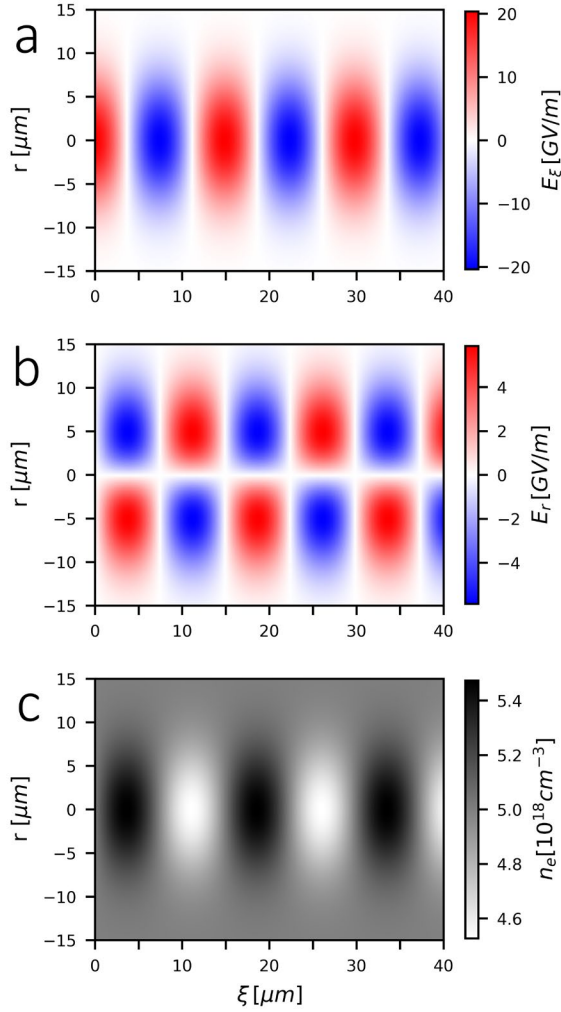


Fig. 12: 2D linear wakefield in co-moving coordinates (r, ξ) . $a_0 = 0.5$, FWHM $\Delta t = 17.7$ fs, spot diameter $D_{FWHM} = 11.8 \mu\text{m}$, $n_e = 5 \cdot 10^{18} \text{ cm}^{-3}$, $\lambda_p = 14.9 \mu\text{m}$. (a) longitudinal electric field E_ξ . (b) radial electric field E_r . (c) perturbed electron density n_e .

$a_0 \gtrsim 1$, the plasma wave's density and field distributions are no longer sinusoidal as in the linear case. In the 3D case, no simple analytical solutions exist. Instead, 3D PIC simulations, theory and experimental work are combined to arrive at phenomenological scaling laws [89]–[91]. Analytical solutions to the plasma's nonlinear response exist for the “1D spatial - 3D momentum” case [33], [78] and the resulting density perturbation and electric fields can be plotted as seen in Fig. 3b of [76]. The electron density exhibits a spiked profile and the longitudinal electric field has a sawtooth form with a maximum value in the few hundreds of GV/m, a factor ~ 30 smaller than peak the electric field of the laser driver. Analysis and simulations show that the phase fronts of the plasma wave begin to curve due to the relativistic motion of the electrons. The phase front curvature and motion of the plasma electrons lead some of the electrons to overtake the phase front and become injected, meaning they are trapped in the wakefields and undergo acceleration or deceleration in the longitudinal electric fields in

a plasma wave. Longer laser pulses will experience both halves of the plasma wave's density perturbation (or more) and will begin to split up or microbunch [88]. Note that for the laser parameters given above, the laser's peak electric field of $2 \cdot 10^{12}$ V/m is a factor of 100 to 1000 times higher than the longitudinal or radial electric fields seen in the linear plasma wave.

One sees that regions with a length of $\lambda_p/4$ exist along the plasma wave in which E_ξ is negative and E_r points away from the ξ axis. In these regions, electrons are not only accelerated in the forward direction, they are also focused by the radial field. If the accelerated electrons overtake this region they will begin to decelerate, they “dephase” from the useful region of focused acceleration behind the laser driver. The dephasing length and other limitations to the maximum kinetic energy of the accelerated electrons will be discussed in the linear and nonlinear cases shortly (see Section 2.5.4).

Nonlinear Regime

As the laser driver's intensity increases, i.e.,

2. Theory

the plasma wave [33], [92]. The plasma wave's period will also lengthen due to the relativistic motion of the plasma electrons as predicted by theory [33] and measured in experiments [26].

2.5.3 Injection Mechanisms

The laser-driven plasma wave described above is only part of the “equation” when trying to accelerate electrons to (ultra)-relativistic energies in an LPA. The properties of the accelerated electron bunch depend heavily on the type of injection mechanism used, i.e., the process with which the electrons are initially positioned into the plasma wave for subsequent acceleration. However, since the current work is primarily interested in the laser-plasma interaction and not directly concerned with the resulting properties of the electron bunches, and since the details of each injection mechanism are numerous and complex, only a list of the currently researched injection mechanisms will be given.

Self-injection of the electrons requires driving the plasma wave until it “breaks” in either the transverse or longitudinal direction, meaning plasma electrons gain momentum greater than the local phase velocity of the plasma wave and can move into a region of the wave in which the local fields focus and accelerate electrons [69], [92]–[95]. The threshold for self-injection has been shown to be an interplay between available laser power and plasma density; the higher the laser power available the lower the plasma density required for self-injection [96]. This mechanism strongly relies on stability of the driving laser, its nonlinear self-focusing and longitudinal compression, and the target gas' density distribution and as such can prove difficult to control. Results showing few mrad divergence and few % shot-to-shot energy stability near 200 MeV can be found in the literature [97].

One method of controlling the location of electron injection is by using a plasma density transition in which a localized decrease in plasma density causes a localized trapping of electrons. The “density down ramp” method [98] relies on a negative gradient in the plasma density with a length-scale longer than the local plasma wavelength [99]–[101]. This causes the plasma wave's phase velocity to reduce along the entire plasma wave, eventually to the point where the plasma wave breaks and traps electrons. While longer density transitions can lead to multiple injection events along the plasma wave, a sharp density transition with a length-scale smaller than the plasma wavelength can be used to better localize the electron injection [102]–[104]. The addition of a knife edge or wire to the gas target to create a sharp transition has proven to be a fairly simple way to improve bunch charge, energy spread and shot-to-shot energy stability [105].

A more experimentally complex method for separating electron injection and acceleration can be found in a group of methods generally known as “colliding pulse injection” proposed by *D. Umstadter* et al. [106]. A pump laser is used to drive a plasma wave below the self-injection threshold. By overlapping the pump laser with a second “colliding” pulse, a beat wave forms whose ponderomotive force pushes plasma electrons into the plasma wave to be accelerated. The collision point of the two laser pulses can be scanned through the gas jet which varies the available acceleration length and tunes the resulting energy of the electron beam. Simulations have been used to both explore alignment

2. Theory

geometries, different polarizations [107] and the general phenomenon itself [108], and have also been used to explain experimental results [109]. Experiments have shown few mrad beam divergences, tunability from 15 MeV to over 250 MeV, and sub-10% energy spreads [110]. Recent results also combined a sharp density transition with colliding pulse injection to create a double bunch accelerator used in a proof-of-concept experiment for an all-optical Compton source [111].

Compared to the various colliding pulse setups, ionization injection is experimentally more straightforward to implement. Instead of using pure Hydrogen or Helium as the target gas, ionization injection relies on adding a small amount, typically less than 10%, of a mid-Z dopant gas such as Nitrogen, or a Noble gas. As the pump pulse enters the gas target, the pulse's intensity is adjusted so that the primary gas and the outer-shell electrons of the mid-Z dopant are fully ionized. Too much dopant leads to ionization defocusing of the pump laser and unstable operation of the LWFA. The pump's intensity and the plasma density must be selected such that the LWFA operates under the self-injection threshold, but the pump's peak intensity is high enough to ionize an inner-shell electron of the dopant gas. For Nitrogen, there is a significant jump in ionization potential between the last L-shell electron (98 eV) and the first K-shell electron (552 eV) which using barrier suppression ionization theory corresponds to a jump in ionization intensity of the laser from $1.5 \cdot 10^{16}$ to $1.0 \cdot 10^{19}$ W/cm² [112], [113]. This results in K-shell electrons of the dopant being ionized only locally in the peak of the pump pulse, which is an ideal location for the electrons to be subsequently trapped and accelerated.

The main drawback of a single gas-jet setup is that ionization injection occurs as long as the pump pulse has the required peak intensity to ionize the dopant. The resulting continuum of accelerating lengths causes the accelerated electrons to have a broadband energy spectrum. Using a dual gas-jet or cell that separates the doped gas from a segment of pure gas can reduce the energy spread by once again spatially separating injection and acceleration of the electrons. Simulations show this setup could obtain few-percent energy spreads, several pC bunch charges at energies in the GeV level [114]. Experiments with single gas-jets show energy spreads over 20% [113], [115] while using a double stage injector/accelerator concept reduced energy spread to $< 5\%$ while still maintaining several tens of pC bunch charge and energies at the 0.5 GeV level [116].

2.5.4 Dephasing, Pump Depletion and Energy Gain

After being injected into the plasma wave, the electrons gain kinetic energy depending on the effective length of acceleration and the longitudinal electric field in the plasma wave [33]. Both variables depend on several parameters of the laser-plasma interaction including the background plasma density, the pump's intensity, its frequency and its pulse duration, and whether the plasma wave is linear or nonlinear. While analytical solutions for the 1D case exist (see references in [33]), phenomenological scalings for the 3D case have been developed using theory and simulation [90].

The effective acceleration length is ultimately limited by three effects: diffraction, pump depletion or dephasing. Without self-guiding or external guiding, the pump laser's intensity will decrease to

2. Theory

10% (1%) of its maximum after three (ten) Rayleigh lengths (see **Section 2.3.3**). A drastic change in intensity (and transverse beam size) prohibits the stable excitation of a plasma wave. Thanks to relativistic self-focusing, diffraction is typically not the limiting factor in experiments. Pump depletion can be a limiting factor, and is observed as the front edge of the laser pulse is “etched”, losing its energy to the plasma electrons [82]. Eventually, the pump pulse loses so much energy that it can no longer drive a plasma wave capable of accelerating electrons. Some pulse etching; however, can be advantageous as it leads to a reduction in the pump’s duration leading possibly to better matching conditions to the background plasma density. The third limiting effect, dephasing, refers to the point at which accelerated electrons begin to “outrun” the plasma wave and enter a region of the wakefield distribution where the fields are no longer focusing and accelerating. Whichever length is the shortest: diffraction, depletion or dephasing, will determine the effective acceleration length of the electrons.

A LWFA experiment depending on ionization injection somewhat complicates the previous discussion due to the continuous injection of electrons into the plasma wave. Furthermore, if the initial pump pulse’s duration and transverse size are not matched to the background plasma density, there can also be significant evolution of the pump pulse and plasma wave. Scaling laws for a linear plasma wave might be more accurate at the beginning of the pump-plasma interaction while, for example, in the second half of the interaction scaling laws for the “Bubble” regime might become more relevant. Clearly, separation of electron injection and acceleration, as well as operating in a “quasi-static”, pump-plasma regime would allow for the easiest application of scaling laws to predict the final bunch energy and potentially its spectrum. Nonetheless **Table 1** of [90] will be used in **Chapter 3**, with relevant experimental parameters, to predict depletion and dephasing lengths as well as the maximum expected electron energies in the experiment.

2.5.5 Particle-in-Cell Simulations

To expedite the understanding and development of high-intensity, laser-plasma experiments, numerical simulations are performed using either Vlasov or particle-in-cell (PIC) numerical codes. Reviews of this subject can be found in references [117]–[119]. These codes are designed to solve the Vlasov-Maxwell model: a combination of the Vlasov equation **Eq. 101** (collisionless Boltzmann equation, see **Appendix A.2**), the relativistic equation of motion **Eq. 53**, and Maxwell’s equations **Eq. 9-12** that create a self-consistent, kinetic description of the collisionless, evolving plasma and its electromagnetic fields. Both types of code used to solve the plasma model require discretizing the fields onto a spatial grid, updating the distribution functions of the particles and then updating the associated charge and current densities in the system. The primary difference between the two codes, Vlasov and PIC, is how the distribution functions are handled and the resulting noise when solving the Vlasov equation. A Vlasov code integrates directly to solve the Vlasov equation while a PIC code randomly samples the distribution functions using macroparticles and updates the position and momentum of these particles. Vlasov codes have less noise but require more computation time, while

2. Theory

PIC codes have higher noise but are less numerically expensive. The decrease in numerical cost of PIC codes has also made them more versatile in modelling different plasma systems, while Vlasov codes are designed and implemented for more specific plasma experiments. For these and other reasons, the following description will concentrate solely on the basic inner-workings of a PIC code.

The Vlasov-Maxwell model constitutes a set of differential equations and as such requires the use of initial conditions and boundary conditions before any numerical code can begin to calculate the system's evolution with each time step. The initial conditions concern the field and particle distributions at the beginning of the simulation and can be more or less determined by the desired experimental conditions being investigated. Contrastingly, the boundary conditions implemented in the simulation can have very non-physical effects on the simulation. They are used to reflect, thermalize, or inject new particles at the spatial borders of the simulation as well as to reflect, absorb or inject EM field components [120]. Careful use of both initial and boundary conditions must be considered in order to keep the size of the simulation box small, and thus computational time low, while also ensuring accurate representation of real-world parameters and physics.

The shape of the macroparticles, how they are interpolated over the simulation's grid, the number of total particles and the grid resolution in transverse and longitudinal directions (relative to the drive laser) all play a role in determining the physics accurately represented by the simulation and the required computation time of the simulation [118], [121], [122]. In general, fluid aspects of the plasma such as the distributions and strengths of the plasma's EM fields can be accurately resolved using lower numbers of macroparticles, lower-order interpolation and a larger grid size. On the other hand, investigation of kinetic aspects of the plasma such as particle trajectories and trapping of the macroparticles in the plasma wave require higher grid resolutions, larger number of particles and higher-order particle interpolation. Details of the various tradeoffs between accuracy and computational time can be found in the literature.

The core algorithm of a PIC code consists of two coupled solvers: a "particle pusher" and a "field solver". The particle pusher solves the relativistic equation of motion for each macroparticle in the simulation using the EM field distributions. The resulting positions and trajectories are then used to calculate the new charge and current densities. The field solver then uses the new densities to update the electric and magnetic field values on the simulation grid which are used in the next time step of the simulation by the particle pusher. This process repeats over the desired number of time steps until the simulation has ended. Each aspect of the simulation, e.g., field representation on the simulation grid, particle pushers, field solvers, and time advancing schemes, are themselves areas of research and development, e.g. Yee staggered grid [123], Finite Difference Time Domain method [118], Boris' rotation algorithm [124], [125], Esirkepov's current deposition [126], and Lorentz boosted simulations [127].

3. Experimental Setup

Beyond the core PIC algorithm of particle pusher and field solver, there is an abundance of extra computational packages that can be used to increase the accuracy of the PIC simulations for better comparison to and prediction of experiments. Three of the most relevant packages for laser-plasma interactions include the proper modelling of ionization processes, collisional processes [128], [129] and QED effects [130]. Ionization processes can have a significant impact on laser propagation in un-ionized or partially ionized media. The Keldysh parameter [131], WKB approximation [132] and a corrected ADK [133], [134] theory can be used to model ionization via MPI, tunneling ionization and BSI while also taking into account redistribution of the charge density on the simulation grid and energy conservation of any absorbed photons and resulting particle kinetic energies. Inclusion of collisional processes in plasma becomes more important as the timescale of the simulation increases into the picosecond and nanosecond regimes. Finally, with the increase in peak laser intensity well above 10^{21} W/cm² and the potential combination of high-intensity lasers with high energy particle beams, the modelling of QED processes in plasma simulations has grown in interest. The emission of high energy photons as well as pair production processes can be included in PIC simulations.

3. Experimental Setup

3.1 Jeti 40 Laser System

The Jena titanium-sapphire 40 TW laser system (Jeti 40 for short) is a chirped-pulse amplification laser system based on the titanium-sapphire (Ti:Sa) laser medium at the Institute of Optics and Quantum Electronics (IOQ) in Jena, Germany. Although the laser was designed for operation with a peak power of 40 TW, FWHM pulse duration of 25 fs and repetition rate of 10 Hz, the typical LWFA parameters from the experimental campaigns covered in this dissertation were closer to 24 TW on target, 27 fs FWHM pulse duration and 0.5 Hz operation. The difference in design and operational parameters depended, more often than not, on a tradeoff between time running the experiments and time invested in maintenance and alignment of the laser.

Chirped-pulse amplification (CPA) is a breakthrough in laser development adapted from RADAR technology in the late 1980's [135] that was awarded a Nobel Prize in Physics in 2018. The CPA technique relies on temporally stretching the laser pulse from the femtosecond regime to the nanosecond regime before further amplification. This reduces the risk of damaging optical components because the laser's power is reduced below the damage threshold of the laser's optics during amplification. After amplification, the pulse is temporally compressed back to the femtosecond regime and guiding in a vacuum beamline using reflective optics to the target chamber. Generally, during and after compression, transmissive optics are avoided due to the resulting pulse lengthening, nonlinear effects and damaging the optic due to self-focusing of the laser pulse in the material.

3. Experimental Setup

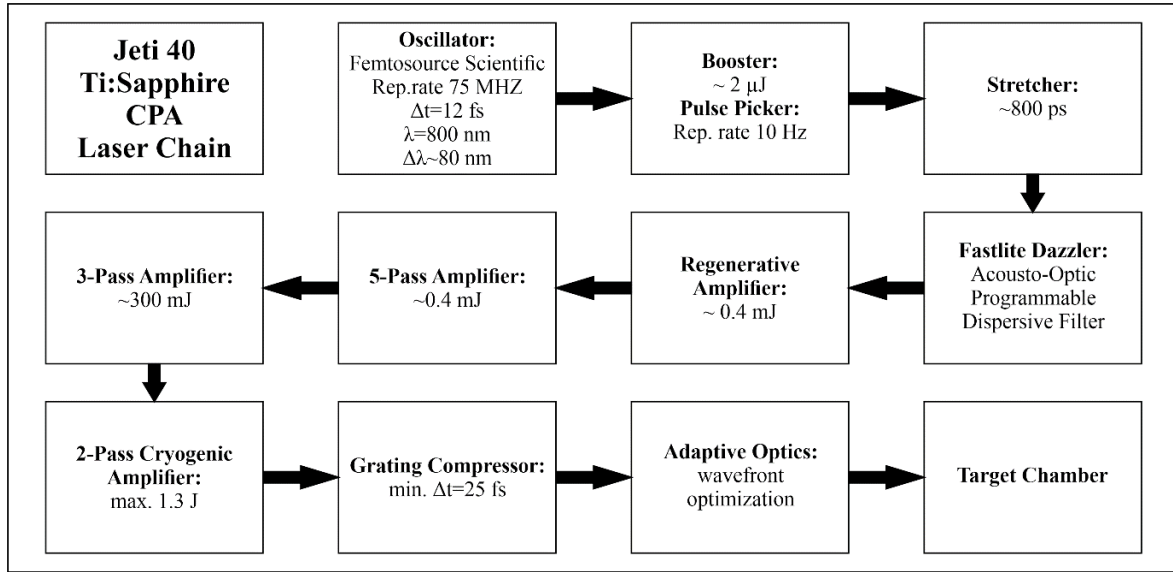


Figure 13: Laser chain of the Jeti 40 laser. Laser parameters were provided by F. Ronneberger.

The block diagram of the Jeti 40 laser chain is shown in **Fig. 13** and depicts the main stages of the system and the properties of the pulses in their respective stages. While an on target power of roughly 24 TW may seem uninteresting compared to modern, commercial Ti:Sa systems with peak powers in the 100s of TW, the Jeti 40 laser has been the workhorse of experimental, high-intensity physics for both local and international research groups spanning topics from ion acceleration [136], surface high-harmonic generation [137], Raman amplification [138], THz-radiation generation [139], [140], LWFA [26], [141], and more.

3.2 Laser Wakefield Acceleration Setup

The general setup of the LWFA experiment is depicted in **Fig. 14** below with the system's global Cartesian coordinates shown in the bottom left of the figure. The pump propagates along the x-axis, is polarized along the y-axis and is focused by an off-axis parabola to the interaction point (IP) inside a gas-cell. Meanwhile, the probe propagates along the negative y-axis and is initially polarized linearly at 45° to the x-axis in the xz-plane. The accelerated electron bunch (e-bunch) is measured using a scintillating screen and imaging camera (setup not shown) or is coupled into a dipole spectrometer for measurement of its energy distribution (also not shown). The VIS-NIR imaging system is aligned to image the xz-plane within the gas-cell, i.e., the plane containing a vertical cross-section of the plasma wave and laser-plasma interaction. Through use of a broadband, non-polarizing 50:50 beamsplitter (NBS) and a silver coated mirror (M), the xz-plane can be imaged simultaneously onto two CCD sensors for each shot of the pump laser. In front of each CCD sensor are polarizers (H-pol, V-pol) and/or various interference filters (IF1, IF2) depending on the measurement being performed. Horizontal polarization of the probe (H-pol) refers to linear polarization along the x-direction while vertical polarization (V-pol) is along the z-direction (see E_H and E_V in **Fig. 14**).

3. Experimental Setup

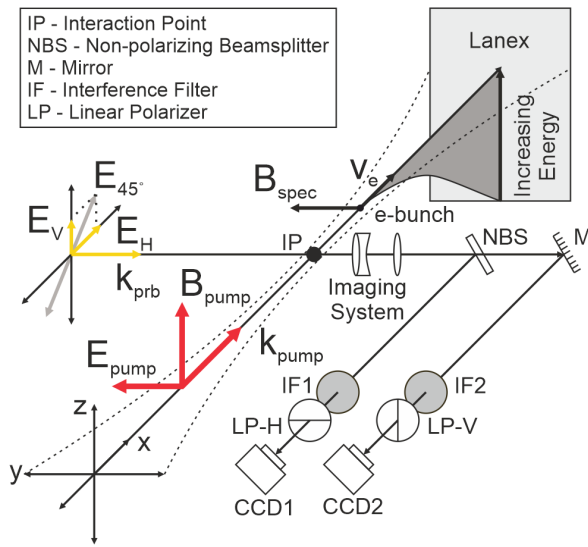


Figure 14: General LWFA Setup with probe beam's imaging system and electron spectrometer.

Shadowgrams of the laser-plasma interaction were recorded over approximately 2.0 mm of propagation through the gas-cell by delaying the probe with respect to the pump and shifting the imaging system along the x -axis as necessary. The very beginning and end of the interaction region were blocked to the imaging system because of the metal entrance and exit walls of the gas-cell.

The pump pulse was focused into the gas target using an F/12 off-axis parabola giving a $(9.7 \pm 0.1) \mu\text{m}$ FWHM focus diameter measured in vacuum with $\sim 37\%$ of the pulse energy inside the FWHM diameter. Its FWHM pulse duration was measured daily with a Fastlite Wizzler to have an average 27 fs, and the pulse energy was measured to be ~ 650 mJ on target. These values give a peak intensity of $2.3 \cdot 10^{19} \text{ W/cm}^2$, an a_0 of 3.3 and a FWHM on target power of 8.9 TW.

To avoid self-injection of electrons such that the interaction only relies on ionization injection, one can follow the discussion from S. P. D. Mangles et al. in [96], in which a threshold pulse energy can be calculated for a given plasma density. Using the enclosed FWHM pulse energy of ~ 240 mJ and a pump laser centered at 800 nm, the self-injection threshold is found to be near an electron density of $1.5 \cdot 10^{19} \text{ cm}^{-3}$. This was later verified in the experiment using shadowgraphic images of the pump's propagation through the plasma. For plasma wave's imaged in a background density near $1.5 \cdot 10^{19} \text{ cm}^{-3}$, no indication of self-injection was observed. However, for increasing background density, signs of wave-breaking radiation as in [142] were seen along the pump's propagation axis.

Using the discussion by W. Lu et al. in [90] for the matched parameters necessary to drive the "Bubble" regime, one can check if the available pump-plasma parameters meet the requirements for said regime. The measured laser intensity in vacuum and desired plasma density (below the self-injection threshold) results in a FWHM matched focus of $5.6 \mu\text{m}$ which is $\sim 40\%$ smaller than the available $9.7 \mu\text{m}$ diameter. This mismatch has a few advantages assuming that the primary goal of the experiment is not to obtain the highest possible electron bunch energies. Specifically, a mismatch in parameters will further avoid a regime where self-injection can cause unwanted wave-breaking radiation in the shadowgraphic images which can cause severe interference with the fc-probe beam [143]. Furthermore, a mismatch will also force a higher degree of self-evolution of the pump pulse. In terms of investigating laser-plasma interactions, a visible change in the plasma wave due to self-evolution through the plasma could present more valuable data compared to a LWFA experiment optimized for electron acceleration.

3. Experimental Setup

Finally, the dephasing and depletion lengths as well as maximum electron energy can now be approximated using the expected experimental values described above. Using the “Linear” and “3D Nonlinear” scalings found in **Table 1** of [90] the two assumed regimes can be quickly investigated. In the mismatched case where the vacuum parameters of the pump laser do not match the plasma density, the linear scaling is used (albeit with an a_0 of 1) giving a dephasing length of 160 μm , a depletion length of 940 μm and a maximum energy of 60 MeV. The 3D Nonlinear scaling with an a_0 of 3 leads to a dephasing length of 370 μm , a depletion length of 940 μm , and a maximum energy of 120 MeV. Both results suggest a dephasing-limited system much shorter than the gas-cell’s length with a maximum electron energy well below the 200 MeV limit allowed at the Jeti 40 laser laboratory.

3.2.1 Gas-Cell Target for LWFA

The gas-cell used in this LWFA campaign at the Jeti 40 laser (see **Fig. 15**) was designed by Wolfgang Ziegler and Dr. Stephan Kuschel and manufactured by the IOQ’s M1 machine shop. To

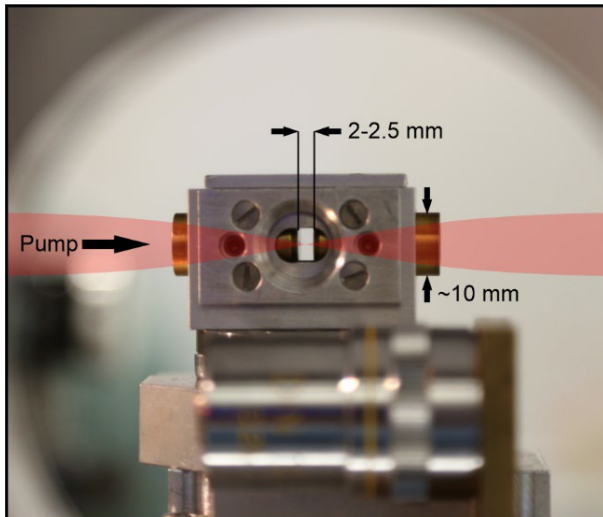


Figure 15: Gas-cell used in the LWFA experiment. Pump pulse is focused into the gas-cell from left to right. The exact vacuum focus position relative to the gas-cell’s entrance iris was unknown. Probe pulse travels into the page through the central window to probe the 2 mm to 2.5 mm length of plasma.

ensure flexibility in the experiment, the gas supply system was designed to cover a range of relevant gas pressures and to supply a tailorable gas mixture. The gas-cell itself could be varied in length from ~ 1 mm to over 10 mm, but for the data in this dissertation, the length of the gas-cell was kept to around 2-2.5 mm. The gas-cell also has two replaceable windows to allow transmission of the fc-probe beam as well as replaceable entrance/exit apertures for coupling in and out the pump laser.

As calculated previously, the required electron-plasma density for a LWFA experiment on the Jeti 40 laser near the self-injection threshold is near $1.5 \cdot 10^{19} \text{ cm}^{-3}$. Assuming pure

Helium as the target gas, each atom contains two electrons that can be ionized contributing to the plasma’s electron density. Using the ideal gas law, one finds that the required gas pressure in the gas-cell is right around one bar depending on the assumed temperature. Further cooling of the gas, expansion into and out of the gas-cell, and addition of a mid-Z dopant like N_2 all change the required backing pressure fed into the gas-cell, but the correct gas pressure can be found in-situ by comparing the plasma wavelength to the expected background plasma density, or by interferometric or wavefront measurements as described shortly. The low backing pressure used in a gas-cell can be compared to the several 10s of bar typically required for supersonic gas-jets [144]. Gas-jets have been used extensively in the literature as underdense and overdense targets having many advantages. These

3. Experimental Setup

include easy access for any diagnostic, simpler integration with knife edges or wires for shock-front injection, and similarly easier integration into multi-beam concepts such as colliding-pulse injection or Raman amplification. In contrast, gas-cells exhibit improved gas homogeneity [97], [145] as well as relatively simple adjustment of the overall laser-plasma interaction length. One final difference to note between gas-cells and gas-jets concerns interference by electro-magnetic pulses (EMPs). The use of a gas-jet often causes problems with motorized linear stages in the target chamber shutting off after every laser shot [146]–[149]. In contrast, a gas-cell acts as a Faraday cage to reduce EMP interference after every shot, reducing failure of motor stages and increasing the general reliability of the experiment.

While both gas-cells and gas-jets have their advantages and disadvantages, a gas-cell target was chosen for this experimental campaign primarily due to three reasons. Firstly, such a target had yet to be characterized on the Jeti 40 laser system in the context of LWFA. Secondly, with the primary goals of investigating ionization injection and probing the laser-plasma interaction, it was important to suppress both self- and shock-induced injection mechanisms. Finally, as already mentioned, the added bonus of reduced EM-interference would allow for more reliable and potentially faster data capture.

Both interferometric measurements using an in-house built Mach-Zehnder interferometer and wavefront sensor measurements using a Phasics SID4 were used to characterize the plasma density in the gas-cell. Details of the setups and analyses can be found in the Master's thesis of Dr. Daniel Ullmann under [150]. The plasma wavelength measured directly from the recorded shadowgrams could also be used to calculate the background electron density; however, care must be taken to consider the possible lengthening of the plasma wavelength due to relativistic effects or beam loading.

3.2.2 Electron Diagnostics

Two electron diagnostics were used in the experiment that characterized either the transverse beam profile of the accelerated electrons or their energy spectrum. The first was a simple scintillating screen placed in the downward path of the electrons from the gas-cell and imaged with a CCD sensor. Based on the distance between the gas-cell and the screen, as well as the imaging optics, scintillator type, sensor type and pixel count measured, the divergence of any electron beams as well as their approximate charge could be calculated. The second diagnostic, i.e., the electron spectrometer, used the same scintillating screen as the transverse beam diagnostic; however, after moving a dipole magnet with a ~ 550 mT field into the path of the electrons, the electrons were dispersed relative to their kinetic energies onto the scintillating screen. A typical data set required first measuring a stable beam pointing of the electrons, the magnet was then driven into the beam path and spectra could be recorded. The uncertainty in the beam pointing measurement then played a role in the uncertainty of the energy measurement of the electrons. For more details see [141], [151]. **Section 4.2** will describe in more detail the methods and reasoning behind sorting each laser shot depending on the results from the electron pointing and spectrum measurements.

3. Experimental Setup

3.3 Few-Cycle Probe System

Like Eadweard Muybridge's experiments in photographing the legs of a galloping horse (ms-timescale), or Harold Edgerton's rapatronic camera that imaged the expansion of nuclear explosions (μs - to ns-timescales), the ability to image the plasma wave in a plasma-based accelerator demands another jump in temporal resolution to the few-femtosecond regime. This requirement is necessary due to the fact that the plasma wave propagates at the group velocity of the pump laser. For tenuous plasma, this means trying to image an object moving roughly at the speed of light, or in microscopic terms $\sim 0.3 \mu\text{m}/\text{fs}$. As a first order approximation, for an optical microscope with a transverse spatial resolution near $1.5 \mu\text{m}$, limiting the effective exposure time of the image, i.e. the probe pulse's duration, to $\sim 3 \text{ fs}$ will keep the temporal blur of the image to that of the transverse spatial resolution. **Appendix B.1** describes the theory behind using self-phase modulation (SPM) to spectrally broaden a laser pulse and dispersion compensating mirrors (DCMs) to temporally compress the probe pulses to a shorter duration than the pump pulses. The following subsections will provide further details on the fc-probe's setup, characterization, important components and a discussion on the achievable temporal and spatial resolution.

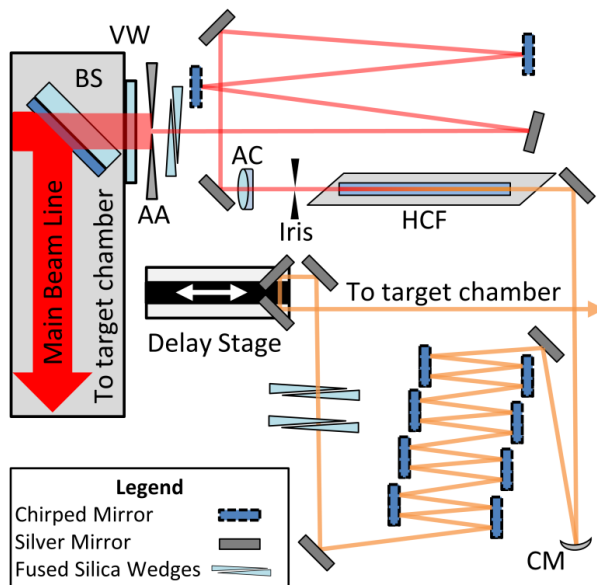


Figure 16: Diagram of the fc-probe beam setup including beamsplitter (BS), vacuum window (VW), apodized aperture (AA), achromatic focusing lens (AC), hollow core fiber (HCF) was filled with argon or neon gas, and a dielectric coated concave mirror (CM).

approximately 8 meters (propagation distance, not line-of-sight) from the target chamber. The extracted probe pulses are then sent through a fused silica window in the vacuum beamline. To ease alignment of the probe beam, the ca. 50 mm beam diameter extracted through the beamsplitter is reduced by an apodized aperture with a $1/e^2$ diameter of roughly 10 mm. The probe pulses are then focused with a 1 meter focal length achromatic lens into a hollow-core fiber (HCF) filled with either

3.3.1 Setup and Characterization

To greatly ease the temporal synchronization between the pump and probe pulses in the experiment, it proves advantageous to seed the probe beam with a fraction of the pump pulse's energy as close to the interaction point of the experiment, i.e., target chamber, as possible. Any excess beam path in the probe's optical chain is a potential source of temporal jitter of the probe's arrival time relative to the pump, which is seen as a variation of position in the shadowgrams.

Figure 16 shows the basic setup of the fc-probe, updated from [25]. The seed energy for the fc-probe beam on the Jeti 40 laser was split from the pump pulse using a 1-2% transmissive beamsplitter in the vacuum beam line

3. Experimental Setup

~0.4 bar of Argon gas or ~3.0 bar of Neon gas. The resulting self-phase modulation (SPM) in the HCF depends on the spatio-temporal intensity distribution of the probe pulses.

To optimize the SPM in the HCF a pair of fused silica wedges, a set of dispersion compensating mirrors (DCMs) and an iris aperture were placed in front of the HCF. Due to the material dispersion of the beamsplitter, vacuum window, achromatic focusing lens and entrance window to the HCF, the probe pulses become temporally stretched before their interaction in the gas-filled HCF. By combining the fused silica wedges and DCMs in front of the HCF, the temporal intensity distribution of the pulses entering the HCF can be optimized for SPM. Note that achieving the shortest pulses possible at the entrance of the HCF does not always lead to the most efficient spectral broadening due to potential ionization of the nonlinear gas [152]. Further studies show that a positive or negatively chirped input pulse can lead to significantly different broadening behaviors [153]. The transverse spatial intensity profile of the probe pulses at the entrance of the HCF were optimized via the apodized aperture and the iris aperture. The apodized aperture was positioned relative to the originally ~50 mm diameter beam to minimize the transmitted wavefront error and provide maximum pulse energy. Due to its serrated edge design, the iris aperture was used to “hard” cut the edge of the smaller ~10 mm diameter beam to avoid the higher spatial frequencies of the beam’s profile. Serrated apertures are typically paired with spatial beam filters to reduce the higher spatial frequencies in the far-field; however, due to mechanical limitations, this standard setup could not be realized. The implementation of the iris aperture was a “quick and dirty” solution that proved useful during the experimental campaign.

The beam exiting the gas-filled HCF is collimated using a concave spherical mirror that compensates the divergence of the beam from the HCF. Note that the beam’s divergence is wavelength dependent and as such cannot be achromatically compensated with a simple mirror. Finally, the combination of fused silica wedges and DCMs are once again used to temporally chirp the probe pulses, so that optimally their Fourier-limited temporal duration is realized at the interaction point in the target chamber. This entails considering the material dispersion of any optical components between the HCF’s exit and the gas-cell at the interaction point. Note that both the DCMs and the fused silica wedges were designed for the spectral properties of the probe beam at their respective positions in the optical system. The fused wedges were coated with a different broadband anti-reflection (BBAR) coating depending on their position: (800 ± 50) nm in front of the HCF and (750 ± 250) nm for use behind the HCF. Likewise, the DCMs spectral reflectivity and GVD per reflection were specifically purchased for use either before or after the nonlinear interaction in the HCF.

The final component in the probe beam system before the imaging optics is a delay stage. A delay stage is nothing more than a motorized linear stage with two mirrors aligned at 90 degrees to each other such that the pulses exiting the delay stage propagate anti-parallel (and displaced) to the pulses entering the stage. The delay stage used in the LWFA campaigns presented in this dissertation covered a total temporal window of ~2 ns (~30 cm travel) with a temporal resolution of 33 fs (5 μ m step size).

3. Experimental Setup

Characterization of the probe's pulse duration was performed before the LWFA campaign using a SPIDER measurement system (see **Appendix B.2**) from APE GmbH and a CEP-Meter developed by the Nonlinear Optics research group at the IOQ [154]. The FWHM pulse duration of the probe was shown to run reliably at ≤ 4 fs with a modulated broadband spectrum ranging from 500 nm to 950 nm with a total pulse energy ~ 120 μ J on target depending on the system's alignment [155].

3.3.2 Microscope, Filters, Polarizers, CCDs

After the probe beam has been spectrally broadened and temporally compressed to fc-pulse duration, it is used as a backlight, like a camera flash, to illuminate the pump-plasma interaction in the gas-cell. Refer to **Section 2.3.4** for a description of shadowgraphic imaging. An imaging system corrected for use in the VIS-NIR spectrum is then used to image the pump-plasma interaction. It consisted of an infinity corrected NIR Mitutoyo M Plan Apo 10x microscope objective with a spatial resolution of 1.5 μ m at 750 nm combined with an achromatic field lens with a focal length of 250 mm. The combined microscope system had a transverse magnification of 12.5. Typical CCD sensors used in the experiments to capture and digitize the images were designed with a pixel size of 5.5 μ m giving a calibration factor of 0.44 μ m/pixel. A thorough optical characterization of a similar setup was performed by Vera Neef for her Bachelor's thesis [156]. The combined system's resolution including the 12,7 mm thick vacuum window between the target and microscope was measured to be between 2.0 and 2.5 μ m using incoherent white light illumination.

As will be described in **Chapter 4** and published in [25], [157], one major advantage of an fc-probe is having the temporal resolution of a fc-pulse combined with the ability to spectrally resolve the pump-plasma interaction. Even when the pulse is linearly chirped, the effective temporal resolution of the non-chirped pulse can be regained if the pulse is spectrally filtered between the interaction point and the CCD sensor. For this reason, and to test the frequency dependence of the plasma electrons' cyclotron motion as described in **Chps. 4** and **5**, interference bandpass filters with several different spectral ranges were placed directly in front of the CCD sensors. The filters were selected with respect to peaks in the probe's spectrum to improve the signal-to-noise ratio of the images.

Another important aspect of the probe beam is its polarization and polarization orientation relative to the pump laser's polarization. Previous results from orthogonal probing methods have shown what was already predicted for scattered light from a charged particle [158], that a linearly polarized pump laser along the z-axis produces Thomson scattering that saturates the area of the pump pulse's propagation axis in a shadowgraphic image as recorded using the pump-probe geometry from **Fig. 14**. For the purposes of imaging the plasma wave, the pump was oriented to be linearly polarized along the y-axis to minimize Thomson scattering into the probe's optical system. The probe's polarization before entering the target chamber was also linear due to it being seeded by the pump laser through a non-polarizing beamsplitter. The DCMs were also optimized in reflectivity for p-polarization (polarization in the xy-plane in the experiment's global coordinates, see **Fig. 14**). Due to the interest in

3. Experimental Setup

investigating the probe's interaction with any electron-cyclotron motion in the plasma, and knowing that the pump's dominate B-field component was oriented along the z-axis, the probe beam was rotated to be linearly polarized at 45° to the x-axis in the xy-plane (again, see **Fig. 14**). This allowed to simultaneously record shadowgrams with horizontally polarized (H-pol) and vertically polarized (V-pol) probe orientations due to the placement of properly oriented polarizers directly in front of the two CCD sensors in the imaging system.

A Note on Polarization Rotation

Faraday rotation measurements of linearly polarized light through magnetized plasma have been used, both in LWFA experiments and elsewhere, to measure magnetic field distributions in plasma [23], [24], [159]–[162]. A linearly polarized probe's rotation in the plasma depends on the local plasma density and strength of magnetic fields aligned parallel or anti-parallel to the probe's propagation vector. The most typical measurement in the LWFA literature is of the accelerated electron bunch's azimuthal magnetic field as well as any azimuthal magnetic fields from plasma currents around the front of the plasma wave. While Faraday rotation of the probe's polarization due to any parallel or anti-parallel magnetic field in the plasma should generally not be ignored, it can, for the experiment presented here, be neglected. Faraday setups, like those in the above references, use linear polarizers in front of two separate CCDs that are slightly misaligned (in opposite directions) from extinction relative to the unperturbed probe's polarization axis. This allows a small component of rotated probe light through to each CCD. Further image processing by combing the two images allows one to identify the location and strengths of magnetic fields in the plasma that are parallel or anti-parallel to the probe beam's propagation vector. Typical magnetic field strengths measured in the literature fall in the range of a few hundred to a few thousand Tesla.

There exists, within the plasma, another magnetic field with a strength of several tens of thousands of Tesla, namely the peak magnetic field of the pump laser, which in this work was oriented along the z-axis. If this field were to impose any anisotropy in the plasma, it would be visible by comparing shadowgrams taken with linearly polarized probe beams along the x- and z-axes. Faraday rotation of the probe beam as described in the previous paragraph will also be present in the shadowgraphic images due to any magnetic fields along the y-axis. However, without the necessary linear polarizers, i.e., a polarimetry setup, and the requisite image processing it will most likely not be a dominant signal in the shadowgram due to the weak nature of these fields compared to B_z of the pump. This is especially true considering the spatial separation of an accelerated electron bunch and the peak of the pump laser for acceleration lengths below the dephasing length. More importantly for this work, the continuous injection caused by ionization injection in a single stage gas-cell would prevent a well-formed electron bunch with high enough current to produce a strong Faraday signal. For these reasons, any direct influence of Faraday rotation on the appearance of the shadowgrams in this work have been

3. Experimental Setup

neglected; although future work should keep in mind possible contributions depending on the expected magnetic field strengths and field orientations in the plasma.

3.3.3 Temporal Resolution of Few-Cycle Microscopy in LWFA

The temporal resolution of the few-cycle microscope system implemented in LWFA depends on several factors including: the effective pulse duration of the probe beam, the depth of field of the imaging system, and the phase velocity of the plasma wave. This is assuming that the plasma wave is the primary object of interest to be imaged. In order to avoid temporal averaging of the plasma wave's micrometer-scale structures, the system must be designed such that the effective temporal resolution is well below the time needed for the plasma wave to travel half of its period, i.e., $t_{res} \ll \lambda_p / (2v_{ph,p})$, where $v_{ph,p}$ is the plasma wave's phase velocity. This is the limit where the peak of a sinusoidal density distribution (linear plasma wave) would overlap with the next dip in that distribution, effectively blurring out the distribution of a linear plasma wave. Assuming $\lambda_p = 9 \mu\text{m}$ then the temporal resolution of the system should be kept well below 15 fs. This effect can be seen computationally in **Figs. 6d** and **13** of [27] and is also reprinted with permission in **Appendix D**.

The plasma wave's phase velocity is the primary driver behind needing an ultra-short effective pulse duration of the probe. The faster the plasma wave travels, the shorter amount of time it needs to cover one half of its period. The plasma wave's phase velocity can be approximated with the group velocity of the laser driver, $v_g = c\eta$. The refractive index of nonmagnetized, underdense plasma has a value very near to one, making the group velocity, and thus the plasma wave's phase velocity very close to c . To be more precise, a laser driver centered at 800 nm in a background electron density of $1 \cdot 10^{19} \text{ cm}^{-3}$ experiences a refractive index of 0.997. The drastic increase in background density, or likewise the increase in the pump's wavelength necessary to cause an appreciable reduction in group velocity both have serious disadvantages. The former detrimentally reduces the dephasing length and the latter demands high-intensity lasers in the mid- to long-infrared.

Since the phase velocity of the plasma wave cannot be easily changed, one is left with the probe's pulse duration and the imaging system's depth of field as design parameters in the experimental setup. The plasma wave has a transverse extent that is roughly equal to its longitudinal extent, which proposes a bit of a riddle. If the plasma wave travels at the speed of light and one must image it before it has travelled at most half of its own wavelength, won't the image inevitably be blurred out since the probe pulse cannot travel faster than c , but must also travel through the plasma wave's transverse extent of $\sim \lambda_p$? This is where the depth of field of the imaging system plays an important role. The "slice" of plasma that is in focus at the detector plane is only that plasma lying within the depth of field of the microscope. Plasma distributions outside of the depth of field will be strongly blurred at the image plane. So, in order to prevent the transit time of the probe through the plasma wave's transverse extent from being too long and blurring out the plasma wave, the depth of field is selected

4. Experimental Data

such that only a small slice of plasma is imaged to the detector. The effective temporal resolution thus becomes that sum of the probe beam's duration and its transit time through the system's depth of field.

Finally, the physics of shadowgraphy also play a role in describing the effective temporal resolution of few-cycle microscopy. As described in **Section 2.3.4**, the intensity variation measured in shadowgraphy depends on the second spatial derivative of the plasma's refractive index in the transverse plane, having been averaged over the longitudinal direction. Depending on the exact distribution of the local plasma density, this can also act to suppress "out-of-plane" contributions to the final image, effectively reducing the temporal smearing due to the co-propagation of plasma wave and probe pulse. A systematic analysis of temporal resolution, either experimental or numerical, has not yet been performed, most likely due to the fact that modern technology can now "easily" image the plasma wave and there are currently more interesting physics to be analyzed. At some point in the future, with more beam time and more stable systems, scanning probe and plasma parameters to analyze the system's temporal resolution will be as "inexpensive" as characterizing a simple lens.

4. Experimental Data

4.1 Introduction to Few-Cycle Shadowgrams

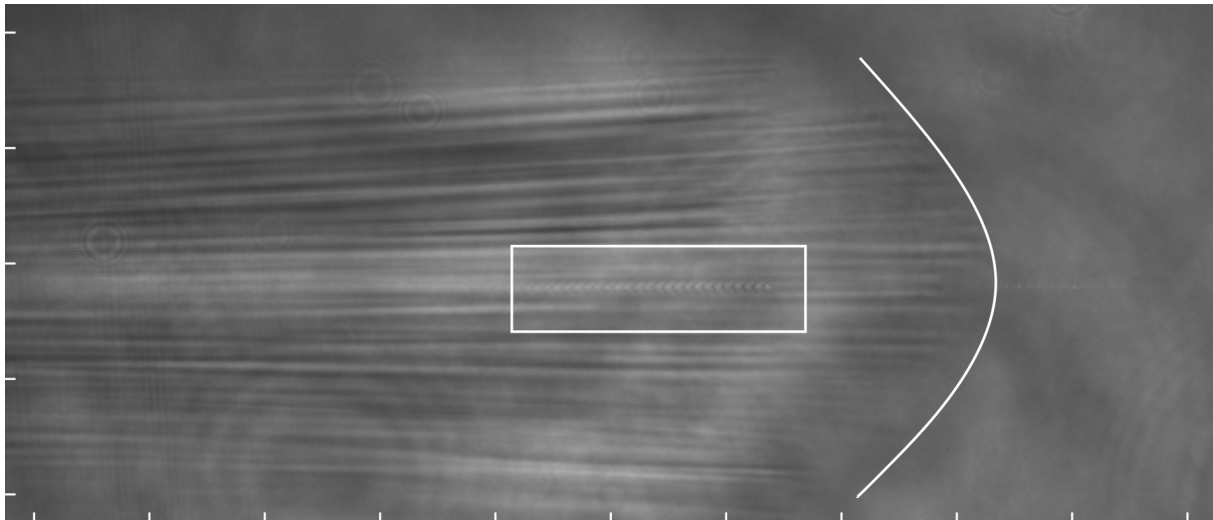


Figure 17: Exemplary shadowgram using the full spectrum of the fc-probe measured with the H-pol orientation. White tick marks indicate 100 μm spacing over $\sim 0.4 \times 1.0$ mm FoV. White rectangle is magnified area of **Fig. 18**. Ionization front marked by concave white curve. Pump pulse travels left to right.

The data presented in this chapter were measured during a LWFA campaign at the Jeti 40 laser at the IOQ in Jena. Pump pulses with a FWHM duration of 27 fs and total energy of 650 mJ on target were focused with an F/12 off-axis parabolic mirror to a (9.7 ± 0.1) μm FWHM focus with 37% of the pulse energy inside the FWHM area. Assuming a Gaussian pulse shape, a peak intensity in vacuum of $2.3 \cdot 10^{19}$ W/cm² is calculated and corresponds to a peak normalized vector potential of

4. Experimental Data

$a_0 = eE_0/(\omega_L m_e c) = 3.3$. The plasma originated from helium gas with 5% nitrogen dopant contained in a gas-cell and ionized by the pump's rising edge [145].

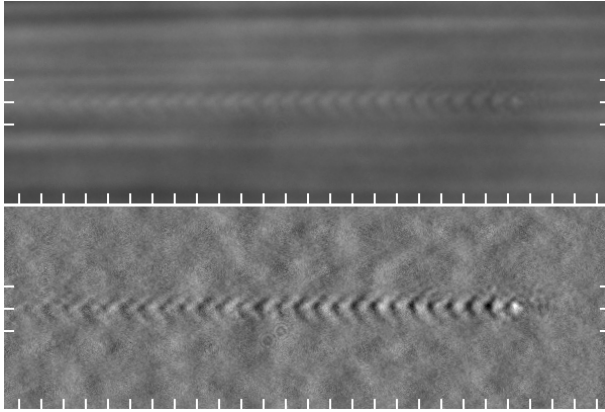


Figure 18: Magnified shadowgram from Fig. 17. Tick marks indicate 10 μm spacing over $\sim 250 \mu\text{m}$ horizontal FoV. Top: normal. Bottom: background removed

A typical shadowgram recorded by the few-cycle imaging system is presented in Fig. 17. With the pump laser traveling from left to right in the plasma, its rising edge creates an ionization front, delineating the boundary between unionized gas and plasma. The distance between the ionization front and the start of the plasma wave ($\sim 600\text{-}700$ fs) correlates to the temporal intensity contrast (TIC) of the laser [163] with the ionization front being situated near the $5 \cdot 10^{15} \text{ W/cm}^2$

intensity level which corresponds to the ionization threshold for $He \rightarrow He^+$ according to BSI theory [26], [112]. The diameter of the ionization front (ca. $350 \mu\text{m}$) correlates to the spatial intensity contrast of the laser and indicates the location at which the laser's transverse intensity profile drops to $5 \cdot 10^{15} \text{ W/cm}^2$. For a perfect Gaussian intensity distribution with $9.7 \mu\text{m}$ FWHM focus the diameter of the ionization front in the focus plane of the laser would be considerably smaller, roughly $36 \mu\text{m}$. By measuring the plasma-wave's periodic structure from the shadowgrams [26], cf., Fig. 18, an average plasma wavelength of $8.6 \mu\text{m}$ was measured, corresponding to an on-axis background electron density n_e/γ of $(1.5 \pm 0.1) \cdot 10^{19} \text{ cm}^{-3}$ with $\gamma = 1$ being the Lorentz factor for plasma electrons more than $30 \mu\text{m}$ behind the driver.

4.2 Electron Spectra as a Sorting Criteria

A primary goal of recording shadowgrams of the LWFA process while varying the pump-probe delay is to investigate the evolution of the plasma wave and any related signals as the pump propagates through the plasma. Due to variability in the shot-to-shot performance of the LWFA setup, the recorded shadowgrams should first be grouped based, e.g., on the characteristics of their respective accelerated electron bunch as measured by either a dipole spectrometer, a pointing and divergence diagnostic, or some other relevant diagnostic. This enables more dependable comparison between shadowgrams taken with different shots but otherwise as near to constant pump and plasma parameters as the experimental setup would allow. The analysis follows the simplifying assumption that similar characteristics of the electron bunches obtained with different shots of the pump laser indicate similar laser-plasma interactions thus allowing for comparison of shadowgrams taken at different propagation distances of the pump, and also comparison of shadowgrams recorded with different probe polarizations and spectral filters that could not be simultaneously recorded.

4. Experimental Data

The following paragraphs describe the sorting operation for any data set that included measurements with the electron spectrometer. Firstly, any spectrum exhibiting a peak in electron energy was labeled as such and sorted out of the data set into its own group. Overall, the remaining spectra exhibited a broad energy spread up to some cutoff energy. Along with the electron bunch's total charge its cutoff energy would have been used to further sort the data. Unfortunately, this was not possible. The magnetic dipole spectrometer did not have an entrance slit to constrain the beam axis of the incoming electron bunches and instead relied on stable beam pointing to define the "undeflected" beam axis through the spectrometer. If the pointing was stable one would measure the electron beam's position on the Lanex screen without the dipole magnet in the system. Then, after driving the magnet into the beam, the electron bunch's spectrum could be measured knowing the original axis of the beam. Regrettably, the variability in the electron beam's pointing resulted in a large uncertainty in calculating the spectra's cutoff energies. Due to this error, each shot was sorted based on the total charge of the electron bunch and the overall shape of the spectrum relative to the set's average.

Along with the aforementioned "peak" group, shots were also sorted into groups labelled "at", "above" and "below". Given a data set's average spectrum and average charge (calculated by ignoring shots already in the "peak" group) each shot was sorted into one of the remaining three groups based on its measured charge. The "at" group contained all shots having a bunch charge falling within $\pm 20\%$ of the average charge (3.2 pC), while the "below" and "above" groups contained shots whose bunch charges were more than 20% below the average charge or more than 20% above the average charge, respectively. Any shot with a spectrum exhibiting a shape or cutoff energy drastically different than the set's average was removed from consideration.

Some data sets relied on the electron pointing diagnostic, i.e., the Lanex screen without the dipole magnet in the beam's path, to help sort the recorded shadowgrams into groups. Each shot's FWHM divergence and charge within the FWHM beam area was calculated and three groups were defined based on the results. Group "G1" contained all shots with a bunch charge between 0.5 and 1.6 pC and a FWHM divergence between 5 and 14 mrad. Group "G2" contained shots between 1.6 to 3.4 pC and 9 to 22 mrad, and group "G3" contained shots between 3.4 to 5.2 pC and 12 to 27 mrad. All shots not within these ranges were ignored.

Finally, having established the groups "at", "above", "below" and "peak" using the electron spectrometer, and "G1", "G2", and "G3" using the beam pointing diagnostic, the shots were sorted within each group based on the pump laser's position in the gas-cell, i.e., the delay between the pump and probe beams. Image sequences depicting the evolution of the plasma wave given the above grouping criteria were then created and are shown in the following two sections.

Despite the invested effort of sorting all the shots based on the respective characteristics of their electron bunches, no significant correlation between bunch charge, divergence or energy distribution and the recorded shadowgrams was seen in the data. The small range in bunch charges of roughly 1 to

4. Experimental Data

5 pC was insufficient to drive the plasma waves into different regimes such as beam-loaded or beam-dominated regime [164]. This is at least true for all shots that produced both a visible and “well-behaved” plasma wave in the shadowgrams as well as an electron bunch measurement with a “well-formed”, i.e., Gaussian-like, spatial distribution. Nonetheless, the following two Sections (4.3 and 4.4) make use of the above-described sorting method and display experimental data of plasma waves grouped into “stitched-images”, which show the possible evolution of the plasma wave as it is driven by the pump laser and propagates through the gas-cell.

4.3 H-pol and V-pol Shadowgrams with Full Spectrum

To establish a baseline of how the plasma waves typically look during propagation through the gas-cell, a series of shadowgrams were recorded using the full spectrum of the probe pulse. Two shadowgrams were simultaneously recorded for each shot of the pump laser: one CCD sensor recorded images using a horizontally oriented polarizer (H-pol) while the second CCD measured with a vertically oriented polarizer (V-pol). The probe beam was incident on the pump-plasma system with linear polarization oriented at 45° to the x -axis in the xz -plane as shown in Fig. 14. Using the sorting criteria described in Section 4.2 shots were grouped based on the characteristics of the measured electron bunches. Their respective shadowgrams were then grouped by propagation distance in the gas-cell and sets of images showing the possible evolution of the plasma wave were selected based on similarities between subsequent images assuming the evolution of the plasma wave within a single $\sim 200 \mu\text{m}$ propagation step was not drastic enough to change the entire shape and size of the structure.

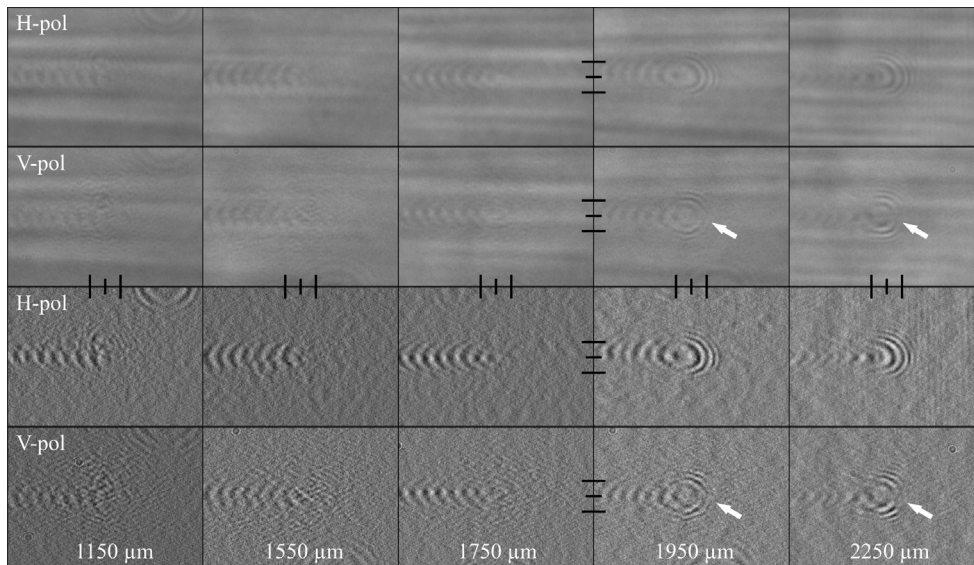


Figure 19: Evolution of the plasma wave as imaged by an H-pol oriented polarizer (rows 1,3) and a V-pol oriented polarizer (rows 2,4). Raw data (rows 1,2) and background subtracted data (rows 3,4). White arrows indicate on-axis break in half-ring signal in V-pol shadowgrams. Black tick marks give $\pm 10 \mu\text{m}$ length.

Figure 19 shows data for the evolution of the plasma wave imaged with the H-pol/V-pol setup. Each sub-image shows a $128 \times 91 \mu\text{m}^2$ cutout of the front of the plasma wave as it propagates through the gas-cell. The distances labelled at the bottom of each column are the approximate

4. Experimental Data

propagation distances of the pump laser's peak relative to the gas-cell's inner entrance wall. The first three imaging positions clearly show a plasma wave but no significant structure near the front of the plasma wave where the peak of the pump laser is expected, whereas the last two imaging positions exhibit half-ring structures in front of the assumed position of the pump laser's peak.

An interesting signal seen in **Fig. 19** is the difference in the half-ring structures seen at the front of the plasma wave at distances 1950 μm and 2250 μm . An on-axis break in the rings is seen in the V-pol images while the H-pol images show no such on-axis break (cf. **Fig. 33**, **Section 6.2**). Every set of H-pol/V-pol images recorded in the experiment, in which these half-ring structures were seen, showed an on-axis break when recorded with the V-pol orientation and no on-axis break when recorded with the H-pol orientation. A theory for the origin of this signal will be described in **Chapter 5**.

4.4 Comparison of Spectrally Filtered H-pol Images

Further propagation scans of the plasma wave travelling through the gas-cell were recorded using interference filters in front of the two CCD sensors in the imaging setup. A total of three different interference filters were used over the various scans, each having a bandwidth of 40 nm and central wavelengths of 850, 800 and 660 nm, respectively. Both linear polarizers in the setup were set to the H-pol orientation. The first stitched image, **Fig. 20**, shows shadowgrams taken with filters centered at wavelengths of 800 nm and 850 nm. The evolution shows very similar behavior as seen in the H-pol/V-pol scan (see **Fig. 19**). During the first half of the pump laser's propagation no clearly visible structure is seen at the front of the plasma wave. Similarly, the half-ring signal forms in the latter half of the gas-cell. In general, only slight differences in the plasma waves, as measured with the two spectral filters, can be seen.

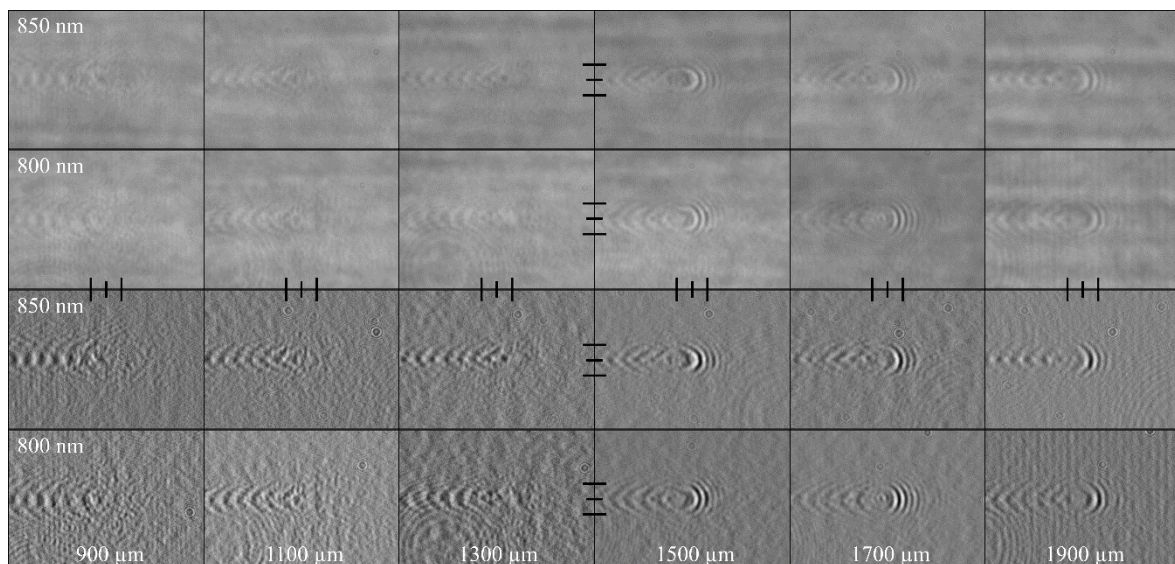


Figure 20: Evolution of the plasma wave imaged with an H-pol oriented probe filtered to (850 ± 20) nm (rows 1,3) and (800 ± 20) nm (rows 2,4). Raw data (rows 1,2), background subtracted data (rows 3,4). Black tick marks give $\pm 10 \mu\text{m}$ length.

4. Experimental Data

After changing the filters to be centered at 850 nm and 660 nm, more significant differences in the spectrally filtered plasma waves can be observed, as seen in **Fig. 21**. Weaker half-ring signals can be seen at the 1500 μm and 1700 μm propagation distances and the plasma waves in general are slightly narrower than those in the previous stitched images. This is not a direct result of the change in probe wavelength but rather the result of grouping shots together that had plasma waves with generally similar structure. The most significant differences are seen in the front part of the plasma waves where after a propagation distance of 1300 μm the images recorded at 850 nm show dark central areas and the images recorded at 660 nm show bright central areas. These signals are best viewed in the raw data (rows 1,2 see arrows) due to the fact that the method for removing the background can change the relative pixel values in the plasma wave (rows 3,4). The signal described by the light/dark areas will henceforth be named the “asymmetric” signal.

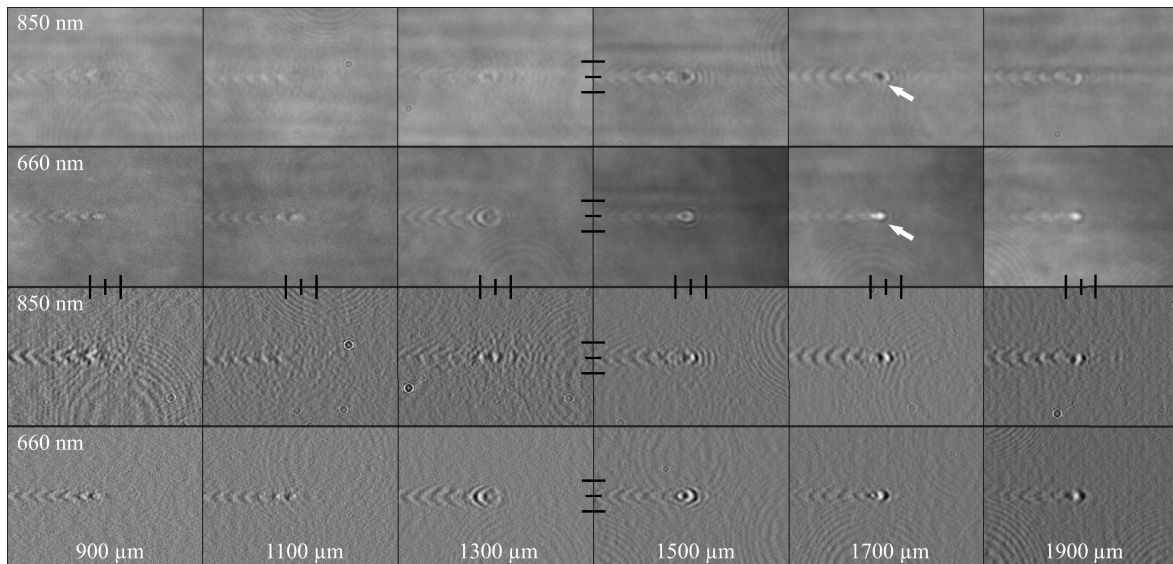


Figure 21: Evolution of the plasma wave as imaged with an H-pol oriented probe filtered to (850 ± 20) nm (rows 1,3) and (660 ± 20) nm (rows 2,4). Raw data (rows 1,2), background subtracted data (rows 3,4). Black tick marks give $\pm 10 \mu\text{m}$ length. Arrows mark examples of the differences as mentioned in the text.

There are many aspects to the few-cycle, shadowgraphic imaging of plasma waves that can alter how the waves appear in the image including properties of the probe beam, pump beam, imaging system, and the plasma itself. The main questions concerning these unidentified signals, i.e., the half-ring and asymmetric signals, are what are the origins of the signals and can they be used to gain information on the evolution of the laser-plasma interaction? Luckily, work has been done by *Siminos* et al. using 3D PIC simulations to understand the changes in the shadowgrams given changes in the probe’s duration, central wavelength and the defocus of the imaging system [27]. Both the half-ring signal and the asymmetric signal are seen in the results of the simulations; however, their origins are not explained. In **Chapter 5**, a mathematical framework for understanding the origins of these signals will be presented. In **Chapter 6**, results from 2D PIC simulations using the aforementioned

mathematical framework will be presented alongside further evaluation of the 3D PIC simulations from *Siminos et al. [27]* to verify the origins and relevance of the signals seen in the experimental data.

5 Methods of Analysis

The formation of the shadowgrams presented in the experimental data results from a complex interplay combining the simultaneous propagation of the pump, probe, and wakefields along with the few-cycle characteristics of the probe and the relativistic motion of the plasma electrons. To help better understand and interpret this interplay, **Section 5.1** describes modifications to the Appleton-Hartree (AH) equation such that it can be used to calculate the effective refractive indices of relativistic, magnetized plasma. **Section 5.2** introduces 2D PIC simulations using VSim which produce data that can be combined with the modified AH equation to test the origins of signals seen in the experimental data. Finally, **Section 5.3** continues with the setup of a 3D PIC simulation using EPOCH whose data was processed to produce simulated shadowgrams. By analyzing these shadowgrams, the origin of the asymmetric and half-ring signals can be further investigated.

5.1 Relativistic Appleton-Hartree Equation

The Appleton-Hartree equation, **Eq. 24**, was introduced in **Section 2.2** and describes EM wave propagation through statically magnetized plasma and the resulting resonance and reflection conditions that can strongly modify the anisotropic system's refractive indices. In underdense plasma magnetized by a relativistically intense pump laser, and assuming static ions, the characteristic frequency of interest is the electron-cyclotron frequency, given here simplified to its non-relativistic form of $\Omega_c = eB/m_e$ with the local magnetic field B . The magnetic field $B = a_0 \lambda_L^{-1} [\mu\text{m}] \cdot 10.7 \text{ kT}$ of a relativistically intense pump centered at 800 nm and with an a_0 in the range of 0.8 to 2.0 is in the tens of kilotesla range. The corresponding cyclotron wavelengths of such a magnetic field lie in the VIS-NIR spectral band of 400 nm to 1000 nm. Any probe with a spectrum near the cyclotron frequency and a polarization component parallel to the plane of cyclotron motion encounters resonance and reflection points and is thus sensitive to the pump's magnetic field. Polarization components perpendicular to the plane of cyclotron motion effectively see unmagnetized plasma.

The LWFA setup using a TW-class laser in underdense plasma complicates direct use of the AH equation primarily due to the relativistic motion of the plasma electrons, but also due to the fast oscillating EM fields and quasi-static fields in the system. The relativistic modifications to the resonance and reflection conditions are only necessary for regions of plasma where the plasma electrons move relativistically, and are also only necessary for regions of plasma with intense magnetic fields such that the local cyclotron frequency overlaps with the probe's frequency spectrum. Fortuitously, these conditions could allow for measurement of the evolving pump's intensity distribution in the plasma, since under the described experimental conditions only the pump's magnetic field is strong enough to increase the cyclotron frequency into the range of a VIS-NIR probe.

5 Methods of Analysis

Qualitatively, the complex pump-plasma system and its influence on the probe can be understood in the following manner. As the pump laser ionizes the target gas and propagates through the resulting plasma, the plasma electrons respond to both the quasi-static and oscillating EM fields in the system. The electrons' motion can be separated into two main components: a quiver motion that plays out on the time scale of the pump's period and a drift motion seen at a time scale of a few cycles of the pump's period. The faster quiver-motion of the electrons arises due to the oscillating electric and magnetic fields of the pump laser. A linearly polarized laser driver will cause quiver-motion in the plane of the laser's electric field. This motion is also referred to as Figure-of-Eight motion (see **Section 2.4.1**), but the appearance of the Figure-of-Eight orbit depends on the chosen reference frame and will not be seen in the lab's inertial frame. The longer time-scale drift motion of a plasma electron's guiding center arises from both the ponderomotive force of the pump and the Coulomb force due to space-charge distributions in the plasma, sometimes referred to as the plasma's restoring force. The motion of each plasma electron can then be represented by using a drift-frame defined by the time-averaged trajectory of the electron's guiding center, in which the electron can still perform more complicated Figure-of-Eight-like oscillations [66].

Because the motion of the plasma electrons can be relativistic, it is advantageous to investigate the Lorentz transformed pump and probe fields in the relativistic drift-frame of the plasma electrons' guiding centers. In general, for an electron drift trajectory that is parallel to the propagation of an EM wave, the wave's wavelength as experienced by this electron becomes red-shifted and the wave's field amplitude decreases. Contrarily, for a drift-frame trajectory that is anti-parallel to the EM wave's propagation, the wave becomes blue-shifted and its electric and magnetic field strengths increase. The system's response does deviate from this simple description depending on the exact angle between the drift trajectory and the wave's propagation vector, as well as the gamma factor of the drift-frame, but the exact behavior can be captured using the full Lorentz transformation in Minkowski space. The rest of **Section 5.1** give a step-by-step description of the relativistic modifications to the AH equation.

5.1.1 Cartesian Coordinate System

The first step toward mathematically explaining the effects seen in the experimental data is to define a Cartesian coordinate system of the lab-frame, or K -space, as used in the experiment. The mathematical model presented here will follow the experimental setup as shown in **Fig. 14**. The x -axis will be used as the propagation axis of the pump laser, whose electric field is polarized along the y -direction. The y -axis will be used for the propagation of the probe, with the probe beam travelling along the negative y -direction. Finally, the z -axis aligns with the dominant magnetic field of the pump.

A second set of Cartesian coordinates will be used to define each individual drift-frame of the plasma electrons' guiding centers as they move in the plasma and in the fields of the pump laser. In general, this set of frames (one for each plasma electron's guiding center) will be denoted as K' -space, with axes x' , y' and z' . The standard configuration in text books only allows the K' -frame to move in

5 Methods of Analysis

the z - or z' -direction relative to the K -frame or lab-frame, with these axes being parallel to each other, which simplifies the mathematics of the Lorentz transformation between the two frames. Here, the K' -frame or drift-frame will be allowed to move in any direction with velocity $\mathbf{v} = v_x \hat{x} + v_y \hat{y} + v_z \hat{z}$ relative to the K -frame or lab-frame. The associated Lorentz or gamma factor is given by $\gamma = 1/\sqrt{1 - v^2/c^2}$ with $v = |\mathbf{v}| = \sqrt{v_x^2 + v_y^2 + v_z^2}$. This necessitates the use of the full Lorentz transformation when switching between mathematical descriptions of the two frames. Note that the terms “drift-velocity” or “drift-frame” will refer to the guiding centers of the electrons and not to the electrons’ motions in the lab-frame directly.

5.1.2 Relativistic Modifications to the AH Equation

The collisionless AH equation, **Eq. 24** from **Section 3.2.2**, is immediately written in the drift-frame of the plasma electrons’ guiding centers by using the above-mentioned prime notation. This equation, **Eq. 72**, will be referred to as the relativistic Appleton-Hartree equation, or RAH equation for short.

$$\eta_{\pm}'^2 = 1 - \frac{\left(\frac{\omega_p'}{\omega'}\right)^2}{1 - \frac{\left(\frac{\Omega_c'}{\omega'}\right)^2 \sin^2 \theta'_{kB}}{2 \left(1 - \left(\frac{\omega_p'}{\omega'}\right)^2\right)} \pm \frac{\left(\frac{\omega_p'}{\omega'}\right)^2}{\sqrt{4 \left(1 - \left(\frac{\omega_p'}{\omega'}\right)^2\right)^2 + \left(\frac{\Omega_c'}{\omega'}\right)^2 \cos^2 \theta'_{kB}}} \quad (72)$$

Some of the drift-frame’s variables have a dependence on the refractive indices in the lab-frame, η_{\pm} , allowing one to solve for these indices numerically. This follows work done by H. Unz [165] in which the plasma’s relativistic motion was restricted to be parallel to the applied magnetic field. This simplification produced an analytical result for the lab-frame’s refractive index. Here; however, the motion of the plasma electron is not restricted to be parallel to the magnetic field, thus no simple analytical expression is achieved. A description of each of the primed variables follows.

The first substitution that can be made is in replacing the drift-frame’s refractive indices with an EM wave’s wave-number $k' = |\mathbf{k}'|$ and angular frequency ω' in the drift-frame, as shown in **Eq. 73**. In most cases, a monochromatic plane-wave representing the probe beam of the experiment will be used as the EM wave. The values for k' and ω' will be introduced later using the Lorentz transformation of the EM wave’s four-vectors \mathbf{k}^{μ} and k'^{μ} . The subscript \pm is often seen used with η or η' and comes from the \pm in the denominator of the AH and RAH equations, corresponding roughly to the O-wave and X-wave in **Section 2.2**. It physically represents the two extrema refractive indices for orthogonal polarization states of the EM wave traveling through the magnetized plasma. Strictly speaking, k' and ω' should have \pm subscripts as their values also depend on which refractive index is being used as will be described shortly by **Eq. 80**.

$$\eta_{\pm}' = \frac{ck'}{\omega'} \quad (73)$$

5 Methods of Analysis

Next, one can substitute the relativistic electron-cyclotron frequency Ω'_c with the expression shown in **Eq. 74** below. This equation represents the cyclotron-frequency of the plasma electrons in the drift-frame of their guiding centers and as such contains the Lorentz transformed magnetic field amplitude $B' = |\mathbf{B}'|$ and the Lorentz factor of the plasma electron's residual velocity in the drift-frame γ'_Q , i.e. its quiver velocity. The use of cycle-averaged values, denoted by the angled brackets $\langle \ \rangle$, refers to temporally averaging the local magnetic field of the plasma electron and its residual velocity in its drift-frame over one half-cycle of the Lorentz transformed pump laser's cycle. This approximates calculating an effective relativistic cyclotron frequency for each half of the electrons' Figure-of-Eight motion around its guiding center.

$$\Omega'_c = \frac{e\langle B' \rangle}{\langle \gamma'_Q \rangle m_e} \quad (74)$$

The relativistic electron plasma frequency shown in **Eq. 75** exhibits a Lorentz invariant quantity $n_e/(\gamma m_e)$ which from the lab-frame can be understood via the "relativistic mass increase" of the electron, and from the drift-frame can be understood via the relativistic contraction of the volume element used to define the electron-plasma density n_e [40].

$$\omega'_p = \sqrt{\frac{n_e e^2}{\epsilon_0 \gamma m_e}} \quad (75)$$

The last direct substitution to be performed with **Eq. 72** concerns the angle θ'_{kB} between the EM wave's propagation vector \mathbf{k}' and the local magnetic field vector \mathbf{B}' in the drift-frame. **Equation 76** gives this angle as the arccosine of the dot product over the product of the vectors' magnitudes. \mathbf{B}' can consider all components of any magnetic fields local to the plasma electron; however, for investigation of RECRs near the peak of the pump laser's intensity distribution, the magnetic fields of the laser dominate any magnetic fields from the surrounding plasma.

$$\theta'_{kB} = \arccos\left(\frac{\mathbf{k}' \cdot \mathbf{B}'}{|\mathbf{k}'||\mathbf{B}'|}\right) \quad (76)$$

In **Eqs. 73-76**, the values of ω' , \mathbf{k}' , and \mathbf{B}' still need to be defined. To do so, the full Lorentz transformation of the four-vector representation of an EM wave is introduced [166]. First, by combining the EM wave's angular frequency ω and the components of its wave-vector, four-vectors defining the EM wave in both the lab-frame, \mathbf{k}^ν , and the drift-frame, \mathbf{k}'^μ , can be given as shown by **Eqs. 77** and **78**, respectively. The indices μ and ν take on integer values 0, 1, 2 and 3 to represent the terms of the four-vector.

$$\mathbf{k}^\nu = \begin{pmatrix} \omega/c \\ k_x \\ k_y \\ k_z \end{pmatrix} \quad (77)$$

$$\mathbf{k}'^\mu = \begin{pmatrix} \omega'/c \\ k'_x \\ k'_y \\ k'_z \end{pmatrix} \quad (78)$$

5 Methods of Analysis

The matrix defining the full Lorentz transformation from one inertial frame to another inertial frame is given by **Eq. 79** below. Here, \mathbf{v} is the relative velocity of the primed frame with respect to the unprimed frame, in other words, it is the velocity of the drift-frame as seen from the lab-frame with the corresponding Lorentz factor γ .

$$\Lambda_{\nu}^{\mu} = \begin{pmatrix} \gamma & -\frac{v_x \gamma}{c} & -\frac{v_y \gamma}{c} & -\frac{v_z \gamma}{c} \\ -\frac{v_x \gamma}{c} & 1 + (\gamma - 1) \frac{v_x^2}{v^2} & (\gamma - 1) \frac{v_x v_y}{v^2} & (\gamma - 1) \frac{v_x v_z}{v^2} \\ -\frac{v_y \gamma}{c} & (\gamma - 1) \frac{v_x v_y}{v^2} & 1 + (\gamma - 1) \frac{v_y^2}{v^2} & (\gamma - 1) \frac{v_y v_z}{v^2} \\ -\frac{v_z \gamma}{c} & (\gamma - 1) \frac{v_x v_z}{v^2} & (\gamma - 1) \frac{v_y v_z}{v^2} & 1 + (\gamma - 1) \frac{v_z^2}{v^2} \end{pmatrix} \quad (79)$$

To calculate the components of the EM wave's four-vector in the drift-frame, one uses multiplication of **Eqs. 77** and **79**, or $\mathbf{k}'^{\mu} = \Lambda_{\nu}^{\mu} \mathbf{k}^{\nu}$. The result is shown below in **Eq. 80**.

$$\begin{pmatrix} \omega'/c \\ k'_x \\ k'_y \\ k'_z \end{pmatrix} = \begin{pmatrix} \frac{\omega}{c} \gamma - \frac{v_x}{c} \gamma k_x - \frac{v_y}{c} \gamma k_y - \frac{v_z}{c} \gamma k_z \\ -\frac{\omega}{c} \gamma \frac{v_x}{c} + k_x \left(1 + (\gamma - 1) \frac{v_x^2}{v^2} \right) + k_y (\gamma - 1) \frac{v_x v_y}{v^2} + k_z (\gamma - 1) \frac{v_x v_z}{v^2} \\ -\frac{\omega}{c} \gamma \frac{v_y}{c} + k_x (\gamma - 1) \frac{v_x v_y}{v^2} + k_y \left(1 + (\gamma - 1) \frac{v_y^2}{v^2} \right) + k_z (\gamma - 1) \frac{v_y v_z}{v^2} \\ -\frac{\omega}{c} \gamma \frac{v_z}{c} + k_x (\gamma - 1) \frac{v_x v_z}{v^2} + k_y (\gamma - 1) \frac{v_y v_z}{v^2} + k_z \left(1 + (\gamma - 1) \frac{v_z^2}{v^2} \right) \end{pmatrix} \quad (80)$$

This result can be greatly simplified by introducing the parameters of the probe's k-vector in the lab-frame given by $\mathbf{k} = (0, -\omega \eta_{\pm}/c, 0)$ in the monochromatic, plane-wave approximation, since the probe is restricted to only propagate along the negative y-direction. By extracting the top component of the four-vector in **Eq. 80**, one sees the Doppler shifted frequency of the probe to be only dependent on the drift-frame's velocity in the y-direction, i.e., $\omega' = \omega \gamma (1 + \eta_{\pm} \beta_y)$ with $\beta_y = v_y/c$. Furthermore, by inspecting all components of the EM wave's four-vector, one sees that any dependence on the lab-frame's k-vector, specifically its k_y component, includes a dependence on the lab-frame's refractive indices η_{\pm} .

Moving on to the value of \mathbf{B}' , special relativity offers simple equations for transforming the EM field strengths from one inertial frame to another. It is important to note that these transformations are to be only used with the amplitudes of the EM fields and not with the fields' full complex representation including their phase. **Equations 81** and **82** show the required transformations to represent \mathbf{E}' and \mathbf{B}' as functions of \mathbf{E} , \mathbf{B} , and \mathbf{v} .

$$\mathbf{E}' = \gamma(\mathbf{E} + \mathbf{v} \times \mathbf{B}) - (\gamma - 1) \frac{\mathbf{v} \cdot \mathbf{E}}{v^2} \mathbf{v} \quad (81)$$

$$\mathbf{B}' = \gamma \left(\mathbf{B} - \frac{1}{c^2} \mathbf{v} \times \mathbf{E} \right) - (\gamma - 1) \frac{\mathbf{v} \cdot \mathbf{B}}{v^2} \mathbf{v} \quad (82)$$

By restricting the probe's EM wave in the lab-frame to not only enter the plasma propagating in the negative y-direction, but also to be either polarized along the x-axis (H-pol) or the z-axis (V-pol), **Eqs.**

81 and **82** can be simplified. The analysis of these simplifications can also show some interesting aspects of special relativity concerning vector orientations. Starting with the H-pol probe in the lab-frame with components E_x and B_z , the Lorentz transformation of its EM fields to the drift-frame, $\mathbf{E}'_{prb,Hpol}$, gives results as shown in **Eq. 83**. Likewise, the V-pol probe in the lab-frame with components E_z and $-B_x$ transforms to $\mathbf{E}'_{prb,Vpol}$ as shown in **Eq. 84**. One sees that although both waves in the lab-frame contained only one component of the electric field, their Lorentz transformed representation in the drift-frame contains all three components depending on the motion of the drift-frame relative to the lab-frame.

$$\mathbf{E}'_{prb,Hpol} = \begin{pmatrix} \gamma E_x + \gamma B_z v_y - (\gamma - 1) \frac{E_x v_x^2}{v^2} \\ -\gamma B_z v_x - (\gamma - 1) \frac{E_x v_x v_y}{v^2} \\ -(\gamma - 1) \frac{E_x v_x v_z}{v^2} \end{pmatrix} \quad (83) \quad \mathbf{E}'_{prb,Vpol} = \begin{pmatrix} -(\gamma - 1) \frac{E_z v_z v_x}{v^2} \\ -\gamma B_x v_z - (\gamma - 1) \frac{E_z v_z v_y}{v^2} \\ \gamma E_z + \gamma B_x v_y - (\gamma - 1) \frac{E_z v_z^2}{v^2} \end{pmatrix} \quad (84)$$

The same behavior can also be seen after transforming the pump's EM fields from the lab-frame to the drift-frame. In the lab-frame, the pump propagates in the positive x-direction and is linearly polarized along the y-axis, i.e. has components E_y and B_z . Its magnetic field in the drift-frame, \mathbf{B}'_{pump} , contains all three components depending on the velocity \mathbf{v} , as shown by **Eq. 85**.

$$\mathbf{B}'_{pump} = \begin{pmatrix} \frac{\gamma E_y v_x}{c^2} - (\gamma - 1) \frac{B_z v_z v_x}{v^2} \\ -(\gamma - 1) \frac{B_z v_z v_y}{v^2} \\ \gamma B_z - \frac{\gamma E_y v_x}{c^2} - (\gamma - 1) \frac{B_z v_z^2}{v^2} \end{pmatrix} \quad (85)$$

This clearly has consequences not only for the orientation of the probe's k-vector to the pump's local magnetic field θ'_{kB} , but also for the probe's polarization angle relative to the pump's magnetic field θ'_{EB} . The simple division into perpendicular and parallel orientations, as expected in the lab-frame, is not accurate when viewing the system from the plasma electrons' relativistic drift-frames. The angle θ'_{kB} is already present in the RAH equation, and solving the RAH equation gives the refractive indices for orthogonal polarizations aligned parallel or anti-parallel to the local magnetic field, i.e., η_{\pm} or η'_{\pm} ; but how should θ'_{EB} be taken into account? This is done by using **Eq. 29** as described in **Section 2.2.3** as will be further described in the next section.

5.1.3 From the RAH Equation and η_{\pm} to the Effective Refractive Index η_{eff}

After a probe beam with H-pol or V-pol orientation is transformed into the drift-frame of a plasma electron's guiding center, the RAH equation can be used to numerically calculate η_{\pm} . That process will be further described in **Section 5.2**. The resulting values are substituted back into the RAH equation and η'_{\pm} are calculated. η'_{\pm} represent the refractive indices that an EM wave traveling in K' -space with wave-vector \mathbf{k}' would experience if its \mathbf{E}' -field were oriented parallel to \mathbf{B}'_{pump} , i.e., η'_{+} , or perpendicular to \mathbf{B}'_{pump} , i.e., η'_{-} . For all other orientations of the probe's \mathbf{E}' -field to \mathbf{B}'_{pump} , i.e.

5 Methods of Analysis

θ'_{EB} , **Eq. 29** is used in primed notation to calculate the effective refractive index experienced by the probe beam. This equation then gives $\eta'_{\theta'_{EB}}$ which will be renamed η'_{Heff} and η'_{Veff} for the effective refractive indices in the drift-frame for initial H-pol and V-pol probes, respectively. Likewise, their unprimed lab-frame equivalents, essentially the desired result of this analysis, η_{Heff} and η_{Veff} will be used. The use of an effective refractive index, instead of decomposing the field components of \mathbf{E}'_{prb} and calculating the resulting elliptically polarized wave, is a simplification which proved sufficient to explain the experimental data, as shown later in **Chapter 6**. In the following discussion, a generalized equation to calculate the effective refractive index will be derived and as such η_{eff} and η'_{eff} are used. Later, when a specific H-pol or V-pol probe is assumed, η_{Heff} and η_{Veff} will be used for clarity.

The final step in calculating the effective refractive index, η_{eff} , experienced by the probe beam in the plasma in the lab-frame requires use of the Lorentz invariance of the phase of a plane wave [63], i.e., $\phi = \phi'$. Using $\phi = \mathbf{k} \cdot \mathbf{r} - \omega t$ and $\phi' = \mathbf{k}' \cdot \mathbf{r}' - \omega' t'$ for an EM wave's phase in the lab and drift-frames, respectively, **Eq. 86** is written as the starting point of this derivation.

$$\mathbf{k} \cdot \mathbf{r} - \omega t = \mathbf{k}' \cdot \mathbf{r}' - \omega' t' \quad (86)$$

One can define $\mathbf{k} = (0, k_y, 0)$ and $\mathbf{r} = (0, d, 0)$ with $k_y = -\omega \eta_{eff}/c$ and d the distance propagated along the y-axis. Furthermore, t in the lab-frame is arbitrarily set to zero. Using \mathbf{k} and \mathbf{r} one can form their equivalent wavevector and position four-vectors as $\mathbf{k}^\nu = (\omega/c, \mathbf{k})$ and $\mathbf{r}^\nu = (ct, \mathbf{r})$. The expressions for ω' and t' can then be extracted from the 0th element of $\mathbf{k}'^\mu = \Lambda_\nu^\mu \mathbf{k}^\nu$ and $\mathbf{r}'^\mu = \Lambda_\nu^\mu \mathbf{r}^\nu$ which results in **Eqs. 87** and **88** as shown below.

$$\omega' = \omega \gamma (1 + \eta_{eff} \beta_y) \quad (87)$$

$$t' = -\beta_y \gamma d/c \quad (88)$$

The final term from **Eq. 86** that needs defining is $\mathbf{k}' \cdot \mathbf{r}'$, which is the scalar product of two three-vectors in K' -space. \mathbf{r}' can be extracted from $\mathbf{r}'^\mu = \Lambda_\nu^\mu \mathbf{r}^\nu$, however; \mathbf{k}' is derived using the value of η'_{eff} as previously calculated from the RAH equation and the uniaxial crystal equation based on the probe's polarization orientation in the drift-frame. Furthermore, the direction of \mathbf{k}' is simplified to be the direction of the probe beam in the drift-frame as if it were propagating in vacuum. This is defined using a unit vector of the form $\mathbf{k}'_{vac}/|\mathbf{k}'_{vac}|$ where \mathbf{k}'_{vac} is the three-wavevector extracted from $\mathbf{k}'^\mu_{vac} = \Lambda_\nu^\mu \mathbf{k}^\nu_{vac}$ with $\mathbf{k}^\nu_{vac} = (\omega/c, 0, -\omega/c, 0)$ being the four-wavevector of an EM wave propagating through vacuum in the negative y-direction. Using these definitions, the resulting expression for \mathbf{k}' is given by **Eq. 89**.

$$\mathbf{k}' = \frac{\omega \eta'_{eff}}{c} \frac{\mathbf{k}'_{vac}}{|\mathbf{k}'_{vac}|} \quad (89)$$

By substituting **Eqs. 87, 88** and **89** into **Eq. 86** and rearranging for η_{eff} , **Eq. 90** is obtained and used to calculate the effective refractive index of the lab-frame's plasma seen by the probe beam.

$$\eta_{eff} = -\frac{\gamma^2 \beta_y d |\mathbf{k}'_{vac}| + \gamma \eta'_{eff} (\mathbf{k}'_{vac} \cdot \mathbf{r}')}{d |\mathbf{k}'_{vac}| + \gamma^2 \beta_y^2 d |\mathbf{k}'_{vac}| + \gamma \beta_y \eta'_{eff} (\mathbf{k}'_{vac} \cdot \mathbf{r}')} \quad (90)$$

Two interesting cases arise. For relativistic motion of the plasma electrons' guiding centers in the xz-plane, $\eta_{eff} = \eta'_{eff}$. Furthermore, for motion in the xy-plane only along the x-axis, i.e., $v_y = v_z = 0$ and $v_x \neq 0$, $\eta_{eff} = \eta'_{eff}$ results as well. For all other cases, $\eta_{eff} \neq \eta'_{eff}$ and the effective refractive index in the lab-frame has to be calculated as explained above. **Section 5.1.4** will use the mathematical model developed in **Sections 5.1.1-5.1.3** to visualize where in velocity-space the resonance and reflection points of the RAH equation are to be expected by using typical pump-probe-plasma parameters that could be found in an experiment.

5.1.4 Example Behavior of the RAH Equation

To give examples of how the effective refractive index of the plasma in the lab-frame as seen by an H-pol or V-pol probe beam changes with varying drift velocity of the guiding centers of the plasma electrons, the analysis presented in **Section 5.1.2** and **5.1.3** will now be used with typical pump and probe parameters over a range of electron drift velocities. Using the transverse pump-probe geometry as depicted in **Fig. 14**, the pump's magnetic field along the z-direction will be given values of 12.5 kT and 20.0 kT corresponding to a normalized vector potential a_0 of 0.9 and 1.5, respectively, assuming a pump wavelength of 800 nm. In this simplified model, the pump's magnetic field is assumed to be constant in space and time. The probe is also only modeled via the orientation of its \mathbf{k} , \mathbf{E} and \mathbf{B} vectors. It is assumed that its field strength is significantly weaker than the pump and plasma's field strengths, such that any influence of the probe's fields on the plasma electrons' motion can be neglected. A probe wavelength of 750 nm was used.

The drift velocity of the plasma electrons' guiding centers are confined to the xy- and xz-planes. This simplifies the system considerably allowing for easier presentation of the results. **Figure 22** shows the results in these two planes for a pump magnetic field of 12.5 kT and **Fig. 23** shows the results after increasing the magnetic field to 20.0 kT. The plotted concentric circles in each subplot represent a drift velocity with a Lorentz factor of 1.1, 1.25, and 1.5 moving from the center of each subplot outwards. The color scale has been selected such that the expected value of the refractive index for underdense, unmagnetized plasma ($\eta \approx 1.0$) appears white, while values diverging drastically from the unmagnetized value appear blue if smaller, and red if greater than 1.0.

The effective refractive index in the xy-plane for an H-pol probe, **Fig. 22a**, shows index values far from 1.0 over a range of drift trajectories of the electrons' guiding centers, while the effective index for a V-pol probe, **Fig. 22b**, shows no strong deviation from 1.0. This is intuitive from the lab-frame since the V-pol probe would not be oriented properly to the pump's magnetic field to couple with any cyclotron motion of the plasma electrons, thus effectively experiencing unmagnetized plasma. The story is different in the xz-plane. The H-pol probe, **Fig. 22c**, as expected shows regions of resonance and reflection points, this time symmetric to the z-axis, while the V-pol probe, **Fig. 22d**, now also

5 Methods of Analysis

shows such regions, albeit with a smaller overall width as compared to the H-pol case. The appearance of refractive index values far from 1.0 in **Fig. 22d** is not intuitive from the lab-frame picture of the system, but arises due to the change in vector orientations after Lorentz transformation as will be described in the next section.

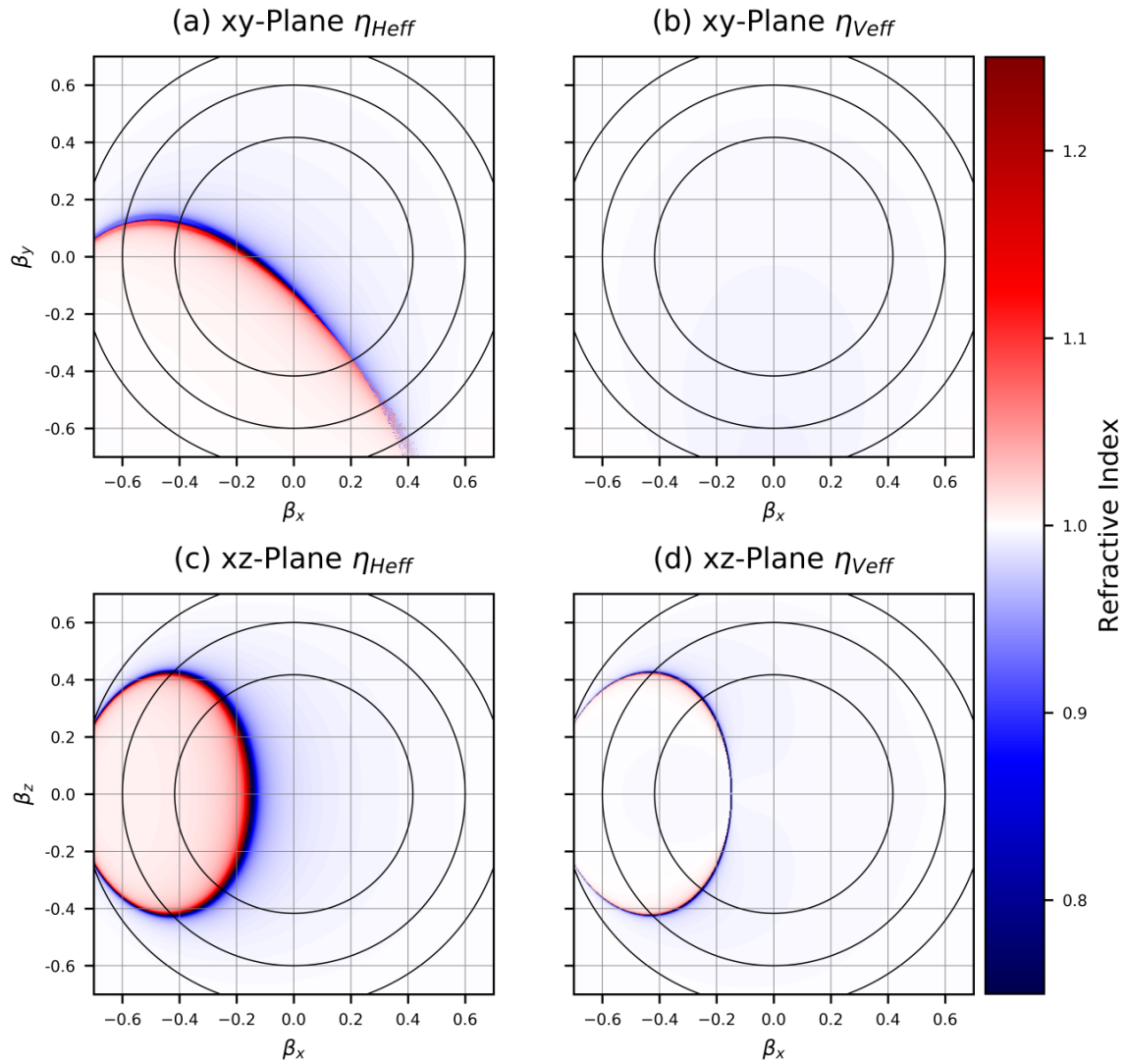


Figure 22: Effective refractive indices for the H-pol (a,c) and V-pol (b,d) probe as calculated from the RAH equation for electron motion in the xy- and xz-planes. $B = 12.5$ kT in a plasma with $n_e = 1.5 \cdot 10^{19}$ cm^{-3} was assumed. Black concentric circles represent Lorentz factors of 1.1, 1.25 and 1.5 from center moving outward.

The results for a pump magnetic field of 20.0 kT in both planes with both probe polarizations are plotted in **Fig. 23**. The xy-plane, **Fig. 23a,b**, once again only shows effective refractive index values far from 1.0 in the case of the H-pol probe. The locations of these resonances have moved in velocity space compared to the case of the 12.5 kT pump magnetic field. The behavior in the xz-plane has also changed compared to the 12.5 kT case. With the increased pump field, not only have the locations of the resonances changed in trajectory space, but the resonances in the V-pol probe now disappear for on-axis drift motion of the electrons in the positive x-direction.

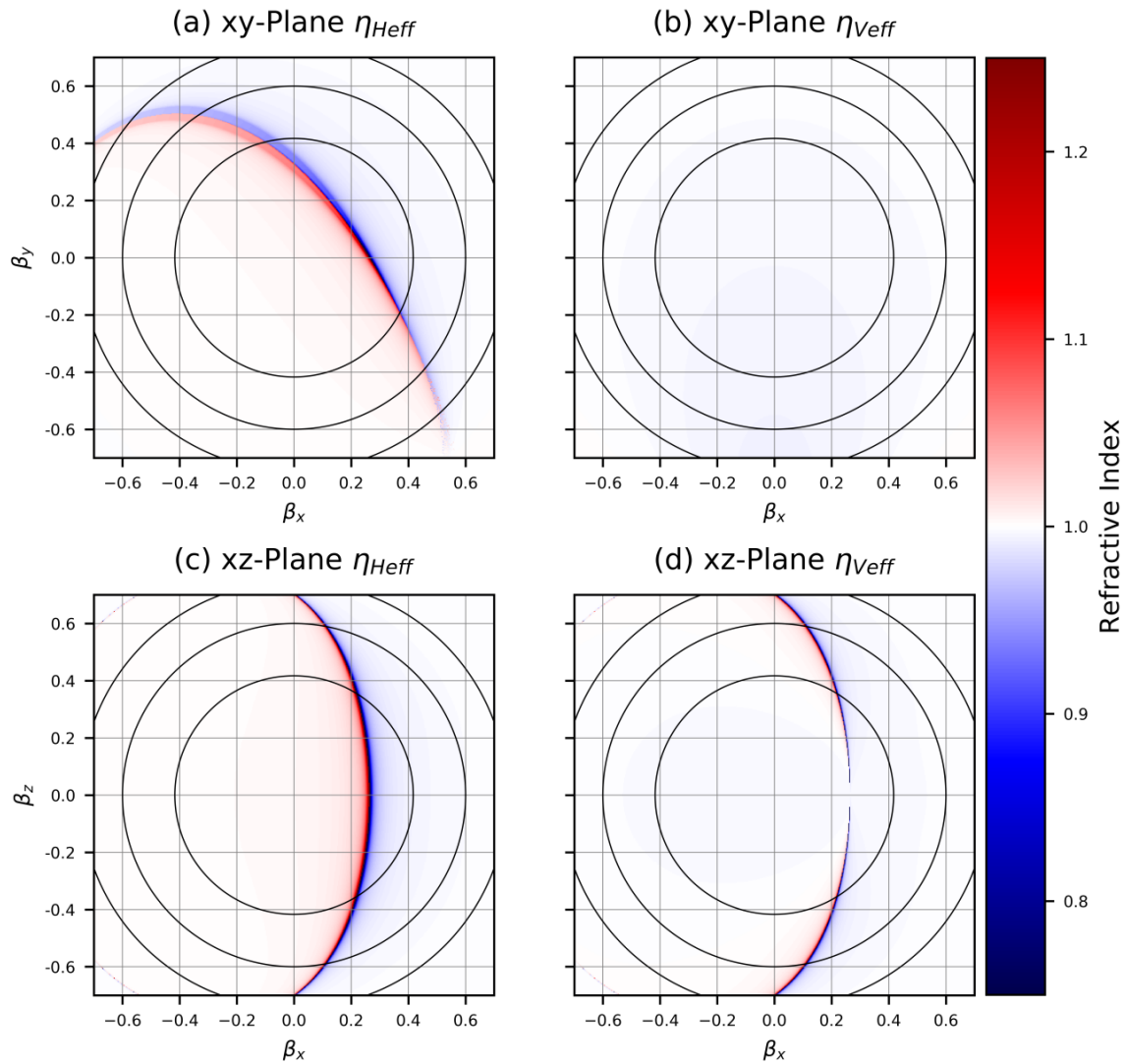


Figure 23: Effective refractive indices for the H-pol (a,c) and V-pol (b,d) probe as calculated from the RAH equation for electron motion in the xy- and xz-planes. $B = 20.0$ kT in a plasma with $n_e = 1.5 \cdot 10^{19}$ cm^{-3} was assumed. Black concentric circles represent Lorentz factors of 1.1, 1.25 and 1.5 from center moving outward.

It is important to note that while the calculated values of effective refractive indices far away from resonance conditions of the RAH equation should be accurate, the exact refractive index near a resonance (or reflection point) should be further investigated. The primary purpose of these plots is to show how the expected conditions for the plasma's refractive index changes with certain parameters of the pump, probe and plasma. **Section 5.2.3** and **5.2.4** will go into detail about why the calculated values of refractive index using the RAH equation cannot, at this time, be entirely trusted.

5.1.5 Lorentz Transformation of Vector Orientations

To investigate more thoroughly the symmetries and asymmetries of the system, the expected vector orientations after Lorentz transformation to an arbitrary drift-frame can be plotted. **Figure 24** shows results that are based on the transverse pump-probe geometry established in the experimental setup. The angle in the drift-frame between the probe's propagation vector and the pump's magnetic field

5 Methods of Analysis

$\theta'_{k_{prb}B_{pump}}$ (previously θ'_{kB}) is shown, as are the angles between the two orthogonal probe polarizations (H-pol and V-pol) and the pump's magnetic field, $\theta'_{EH_{prb}B_{pump}}$ and $\theta'_{EV_{prb}B_{pump}}$ respectively (previously θ'_{EB}). These angles have been calculated for electron plasma motion in the xy- and xz-planes for varying direction and drift gamma values.

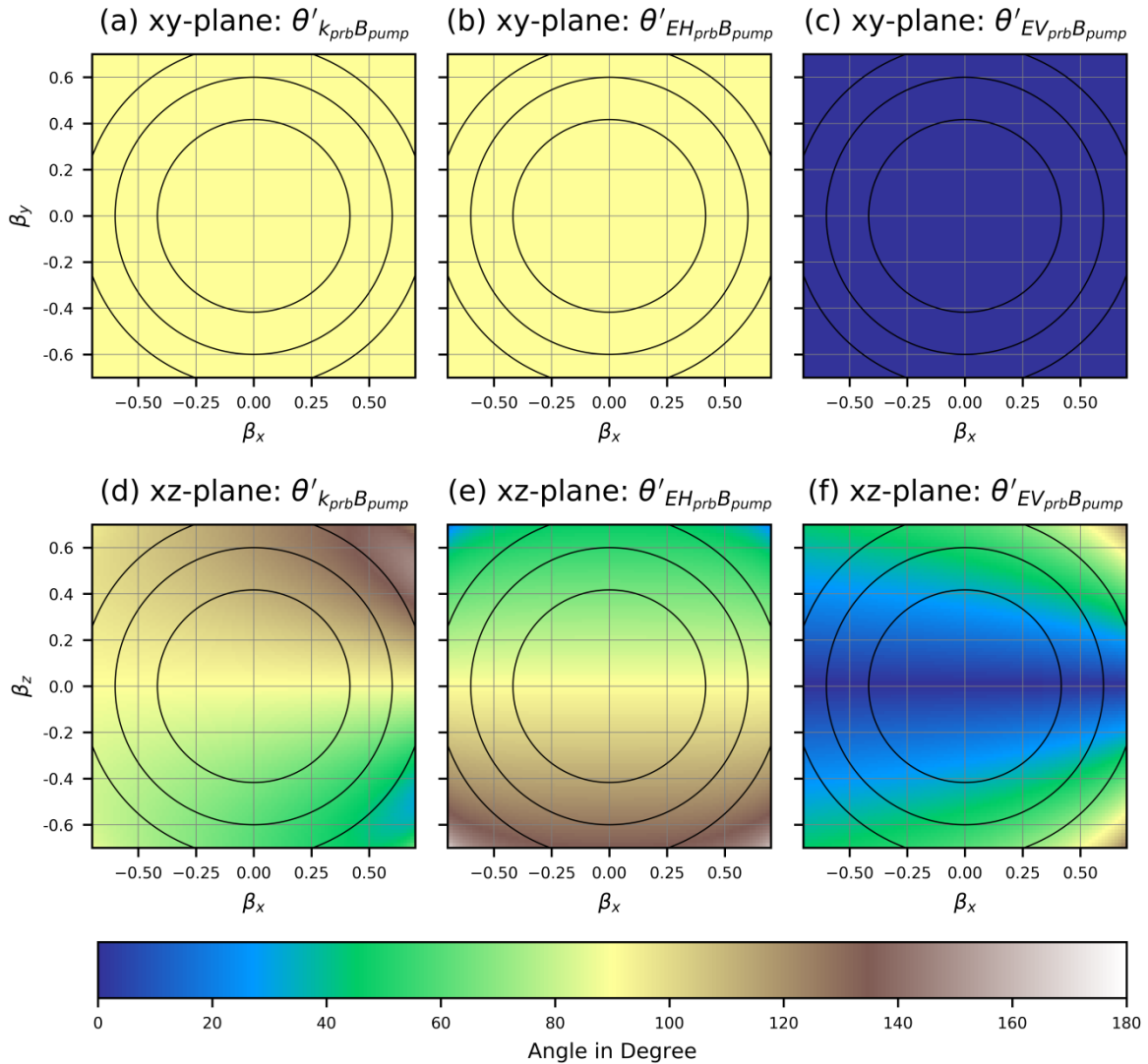


Figure 24: Vector orientations of $\theta_{k_{prb}B_{pump}}$, $\theta_{EH_{prb}B_{pump}}$, and $\theta_{EV_{prb}B_{pump}}$ after Lorentz transformation to a drift-frame traveling at (β_x, β_y) in the xy-plane (a-c) or traveling at (β_x, β_z) in the xz-plane (d-f) relative to the lab-frame. Black concentric circles represent Lorentz factors of 1.1, 1.25 and 1.5 from center moving outward.

Upon inspection, one sees that the vector orientations of the pump and probe in the xy-plane are invariant to the Lorentz transformation into the drift-frame, **Fig. 24a-c**. The probe in the drift-frame still propagates perpendicularly to the pump's magnetic field (simplified to only the B_z component). An H-pol probe in the lab-frame remains H-pol in the drift-frame, and a V-pol probe also remains vertically polarized. The physics is quite different in the xz-plane where the vector orientations depend on the direction and drift gamma of the electrons, **Fig. 24d-f**. This behavior will be essential later for understanding the asymmetric and half-ring signals in the experimental and simulated shadowgrams.

5 Methods of Analysis

One further important point to address concerning the Lorentz transformed vector orientations is their behavior outside of the xy - and xz -planes, in what will be called oblique planes rotated about the x -axis (pump's propagation axis) measured by the angle ϕ relative to the positive y -axis. For plasma electron motion in an oblique plane, the expected behavior of the Lorentz transformation is akin to a weighted average of the behavior seen in the two planes already plotted. The closer the oblique plane is to the xy -plane, the stronger its behavior will mimic that of the xy -plane, with the same being true for the xz -plane. For the interested reader, plots similar to those plotted in **Fig. 24** but for the $\phi = \pm 45^\circ$ oblique planes are described in **Appendix C.1**.

5.1.6 Resonance Points, Reflection Points and Shadowgraphy

The AH and RAH equations, with their derivation based in magnetoionic theory, describe resonance and reflection points (RECRs) for EM waves traveling in magnetized plasma. Waves that approach a resonance point, i.e., refractive index $\eta \rightarrow \infty$, would experience strong absorption in bulk plasma (cf. electron-cyclotron resonant heating [167], [168]), while waves that encounter reflection points, i.e., $\eta \rightarrow 0$, can be described by an evanescent wave mode and a reflected wave (cf. plasma mirror [169]). However, for the present case, strong absorption and reflection of the probe are not expected. At the sub-picosecond timescale presently considered, the electron-electron and electron-ion collision rates are not effective in converting electron motion due to the probe into thermal motion, i.e., absorption of the probe by the plasma. Furthermore, the few- to sub-micrometer extent of local plasma that exhibits reflection behavior is also not effective in fully reflecting the EM wave. Thus, both resonance and reflection are henceforth typically referred to as anomalous dispersion ($\eta \neq 1$) in this work, as their effect on shadowgraphic imaging manifests itself primarily via strong refraction of the probe relative to non-magnetized, tenuous plasma and not via absorption and reflection.

The next step towards analyzing how RECRs manifest themselves in shadowgraphic images of magnetized plasma is to use the mathematical model described in **Section 5.1** with realistic plasma parameters, e.g., simulated trajectories of plasma electrons and EM field values. It will be necessary to calculate how the resulting refractive index distribution correlates to the intensity modulation in a shadowgram of the plasma recorded by an fc -probe. To produce data of the pump-plasma interaction in LWFA, Particle-in-Cell (PIC) simulations can be used. PIC simulations treat the plasma as a collection of charged macro-particles representing the electrons and ions in the system. In a recursive manner the changes in the system's fields alter the distributions of particles and the changes in the particle distributions and propagation of the laser driver change the system's field distributions. This interaction is iterated over the duration of the simulation to investigate the physics between pump and plasma. Further details of PIC simulations can be found in **Section 2.5.5**. The next section describes the use of 2D PIC simulations to further investigate the interaction between pump, plasma, and probe.

5.2 2D PIC Simulations with VSim Code

The example refractive index calculated in **Section 5.1.4** using the RAH equation in the xy - and xz -planes was based on arbitrary pump, probe, and plasma parameters. To test the hypothesis that the asymmetric and half-ring signals truly come from relativistic electron-cyclotron resonances, characteristic data from a PIC simulation modelling a LWFA experiment need to be used with the RAH equation. For this purpose, 2D simulations using the PIC code VSim were performed. There are two significant advantages to this approach with the first being the minimal computational cost of a small 2D simulation (relative to a 3D simulation) that still accurately reproduces the general motion of plasma electrons for a given pump laser and plasma density. The current goal is to capture the motion of plasma electrons in the EM fields of the pump, not to investigate the accelerated electron bunch or other aspects of the LWFA process. To this end, a relatively simple 2D simulation will suffice.

Secondly, the VSim code has integrated particle- and field-tracking functions that allow the user to define the start location of certain macro-particles in the simulation. The position (x,y) or (x,z) , and last three components of the four-velocity $(\gamma v_x, \gamma v_y, \gamma v_z)$ of each pre-defined macro-particle is then tracked at every time-step throughout the simulation. Furthermore, a field box can also be pre-defined, within which all EM field components are also tracked and the electron density at each particles' position can also be similarly recorded. This tracking is done for each individual time-step of the simulation and as such differs from the typical "restart dump" that only occurs a few times per simulation. "Restart dumps" are used to restart simulations after large numbers of time-steps so that the amount of saved data is kept to a manageable size. A single "restart dump" would not allow for individual particle tracking nor have the temporal resolution to accurately calculate the drift-frames of the particles' guiding centers. Using the tracked data, the drift-frame of each macro-particle's guiding center is calculated which allows the lab-frame's refractive index to be calculated via numerically solving the RAH equation for a given pump-probe geometry. These results can then be compared to experimental data as well as 3D PIC simulations performed with the EPOCH code. It should be noted that setup of the VSim simulations' start files and administration of the simulations themselves were performed by Thomas Heinemann and Dr. Daniel Ullmann [170].

5.2.1 Setup of the 2D VSim Simulations

2D LWFA simulations with VSim were used to gather data to solve the RAH equation in the vicinity of the pump laser in the xy - and xz -planes (cf. **Fig. 14** for system's coordinates). In each simulation, the data from a line of macro-particles (cf. **Fig. 25**) were defined as the tracked electrons. The probe pulse was not present in the simulations but could be mathematically represented (in a simplified manner) during processing of the data using the RAH equation. The simulations were setup as follows. The simulation boxes had 4850 cells in the longitudinal direction with a cell size of 25 nm ($\lambda/32$) for a total length of 121.25 μm . In the transverse direction there were 420 cells with 100 nm resolution ($\lambda/8$) for a total width of 42 μm . The pump laser with a center wavelength of $\lambda = 800$ nm

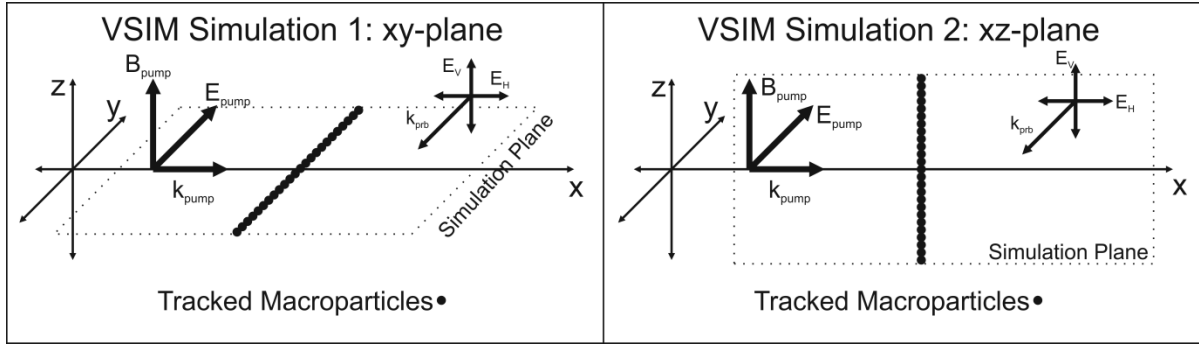


Figure 25: VSIM LWFA simulation setup in the xy- and xz-plane.

was focused to the middle of the simulation box to a FWHM spot size of $10\ \mu\text{m}$. Each simulation ran for 5220 temporal steps over a total duration of roughly 420 fs, but the data from the particle- and field-tracking used with the RAH equation was only recorded over 999 temporal steps (~ 80 fs) during which the pump pulse overtook the line of macro-particles. Each simulation was run twice (total of four simulations), once with a pump pulse FWHM duration of 15.7 fs and an $a_0 = 3.5$, and again with FWHM duration of 6 fs and $a_0 = 5.0$. The chosen pulse durations were shorter than the experimentally measured vacuum pulse duration due to the intention of investigating the laser-plasma interaction after significant self-compression of the pump had occurred. Furthermore, the latter parameters match more accurately the parameters of the pump laser from the EPOCH simulation at a propagation distance of $913\ \mu\text{m}$, which will be described in **Section 5.3**.

5.2.2 Calculating the Drift Velocity and Residual Quiver Velocity

In order to identify the drift-frame of each plasma electron's guiding center, the particle-tracking data from the VSIM simulations must be analyzed. The last three components of the four-velocity, $\gamma_{ins}v_{i,ins}$ with $i = x, y, z$, at each time-step is used to calculate each particle's Lorentz factor γ_{ins} and three-velocity $(v_{x,ins}, v_{y,ins}, v_{z,ins})$. The velocity components are then normalized to c as $\beta_{i,ins} = \frac{v_{i,ins}}{c}$. The subscript "ins" is used to denote the particle's instantaneous velocity from the simulation. Use of no subscript will denote the drift velocity of the particle's guiding center. Finally, the subscript "res" will be used to indicate the particle's residual velocity in the drift-frame of its guiding center.

As the particles move in the lab-frame under the influence of the linearly polarized pump laser, their motion can be described as a combination of Figure-of-Eight motion and a drift motion, see **Section 2.5**. While not strictly accurate, one can qualitatively think of the Figure-of-Eight motion being caused by the Lorentz force acting on the particle via the pump laser's fields and the drift motion as a Ponderomotive scattering from the pump's intensity gradient. Along the particle's trajectory in the xy-plane of the lab-frame simulation there are extrema in the particles' $\beta_{x,ins}$ and $\beta_{y,ins}$ values. Likewise, the electrons in the simulation of the xz-plane show extrema in their $\beta_{x,ins}$ and $\beta_{z,ins}$ values. In the xy-plane, the local maximums of $\beta_{x,ins}$ occur when the electron passes through the central point of each Figure-of-Eight orbit. These points also correspond to a local

5 Methods of Analysis

maximum of $|\beta_{y,ins}|$; however there exists a range of motion where these local maxima are actually local minima of a double-peak structure, see **Fig. 26** for details.

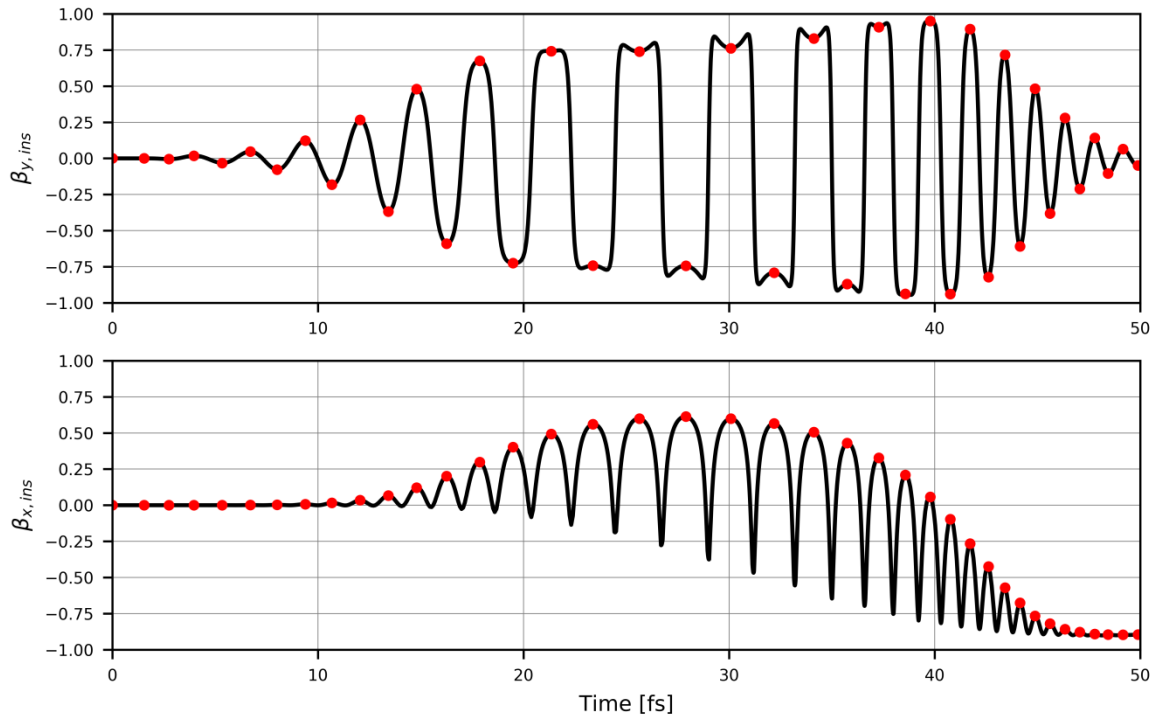


Figure 26: Beta values for an electron in the VSim simulation of the xy-plane. Local extrema that correspond to the velocities of the electron at the center of its Figure-of-Eight orbit have been marked with red dots.

An approximate drift trajectory of the particle's guiding center can be calculated by using the times and locations of maximum $\beta_{x,ins}$ and $|\beta_{y,ins}|$ and interpolating the motion of the particle's guiding center between these points. This process can also be performed for particles in the simulation of the xz-plane. The use of maximum $\beta_{x,ins}$ and $|\beta_{y,ins}|$ in the xy-plane to identify the drift-frame of the guiding center is only applicable for the particle while it is in the laser field. After the passage of the laser, the Figure-of-Eight motion stops and every point along the particle's lab trajectory is taken to be the trajectory of its guiding center because at this point in the simulation it is accelerated by the quasi-static fields of the plasma wave and no longer experiences any fast-oscillating EM fields.

By subtracting the trajectory of the particle's guiding center from the particle's instantaneous trajectory at each time-step of the simulation, the Figure-of-Eight motion of the particle in the co-moving frame of its guiding center can be visualized. **Figure 27** shows these results for three particles with transverse starting positions of $-3.05 \mu\text{m}$, $-0.05 \mu\text{m}$, and $3.05 \mu\text{m}$ in the xy-plane. The slanted orientation of the Figure-of-Eight orbits depends on the particle's relative transverse position to the pump's propagation axis as well as the pump's longitudinal and transverse field distributions [66].

The next step in data analysis is to calculate each guiding center's drift-frame velocity \mathbf{v} and Lorentz factor γ as well as to calculate the particle's residual velocity in the drift-frame \mathbf{v}_{res} corresponding to the Lorentz factor γ'_Q . Knowing the drift-frame's trajectory in position and the time

5 Methods of Analysis

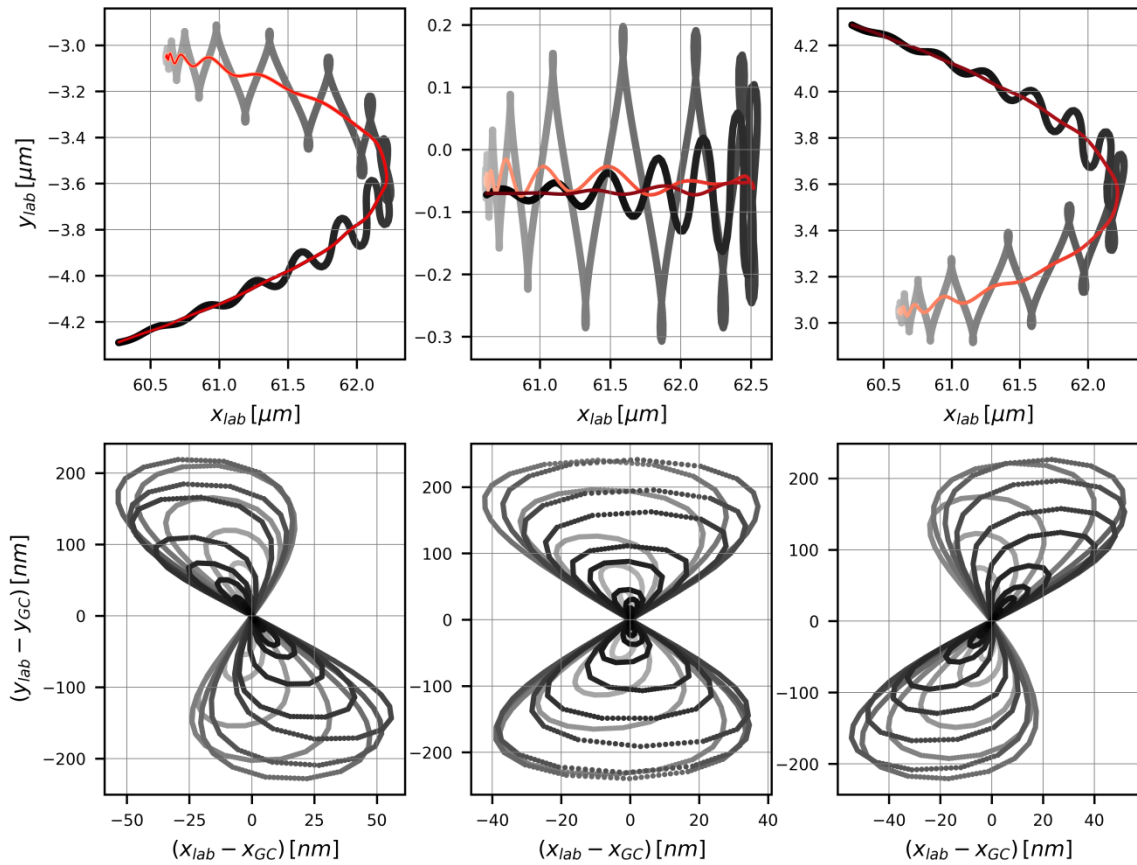


Figure 27: Upper row shows lab-frame trajectories (x_{lab}, y_{lab}) in black/white colormap and guiding center trajectories in red/white colormap for three transverse starting positions in the VSim simulation of the xy -plane. Lower row shows co-moving trajectories $(x_{lab} - x_{GC}, y_{lab} - y_{GC})$. Time is encoded onto the colormap from white to black or red running from 0.0 fs to ~50.0 fs of the simulation. Axes' aspect ratio is not 1:1.

interval between each position allows for the calculation of the drift-frame's velocity \mathbf{v} at each time-step of the simulation. The residual velocity, or quiver velocity, of the particle in the drift-frame of its guiding center, \mathbf{v}_{res} , can be calculated using Eq. 91. \mathbf{v}_{ins} is the electrons velocity in the lab-frame and \mathbf{v} is, as before, the relative velocity of the drift-frame of the electron's guiding center to the lab-frame with $\beta = v/c$ and $v = \sqrt{v_x^2 + v_y^2 + v_z^2}$.

$$\mathbf{v}_{res} = \frac{1}{1 - \frac{\mathbf{v}_{ins} \cdot \mathbf{v}}{c^2}} \left\{ \sqrt{1 - \beta^2} \mathbf{v}_{ins} + \left[\left(1 - \sqrt{1 - \beta^2} \right) \frac{\mathbf{v}_{ins} \cdot \mathbf{v}}{v^2} - 1 \right] \mathbf{v} \right\} \quad (91)$$

The final step before plugging all values into the RAH equation and solving for the refractive indices in the lab-frame is calculating half-cycle-averaged values in the drift-frame. The goal is to approximate each half-orbit of the Figure-of-Eight motion with a cyclotron gyration and to use this effective cyclotron frequency in the RAH equation. Not only can the half-cycle-averaged values of \mathbf{B}' and γ'_Q be used in calculating Ω'_{ce} , the vector orientations can also be averaged in the same manner for calculating $\theta'_{k_{prb} B_{pump}}$, $\theta'_{EH_{prb} B_{pump}}$ and $\theta'_{EV_{prb} B_{pump}}$. Non-relativistically, it would be simple to average, for example, the magnetic field experienced by a particle over one period of the pump laser

5 Methods of Analysis

as the particle does not move fast enough to merit a relativistic treatment. The period of the pump in the non-relativistic case is constant. In the relativistic case, the pump's period, as seen by a particle, changes depending on the velocity of the particle. By using the previously identified extrema in the particles' lab-frame velocities, one can define the durations over which the averaging is performed.

5.2.3 Numerically Solving the RAH Equation with Results from VSim

The analyzed data from the 2D VSim simulations is used with the RAH equation to calculate the effective refractive indices in the lab-frame for different polarization states of the probe. There is an underlying assumption in calculating a “bulk” parameter such as a refractive index from individual particle data such as that recorded using the tracked macro-particles. This assumption is that discrete macro-particles in the VSim simulation represent a plasma fluid such that the calculated refractive index using data from a single macro-particle is valid for the local region around that macro-particle. This assumption was taken to be valid only for locations and times in the VSim simulation where the tracked macro-particles' trajectories do not cross. Trajectory crossings of the macro-particles in a PIC simulation of LWFA are typically first seen after the macro-particles have already moved behind the pump pulse and begin interacting with the fields of the plasma-wave [92]. Said trajectory crossings would produce, for the same local plasma, two different drift velocities in the RAH equation resulting in an ambiguity as to which drift velocity is used to calculate the local plasma's refractive indices.

Due to the short longitudinal length of the tracked simulation box, the low plasma density and the short duration of the pump laser, the self-evolution of the pump pulse does not need to be accounted for. This allowed, during post-processing of the data, for the approximate mapping of the resulting refractive index over the entire tracked 2D simulation plane, described as follows. As the pump propagates through the simulation box, the line of macro-particles “line-scans” the parameters in the simulation plane, i.e., plasma density, particle trajectories and electromagnetic fields. Since the pump-plasma system is in a steady-state, one can remap the recorded parameters over the whole 2D simulation plane by accounting at each time-step of the simulation for the distance between the pump's peak intensity and the position of each macro-particle. These 2D parameter maps can then be used not only to visualize the encountered EM fields of the pump and plasma but to also calculate 2D plots of the refractive indices for comparison to experiment and to the EPOCH simulation.

Calculating the solutions to the RAH equation was performed for each tracked macro-particle sequentially from the start to the end of each VSim simulation. The RAH equation is rewritten to be a polynomial of η_+ or of η_- depending on the initial polarization state of the probe pulse under investigation. The zero-crossings of the polynomial then give possible values of the refractive index of the plasma in the lab-frame as experienced by that probe pulse. The refractive index at the start of the simulation is that of unmagnetized plasma, easily calculable, because the fields of the pump pulse have yet to arrive at the line of macro-particles and the background plasma density is predefined in the simulation. By assuming that the solution to the RAH equation over time is smooth and continuous,

5 Methods of Analysis

one can track the physical solution (a zero-crossing of the polynomial) with each time-step of the simulation. The only complication arises when the solution to the polynomial passes through a resonance or reflection point of the RAH equation. At these locations, the value of refractive index can pass through zero or move quickly towards ∞ . Due to this discontinuous behavior and the resulting ambiguity in the physical solution of the RAH equation around the time/location of a resonance, the reconstructed maps of refractive index were used to locate areas of anomalous dispersion and birefringence. They should not be considered to show the exact refractive index in the plasma.

5.2.4 Testing Physical Solutions

The process of numerically solving the RAH equation can produce several possible solutions depending on the data used from the PIC simulations. At the beginning of the simulation, before the arrival of the pump laser's high-amplitude fields, the correct value of the plasma's refractive index is trivial to identify as it is that of isotropic, unmagnetized plasma, predefined in the simulation. However, later in the simulation, identifying the physical solution to the RAH equation for time-steps involving highly magnetized and relativistically moving plasma becomes more involved. The following section describes one possible method to determine the physical solution or solutions.

Taking the AH equation (**Eq. 24**) as a starting point, two general cases can be plotted and investigated. In both cases, it is assumed that the plasma is underdense, meaning the probe beam can propagate unhindered through the plasma, i.e., $\omega_{prb} \gg \omega_p$. In **Fig. 28a**, a magnetic field of 15.3 kT and plasma density of $1 \cdot 10^{19} \text{ cm}^{-3}$ is used to produce a cyclotron-resonance at approximately 700 nm, creating the case where $\Omega_c > \omega_p$. **Figure 28b** shows the case of $\Omega_c < \omega_p$ in which a magnetic field of 8.9 kT and a plasma density of $1.5 \cdot 10^{21} \text{ cm}^{-3}$ is used, which also creates a resonance at approximately 700 nm. The horizontal-axis of the subplots is plotted in wavelength for better comparison to the probe beam's spectrum in the experiment; however, the characteristic frequencies of the plasma are labelled as angular frequencies as is typically done in the literature. Both plots show the refractive index of the H-pol probe η_- (X-wave in magnetoionic theory, i.e., $\theta_{kB} = 90^\circ$ and $\theta_{EH_{prb}B_{pump}} = 90^\circ$). Relativistic effects are ignored.

Upon inspection of **Fig. 28a** and its inset, one easily sees that for probe wavelengths shorter than the wavelength corresponding to the resonance frequency ω_{02} the expected refractive index is less than one. On the other hand, probe wavelengths longer than that of the cyclotron frequency Ω_c will experience a refractive index above one. As the probe's wavelength approaches the wavelength corresponding to the plasma frequency ω_p (in this case $\sim 10.6 \text{ } \mu\text{m}$) the plasma does not become overdense due to the magnetic transparency caused by the cyclotron frequency being greater than the plasma frequency. This is not directly shown in **Fig 28a** due to space considerations in the subplot.

Fig. 28b shows the second case of interest, $\Omega_c < \omega_p$, for analyzing the physical solutions of the AH or RAH equations. The behavior of the refractive index curve η_- is more complicated than in the

5 Methods of Analysis

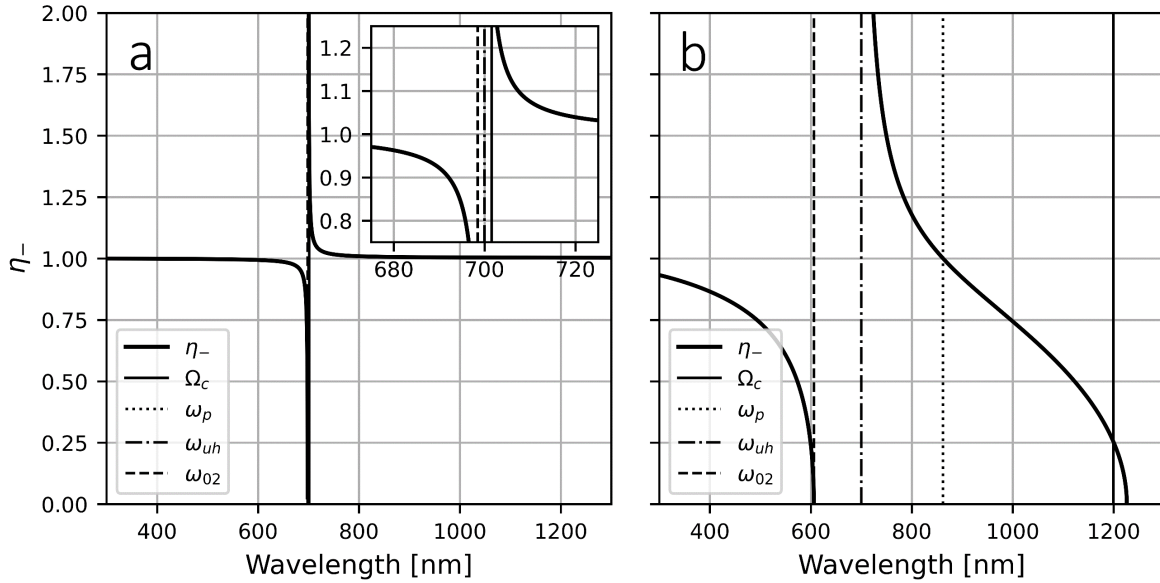


Figure 28: Characteristic behavior of refractive index η_- for (a) $\Omega_c > \omega_p$ and (b) $\Omega_c < \omega_p$. Inset in (a) shows frequencies ω_p , ω_{uh} and ω_{02} . (a) $n_e = 1 \cdot 10^{19} \text{ cm}^{-3}$, $B = 15.3 \text{ kT}$ (b) $n_e = 1.5 \cdot 10^{21} \text{ cm}^{-3}$, $B = 8.9 \text{ kT}$.

first case. For probe frequencies above ω_{02} (or probe wavelengths shorter than the wavelength associated with ω_{02}), the refractive index remains below one. The region between ω_{02} and ω_{uh} has no solution and would be experienced by the probe as something akin to overdense plasma. Increasing the probe's wavelength to a value between ω_{uh} and ω_p sees a solution to the AH equation that is between $+\infty$ and one, whereas further increasing the probe's wavelength beyond the corresponding wavelength to ω_p causes the expected solution to drop below a value of one. In the weakly relativistic regime where the maximum Lorentz factor of the plasma electrons' drift velocities does not exceed a value of two, there is no immediate need to investigate the refractive index curves for probe wavelengths beyond half or double the lab-frame's values.

The general form of the plots for the cases $\Omega_c > \omega_p$ and $\Omega_c < \omega_p$ relative to the plasma's characteristic frequencies, i.e., Ω_c , ω_p , ω_{uh} and ω_{02} , remain constant regardless of the propagation angle θ_{kB} . This allows one to verify the solutions to the AH or RAH equation calculated numerically using the PIC data. All relevant frequencies and refractive indices must be determined in a given frame (lab or drift), and if a solution to the RAH equation does not follow the behavior of the two plotted cases in **Fig. 28**, then it should not be considered as a physical solution to the system.

The analysis of the VSim data using the RAH equation as will be described in **Chapter 6** did not use this stringent testing for physical solutions. To understand physically why the anomalous dispersion in the plasma is occurring it was sufficient to simply identify regions of plasma where resonances and reflections arose due to relativistic cyclotron effects. Any desire, however, to further use the results of the RAH equation to then simulate shadowgraphic images of the plasma should consider proper testing of the physical solutions. Luckily, 3D simulations of the plasma using the EPOCH PIC code were available for further analysis and comparison to experimental shadowgraphy.

5.3 3D PIC Simulation with the EPOCH Code

The 2D simulations using VSim will help test the hypothesis that the asymmetric and half-rings signals in the experimental data originate from RECRs in the vicinity of the pump's peak intensity. However, the 2D simulations will not be sufficient to create simulated shadowgrams for comparison to the experimental shadowgrams, for that, 3D simulations are necessary. Luckily, extensive and detailed work has already been done by Dr. Evangelos Siminos [27] in investigating few-cycle shadowgraphy and LWFA using a 3D simulation of LWFA with the EPOCH code [118]. There are three clear advantages to using such a computationally expensive simulation: the simulation can model many physical aspects of the 3D evolution of the pump and plasma, the results from the simulation can be used to create simulated shadowgrams, and finally the general extent to which the simulation accurately represents the real physics is greatly improved compared to the 2D VSim simulations. The following section will summarize the relevant setup of his work and how it can aid in understanding how RECRs appear in few-cycle, shadowgraphic images of the pump-plasma interaction. The interested reader should refer to Dr. Siminos' work [27] as well as his collaboration with Dr. Alexander Sävert in analyzing the self-injection mechanism of LWFA [26] for more details.

5.3.1 Setup of the 3D EPOCH Simulation

The pump-probe geometry in the EPOCH simulation follows the same geometry used in this dissertation as shown in **Fig. 14** with the pump propagating along the x -axis and linearly polarized along the y -axis, while the probe is first introduced during post-processing with its propagation direction in the negative y -direction and its linear polarization either along the x -axis (H-pol) or the z -axis (V-pol). The simulation modelled a super-Gaussian plasma density distribution to better represent the rising and falling edge of a gas-jet used in LWFA experiments. The pump was defined to have a central wavelength at 810 nm and an intensity FWHM duration of 36 fs with a peak vacuum intensity of $2.5 \cdot 10^{18}$ W/cm². This peak intensity is lower than that measured in the experiments covered in this dissertation; however, since the 3D simulation captures the evolution of the pump in plasma, it is possible to investigate different locations in the pump's propagation in which its peak intensity has increased and pulse duration has decreased. Similarly, the simulation used a background plasma density of $1.7 \cdot 10^{19}$ cm⁻³, meaning self-focusing and -compression of the pump will occur faster than for lower background densities.

The "sliding window" configuration of the simulation used a $150 \times 70 \times 70$ μm^3 size box that propagates with speed c through the plasma. The box had $2700 \times 525 \times 525$ cells with 2 particles per cell and fifth-order particle weighting to reduce noise. This gave the simulation, relative to the pump wavelength, a resolution of roughly $\lambda/15$ (55.6 nm) in the longitudinal direction and $\lambda/6$ (133.3 nm) in the transverse direction. A sixth-order (in space) finite-difference-time-domain (FDTD) Maxwell solver was used to reduce resolution limits while maintaining accuracy of the pump and probe's dispersion properties. Two major goals of the simulation were to investigate changes in the plasma

6 Analysis of Experimental Results

wave behind the pump during propagation through the plasma and how to understand how these changes are visualized via few-cycle shadowgraphy. These goals were the main driver behind having an extended longitudinal length of the sliding window as will be described in the following section.

5.3.2 Simulating Shadowgrams with Results from EPOCH

After the pump-plasma simulation had been computed, the next step was to accurately simulate the transverse propagation of the probe through the system as well as include the numerical aperture of the imaging optics. The EPOCH simulation produced “restart dumps” at several propagation distances of the pump. Using each “restart dump” the “sliding-window” was stopped and the probe was injected into the simulation volume with user defined parameters and allowed to propagate transversely through the restarted pump-plasma system. Modifications to the simulation box were also performed to reduce unphysical diffraction effects and to ensure that the probe, depending on its pulse duration, could fully propagate through the plasma wave. After the probe completed its propagation, the fields belonging solely to the probe were identified by comparing all fields from the pump-plasma-probe simulation to the same simulation excluding the probe. This allowed for the removal of background field components that might appear in the shadowgram but are not associated with the probe and was performed to investigate changes to the probe’s fields due to only the pump-plasma distribution.

The probe’s fields become highly diffracted due to the wavelength-sized density perturbations in the plasma distribution and as such, the numerical aperture of the imaging system must be included to produce simulated shadowgrams that can be compared to the experimental shadowgrams. A generic 4f-imaging system was modelled to approximate the numerical aperture used in the experiments. For further details on the imaging system, varying the object plane of the imaging system, varying the probe’s temporal chirp and polarization, as well as spectrally filtering the shadowgrams, refer to [27]. Specific results of Dr. Siminos’ work as well as further investigation of the asymmetric and half-ring signals will be presented and compared to experimental and VSim data in **Chapter 6**.

6 Analysis of Experimental Results

In the following chapter the experimental data from **Chapter 4** will be analyzed using the methods established in **Chapter 5**. By combining simulation data from the 2D VSim simulations with the RAH equation, effective refractive index maps of the xy- and xz-planes in the vicinity of the pump laser were calculated to search for areas of anomalous dispersion caused by strongly magnetized, relativistic plasma. Results from the 3D EPOCH simulation were used to locate areas of plasma that impart the probe beam with large relative phase contributions and were also used to calculate simulated shadowgrams for direct comparison to experimental shadowgrams. The primary goal of this chapter is to compare simulation to experiment to identify how changes in the relativistic and magnetized pump-plasma system manifest themselves in shadowgraphic images. Beyond simply better understanding the

pump-probe-plasma system, these results could help in designing a future nondestructive diagnostic to evaluate the evolution of the pump's intensity profile during propagation through plasma.

6.1 Asymmetric Signal

The asymmetric signal was presented in **Figs. 21** and **20** in **Chapter 4.4** as an on-axis change in the appearance of the front of the plasma wave near the presumed location of the pump's peak intensity. A very weak change in appearance was seen when comparing shadowgrams taken with bandpass filters centered at 800 nm and 850 nm, whereas a much more pronounced change in the appearance was seen between shadowgrams at 660 nm and 850 nm. The spectral dependence of the cyclotron resonances as visualized using shadowgraphy can be explained with the use of a simple model. Assuming that a single electron is situated in a homogenous magnetic field, the electron's cyclotron frequency is $\Omega_c = eB/\gamma m_e$ with γ being this electron's relativistic Lorentz factor. By using the pump laser's normalized vector potential in terms of its magnetic field $a_0 = eB/\omega_L m_e$ one can arrive at one of two equations for a_0 as a function of the pump's wavelength λ_L and the cyclotron wavelength λ_c .

$$a_0 = \frac{\sqrt{2}\lambda_L}{\sqrt{2\lambda_c^2 - \lambda_L^2}} \quad (92)$$

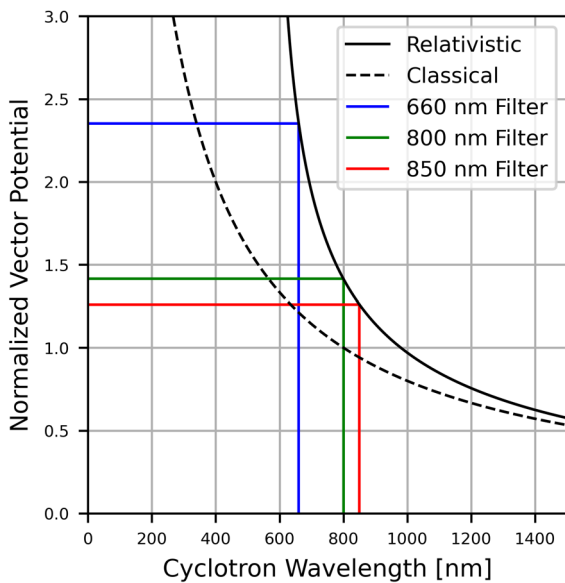


Figure 29: Classical (dashed) and simple relativistic (solid) models showing the dependence between the normalized vector potential and the corresponding cyclotron wavelength of a single electron using a pump wavelength λ_L of 800 nm. The three colored lines correspond to the central wavelengths of the filters mentioned in the text. The classical curve increases asymptotically towards $\lambda_c = 0$ nm. The relativistic curve increases asymptotically to $\lambda_c = \lambda_L/\sqrt{2}$ and has a value of $a_0 = 1$ for $\lambda_c = \sqrt{3}\lambda_L/\sqrt{2}$.

for longer cyclotron wavelengths and, as expected, converge in the classical case of $a_0 \ll 1$. In other

First, classical motion of the electron can be assumed resulting in the expression $a_0 = \lambda_L/\lambda_c$ which is shown as the dashed black line in **Fig. 29**. Second, the Lorentz factor of the electron can be described by its cycle-averaged quiver motion in a linearly polarized laser field given by $\gamma = \sqrt{1 + a_0^2/2}$. In this relativistic case, **Eqn. 92** is derived (see solid black line in **Fig. 29**).

The two plotted curves show very simplified cases of the expected cyclotron frequency (or wavelength) given a certain laser intensity in the plasma. The large parameter-space of the RAH equation, or the even more complex physics of the full pump-probe-plasma system cannot be reduced down to a single 2D plot. Despite the simplifications used in plotting **Fig. 29**, it shows why the shadowgrams taken at 800 nm and 850 nm show very little difference compared to the shadowgrams at 660 nm. The curves flatten out

6 Analysis of Experimental Results

words, a probe beam around 800 nm will experience a very similar spatio-temporal distribution of the cyclotron resonances in the plasma as by a probe around 850 nm. However, a probe in a different spectral range, say 660 nm, will experience a very different spatio-temporal distribution of resonances. In retrospect, evenly spaced filters covering the fc-probe's bandwidth should have been used in order to best sample the dependence between the pump laser's intensity distribution and the corresponding spatio-temporal distribution of cyclotron resonances.

6.1.1 2D PIC Simulation Results

As described in **Chapter 5.2** data from a 2D PIC simulation using the VSim code was combined with the proposed RAH equation (**Eq. 72**) to further investigate the signals seen at the front of the plasma wave recorded using polarization and spectrally filtered few-cycle shadowgraphy. The effective refractive index for an H-pol (η_{Heff}) and a V-pol (η_{Veff}) oriented probe beam propagating through the simulated pump-plasma interaction was calculated for each macroparticle and each time step in the simulation (see **Eq. 90**, **Section 5.1.3**). Using the line of macroparticles and assuming negligible pump-plasma evolution over the $\sim 15 \mu\text{m}$ propagation length, a 2D snap shot of the plasma's refractive index is plotted for each polarization and spectral combination as shown in **Figs. 30** and **31**.

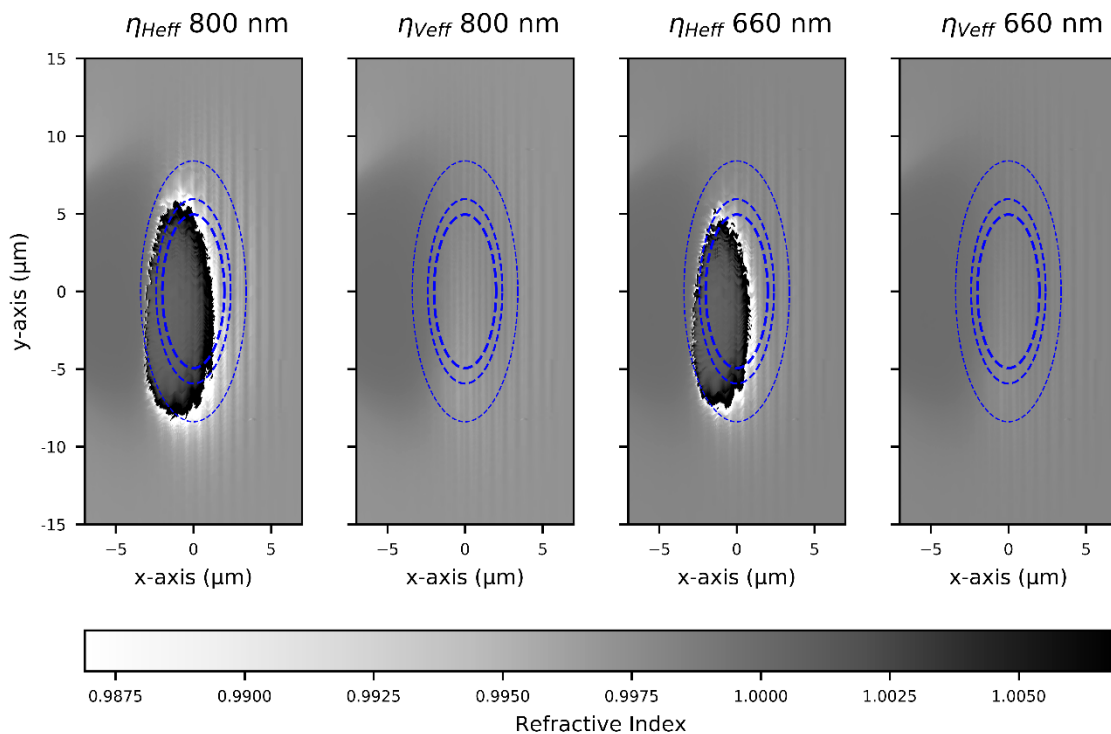


Figure 30: Refractive index of the plasma in the xy -plane for different probe polarizations and wavelengths induced by a pump pulse with 15.7 fs FWHM duration and an a_0 of 3.5. The blue, dashed lines represent the FWHM, $1/e$, and $1/e^2$ intensity contours of the Gaussian pump pulse. Each subplot is labeled with the probe beam's polarization (η_{Heff} is H-pol and η_{Veff} is V-pol) and wavelength (800 or 660 nm). The figures are calculated from data produced from VSim in simulating the xy -plane with $z = 0$.

The first set of plots for the effective refractive index in the xy -plane is seen in **Fig. 30**. The pump laser is travelling in each subplot from left to right. As expected, the refractive index η_{Veff} of the V-

6 Analysis of Experimental Results

pol oriented probe shows no sign of cyclotron resonances regardless of probe wavelength. This was explained using **Fig. 24** in **Section 5.1.5** which showed no change in the vector orientations after Lorentz transformation into the guiding center of the plasma electrons moving in the xy -plane. A vertically polarized probe is orthogonal to the plane of electron-cyclotron motion and thus encounters the refractive index of unmagnetized plasma. Only a slight difference in refractive index is seen due to the change in wavelength from 660 nm to 800 nm.

The refractive index experienced by the H-pol probe is quite different. A large area of resonance can be seen centered slightly off-axis (asymmetric) from the pump's propagation axis. The 800 nm H-pol probe sees a somewhat larger area of resonance as compared to the 660 nm H-pol probe. In a non-relativistic model, the intensity iso-surface of the pump pulse whose magnetic field correlates to a cyclotron resonance at 800 nm has a larger diameter than the intensity iso-surface corresponding to 660 nm, simply due to the Gaussian intensity distribution of the pump pulse having larger diameters at lower intensity contours. The relativistic modifications to the resonances cause them to be centered behind ($-x$) and in this case "below" ($-y$) the center of the pump's intensity distribution.

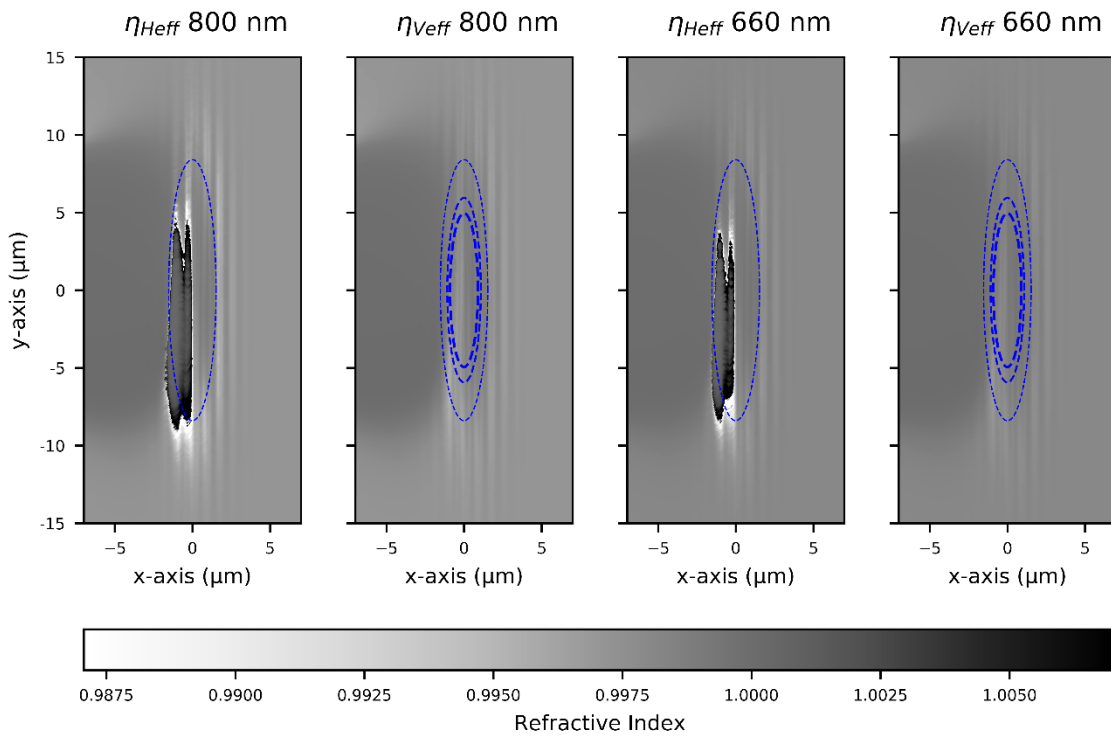


Figure 31: Refractive index of the plasma in the xy -plane for different probe polarizations and wavelengths induced by a pump pulse with 6.0 fs FWHM duration and an a_0 of 5.0. The blue, dashed lines represent the FWHM, $1/e$, and $1/e^2$ intensity contours of the Gaussian pump pulse. Note that in both H-pol subplots the two inner contour lines have been omitted for visibility of the asymmetric signal. Each subplot is labeled with the probe beam's polarization (η_{Heff} is H-pol and η_{Veff} is V-pol) and wavelength (800 or 660 nm). The figures are calculated from data produced from VSim in simulating the xy -plane with $z = 0$.

After running the same simulation with an increase in laser intensity **Fig. 31** shows again the effective refractive indices seen by the four wavelength and polarization combinations of the probe beam in the xy -plane. The pump pulse is propagating in each subplot from left to right. As expected,

6 Analysis of Experimental Results

the V-pol probe still shows no resonances. Due to the steeper pump intensity distribution, the resonances seen by the 800 nm and 660 nm H-pol probe have decreased in size compared to the case of lower pump intensity. The area of resonance is still offset relative to the pump's propagation axis and one now sees a more complicated structure as compared to the previous elliptical area.

The reader should be reminded of the “gap” between the meaning of these refractive index plots and the signals seen in the experiment's shadowgraphic images. The plots in **Figs. 30** and **31** only represent a single plane in the 3D plasma and do not attempt in any way to include the results of simultaneous propagation of the pump, probe, and plasma, nor the details of the shadowgraphic imaging system. The goal of the previous analysis using 2D PIC data was to test whether or not combining the RAH equation with PIC data would produce resonances at locations relevant for explaining the signals seen in the recorded shadowgrams. Such a signal was found, as presented above, and fortunately a similar analysis using a more elegant and detailed 3D simulation was possible as will be described in the next section.

6.1.2 3D PIC Simulation Results

As described in **Chapter 5.3** the EPOCH code was used to run a higher resolution 3D LWFA simulation with parameters similar to those used in the experiment. Furthermore, as described in [27], the simulation data could be further processed to produce simulated shadowgrams not only at different points along the pump's propagation, but also using a variety of different parameters for the probe.

To investigate the asymmetric signal seen in the experimentally recorded shadowgrams and the cyclotron resonances seen in the 2D PIC analysis, a snapshot of the 3D EPOCH simulation was used in which the pump had travelled approximately 920 μm through the plasma, see **Fig. 32**. The probe pulse is then allowed to propagate along the negative y-axis through the plasma during which the pump-plasma system also continues to propagate as normal. The local phase accumulation of the probe beam at different locations is investigated and displayed using a green/yellow color scale in **Fig. 32 (a)-(f)**. The phase is measured relative to the equivalent phase that the probe would have accrued were it to travel through the background plasma density with an index of $\eta = 0.996$.

The signal of interest can be seen by comparing the two areas designated by a dotted ellipse in **Fig. 32 (a)** and **(c)**. Both locations exhibit the same plasma density distribution, as well as local magnetic field strength (red/blue color scale); however, subplot **(c)** shows a significantly higher phase contribution to the probe than subplot **(a)** indicating an area in the plasma with refractive index above the background value of $\eta = 0.996$. This phase contribution is positioned relative to the pump pulse and plasma wave at the same position as the resonance signal seen in the 2D PIC analysis. Furthermore, the positive phase value relative to the background phase value is consistent with the refractive index values seen in the 2D PIC analysis, see **Figs. 30** and **31**.

The last row of subplots, **Fig. 32 (g)-(i)**, show simulated shadowgrams using only the accumulated phase of the probe pulse up to the respective positions of the probe as depicted in the xy-plane

6 Analysis of Experimental Results

subplots. Subplots (g) and (h) show no significant irradiance modulation in the shadowgrams at the position of the pump pulse's peak intensity, but subplot (i) does, indicating that the phase contribution from the encircled signal in subplot (c) has a significant contribution to the appearance of the brighter area in the shadowgram at the location of the pump pulse's peak intensity.

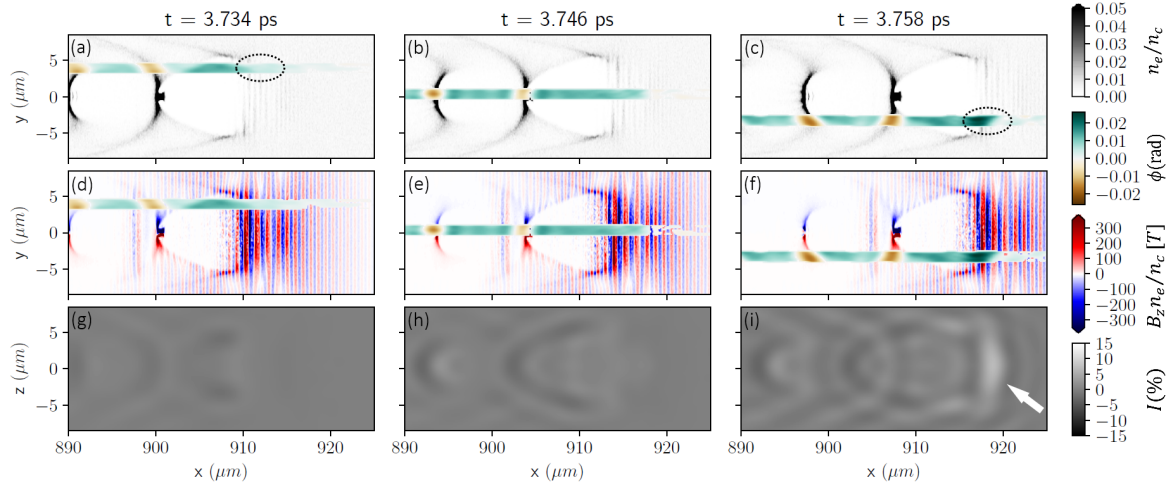


Figure 32: (a)-(c) normalized plasma density with an overlay of the probe's relative phase in radians. (d)-(f) scaled magnetic fields (red/blue color scale) with the probe's phase overlay. (g)-(i) relative irradiance modulation of the simulated shadowgram in %. The H-pol, full-spectrum probe propagates in the $-y$ direction and its ~ 6 fs FWHM temporal extent is coincident with the green/yellow phase colormap. Shadowgrams (g)-(i) are created using only the phase accumulated up to the indicated probe position. Plots (a)-(f) correspond to xy planes at $z = 0 \mu\text{m}$. The white arrow denotes the strong brightness modulation described in the text.

Having only the analysis from the 3D EPOCH simulation, one can explore the correlation between the asymmetric phase signal and the irradiance modulation in the shadowgrams, but the link to relativistic electron-cyclotron resonances would still be missing. Adding the analysis of the RAH equation using particle and field data from the VSim PIC simulations is therefore crucial to establish the overall picture that RECRs are the source of these signals.

The spectral dependence of the asymmetric signal as seen in simulated refractive index plots and experimentally recorded shadowgrams has already been described in previous sections. Simulated shadowgrams that also show this effect can be found in [27] from Dr. Evangelos Siminos. All cited figures can be found in **Appendix D** for ease of reference. Two interesting comparisons can be found in that publication. Firstly, **Figs. 6d, 11a, and 11b** from [27] show simulated shadowgrams using 12 fs FWHM probe pulses centered at 750 nm, 600 nm, and 450 nm, respectively. The train of plasma oscillations behind the pump laser in the transverse region of $\pm 5 \mu\text{m}$ shows little change in appearance between the three different probe pulses. The more outer region between $\pm 5 \mu\text{m}$ and $\pm 10 \mu\text{m}$ shows a clear loss in irradiance modulation with decreasing probe wavelength most likely due to the decrease in refractive index modulation at shorter wavelengths for a given plasma density distribution. Interestingly, the area of the plasma wave overlapping with the pump's peak intensity strongly changes in appearance. The radial extent of the irradiance modulations decreases with decreasing

6 Analysis of Experimental Results

wavelength, which correlates with the fact that shorter wavelengths of the probe will experience cyclotron resonances at higher intensities, i.e., a smaller spatial extent assuming a Gaussian-like intensity distribution. Most interesting is the case of the 450 nm centered probe, in which almost no significant irradiance modulation is seen at the head of the plasma wave. This correlates with **Fig. 29** of this work that shows the resonant normalized vector potential of the relativistic curve increasing asymptotically for wavelengths approaching $\lambda_c = \lambda_L/\sqrt{2}$, which in this case is a wavelength of ~ 570 nm. If the simplified model summarized by **Eqn. 92** holds, it defines a spectral limit to measuring, via RECRs, the pump's peak laser intensity depending on its central wavelength. A more detailed analysis is needed to investigate the change in irradiance modulation in the shadowgrams due to a change in the probe's wavelength that is either attributed to a change in the unmagnetized refractive index, or is attributed to the spectral dependence of a relativistic cyclotron resonance.

The second interesting comparison in [27] can be seen in **Fig. 14** of that work (see also **Appendix D**). Originally, the figure was meant to show the recorded propagation of the plasma wave as measured by a single probe pulse that has been linearly chirped to 30 fs FWHM and subsequently spectrally filtered using 20 nm FWHM bandpass filters centered at 600 nm, 700 nm, 800 nm, and 900 nm. This type of 2D-space, femtosecond-temporally resolved diagnostic has been a point of interest in recent research [30]. Now, using the knowledge gained from the analysis of RECRs in shadowgrams, one can recognize the changes in irradiance modulation in the head of the plasma wave with changing probe wavelength as a signature of cyclotron resonances.

6.2 Half-Ring Signal

The half-ring signal was identified in propagation scans of the plasma wave through the gas-cell

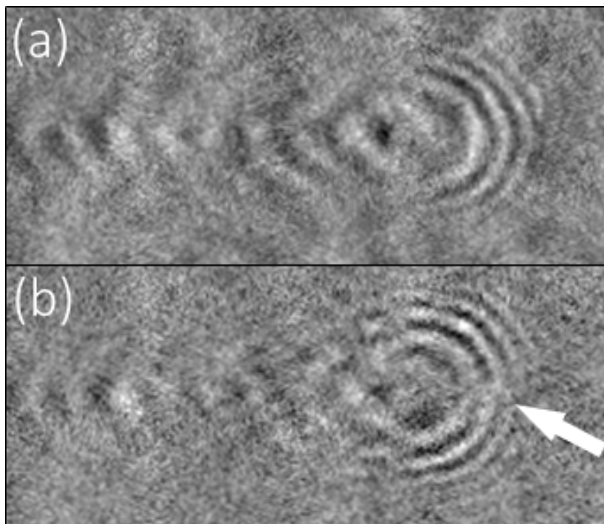


Figure 33: Half-ring signal. (a) H-pol and (b) V-pol shadowgrams with the probe's full spectrum after 1190 μm pump propagation. Both images have undergone contrast enhancement. White arrow indicates location of the on-axis break seen in the V-pol image.

using a full-spectrum probe pulse measured simultaneously in the H-pol and V-pol orientations as shown in **Fig. 19** and an example is again displayed here in **Fig. 33** with the background having been removed. The ring structures seen developed in the second half of the gas-cell after the pump pulse had already propagated 1 to 1.5 mm through the plasma. The ring structures imaged using the H-pol oriented probe were always continuous, whereas the rings imaged using the V-pol oriented probe always exhibited a break in the rings located on the propagation axis of the pump laser. Just as in the case of the asymmetric signal, the half-ring

6 Analysis of Experimental Results

signal can be explained with a combination of the RAH equation and 2D PIC data as well as the 3D EPOCH simulation and simulated shadowgrams.

6.2.1 2D PIC Simulation Results

Following **Figs. 14** in **Section 3.2** and **Fig. 25** in **Section 5.2.1**, the xz -plane was investigated using 2D PIC simulations, from which particle- and field-tracking data was combined with the RAH equation. As described previously, under certain assumptions a snapshot of the refractive index experienced by the probe beam can be reconstructed, shedding light on whether or not RECRs play an important role in the refractive index distribution of the plasma as seen by the probe beam.

Figure 34 shows the results of the refractive index reconstruction using the VSim data. As seen previously, an area of resonant plasma overlaps spatially with the pump laser, indicating that the magnetic field of the pump laser and the electrons' trajectories fulfil the condition for cyclotron resonance with the probe beam. The extent of the resonance area decreases with decreasing wavelength as seen by both the H-pol and V-pol oriented probes, which can be understood using **Fig. 29** showing that higher magnetic fields are resonant with shorter wavelengths of the probe beam. Curiously, the reconstruction using V-pol probe, η_{Veff} , shows a resonant refractive index, which is not initially expected considering the orientation of the V-pol probe's electric field and the dominant plane of cyclotron motion as viewed from the lab-frame.

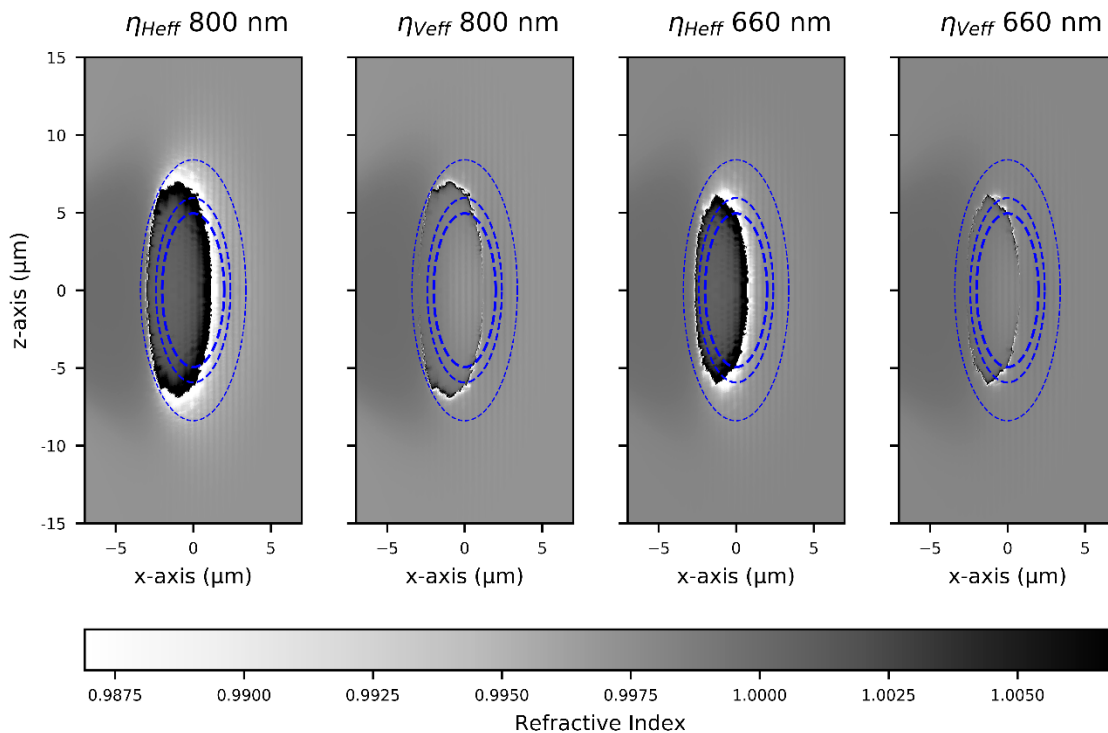


Figure 34: Refractive index of the plasma in the xz -plane for different probe polarizations and wavelengths induced by a pump pulse with 15.7 fs FWHM duration and an $a_0 = 3.5$. The blue, dashed lines represent the FWHM, $1/e$, and $1/e^2$ intensity contours of the Gaussian pump pulse. Each subplot is labeled with the probe beam's polarization (η_{Heff} is H-pol and η_{Veff} is V-pol) and its wavelength (800 or 660 nm). The figures are calculated from data produced from VSim in simulating the xz -plane with $y = 0$.

6 Analysis of Experimental Results

After increasing the intensity of the laser and running the simulation and reconstruction, **Fig. 35** shows a decrease in the size of the resonant signal as compared to the low intensity case. This behavior follows the expectation for a Gaussian-like intensity distribution considering again that the iso-surfaces of the pump's intensity distribution will primarily determine the location of resonant plasma depending on the wavelength of the probe beam. The unexpected appearance of resonant plasma recorded by the V-pol probe, and the on-axis break in the resonant area seen by the V-pol probe can be explained by considering the relativistic motion of the plasma electrons.

First, as seen in **Fig. 24(f)** in **Section 5.1.5**, the vector orientation of the V-pol probe's electric field in the electron's drift-frame depends on the velocity of the plasma electrons in the xz -plane. The subplot shows a symmetry axis which corresponds to the pump laser's propagation axis. For electron motion along this axis, the V-pol probe's electric field remains orthogonal to the plane of electron-cyclotron motion, thus no resonance is seen and the refractive index follows the unmagnetized case. In the reference frame of plasma electrons that are moving off-axis and with a $\gamma > 1.1$, the electric field of the V-pol oriented probe will appear to also have a component in the H-pol orientation. This causes a resonant area of plasma to be seen by the V-pol probe for off-axis motion of the electrons, but no or very weak resonance seen in areas where plasma electrons primarily move in the forward or backward directions, i.e., along the z -axis.

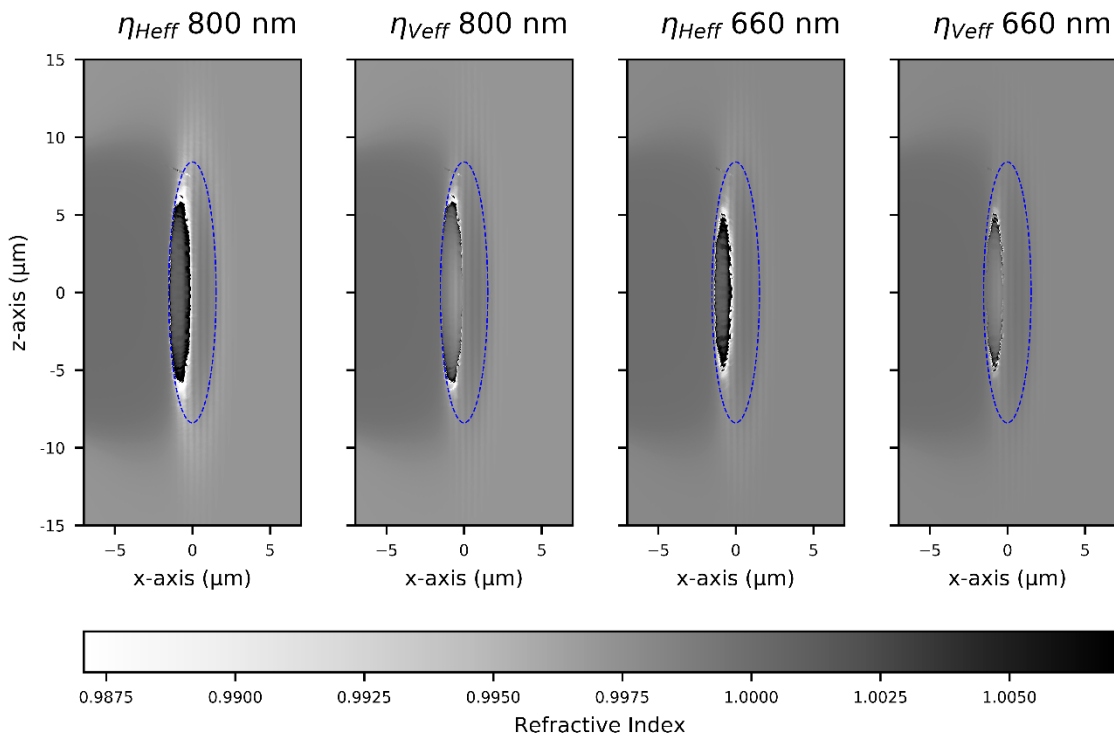


Figure 35: Refractive index of the plasma in the xz plane for different probe polarizations and wavelengths induced by a pump pulse with 6.0 fs FWHM duration and an $a_0 = 5.0$. The blue, dashed lines represent the $1/e^2$ intensity contour of the Gaussian pump pulse. FWHM and $1/e$ contours have been omitted for visibility. Each subplot is labeled with the probe beam's polarization (η_{Heff} is H-pol and η_{Veff} is V-pol) and its wavelength (800 or 660 nm). Figures are calculated from data produced from VSim simulating the xz -plane with $y = 0$.

6 Analysis of Experimental Results

6.2.2 3D PIC Simulation Results

The appearance and the formation of the half-ring signal in simulated shadowgrams have also been confirmed by the work of Dr. Siminos; however, both were not at that time the primary interest of his work. The rings can be seen in several of the simulated shadowgrams from [27] including **Figs. 2e, 6d, 8b, 12, 13, and 14** (as reproduced with permission in **Appendix D**). The original simulated shadowgrams were produced with the purpose of investigating the changes in the train of plasma oscillations behind the pump laser. This has caused the simulation box for the simulated shadowgrams to be poorly positioned for investigating the half-ring signal ahead of the pump laser. Furthermore, all of the simulated shadowgrams were produced using the H-pol probe. Nonetheless, there is enough data to present an explanation for the origin of the half-ring signal.

Figure 8b of [27] and **Fig. 3** of [26] show the underlying evolution of the signal. Both figures show the change in the plasma wave with propagation through 1 mm of plasma, but **Fig. 3** of [26] also shows contours of the pump laser's B_z magnetic field component (see **Appendix D**). As the pump laser propagates through the plasma, it self-focuses and steepens to a shorter, more intense laser pulse. The front edge of the pump pulse is already steep enough to produce a faint half-ring signal after ~ 800 μm propagation, but becomes more pronounced around 1 mm of propagation and produces a stronger half-ring signal. The appearance of the half-ring signal after ~ 1.5 mm propagation in the experimental data correlates to the slightly lower background plasma density used compared to the simulations.

Knowing that, in the classical case, a specific iso-surface of intensity (or magnetic field) is resonant with a spectral component of the probe, one can piece together the origin of the half-ring signal. At the beginning of the pump-plasma interaction, the iso-surfaces of the pump that are resonant with different spectral components of the probe are spread out in space. This creates on average a “soft” distribution of refractive index in the plasma, from which no coherent diffraction will be seen. As the pump steepens, the areas of resonance for each spectral component of the probe begin to converge on the same step-like intensity distribution of the pump pulse. The refractive index distribution of the plasma likewise becomes step-like at this location causing any image of the plasma to contain a diffraction pattern from this resonant “hard edge” given the correct properties of the probe beam, which will be discussed shortly. Both the significant drop in electron density behind the pump pulse, as well as potentially “flatter” steepening of the pump intensity's trailing edge lead to the absence of diffraction rings oriented toward the back of the plasma wave, thus leading to the name “half-ring” signal.

Further evidence that the half-ring signal can be attributed to diffraction rings is the dependence of the half-ring signal's period on the probe's wavelength and the NA of the probe's imaging system. An increase in NA of the imaging system should correspond to a decrease in the half-ring signal's period which can be clearly seen when comparing **Fig. 6d** with $\text{NA} = 0.26$ to **Fig. 12** with $\text{NA} = 0.35$ in [27]. Additionally, spectrally filtering the probe's spectrum to longer wavelengths should correspond to an increase in the half-ring signal's period. This can be seen in **Fig. 14** of [27] in which a linearly chirped

6 Analysis of Experimental Results

probe was spectrally filtered to 600 nm, 700 nm, 800 nm and 900 nm with 20 nm FWHM bandpass filters to show propagation of the plasma wave. The observed changes in the half-ring signal matches the expected behavior of diffraction rings when imaging a small object with coherent illumination of different central wavelengths as summarized by the Abbe diffraction limit $d = \lambda/2NA$. The airy disk's diameter d increases (decreases) with increasing illumination wavelength (NA).

As described previously, motion of the plasma electrons in the xz -plane shows interesting characteristics with respect to the system's symmetry. **Figure 24(e)** in **Section 5.1.5** indicates a radial symmetry in the change of the H-pol probe's E-field orientation with respect to the pump's B_z component along the pump's propagation axis for different plasma electron velocities. Succinctly put, as long as the pump's ponderomotive force is cylindrically symmetric along its propagation axis, the cyclotron resonances seen by the transverse H-pol probe in the xz -plane will also be symmetric and the shadowgrams should form half-ring like structures given sufficient self-steepening of the pump.

An indication of the "correct" properties of the probe beam for the appearance of the half-ring signal can also be seen in the simulated shadowgrams. Specifically, by comparing **Figs. 6d** and **13** of [27] one sees the influence of the probe beam's pulse duration on the irradiance modulation of the diffraction rings. **Figure 6d** is produced with an H-pol probe centered at 750 nm with a FWHM duration of 12 fs, which was negatively and linearly chirped from the Fourier limit of 4.4 fs. **Figure 13a** uses the same parameters except that the probe has its Fourier limited 4.4 fs FWHM pulse duration and **Fig. 13b** uses the probe chirped to 30 fs FWHM. Both **Figs. 6d** and **13a** display the half-ring signal, but the rings in **13a** have a higher contrast. **Figure 13b** shows neither the half-ring signal nor a plasma wave due to the temporal averaging effects of a probe pulse's duration whose spatial extent is longer than roughly half the plasma wavelength, or in this case, also longer than roughly half of the diffraction period of the half-ring signal.

It follows that the formation and visualization of the half-ring signal in shadowgraphy is a mixture of several effects: self-steepening of the pump laser during propagation in underdense plasma, electron-cyclotron resonances in the plasma that spatially converge to form a step-like refractive index distribution, and finally a coherent probe pulse that is short enough to avoid temporally averaging the diffraction rings due to the simultaneous propagation of pump, plasma and probe. The existence of the half-ring signal and the on-axis break seen in the shadowgrams recorded with the V-pol oriented probe beam can be explained using the change in vector orientations during Lorentz transformation, but simulation of this signal using the 3D EPOCH simulation was not performed. The final sections of this chapter will compare results from a coherent imaging model to the experimental results from the half-ring signal to further verify the signal's origin.

6.2.3 Coherent Imaging Model for Relativistic Objects

The coherent imaging model from **Section 2.3.5** can be modified to investigate the origin of the half-ring signal seen in the experimental and simulated data. Due to the relativistic phase velocity of

6 Analysis of Experimental Results

the plasma wave, a model of the coherent imaging system is required, in which significant transverse motion of the object within the pulse duration of the illuminating pulse and its propagation through the object, can be considered. The following section describes a first approximation of such a model and the following section presents the results.

To begin, the probe beam illuminating the object plane is modelled as the sum of plane waves, with flat phase and spectral amplitudes following that of a Gaussian spectrum. The fields are assumed to be homogenous across the xz -plane, traveling in the $-y$ -direction, and the pulse itself is constructed with N_ω spectral samples and N_t temporal samples. Note that this coordinate system is the same as that used to describe the imaging system in the experiment. **Eq. 93** shows such a pulse with a central angular frequency ω_0 and FWHM spectral width of $\Delta\omega$.

$$E_{pr}(t_m, x, z) = \sum_{n=1}^{N_\omega} \exp\left(\frac{-2\ln 2(\omega_n - \omega_0)^2}{\Delta\omega^2}\right) \exp(i\omega_n t_m) \quad (93)$$

The electric field of the probe pulse in the object plane at each time step t_m and each spectral component ω_n is then multiplied by a function named *Droplet* in **Eq. 94**, which is an exponential function representing the phase or amplitude of the object as described in **Section 2.3.5**. The function *Droplet* can represent a sphere with diameter 20 μm that can be either a pure phase object such as underdense plasma or water, or it can be an amplitude object such as overdense plasma. The opaque sphere was used for two reasons. First, data existed from another experiment, in which $\sim 20 \mu\text{m}$ diameter droplets of water were imaged with the same fc-probe beam imaging system. Second, by varying the speed v_{obj} of the simulated “droplets” to be either zero or the group velocity of the pump laser in plasma, the model’s results could be checked against the experimentally measured droplets (as water or as overdense plasma), or used to investigate the results of coherently imaging an object moving at the relativistic speed of the plasma wave in the LWFA experiment.

$$u_{obj}(t_m, \omega_n, x, z) = E_{pr}(t_m, \omega_n, x, z) \text{Droplet}(x - v_{obj}t_m, z) \quad (94)$$

Using a coherent transfer function (CTF) for each spectral component of the probe pulse, $H(\omega_n, f_x, f_z)$, the electric fields at the object plane $u_{obj}(t_m, \omega_n, x, z)$ are “imaged” to the image plane via Fourier transformations as shown in **Eq. 95**. The cutoff frequency f_0 of the CTF scales with ω_n .

$$u_{img}(t_m, \omega_n, x, z) = \mathcal{F}^{-1}\left\{H(\omega_n, f_x, f_z)\mathcal{F}\{u_{obj}(t_m, \omega_n, x, z)\}\right\} \quad (95)$$

The fields at the image plane for a single time step t_m of the simulation are allowed to interfere via a summation over all spectral components ω_n of the probe pulse as seen in **Eq. 96**. At this point, any spectral properties of the CCD sensor or any optical components directly in front of the sensor such as bandpass filters can be considered. The field described in **Eq. 96** is Fourier transformed into the spectral domain so that the spectral amplitude and phase can be modified depending on what filters or

6 Analysis of Experimental Results

sensors are used. The spectrally modified field is then inverse Fourier transformed back to the temporal domain.

$$u_{img}(t_m, x, z) = \sum_{n=1}^{N_\omega} u_{img}(t_m, \omega_n, x, z) \quad (96)$$

At each time step the intensity is then calculated as shown in **Eq. 97**, and finally, the simulated image at the detector is produced by summing the intensity over all time steps within the detector's response time as shown in **Eq. 98**.

$$I_{img}(t_m, x, z) = \text{Re}\{u_{img}(t_m, x, z)\}^2 + \text{Im}\{u_{img}(t_m, x, z)\}^2 \quad (97)$$

$$I_{img}(x, z) = \sum_{m=1}^{N_t} I_{img}(t_m, x, z) \quad (98)$$

The effect of defocus was also added to the coherent imaging model using the Rayleigh-Sommerfeld transfer function $H_{RS} = \exp(iky\sqrt{1 - (\lambda f_x)^2 - (\lambda f_z)^2})$ [50]. Use of H_{RS} to propagate the object field a few micrometers away from the object plane along the y-axis follows the same procedure as described in **Eq. 95**. The object field is Fourier transformed and multiplied by H_{RS} with the desired amount of defocus giving by y . The result is subsequently inverse Fourier transformed back to the spatial domain and used as the new “defocused” object field to be imaged by the imaging system via its CTF as previously explained. Use of the Rayleigh-Sommerfeld demands that $\lambda\sqrt{(\lambda f_x)^2 + (\lambda f_z)^2} < 1$, which is satisfied for probe wavelengths between 400 nm and 900 nm and spatial details larger than 1 μm .

The modified imaging model was tested against the results of the original model described in **Section 2.3.5** and found to produce the same results for a stationary droplet (as water and as overdense plasma) with $v_{obj} = 0$ m/s, and without defocus as presented in **Fig. 9**. Before proceeding to investigate the origin of the half-ring signal, the model was further tested by comparing it to the images of ionized water droplets recorded by the probe beam in another Jeti 40 experimental campaign. The probe's spectrum and pulse duration were better represented by a sum of three Gaussians resulting in an FTL FWHM pulse duration of ~ 3 fs as measured in [155]. A bandpass filter centered at 710 nm with a 40 nm width was used in the Droplet experiment to reduce unwanted light in the shadowgraphic images [171]. This filter was also accounted for in the coherent imaging model. Using stationary 20 μm opaque droplets in the model resulted in interference fringes around the image of the droplets with a fringe period of 2.65 μm which matches well with the experimentally measured fringe period of 2.75 $\mu\text{m} \pm 0.20$ μm (see **Fig. 36a**).

6.2.4 Coherent Imaging Model and the Half-Ring Signal

By increasing the modelled object's speed to that of the group velocity of the pump laser in plasma, the plausibility of the half-ring signal being diffraction from the front of the plasma wave was tested.

6 Analysis of Experimental Results

Again, the theory is that cyclotron resonances near the peak magnetic fields of a self-steepened pump laser in underdense plasma cause diffraction of the probe beam which appears as diffraction rings in the recorded shadowgrams.

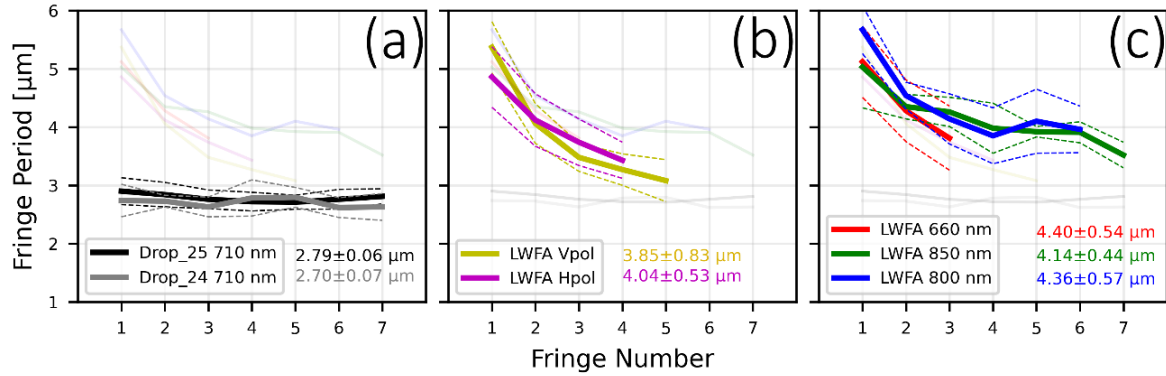


Figure 36: Experimentally measured diffraction ring periods from Droplet and LWFA campaigns. (a) two sets of stationary droplet data used to test the imaging model. (b) full spectrum H-pol and V-pol probe measurements of the half-ring signal. (c) spectrally filtered H-pol probe measurements of the half-ring signal using 40 nm FWHM bandpass filters. Dashed lines indicate ± 1 standard deviation from average (solid lines). The labels “ $x.xx \pm x.xx \mu\text{m}$ ” are the mean and standard deviation of each set’s fringe values using only the mean values measured. Each subplot contains the greyed-out averages of the other subplots for comparison.

Experimentally, the period of the half-ring signal was measured using several configurations of the few-cycle imaging system including full spectrum in H-pol, full spectrum in V-pol, 660 nm \pm 20 nm in H-pol, 800 nm \pm 20 nm in H-pol and finally 850 nm \pm 20 nm in H-pol. The measured fringe periods corresponded to the distances between the bright rings along the pump’s propagation axis in the H-pol cases and slightly off this axis for the V-pol case. The results of all measurements are summarized in **Fig. 36b** and **c**. The first four fringe periods could typically be measured over 20-40 individual images for each configuration of the imaging system. Fringes 5-7 were typically measured with fewer than 20 individual shots with some fringe periods being measured and averaged over only three images.

Interestingly, while the stationary droplets (**Fig. 36a**) show a fairly constant period over seven diffraction rings (only a 0.06 μm to 0.07 μm standard deviation in the measurements) the measured fringes in front of the moving plasma waves (**Fig. 36b** and **c**) show a large decrease in period for increasing fringe number, indicated also by much larger standard deviations. Regardless of the spectrum and polarization used in the image, the rings show a large decrease in period over the first few fringes and then a potential leveling-off or oscillation of their value. The variability of the values measured have been displayed in the subplots as “ $x.xx \pm x.xx \mu\text{m}$ ” being the mean fringe period and the standard deviation of typically three to five fringe periods for each measured set. This behavior is quite different than the near constant fringe period seen in the case of a stationary droplet. Furthermore, the value of the fringe periods to which the curves level off would correspond to a probe pulse with a much longer central wavelength than that used, e.g., a fringe period between 3.5 μm and 4.0 μm corresponds to a central probe wavelength of 900 nm to 1030 nm. This is assuming the maximum NA of the used microscope objective of 0.26.

6 Analysis of Experimental Results

The coherent imaging model of an opaque droplet moving at v_g of the pump laser in plasma was used to test any changes in fringe period due to changes in several parameters: the probe pulse's duration, spectrum, and spectral phase (β_2 and β_3) as well as the imaging system's NA, defocus and spectral filtering. The results, as discussed in the next few paragraphs, confirm the trends already seen in the simulated shadowgrams from [27]. The model was simplified to 1D along the axis of object motion due to the computational time of modelling the system in 2D and the large number of variables to be tested; however, after identification of the most plausible set of system variables using the 1D model, the results were tested using the 2D model. Note that the curves plotted in **Figs. 37** and **38** have been separated vertically for better visibility, i.e., their relative intensities should not be compared.

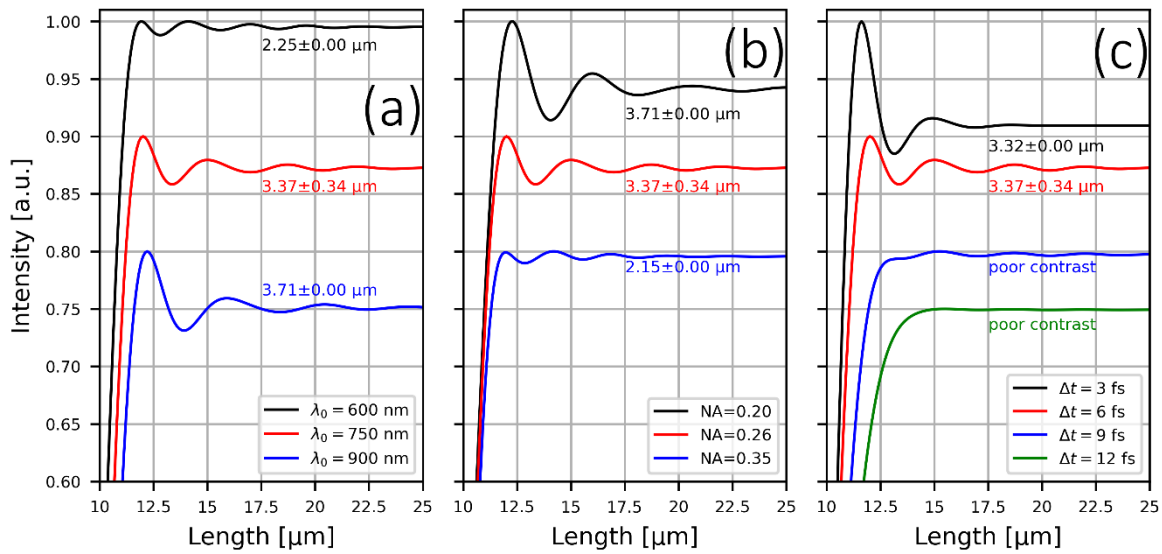


Figure 37: Calculated intensity distributions for interference rings on the right-hand side of the droplet moving to the right with the v_g of the pump laser illuminated with ideal Gaussian probe pulses having flat spectral phase. (a) varying central wavelength, constant FWHM pulse duration (6 fs) and constant NA (0.26). (b) varying NA, constant FWHM pulse duration (6 fs) and constant central wavelength (750 nm). (c) varying FWHM pulse duration, constant central wavelength (750 nm) and constant NA (0.26). Colored numerical labels show mean \pm standard deviation of the measurable fringe periods (contrast $>$ 0.005).

The first parameters tested covered the Abbe diffraction limit as well as a simplified temporal resolution of the shadowgram assumed to be the FWHM pulse duration of the probe pulse. **Figure 37** shows the calculated intensity distributions of the first few interference fringes on the right-hand side of the modelled droplet with the droplet moving to the right with v_g of the pump laser in plasma. As expected, the period of the diffraction rings is proportional to the central wavelength and inversely proportional to the NA of the imaging system (see **Fig. 37a** and **b**). A change in FWHM pulse duration at a constant central wavelength primarily changes the contrast of the diffraction rings due to temporal averaging (**Fig. 37c**) so that pulses with an FTL FWHM duration of ~ 9 fs or longer would not show any interference rings given the typical noise of an uncooled CCD sensor and assuming no spectral filtering of the images. The number of visible fringes increases from the 3 fs pulse to the 6 fs pulse because of the increase in coherence length of the pulse which is proportional to $\lambda_0^2/\Delta\lambda$. No single

6 Analysis of Experimental Results

variation in central wavelength, NA, or pulse duration exhibited the large reduction in fringe period with fringe number as seen in the experiment. The maximum standard deviation in fringe period of $0.34 \mu\text{m}$ is below the measured range of $0.44 \mu\text{m}$ to $0.83 \mu\text{m}$ seen in the experiment (see **Fig. 36**).

The second set of parameters to be tested was defocus, β_2 , and β_3 , i.e., second and third order spectral dispersion. **Figure 38a** shows a small decrease in fringe period for a defocus within the step size of the linear motors used in the experiment, i.e., $2.5 \mu\text{m}$, but this period remains constant for all measurable fringes. The addition of 15 fs^2 and 22.5 fs^2 $\beta_2 L$ to the FTL 6 fs pulse stretched the pulse to 9 fs and 12 fs respectively (dotted lines correspond to -15 fs^2 and -22.5 fs^2 respectively). As shown in **Fig. 38b**, the two positive chirped cases ($\beta_2 L > 0$) show a slight reduction in fringe period with some variability in the 15 fs^2 case, and an improved fringe contrast compared to **Fig. 37c** with FTL pulses at 9 fs and 12 fs FWHM duration. Interestingly, the system does not respond symmetrically with second order dispersion; the two cases of negative chirp (dotted lines) show no measurable fringes. Finally, with the addition of third order dispersion ($\beta_3 L$) to the pulse the fringe period measured depends on both the sign of the dispersion as well as the fringe number or distance from the test object. Importantly, the standard deviation of the fringe periods is finally seen to increase above $0.4 \mu\text{m}$ in the case of $\beta_3 L = -50 \text{ fs}^3$, which could indicate that the probe pulses in the experiment had residual negative third order dispersion.

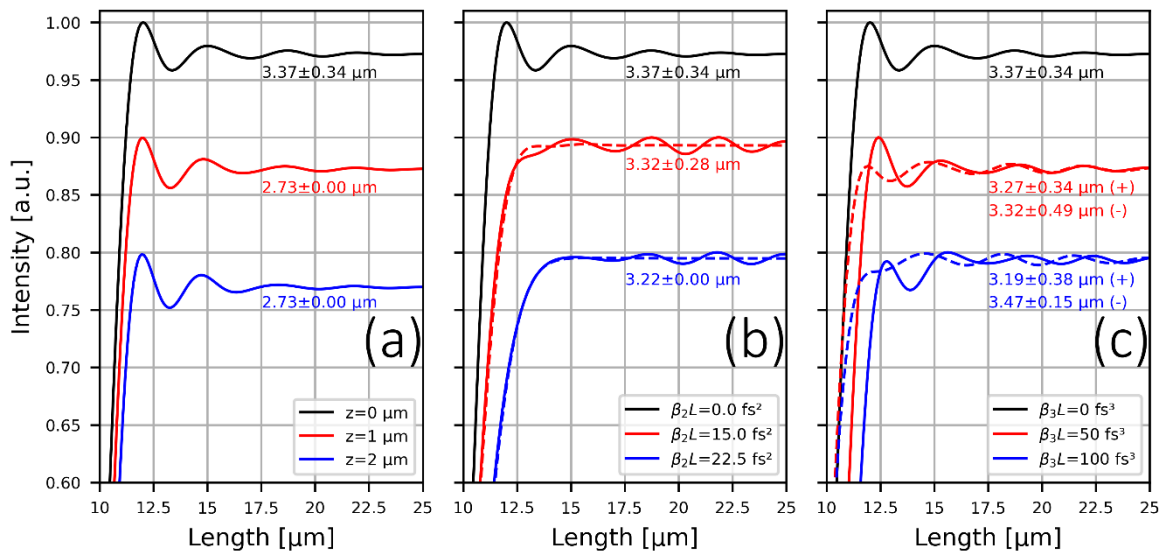


Figure 38: Calculated intensity distributions for interference rings on the right-hand side of the droplet moving to the right with the v_g of the pump laser illuminated with ideal Gaussian pulses originally with $\lambda_0=750 \text{ nm}$, 6 fs FWHM duration and imaged with an NA of 0.26. (a) varying defocus and flat spectral phase. (b) varying $\beta_2 L$ with solid lines having (+) and dotted lines having (-) dispersion values, no defocus and zero $\beta_3 L$. (c) varying $\beta_3 L$ with solid lines having (+) and dotted lines having (-) dispersion values, no defocus and zero $\beta_2 L$. Colored numerical labels show mean \pm standard deviation of the measurable fringe periods (contrast > 0.005).

The goal of this analysis is not only to understand how each parameter affects the resulting fringe pattern that could be measured in the experiment, but also to identify the probe pulse and imaging parameters that were present in the experiment that could cause the measured distribution of

6 Analysis of Experimental Results

interference rings seen and described as the half-ring signal. The spectrum, pulse duration and spectral phase of the probe beam were not simultaneously measured with every shadowgram recorded in the experiment. This resulted in an uncertainty in the probe beam's parameters that to a certain extent could be tested here by the coherent imaging model. For example, while testing the model and the resulting interference rings it became apparent that the geometry of the gas-cell and the working distance of the probe system's microscope objective caused the effective NA of the imaging system to be less than the specified 0.26 value that had been previously assumed (but still valid for the Droplet experiment due to lack of a gas-cell in that setup).

By testing several combinations of the above described parameters, the validity of claiming the half-ring signal to be an interference pattern was tested. 11 different spectral distributions of the probe pulse were tested, including simple Gaussian distributions, double Gaussian distributions and triple Gaussian distributions all of which produced FTL pulse durations around 3 fs FWHM. Furthermore, a range of plausible values for the effective NA (0.16 to 0.21 in steps of 0.1), $\beta_2 L$ (-13 fs² to 13 fs² in steps of 1.5 fs²), and $\beta_3 L$ (-200 fs³ to 200 fs³ in steps of 25 fs³) were tested and the effect of spectrally filtering the images as done in the experiment was also considered. Finally, the periods of the interference rings with contrast above 0.005 (corresponding to 20 counts out of 4092 on a 12-bit CCD sensor) were measured and compared to the experimentally measured values summarized in **Fig. 36** using a root-mean-square measurement.

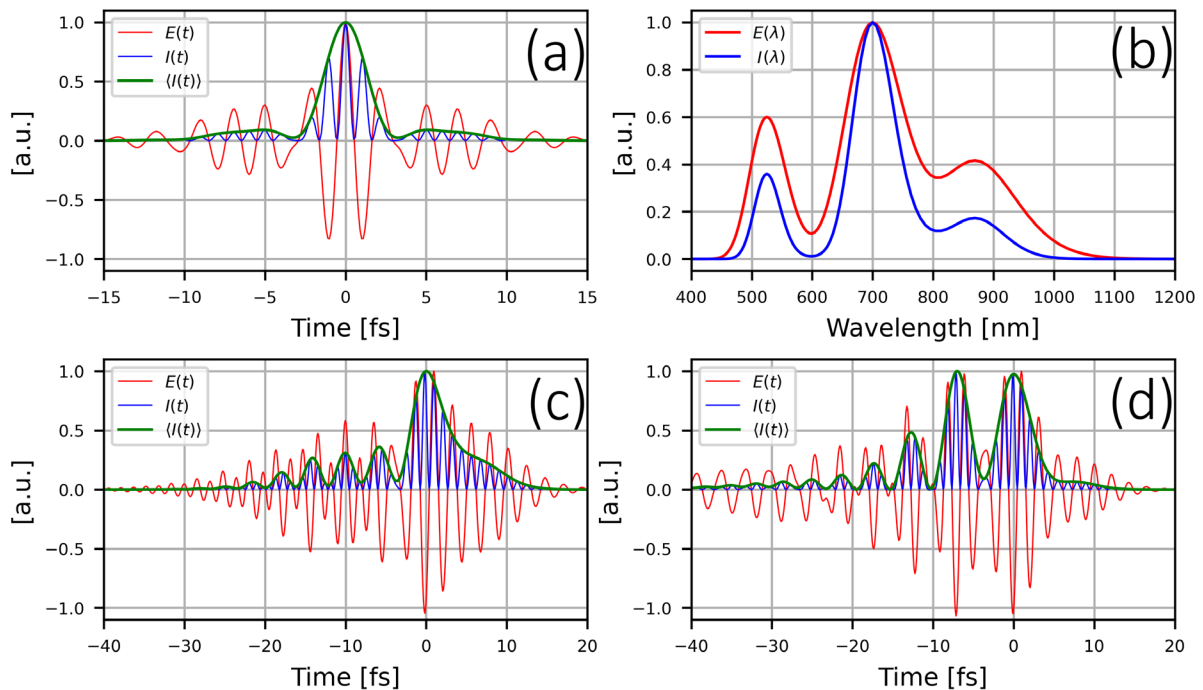


Figure 39: Fc-probe using the best results of the parameter scan. (a) 3 fs FWHM FTL pulse with electric field (red), intensity (blue) and intensity envelope (green). (b) spectral electric field amplitude (red) and spectral intensity (blue). (c) temporal electric field and intensity for best match to the full spectrum case, uses $\beta_2 L = -6$ fs² and $\beta_3 L = -50$ fs³ for a FWHM pulse duration of 5 fs. (d) temporal electric field and intensity for best match to the bandpass filter cases, uses $\beta_2 L = 7.5$ fs² and $\beta_3 L = -75$ fs³ for a FWHM pulse duration of 10 fs.

6 Analysis of Experimental Results

While several combinations of the tested parameters produced interference rings with periods that matched those of a single experimental measurement, i.e., a single bandpass filter or the full spectrum measurement, only a few combinations showed a good fit for all four experimental data sets. The best fit with a realistic spectral distribution was produced using a triple Gaussian distribution. The pulse's temporal FTL distribution, spectral distribution and chirped distributions are summarized in **Fig. 39**. One sees that while the spectral distribution can produce a 3 fs FWHM FTL pulse duration (see **Fig. 39a**) small amounts of uncompensated second or third order dispersion (see **Figs. 39c** and **d**), e.g. from the chirped mirrors, glass components or the plasma, causes the pulse to break into multiple pulses. This has little effect on imaging the plasma wave using bandpass filters because a shorter effective pulse duration would be restored for small dispersion values; however, using the full spectrum to image the plasma wave might cause too much temporal averaging if the total FWHM pulse duration of the multi-pulse structure increases beyond ~ 10 fs. Simpler single and double Gaussian spectral distributions also showed decent matches to the experimentally measured interference rings; however, given that the probe beam relies on SPM for spectral broadening, any "well-behaved" spectrum is not plausible in terms of proper modelling the probe beam used in this experiment. Several of the modulated and chirped spectrums were also tested with a stationary object to see if the fall-off in fringe period with fringe number is dependent on the motion of the object. While some of the resulting diffraction patterns did show a variability in fringe periods similar to that found in **Fig. 38c**, none of the results showed the type of decrease seen in the experimental measurements of the half-ring signal.

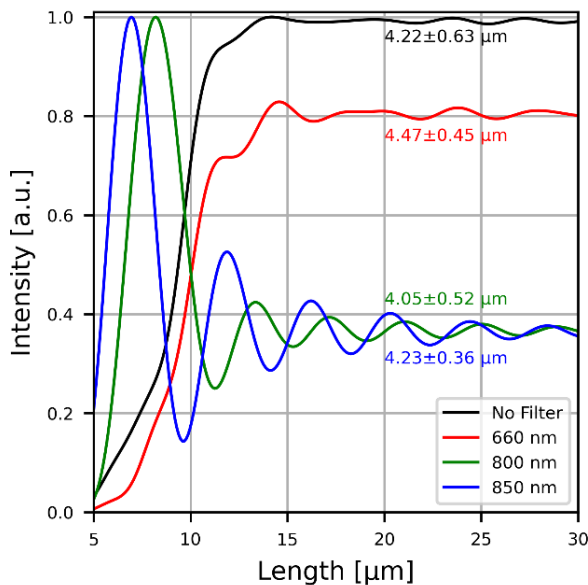


Figure 40: Right halves of the simulated images of a 1D droplet moving to the right at the v_g of the pump laser. Imaging with no bandpass filter (black) and with 40 nm FWHM bandpass filters centered at 660 nm, 800 nm and 850 nm. Mean and standard deviation of the detectable (contrast > 0.005) fringe periods are shown.

The resulting intensity distributions from the 1D imaging model for the four tested spectral filtering cases are shown in **Fig. 40**. Only the right half of the simulated 1D image is shown, corresponding to the leading edge of the plasma wave in the LWFA experiments. The detection limit seen in the experiment for an almost saturated detector at 4000 counts was ~ 20 counts corresponding to 0.005 in the arbitrary intensity units shown. Any contrast of the fringes below this limit was undiscernible with the detector's noise level. The fringe pattern seen imaged through bandpass filters centered at 800 nm and 850 nm have very high contrast; however, the interference rings imaged without a filter and with a filter centered at 660 nm have very poor, almost undetectable contrast. These results do not

6 Analysis of Experimental Results

align especially well with the experiment, in which the fringes' contrast was fairly similar across the various spectral bands tested (c.f. **Figs. 19** and **20**). However, **Fig. 38c** does show a reduction in fringe contrast for increasing negative third-order dispersion as compared to the FTL case and a simultaneous increase in the fringe periods' standard deviation. The results of the model are consistent with previous tests with changes to only one parameter of the system, but unfortunately the exact source of the discrepancy between the fringe contrast seen in the experiment and that recreated with the simulation would require either further parameter scans or perhaps a more accurate model.

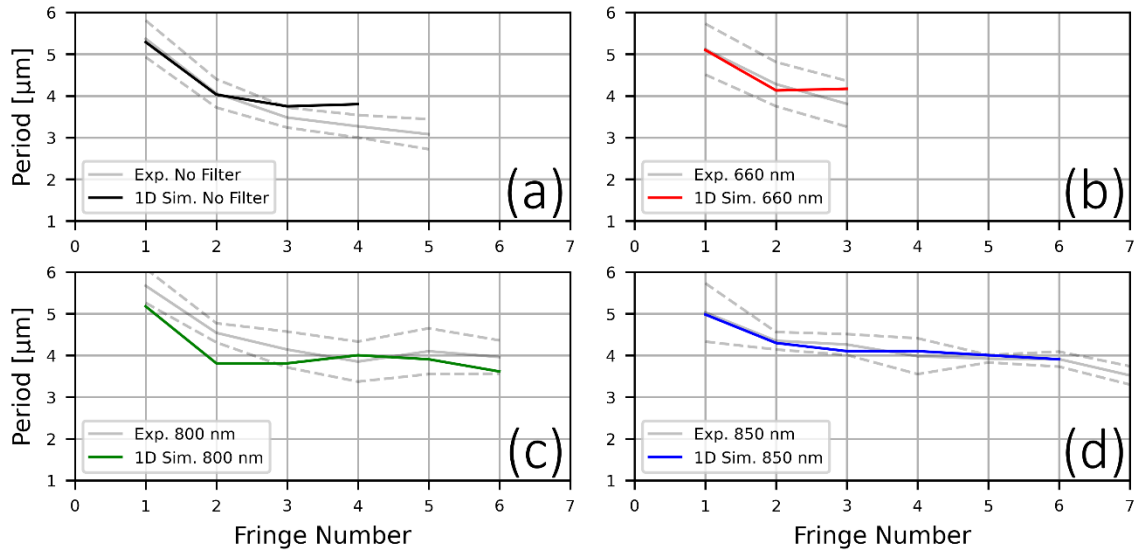


Figure 41: Plotted fringe period in μm vs. fringe number with fringes being numbered from left to right starting at the right edge of the 1D simulated droplet. All four spectral bands are shown: (a) no filter used, (b) 660 ± 20 nm, (c) 800 ± 20 nm, and (d) 850 ± 20 nm. Each subplot displays in gray the mean (solid) and mean \pm standard deviation (dashed) of the fringe periods from the experiment as previously shown in **Fig. 36**.

The measured fringe periods from the simulation are shown overlaid with the measured fringe periods from the experiment in **Fig. 41**. Most measurements from the simulation fit to within the standard deviation of the experimental measurements. As noted in **Fig. 39**, excluding the probe pulse's spectrum, the best parameters used to model the “no filter” results differed from those used to model the bandpass-filtered results. The filtered measurements and the full-spectrum measurements were taken on different days in the campaign. Other than changes in the probe beam's parameters due to daily alignment of the Jeti 40 laser, a change in the gas-cell's length from ~ 2 mm to ~ 2.5 mm length was also performed between the two measurement sets. Unsurprisingly, the best results from the coherent image model's parameter scan mirror this change in gas-cell length via the imaging system's effective NA. The effective NA in the experiment was, at the time, unknowingly reduced due to clipping by the entrance and exit plugs of the gas cell and the exact positioning of the microscope objective relative to the gas cell's center. The experimental measurements using a ~ 2 mm cell length were best matched with an NA of 0.17, while the measurements using ~ 2.5 mm cell length were best matched with an NA of 0.20.

6 Analysis of Experimental Results

Using the best matching parameters of the probe pulse and effective NA from the 1D model, two 2D simulations were run in which opaque disks with 20 μm diameters were imaged with the probe pulses while moving to the right with the v_g of the pump laser in underdense plasma. Again, the parameters for the “no filter” case differ from the parameters for the “bandpass-filtered” cases due to the experimental data having been recorded on different days. Results are shown in **Figs. 42** and **43**.

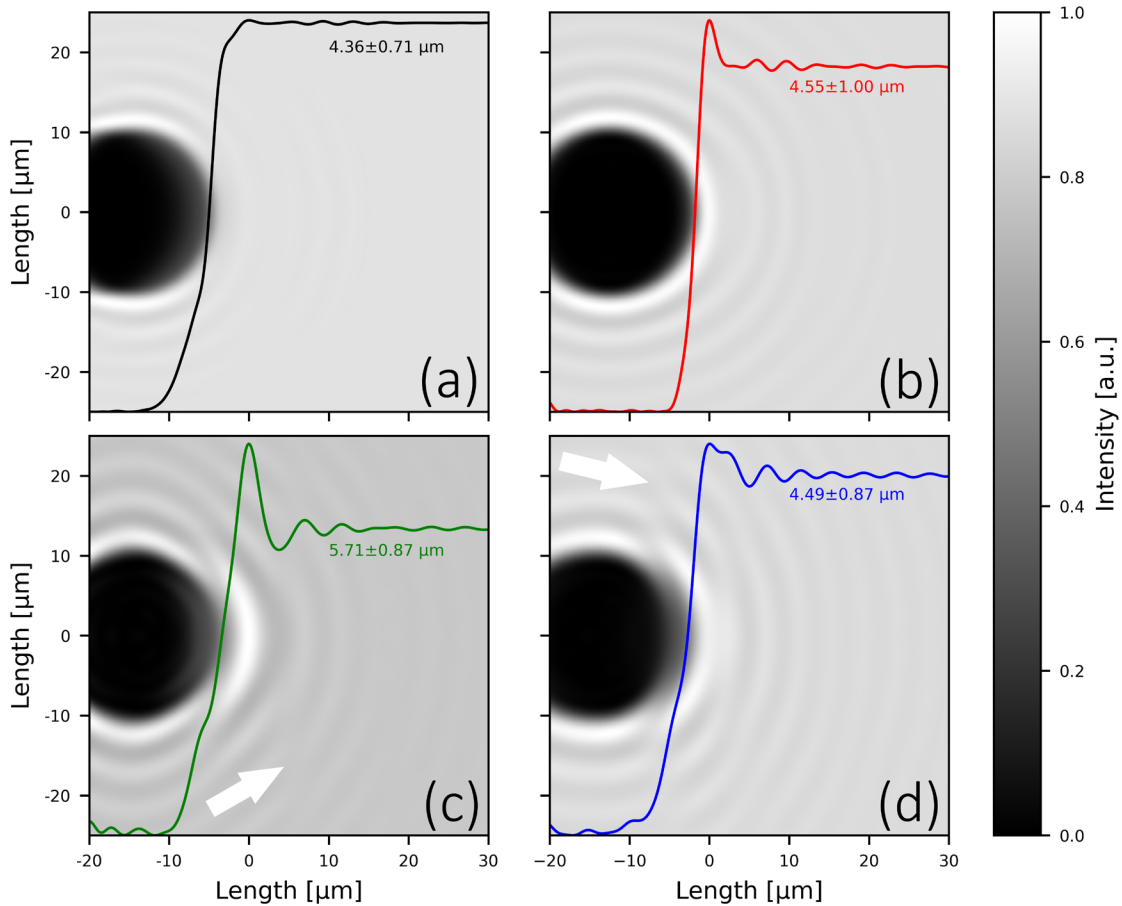


Figure 42: 2D imaging simulations using best matched parameters from 1D parameter scan. The object in each subplot is moving at v_g of the pump laser in underdense plasma to the right. Images have been shifted horizontally such that the first fringe peak is centered at 0 μm . (a) No filter case using $\text{NA} = 0.20$, $\beta_2 L = 7.5 \text{ fs}^2$ and $\beta_3 L = -75 \text{ fs}^3$ for a FWHM pulse duration of 10 fs. (b) $660 \pm 20 \text{ nm}$ bandpass filter using $\text{NA} = 0.17$, $\beta_2 L = -6 \text{ fs}^2$ and $\beta_3 L = -50 \text{ fs}^3$ for a FWHM pulse duration of 5 fs. (c) $800 \pm 20 \text{ nm}$ bandpass filter and (d) $850 \pm 20 \text{ nm}$ bandpass filter, both with parameters from case (b). mean \pm std values given are for fringes with contrast above 0.005. Horizontal lineouts through the middle of the image are shown.

As expected, the contrast of the interference rings in the “no filter” case puts them almost below the 0.005 threshold, see **Fig. 42a**. This is due to the $\sim 10 \text{ fs}$ FWHM pulse duration used causing temporal averaging of the fringes as well as the very short coherence length of the probe pulse. The bandpass-filtered cases (**Fig. 42b-d**) show much better contrast due to the shorter 5 fs FWHM pulse used, but also due to the increase in coherence length caused by spectrally filtering the pulses. One significant difference between the 2D simulations and the experimental measurements is seen in the transition of concentric fringes around the droplet. The signal in the experiment was named the “half-ring” signal

6 Analysis of Experimental Results

because the fringes appeared to be continuous and somewhat concentric around the front of the plasma wave. The only breaks observed were in the V-pol measurements as described in **Chapter 4.3** and later explained via relativistic corrections to the plasma's refractive index. Here, the images created by filters centered at 800 nm and 850 nm (**Figs. 42c** and **d**) display a boundary or phase transition in the fringes for angles at roughly $\pm 60^\circ$ from the horizontal axis centered at the droplet (see arrows).

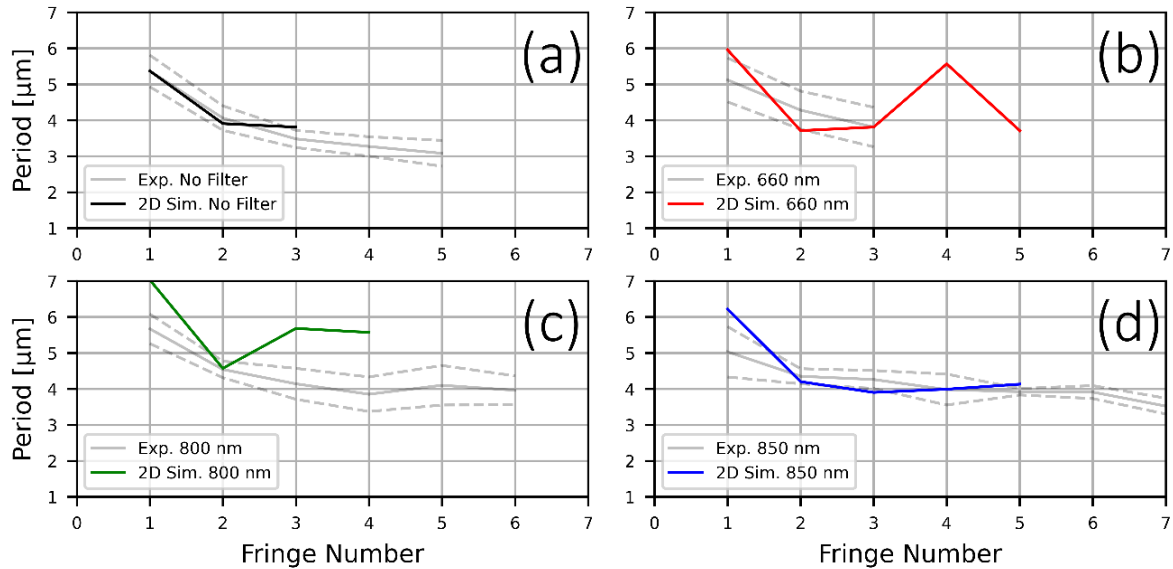


Figure 43: Plotted fringe period in μm vs. fringe number with fringes being numbered from left to right starting at the right edge of the 2D simulated droplet. All four spectral bands are shown: (a) no filter used, (b) 660 ± 20 nm, (c) 800 ± 20 nm, and (d) 850 ± 20 nm. Each subplot also displays in gray the mean (solid) and mean \pm standard deviation (dashed) of the measured fringe periods from the experiment as previously shown in **Fig. 36**.

The fringe periods measured from the 2D simulated images were plotted against the fringe periods measured in the experiment as displayed in **Fig. 43**. While almost all fringes from the “no filter” and 850 ± 20 nm cases still match the experimental measurements to within the measured standard deviation (see **Figs. 43a** and **d**), the simulated fringes created by using filters centered at 660 nm and 800 nm now show significant differences as compared to the experiment (see **Figs. 43b** and **c**). Both the appearance of phase transitions in the fringes as described above and the significant differences in fringe periods highlight what was essentially already known. Not only do the parameters of the probe pulse and imaging system play a significant role in influencing the interference rings, the exact shape of the relativistic object being imaged also plays a primary role. Furthermore, whether the object acts only on the amplitude of the probe pulse (as used in these simulations), only on the phase of the probe, or on both is also an important aspect to investigate.

While the above analysis does not conclusively demonstrate the exact parameters of the probe, imaging system, plasma, and pump that combine to produce the half-ring signal it does show the feasibility of the system to generate such diffraction rings and also underlines the complexity of said system. Many improvements to these measurements and calculations could be made in the future. Experimentally, single-shot characterization of the probe pulse's duration, spectrum and spectral dispersion with every laser shot, as well as stabilized conditions for the laser-plasma accelerator would

7. Summary and Conclusion

be a good start. Numerically, moving towards a full 3D simulation of the pump-plasma interaction including the probe beam and imaging system as performed in [27], but with a larger scan of the probe's parameters would also be advantageous.

7. Summary and Conclusion

Within the scope of this dissertation, relativistic electron-cyclotron resonances (RECRs) in the laser wakefield acceleration (LWFA) scheme have been studied. Their existence and dependence on the pump laser's relativistic intensity distribution make RECRs a candidate for future, non-invasive analysis of the evolution of the pump laser propagating in underdense plasma.

The experimental side of this work depended on combining a 40 TW-class, titanium-sapphire, CPA laser with a few-cycle probe beam imaging system having a $\sim 2 \mu\text{m}$ transverse resolution in the VIS-NIR spectrum. The relativistically intense driver or pump pulse was focused into a gas-cell with a propagation length between 2 mm and 2.5 mm and a 95:5 gas mixture of He:N₂ creating a background electron-plasma density near $1.5 \cdot 10^{19} \text{cm}^{-3}$. The LWFA interaction could then be shadowgraphically imaged with the transverse probe beam using two orthogonal polarization states and different spectral bands between 650 nm and 900 nm. After sorting the data based on the characteristics of the produced accelerated electron bunch, individual shadowgrams were stitched together relative to their pump-probe timing delay to investigate the evolution of the plasma wave through the gas-cell target. The shadowgrams revealed a spectrally-dependent brightness modulation at the front of the plasma wave at the location associated with the pump laser. This brightness modulation was also dependent on the propagation distance in the plasma. Furthermore, a polarization-dependent signal seen as diffraction rings at the very front of the plasma wave was also recorded using the above described system.

Owing to the signals' proximity to the strong magnetic fields of the pump laser, a mathematical model was developed to analyze changes in the plasma's refractive index due to not only the local electron density, but also the local magnetic fields and the relativistic motion of the plasma electrons. The resulting "Relativistic Appleton-Hartree" (RAH) equation considers the relativistic motion of the plasma electrons in two components: their ponderomotive motion due to the pump laser's intensity envelope and additionally their "quiver" motion in the pump's electromagnetic fields. The RAH equation also takes into account the full Lorentz transformation of the pump's and probe's fields, frequencies and orientations into the relativistic drift frame of the plasma electrons' guiding centers. What results is a plasma that exhibits a spectrally-dependent, anisotropic refractive index in the vicinity of the pump's peak intensity.

The RAH equation was implemented using field data and particle tracking data from 2D PIC simulations using the VSim code. The resulting birefringent refractive index distribution at the location of the pump pulse revealed the origins of the previously unknown signals measured in the experimental LWFA campaign. The spectrally dependent brightness modulation at the front of the

7. Summary and Conclusion

plasma wave, called the asymmetric signal in this work, is primarily visualized using a probe beam that is polarized in the plane of electron-cyclotron motion around the pump's dominant magnetic field, i.e., the H-pol probe. For parameters considered in this dissertation, the H-pol probe's polarization remains primarily in the horizontal plane when observed in the drift frame of the plasma electrons and as such can be resonant with the cyclotron frequency of the electrons gyrating in the pump's magnetic field. The resonance causes a significant change in the local refractive index of the plasma and is visualized in shadowgrams as the asymmetric signal described in this work. The spectral dependence of the RECRs, and thus the asymmetric signal, arises from the dependence of the electron-cyclotron frequency on the local magnetic field strength. Analysis of data from a 3D PIC simulation using the EPOCH code corroborated the location of the asymmetric signal and its effect on shadowgraphic images. Finally, the asymmetric signal's spectral dependence was demonstrated using both previously published work with simulated shadowgrams based on the EPOCH data as well as results from combining the RAH equation with data from 2D PIC simulations with the VSim code.

The second unknown signal, i.e., the half-ring signal, appears as polarization-dependent diffraction rings in front of the plasma wave and is also described by the RAH model when considering the self-steepening of the pump laser during propagation. For a step-like distribution of the pump laser's intensity profile, the ponderomotive force would create a similarly steep electron-plasma distribution at the front of the plasma wave. Diffraction of the probe pulse from this distribution might cause diffraction rings to appear in both the H-pol and V-pol shadowgrams; however, the on-axis break in the diffraction rings imaged with the V-pol probe hint at relativistic effects. The full Lorentz transformation of the probe beam's electric field into the drift frame of the plasma electrons shows that for the relevant LWFA parameters in this thesis, the V-pol probe has a significant H-pol component for off-axis drift motion of the plasma electrons relative to the pump's propagation axis. This causes the V-pol probe to also interact with RECRs in the plasma even though its lab-frame orientation would not permit this. For on-axis drift motion; however, the V-pol probe in the drift frame remains vertically polarized and interacts with non-magnetized plasma, leading to the on-axis break in the diffraction rings. The steepened pump causes the resonances to have a steepened distribution further adding to the step-like distribution that is necessary to cause diffraction rings in the recorded shadowgrams. The simulated shadowgrams from the 3D EPOCH simulation also show diffraction rings at the front of the plasma wave depending on the probe beam's spectrum, pulse duration and the NA of the imaging system. However; due to windowing of the PIC simulation's data, the on-axis break in the diffraction rings recorded by a V-pol probe could not be confirmed via 3D simulation.

The diffraction rings at the front of the plasma wave exhibited a curious distribution that differed from those both measured experimentally using the same probe beam but imaging a stationary object as well as from diffraction rings described in common text books. Specifically, the period of the diffraction rings decreased with distance from the diffracting object. To understand this phenomenon,

7. Summary and Conclusion

a coherent imaging simulation was modified to consider relativistic motion of the object being imaged, the fc-pulse's duration, its spectral dispersion and any spectral filtering of the coherent illumination. By comparing the model's results to experimental measurements of both static objects as well as the transient refractive index distribution observed in LWFA, a dependence of the interference rings' period on the probe beam's third-order spectral dispersion was found. However, the complicated interaction between the probe's spectrum, spectral dispersion, pulse duration and spectral filtering with the exact refractive index distribution of the relativistic plasma wave meant that only plausible parameters of the probe-plasma system could be identified that could lead to the observed diffraction patterns. A more detailed numerical study, or an improved LWFA experiment including a detailed characterization of the probe's spectral phase would be necessary to fully understand the diffraction rings' distribution as it pertains to the imaging system and the refractive index's distribution.

The implementation of a few-cycle imaging system on a LWFA experiment has given researchers the ability to observe the relativistic laser-plasma interaction at the fs- and μm -scale. Some of the effects that have been imaged and presented in literature were already predicted and well understood by theory and simulations while other effects still elude a proper description. The RAH model presented in this work can, for the first time, qualitatively describe the origins of signals associated with the relativistically intense pump laser of a LWFA and how they are visualized via shadowgraphy with a few-cycle imaging system. These results constitute an important first step in indirectly imaging the pump pulse and its non-linear evolution using the dispersive anisotropy that arises from the locally magnetized and relativistic plasma. Future experiments would benefit from a few-cycle probe beam with a stabilized spectrum to simultaneously produce polarized shadowgrams in two to four spectral bands for each laser shot. An improved numerical solver for the RAH equation is also recommended as is theoretical work for understanding the temporal dynamics of the cyclotron resonances associated with the pump pulse. PIC simulations with integrated shadowgraphic imaging would also be extremely advantageous not only to better understand the plasma dynamics, but also how the various parameters of the probe beam and imaging system combine to visualize the interaction. As plasma-based accelerators are further developed there will be a need for reliable and accurate diagnostics. This author hopes that the presented work contributes to that end.

Appendix A – Plasma Physics

A.1 Collisional Processes

For any collection of moving particles, there will inevitably be collisions that affect the behavior of the system. The question is how often do these collisions occur, what do they depend on, and how do they affect the system's properties. The effect of collisions on the plasma is qualitatively easy to describe as collisions between particles, neutral or charged, result in a return to thermal equilibrium of the system. Particles with higher kinetic energies give up that energy, via collisions, to particles with lower energy until the system returns to an equilibrium state, in which no net energy transfer takes place. Thus, the collisional frequency answers the question, “to what extent is the particles' kinetic energy distribution a function of time?” The higher the collisional frequency is, the faster the distribution of kinetic energy approaches the equilibrium state and a clear temperature can be defined.

In plasma that is not fully ionized, collisions between neutral and charged particles are not governed by the Coulomb force. Instead, charged-neutral collisions occur over very short distances compared to Coulomb interactions, much like scattering by hard spheres. Assuming the neutral particles to be immobile, the charged-neutral collision frequency ν_{ns} behaves as $\nu_{ns} = n_n C_s \sigma_n$, with n_n being the number density of the neutral particles, C_s the thermal speed of the charged particles of species s , and σ_n being the collisional cross-section of the neutral particles. Since the thermal speed increases with temperature, one sees that the collisional frequency also increases with increasing particle temperatures, which differs from the case of charged-charged collisions as described shortly. For LWFA, the laser intensity used is typically high enough such that the low- Z target gases, e.g. Hydrogen and Helium, are fully ionized before the peak of the laser arrives, thus charged-neutral collisions will not be of significant interest here.

In contrast, it is important to investigate the charged-charged collisional frequency and compare it not only to the plasma and cyclotron frequencies described previously, but also to the time-scale of any other processes of interest that evolve inside the plasma. Since charged-charged particle motion is dictated by the Coulomb force weakened by Debye shielding, the range of distances between two charged particles that can cause scattering, known as the impact parameter, is quite large ranging from the average interparticle distance of a few nanometers to the Debye length of several 10s of nm depending on temperature and density. The electron-ion collisional frequency ν_{ei} for immobile ions is given by **Eq. 99**. The equation for ν_{ei} exhibits a $T^{-3/2}$ temperature dependence which is very different from the temperature dependence of the charged-neutral collisional frequency [37].

$$\nu_{ei} = \frac{n_e e^4}{32 \epsilon_0^2 \sqrt{\pi m_e} (2k_B T_e)^{3/2}} \ln(12\pi N_D) \quad (99)$$

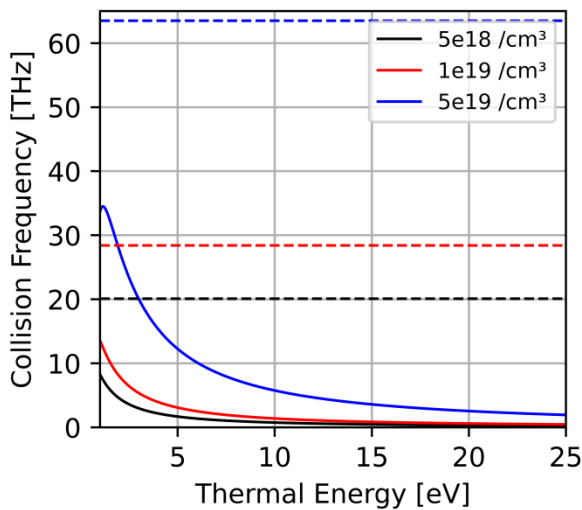


Figure 44: Electron-ion collision frequency (solid lines) and electron plasma frequency (dashed lines) for three different plasma densities.

Figure 44 shows ν_{ei} plotted (solid lines) at three different electron plasma densities over varying thermal energies as well as the corresponding electron plasma frequencies (dashed lines) at those densities. It is clear that for thermal energies above 10 eV the electron-ion collision rate is significantly lower than the corresponding cold plasma frequency, meaning the electrons can perform several plasma oscillations without interacting with the background ion density via collisions. The Bohm-Gross dispersion relation [37], **Eq. 100**, takes into account the change in the oscillation

frequency of the longitudinal electrostatic plasma wave with increasing electron temperature, where k is the wavenumber. The equation shows that the longitudinal electrostatic oscillations reduce back to the electron plasma frequency of cold plasma for decreasing electron temperature while any increase in the temperature of the electrons will increase the oscillation frequency of the longitudinal electrostatic wave, leading to an even larger frequency difference between the oscillation frequency

$$\omega^2 = \omega_p^2 + \frac{3k_B T_e}{m_e} k^2 \quad (100)$$

and the collision frequency. This further reinforces the neglect of electron-ion collisions considering their collisional frequency decreases with increasing thermal energy.

A.2 Phase Space Distribution Function

As shown in **Section 2.1.2** on Debye shielding and the Debye length, the typical plasma parameters used in LWFA experiments produce Debye volumes with several tens to hundreds of plasma electrons that strongly interact with each other. Handling the behavior of groups of many particles lends itself to a statistical approach where a distribution function relates the macroscopic average values of the system to the microscopic individual values of the constituent particles. The distribution function for the electrons (denoted by subscript e) can be written as $f_e(\mathbf{r}, \mathbf{v}, t)$ which is the density of electrons in single-particle phase space. Each electron is described in 6-dimensional phase space consisting of a position \mathbf{r} and a velocity \mathbf{v} at time t . Here, $\mathbf{r} = x\hat{x} + y\hat{y} + z\hat{z}$ and $\mathbf{v} = v_x\hat{x} + v_y\hat{y} + v_z\hat{z}$ are position and velocity vectors in Cartesian coordinates. The number of electrons in a volume element of phase space $d^3r d^3v = dx dy dz dv_x dv_y dv_z$ at the phase space position $(\mathbf{r}, \mathbf{v}, t)$ can be written as $d^6 N_e(\mathbf{r}, \mathbf{v}, t)$, meaning $f_e(\mathbf{r}, \mathbf{v}, t) = d^6 N_e(\mathbf{r}, \mathbf{v}, t) / d^3r d^3v$. The distribution function is assumed to be continuous, positive and finite and must tend to zero as the particle speeds become very large.

So why use a phase space distribution function to describe the plasma? Simple advantages are in identifying if the plasma is spatially inhomogeneous, $f_e = f(\mathbf{r})$, or at equilibrium, $f_e \neq f(\mathbf{r})$. In velocity space, one sees if the plasma is anisotropic $f_e = f(\mathbf{v})$, or isotropic, $f_e = f(|\mathbf{v}|)$. The Boltzmann equation is used to show the dependencies of f_e on $(\mathbf{r}, \mathbf{v}, t)$ and is the starting point for studying the dynamics of the plasma as described shortly. Furthermore, two important hydrodynamic variables necessary for the treatment of magnetoionic theory can be derived from the phase space distribution function of the plasma: the number density $n(\mathbf{r}, t)$, and the average velocity $\mathbf{u}(\mathbf{r}, t)$, of the particles. This is the starting point of magnetoionic theory back in **Section 2.2**. Here, a short description of the Boltzmann equation is given.

The Boltzmann equation is a kinetic, differential equation shown in **Eq. 101** neglecting collisions where D/Dt represents the total time derivative in phase space given by **Eq. 102** and ∇_v is the nabla operator for velocity space given by **Eq. 103** with \mathbf{a} being the acceleration of the particles.

$$\frac{D}{Dt} f_e(\mathbf{r}, \mathbf{v}, t) = \frac{\partial}{\partial t} f_e(\mathbf{r}, \mathbf{v}, t) + \mathbf{v} \cdot \nabla f_e(\mathbf{r}, \mathbf{v}, t) + \mathbf{a} \cdot \nabla_v f_e(\mathbf{r}, \mathbf{v}, t) = 0 \quad (101)$$

$$\frac{D}{Dt} = \frac{\partial}{\partial t} + \mathbf{v} \cdot \nabla + \mathbf{a} \cdot \nabla_v \quad (102)$$

$$\nabla_v = \frac{\partial}{\partial v_x} \hat{x} + \frac{\partial}{\partial v_y} \hat{y} + \frac{\partial}{\partial v_z} \hat{z} \quad (103)$$

It can be shown that the collisionless Boltzmann equation above is an expression of Liouville's theorem from statistical mechanics. Assuming no losses, e.g. collisions or radiative effects, the phase space volume of the particles in the system is constant. This is typically seen when observing the evolution of a particle beam's phase space during propagation through a conventional accelerator [172]. The background gas density in a conventional accelerator is so low that collisions can be ignored. In dealing with plasma over longer time scales in which collisions can no longer be neglected, how the electron-ion and electron-electron collisions affect the distribution function can be investigated by equating the total time derivative of the distribution function to a collisional term $\left(\frac{\partial f_e}{\partial t}\right)_{coll}$ that captures the changes in the distribution function due to those collisions.

One last point concerning the Boltzmann equation is of interest for discussion of Particle-in-Cell or PIC simulations. By recognizing that the acceleration of the particles in the plasma arises from local, internal electric and magnetic fields \mathbf{E}_i and \mathbf{B}_i , the acceleration term \mathbf{a} in the Boltzmann equation can be replaced by the Lorentz force as well as any external forces \mathbf{F}_{ext} that could also contribute to the motion of the particles. The resulting equation, known as the Vlasov equation as shown in **Eq. 104**, takes into account the internal macroscopic fields of the plasma and any external fields to capture the dynamics of the plasma. It is written here again for the electrons with subscript e and for plasma with no collisions.

$$\frac{\partial f_e}{\partial t} + \mathbf{v} \cdot \nabla f_e + \frac{1}{m_e} [\mathbf{F}_{ext} - e(\mathbf{E}_i + \mathbf{v} \times \mathbf{B}_i)] \cdot \nabla_{\mathbf{v}} f_e = 0 \quad (104)$$

The fields in the Vlasov equation obey Maxwell's equations and the distribution function(s) can be used to calculate the charge density and current density in the plasma at each point in time. This creates a set of self-consistent equations that can be incrementally solved to investigate the evolution of the plasma and is the basis for PIC simulations as is described in **Section 2.5.5**.

A.3 Ionization Mechanisms

Photoelectric Effect

Before the invention of lasers, collimated light sources were typically gas discharge or thermal sources that inherently emitted in all directions. Pinholes were used to reduce the divergence of the light and so the resulting photon fluxes were comparably low to today's standards. By illuminating a clean metal surface placed in a vacuum with light of various frequency and intensity it was found that the number of electrons emitted from the metal's surface was proportional to the intensity of the light, and their kinetic energy proportional to the light's frequency. This supported the photon description of light where the photon's energy is given by its frequency and Planck's constant, $\mathcal{E} = h\nu$. Photons with too low a frequency produced no photo-electrons, regardless of the light source's intensity. Viewed in terms of a low pressure gas whose electrons' have an ionization energy of \mathcal{E}_{ion} , the resulting kinetic

$$\mathcal{E}_{kin} = \hbar\omega - \mathcal{E}_{ion} \quad (105)$$

energy of the emitted electrons is given by **Eq. 105**, where $\hbar = h/2\pi$, h is Planck's constant, and ω the photon's angular frequency. This classical view of ionization would mean that only photon's with an energy over 24.6 eV could ionize the first electron of Helium; meaning a photon energy corresponding to the wavelength 50.4 nm would be necessary. Naturally this is not the case.

Multi-Photon Ionization (MPI)

One might assume that increasing the number of photons per second incident on the material would allow for ionizing electrons even if the photon energy were below the ionization energy; multiple photons could interact with one electron. The problem lies in the "simultaneity" of the interactions. If the photons do not interact often enough, then the excited, but not ionized, electron will simply reemit the absorbed photon instead of being excited to the next virtual state by a subsequent photon. The virtual energy states of excited electrons have a lifetime based on Heisenberg's uncertainty principle, $\Delta\mathcal{E}\Delta t \geq \hbar$ where the uncertainty in energy is given by the photon energy $\Delta\mathcal{E} = \hbar\omega$. For photons in the VIS-NIR range the resulting lifetimes are in the sub-femtosecond range, demanding greater than 10^{15} photons/s or an equivalent power in the mW range for this simple comparison. Although the theory of "Multiphoton Ionization" (MPI) was proposed in 1931 [173], the necessary photon fluxes were not available until the invention of the laser.

$$\mathcal{E}_{kin} = n\hbar\omega - \mathcal{E}_{ion} \quad (106)$$

Assuming enough photons can interact with a single electron, the resulting kinetic energy is given by **Eq. 106**, where n is the number of photons necessary to exceed the electron's ionization energy. Comparing the electron density of the material to be ionized with the photon density of the light source can put things into perspective. The original papers from the late 1970's report measurements of MPI reduced the demands on photon density by reducing the gas density used (fewer atoms per photon) and also by reducing the ionization energy required by using the heavy noble gas Xeon. Outer electrons of heavier atoms have reduced ionization energies because the inner electrons reduce the effective nuclear charge seen by the outer electrons. In **[174]**, *Agostini* et al. used an Nd:glass laser (1.17 eV photon energy) with 12 ns pulses, 2 Joules of energy and a reported intensity of $4 \cdot 10^{13}$ W/cm² giving a photon density of $6.7 \cdot 10^{23}$ photon/cm³, roughly $8.9 \cdot 10^{26}$ photons/s or $5 \cdot 10^{11}$ photons/lifetime. The pulses were focused into Xe gas (12.27 eV ionization potential) with roughly $6.5 \cdot 10^{-8}$ atm of pressure, giving a photon:electron ratio around $1 \cdot 10^9$. The cross-sections for multiphoton ionization scales to the negative power of the order of interaction, meaning the more photons needed to quasi-simultaneously interact with the atom or molecule, the lower the cross section becomes **[175]**, **[176]**. This is an indicator as to why significant photon densities per electron are necessary for the multiphoton ionization process to be measured depending on the ratio between ionization energy and photon energy.

Above Threshold Ionization (ATI)

By increasing the photon density even further, an electron can absorb not only the required number of photons for ionization, but also additional photons that will increase its resulting kinetic energy. Called "Above Threshold Ionization" (ATI), its characteristic spectrum in the long-pulse, low-intensity regime displays peaks in electron kinetic energy separated by the incident photon energy as seen in **Eq. 107**, where m represents the excess number of photons absorbed. The height of the peaks falls off with increasing m , due to decreasing cross-section for increasing number of absorbed photons **[174]**.

$$\mathcal{E}_{kin} = (n + m)\hbar\omega - \mathcal{E}_{ion} \quad (107)$$

The above equation represents a simplified view of the mechanism. Over the past 30 years researchers have investigated several regimes of ATI: long/short wavelength, low/high intensity, long/short pulse duration and finally linearly or circularly polarized pulses **[177]**–**[180]**. Each regime presents its own unique spectrum of the electrons' kinetic energies or electron plasma temperature which have been investigated in the context of using low temperature plasma for recombination lasers **[181]** and lowering the injection threshold of electrons in LWFA by using heated plasmas **[182]**. ATI is also at the core of a novel fc-pulse measurement method described in **[51]**.

Tunnel Ionization

Given a strong enough laser source, its electric field can begin to suppress the Coulombic potential that restrains the electron to its parent atom or molecule. With enough reduction in the coulombic potential, the electron has a non-zero probability of tunneling out of the potential well. This process is called tunnel ionization. Intuitively, the longer the barrier is suppressed the higher the probability there is for the electron to tunnel. This is quantified in the Keldysh parameter given by **Eq. 108**.

$$\gamma_K = \omega_L \sqrt{\frac{2\mathcal{E}_{ion}}{I_L}} \quad (108)$$

For low laser frequencies and high laser intensities, the Coulombic barrier is suppressed and the electron has a longer time to possibly tunnel, meaning that Tunnel Ionization is dominant for a Keldysh parameter $\gamma_K < 1$. Likewise, for higher laser frequencies and higher ionization potentials, $\gamma_K > 1$, and MPI or ATI are the dominant ionization processes [131].

Barrier Suppression Ionization

Continuing along this line of increasing laser or source intensity, one final ionization mechanism called BSI, or Barrier Suppression Ionization, can be seen when the Coulombic potential is distorted to below the ionization potential of the electron. To understand this process a simple model using the Bohr model of Hydrogen is used. Using the Bohr radius, a_B , of 52.9 pm, the electric field E_a (**Eq. 109**) and associated laser intensity I_a of this electric field (**Eq. 110**) for an electron at the Bohr radius can be calculated.

$$E_a = \frac{e}{4\pi\epsilon_0 a_B^2} \quad (109)$$

$$I_a = \frac{\epsilon_0 c}{2} E_a^2 \cong 3.45 \cdot 10^{16} \frac{W}{cm^2} \quad (110)$$

A laser with this intensity would completely suppress the Coulombic potential of the electron at the Bohr radius; however, experimentally, increased ionization rates not expected with Tunnel Ionization were already measured with lower laser intensities. A slightly more refined model by Bethe and Salpeter [183] represented the 1D potential $V(x)$, as a static superposition of the Coulomb potential and an externally applied electric field E , where Z is the charge that the ion will assume after ionization of the electron, as seen in **Eq. 111**.

$$V(x) = -\frac{Ze^2}{x} - eEx \quad (111)$$

By calculating the location of the maximum barrier via $\frac{dV}{dx} = 0$ and setting $V(x_{max}) = \mathcal{E}_{ion}$ one can solve for the field necessary to fully suppress the barrier, $E_{crit} = \frac{\mathcal{E}_{ion}^2}{4Ze^3}$, and the corresponding minimum intensity for BSI in general, I_{BSI} , **Eq. 112**. Comparing the previous intensity for the Bohr model (**Eq. 110**), with I_{BSI} for the ionization Hydrogen ($1.37 \cdot 10^{14} \frac{W}{cm^2}$), one finds a factor 256 lower

Appendix A – Plasma Physics

intensity necessary for the simple 1D model. Comparisons of ionization models for MPI, TI and BSI can be found in [184], [185] and references therein.

$$I_{BSI} = \frac{\pi^2 c \epsilon_0^3 \mathcal{E}_{ion}^4}{2Z^2 e^6} \cong 4 \cdot 10^9 (\mathcal{E}_{ion}[eV])^4 Z^{-2} \frac{W}{cm^2} \quad (112)$$

Appendix B – Laser Physics

B.1 Creation of Few-Cycle Pulses

The duration of an optical cycle for wavelengths spanning the spectral range of 400 nm to 1000 nm varies between 1.3 fs and 3.3 fs, giving a lower limit to the pulse duration possible in the VIS-NIR. Through rearranging the TBP from Eq. 34 by defining the FWHM pulse duration Δt as a multiple n of the laser period T , one arrives at the simple expression of $\Delta\lambda \geq \lambda_0\kappa/n$, which gives the minimum necessary FWHM bandwidth for an n -cycle pulse duration. As an example, a Gaussian pulse centered at 800 nm with a FWHM duration of two optical cycles (ca. 5 fs) needs a minimum FWHM spectrum of 176.4 nm. Many methods exist for creating such broadband laser pulses [47]–[49].

For the purposes of pump-probe experiments needing synchronization at femtosecond-timing levels and probe pulse energies in the μJ to mJ range, the combination of self-phase modulation of the laser pulse in a hollow-core fiber (HCF) filled with a noble gas followed by spectral dispersion correction with dispersion compensating mirrors (DCMs) or prisms and glass wedges is one of the more well-established methods. This technique was demonstrated by *Nisoli et al.* and has been further developed and implemented by many groups [186]. Other schemes using independent amplifier stages are also capable of creating μJ to mJ or energies with <10 fs pulse durations; however, the induced timing jitter in a pump-probe setup can be problematic depending on the experimental conditions.

For a simplistic theoretical understanding of how self-phase modulation (SPM) can affect a laser pulse propagating in a nonlinear medium one can begin with the Nonlinear Schroedinger Equation (NLSE) given by Eq. 113 using a laser pulse with temporal electric field E and carrier frequency ω_0 [48]. An instantaneous and frequency independent Kerr nonlinearity is assumed which causes a change in the refractive index proportional to the temporal intensity distribution of the pulse as $\delta n_{NL} = n_2|E|^2$. Here, n_2 is the medium's nonlinear refractive index.

$$\frac{\partial E}{\partial z} + \beta_1 \frac{\partial E}{\partial t} - i \frac{\beta_2}{2} \frac{\partial^2 E}{\partial t^2} + i \frac{\omega_0 n_2}{c} |E|^2 E + \frac{\alpha}{2} E = 0 \quad (113)$$

In the simplest case, one can assume that the nonlinear medium is lossless, i.e., loss coefficient $\alpha = 0$, and that group velocity dispersion does not play a significant role, $\beta_2 = 0$ (likewise, higher order dispersion terms are also ignored). The NLSE from above can be further simplified by rewriting it in a frame that is co-moving with the laser pulse as well as by introducing the factor $\gamma = (\omega_0^2 n_0 n_2) / (\beta_0 c^2 A_{eff})$ with n_0 being the medium's linear refractive index and A_{eff} representing an effective area of the laser's spatial mode. This results in Eq. 114 with a general solution given by Eq. 115. One sees that with propagation through the nonlinear medium, the pulse accumulates a nonlinear temporal phase component $\phi(z, t) = -\gamma|E(0, t)|^2 z$ that depends on the pulse's temporal intensity distribution and on the nonlinear refractive index via the factor γ . Again, the electric field's envelope function E is not a function of propagation in z as losses in the medium have been ignored.

$$\frac{\partial E}{\partial z} = -i\gamma|E|^2 E \quad (114)$$

$$E(z, t) = E(0, t)\exp(-i\gamma|E(0, t)|^2 z) \quad (115)$$

Assuming one had a plane wave as in **Eq. 30** or a Fourier-limited Gaussian pulse as in **Eq. 31**, the temporal derivative of the electric field's temporal phase in both cases gives the time-independent carrier frequency ω_0 . Now, in the case of the nonlinear phase shown above, its temporal derivative shows a time-dependent shift of the carrier frequency that depends on the temporal intensity distribution of the laser pulse in the medium. So the instantaneous frequency ω_{inst} of the pulse can be written using **Eq. 45** as **Eq. 116** below.

$$\omega_{inst}(z, t) = \omega_0 + \Delta\omega(z, t) = \omega_0 - \frac{\partial}{\partial t}(\gamma|E(0, t)|^2 z) \quad (116)$$

Clearly, the steeper the temporal profile of the laser is the larger the frequency shift achievable. For a medium with a positive n_2 , the leading edge of the pulse becomes red-shifted and the trailing-edge becomes blue shifted. The resulting spectrum of the pulse has a signature oscillatory pattern that arises due to interference effects. Depending on the temporal intensity profile of the pulse, the same frequency shift can be created at two or more different points in time along the pulse. The phase between these points then dictates whether that spectral component undergoes constructive interference (a peak in the spectrum) or destructive interference (a dip in the spectrum). The number of peaks in the spectrum is related to the maximum nonlinear phase shift accumulated in the medium. A more detailed model of the nonlinear interaction that considers loss, dispersion of the medium, and non-ideal input pulses typically must be numerically solved.

When including dispersion effects in the NLSE for propagation through a nonlinear medium, or when simply considering linear dispersion during pulse propagation through air or glass as described in **Section 3.3.2**, the resulting temporal electric field distribution of the pulse will develop an instantaneous carrier frequency that is time dependent. Even if the pulse's spectrum has been broadened via SPM, the uncorrected temporal chirp results in temporal pulse distortion, i.e., a pulse duration that is not Fourier-limited. There are three main techniques for compensating temporal chirp, also known as spectral dispersion. Propagation in fiber optics with a negative GVD can compensate for the positive GVD found in most linear materials **[187]**; however, higher order dispersion coefficients are difficult to compensate in this manner, and high power laser pulses run the risk of destroying the fiber. Use of a prism or grating stretcher/compression system **[188]**, **[189]** in a laser amplification chain is a proven technology for stretching high energy pulses from the femtosecond- or picosecond-scale up to the nanosecond-scale and subsequently compressing the pulses again after amplification. This is the basis of the ‘‘Chirped-Pulse Amplification’’ scheme that will be discussed later. Finally, dispersion compensating mirrors (DCMs) or ‘‘chirped’’ mirrors have been developed based on thin-film mirror coating technology **[190]**. The Bragg condition for reflection from the mirror is varied for each wavelength as a function of depth in the thin-film coating. This control on the

micrometer-scale in the thin-film coating allows for compensation of relatively small amounts of GVD per reflection compared to prism or grating systems. Furthermore, matched DCMs can be manufactured that, when combined, correct or minimize contributions from higher order dispersion. The fine dispersion control offered by DCMs make them the solution of choice when compressing pulse durations of 10's to 100's of femtoseconds down to the sub-10 femtosecond-timescale.

The technological ability to spectrally broaden pulses and subsequently compress them to Fourier limited durations of only a few femtoseconds developed simultaneously with the ability to not only accurately measure their pulse duration but also their spectral dispersion. The next section introduces the three main pulse characterization techniques used in this work.

B.2 Single-Shot Characterization of Few-Cycle Pulses

Research into the characterization of ultra-short laser pulses is extensive and review papers have been written describing the various methods available depending on pulse duration, spectral region and repetition rate [191], [192]. This section will briefly describe three characterization methods capable of reconstructing the electric fields of fc-pulses in the VIS-NIR spectrum: spectral phase interferometry for direct electric-field reconstruction (SPIDER), self-referencing spectral interferometry (SRSI), and stereographic above-threshold ionization (SATI). Another widely used method of pulse characterization with several variants is frequency-resolved optical gating (FROG) [193], which will not be described here as it was not used in this work. Finally, a third-order auto-correlation measurement used to characterize the temporal intensity contrast (TIC) of a terawatt laser system will be described. The TIC of the pump laser in laser-plasma interactions plays an important role and will be mentioned later when discussing images recorded in the pump-probe experiments.

SPIDER

Introduced in the late 1990's [194], SPIDER devices have been developed for use ranging from the UV to the mid-IR covering pulse durations from several hundred femtoseconds down to below 5 femtoseconds. The measurement is based on both temporal and spectral shearing of the pulse to be measured. The input pulse, represented by its spectral field amplitude $E(\omega)$, is first split into two replicas. One replica goes to a stretcher system to be linearly chirped, while the other replica is split into a pulse pair with a temporal delay τ . The chirped pulse and the delayed pulse pair then interact in a nonlinear medium, typically being upconverted by a process such as second harmonic generation (SHG). With proper chirp and delay parameters, each pulse in the pulse pair interacts with a different instantaneous frequency of the chirped pulse during SHG conversion. This produces two final pulses that are described by their temporal shear τ and their spectral shear Ω and are focused to the entrance of a spectrometer where the spectral interferogram $S(\omega)$ is recorded.

$$S(\omega) = |E(\omega)|^2 + |E(\omega + \Omega)|^2 + 2|E(\omega)E(\omega + \Omega)| \cdot \cos[\phi(\omega + \Omega) - \phi(\omega) + \omega\tau] \quad (117)$$

The resulting spectrogram, given by **Eq. 117**, is analyzed via the method of Fourier Transform Spectral Interferometry (FTSI) [195]. The spectrogram is Fourier transformed to the temporal domain where three signals can be identified: a DC signal and two signals centered at $\pm\tau$. The signal centered at $+\tau$ is extracted and inverse Fourier transformed back to the frequency domain where knowledge of the temporal delay, τ , is used to subtract a linear phase from the data. The difference phase from the cosine's argument given by $\phi(\omega + \Omega) - \phi(\omega)$ can then be used to reconstruct the spectral phase of the input pulse. Pre-calibration of the delay and chirp parameters allows the input pulse to be fully characterized in single-shot mode.

Several optimizations to the original design can be implemented in order to measure fc-pulses while still keeping the overall design comparatively simple in terms of alignment and size. These include switching to reflective optics, using a Fabry-Pérot etalon to generate the delayed pulse pair, and optimizing the nonlinear crystal thickness for the expected bandwidth being measured. These improvements, along with the proper design of τ and Ω have enabled measurements of pulse durations of sub-5 fs pulses in the VIS-NIR regime [196].

SRSI

Ideally, pulse characterization is performed using a reference pulse with a known spectral phase and amplitude. Furthermore, the reference's spectral width should also be larger than that of the input pulse being measured; otherwise the pulse to be measured cannot be properly sampled. SRSI [197] exploits an acoustic-optical programmable dispersion filter (AOPDF) and cross-wave polarization nonlinearity (XPW) to create such a reference pulse from a replica of the input pulse, enabling the measurement method to characterize ultra-short and fc-pulses with a straightforward collinear optical system. For a given input pulse, a feedback loop is established between the AOPDF and the output of the XPW stage. The AOPDF systematically varies the pulse's spectral phase creating a so-called "corrected pulse" E_{CP} . If the corrected pulse has no significant chirp, the output of the XPW stage, called the "reference pulse" E_{ref} , will have an almost flat spectral phase and a spectrum broadened by a factor of $\sqrt{3}$. When the loop finds the broadest XPW spectrum, the remaining phase difference between the corrected pulse and reference pulse can be measured via FTSI to further improve the AOPDF's correction of the spectral phase. **Equation 118** shows the signal measured by a spectrometer for the two aforementioned pulses and a delay τ . Following the FTSI procedure, the signal is inverse Fourier transformed resulting in three localized signals as described in the SPIDER measurement. By selecting the signal at $+\tau$ and Fourier transforming it back to the spectral domain, the phase of the resulting signal $\phi_{ref}(\omega) - \phi_{CP}(\omega) + \omega\tau$ can be used, with accurate measurement of the delay τ , to further improve the phase optimization and thus the determination of the original input pulse's spectral phase. Depending on the stability of the laser system being measured single-shot characterization of the pulse to be measured can be obtained.

$$S(\omega) = |E_{ref}(\omega)|^2 + |E_{CP}(\omega)|^2 + \text{Re}(E_{ref}E_{CP}^* + E_{ref}^*E_{CP}) \cos(\omega\tau) \quad (118)$$

Fc-pulse systems that are based on hollow-core fiber and chirped mirror technology typically do not make direct use of an AOPDF for measurement with the SRSI method. Instead, thin glass wedges and negatively chirped mirrors are used to linearize the pulses' spectral phase to almost FTL levels. As described in [198], the SRSI method can be designed for such ultra-broadband, fc-pulses. Their system is capable of measuring down to 4 fs FWHM pulses in intensity while also characterizing the rising and falling flanks of the pulse over a ± 500 fs temporal window with a dynamic range of 40 dB.

CEPM/SATI

A third method suitable for measuring fc-pulses in the VIS-NIR spectrum has been developed for research in strong-field laser-matter interactions, in which reconstructing the laser's waveform is pivotal to understanding the dynamics of several laser-matter interactions [51], [154], [199]. Called the Carrier Envelope Phase Meter (CEPM), this device is based on stereo-above threshold ionization (SATI) of Xe gas and along with pulse duration measurements between approximately 4 and 12 fs, it is capable of single-shot tagging of the pulse's carrier envelope phase (CEP). The laser pulse to be measured is focused into Xe gas producing photo-ionized electrons that are detected orthogonally to the laser's propagation direction, on opposite sides of the laser's propagation axis and in the plane of the laser's linear polarization by two micro-channel plate (MCP) detectors. The interaction produces two types of electrons discernable via their energy spectra, which is calculated by their time-of-flight to the MCPs. The direct electrons are ionized and accelerated by the laser field to around twice the laser's ponderomotive energy, which constitutes the lower energy portion of the spectrum. Meanwhile, the rescattered electrons build a high energy plateau in the energy spectrum as they are driven back to their parent ion and accelerated to up to ten times the laser's ponderomotive energy. There are far fewer ($\sim 1\%$) rescattered electrons due to the conditions necessary for rescattering, but their amount is strongly dependent on the CEP of the pulse.

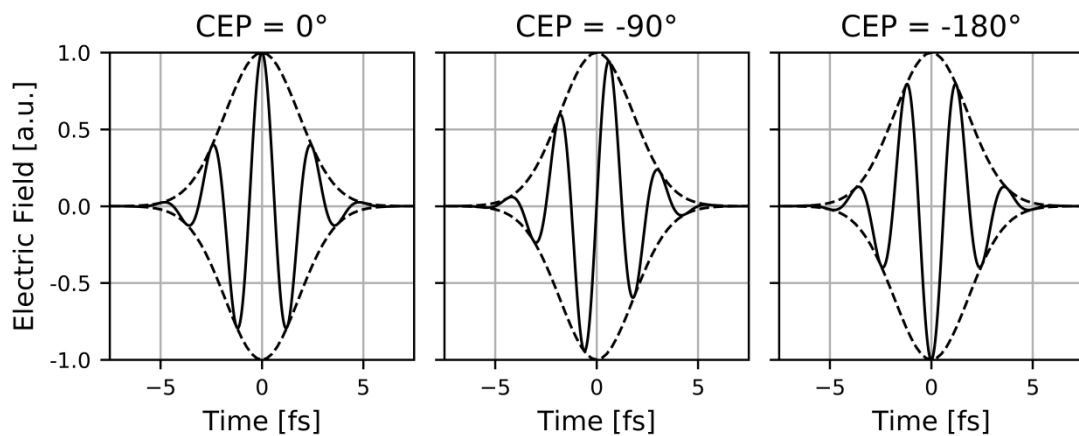


Figure 45: Examples of a 3 fs FWHM Fourier-limited pulse with varying CEP values. The asymmetric field distributions produce different amounts of electrons to be measured in the two opposing MCP detectors.

As the duration of the fc-pulse decreases the asymmetry in the electron yields measured by the MCPs will increase due to the asymmetry in the electric field. The asymmetry can be seen in **Fig. 45** for varying CEP values. The data is typically displayed in a parametric asymmetry plot whose radius corresponds to the measured pulse duration and polar angle to the measured CEP. The asymmetric electric field seen in fc-pulses is no longer measureable in pulses of longer duration [199]. While a CEPM enables real-time optimization and measurement of the near-FTL, fc-pulse duration with CEP tagging, it unfortunately does not allow for simple quantitative analysis of the spectral dispersion of the pulse. Scanning methods using varying amounts of glass dispersion can qualitatively indicate higher order dispersion in the pulse, but quantitative, single-shot measurements of spectral phase are best left to FROG, SPIDER or SRSI measurements as previously described.

Third-Order Autocorrelation

Ionization effects can begin to affect solid or gaseous material starting around 10^{11} W/cm² and due to the high intensities achieved in laser-plasma interactions using TW-class lasers (10^{18} to 10^{21} W/cm²) a method for characterizing the rising and falling edges of the laser pulse at a high dynamic range is necessary. Third-order autocorrelation allows such a measurement with current systems achieving a dynamic range factor around 10^{13} on the picosecond to nanosecond timescales [200]. These timescales allow aspects of a TW laser chain to be diagnosed that could generate prepulses that cause pre-ionization of the target material, e.g., amplified spontaneous emission, reflections from air-glass interfaces, and uncorrected spectral phase affecting the picosecond rising edge [53], [201]. The pulse to be measured is split by a beamsplitter. One of the duplicates is sent to a delay stage while the other is upconverted to its second harmonic (2ω) in a nonlinear crystal. The delayed pulse and the 2ω pulse are then combined in another nonlinear crystal to produce the third harmonic (3ω) whose pulse energy as a function of delay is measured [202]. The delay stage is scanned over the desired temporal window. For a temporal electric field distribution given by $E(t) = E_0(t) \cos(\omega t)$, where $E_0(t)$ is the pulse's amplitude function, e.g., Gaussian, Sech², etc., **Eqn. 119** shows the autocorrelation signal $I_{AC}^{(3\omega)}(\tau)$.

$$I_{AC}^{(3\omega)}(\tau) = \frac{5}{8} \int E_0^6(t) dt \left[1 + \frac{9/2}{E_0^6(t) dt} \int (E_0^4(t) E_0^2(t - \tau) + E_0^2(t) E_0^4(t - \tau)) dt \right] \quad (119)$$

Appendix C – Lorentz Transformations

C.1 Vector Orientations in Oblique Planes

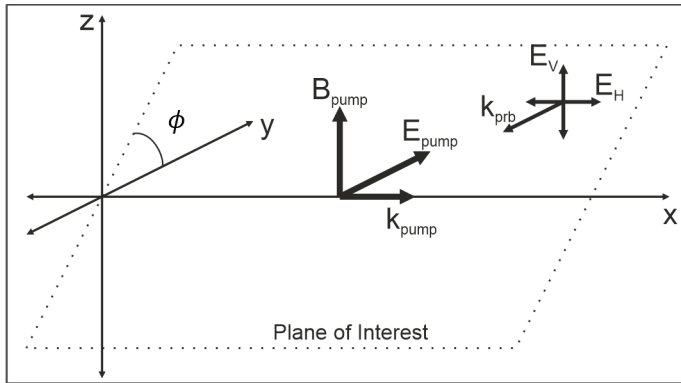


Figure 46: System geometry for showing the Lorentz transformed vector orientations of $\theta_{k_{prb}B_{pump}}$, $\theta_{E_HprbB_{pump}}$, and $\theta_{E_VprbB_{pump}}$ in a plane parallel to the x -axis and rotated by an angle ϕ relative to the y -axis.

By using the full Lorentz transformation without simplification to drift velocities constrained to the xy - or xz -planes, the vector orientations of \mathbf{k}_{prb} , \mathbf{B}_{pump} , \mathbf{E}_H and \mathbf{E}_V can be investigated in the full 3D Cartesian space for various drift velocities \mathbf{v} . Nonetheless, displaying the full 3D results is not possible with the current standard format for a dissertation, so only certain planes of interest have been plotted. Due to the system's cylindrical symmetry in terms of the plasma electrons' velocities relative to a symmetric pump pulse propagating along the x -axis, the planes of interest are here defined by the angle ϕ as measured from the y -axis in a counter-clockwise direction. This causes the drift velocity to separate into a transverse velocity \mathbf{v}_\perp and longitudinal velocity \mathbf{v}_x , with $v_\perp^2 = v_y^2 + v_z^2$ as depicted in **Fig.46**.

Although the system is cylindrical symmetric in terms of the pump's propagation along the x -axis, the use of a transverse probe breaks this symmetry when considering the orientation of vectors in each drift-frame of the plasma electrons. To demonstrate this, the Lorentz transformed angles of $\theta_{k_{prb}B_{pump}}$, $\theta_{E_HprbB_{pump}}$, and $\theta_{E_VprbB_{pump}}$ are plotted for $\phi = +45^\circ$ in **Fig. 47** and $\phi = -45^\circ$ in **Fig. 48**.

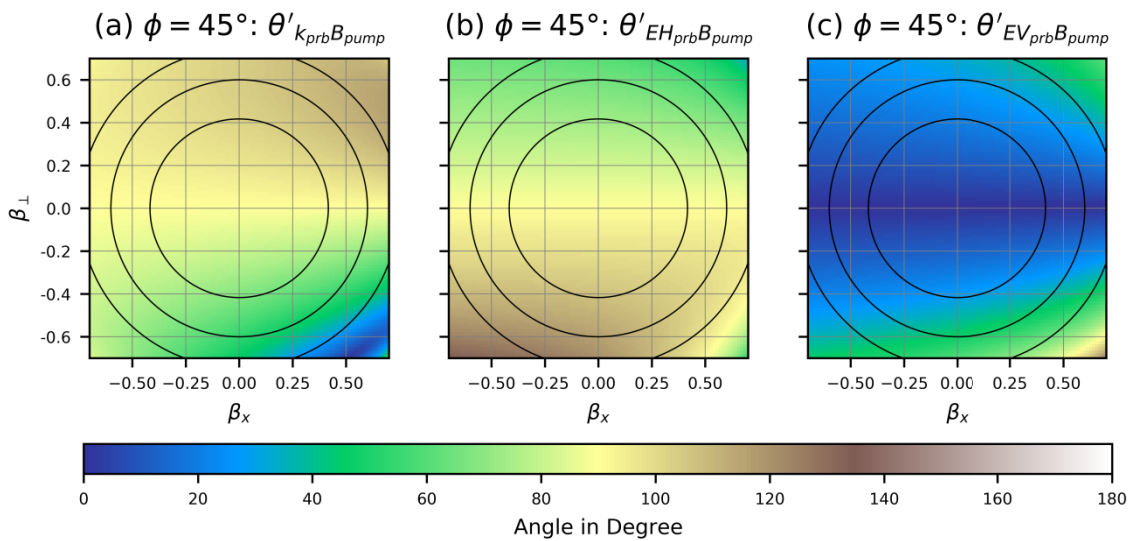


Figure 47: Resulting vector orientations of $\theta_{k_{prb}B_{pump}}$, $\theta_{E_HprbB_{pump}}$, and $\theta_{E_VprbB_{pump}}$ after Lorentz transformation to a frame traveling at (β_x, β_\perp) at $\phi = +45^\circ$ to the y -axis. Black circles represent Lorentz factors of 1.1, 1.25 and 1.5 from center moving outward.

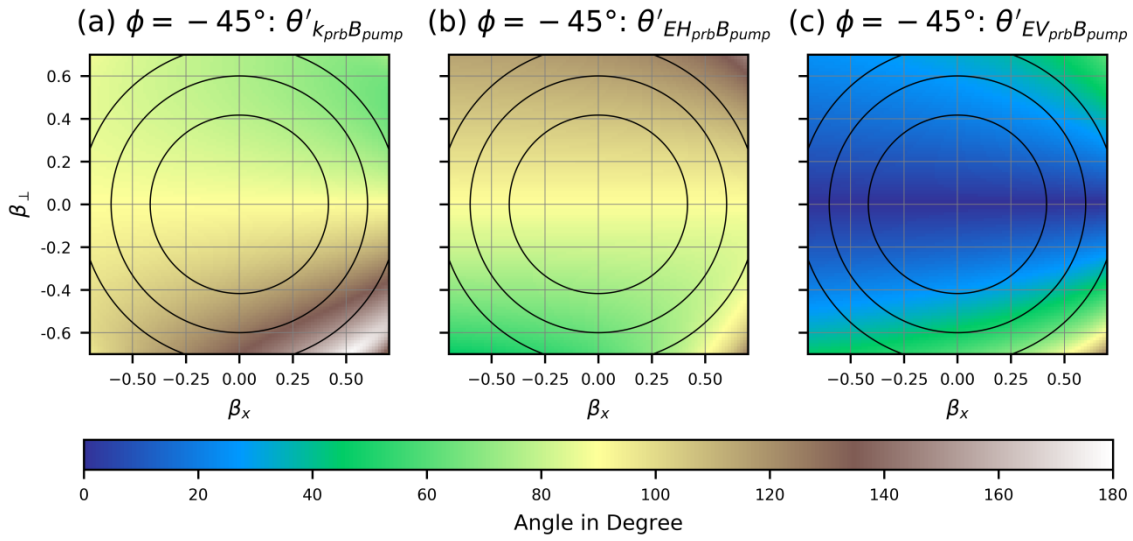


Figure 48: Resulting vector orientations of $\theta_{kprbB_{pump}}$, $\theta_{EHprbB_{pump}}$, and $\theta_{EVprbB_{pump}}$ after Lorentz transformation to a frame traveling at (β_x, β_\perp) at $\phi = -45^\circ$ to the y -axis. Black circles represent Lorentz factors of 1.1, 1.25 and 1.5 from center moving outward.

Appendix D – Cited Figures

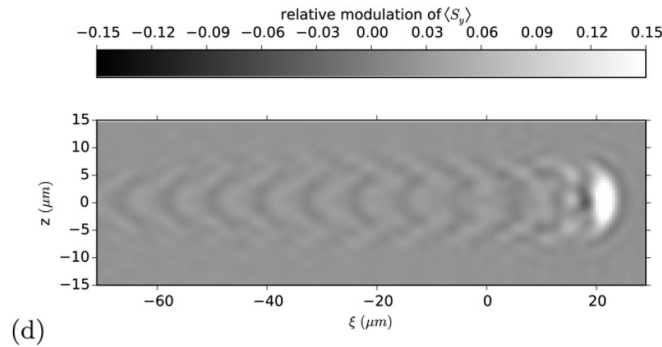


Figure 6. Snapshots of density distributions n/n_0 from the PIC simulation for (a) $z = 0$ and (b) $y = 0$ at the time when the probe passes through $y = 0$. We introduced the coordinate $\xi = x - ct$. (c) Map of the $y = 0$ cross-section of $n/(\gamma n_0)$. (d) artificial shadowgram obtained with probe pulse with duration $\tau_{pr} = 12$ fs, central wavelength $\lambda_{pr} = 750$ nm and object plane at $y_f = 0$ (see section 2.2). For the remainder of this paper we use the same pump-probe delay as in this figure and the same probe pulse characteristics unless otherwise specified. The color scale in all the following figures is the same as in panel (d).

Figure 6d from Siminos et al. [27]: Simulated shadowgram produced with a central wavelength of 750 nm to be compared with **Fig. 11** from [27] below showing simulated shadowgrams at 600 nm and 450 nm. A change in wavelength correlates with a strong change in intensity modulation at the front of the wakefield. Potential diffraction rings, i.e., the half-ring signal, are also visible in front of the wakefield.

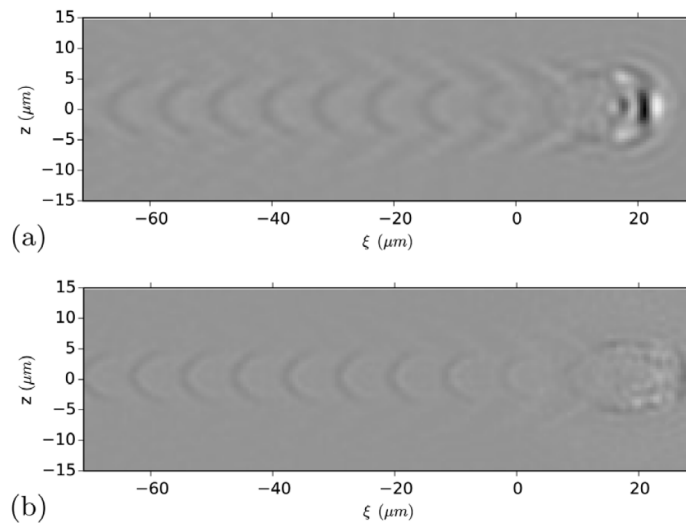


Figure 11. Effect of varying probe pulse wavelength, while keeping its duration constant. Both images have been obtained for the same pump-probe delay and the object plane position is fixed to $y_f = 0$. (a) $\lambda_{pr} = 0.6 \mu\text{m}$, (b) $\lambda_{pr} = 0.45 \mu\text{m}$. To be compared to figure 6(d) where $\lambda_{pr} = 0.75 \mu\text{m}$.

Figure 11 from Siminos et al. [27]: Simulated shadowgrams produced with a central wavelength of 600 nm (a) and 450 nm (b), to be compared with **Fig. 6d** from [27] above showing simulated shadowgrams at 750 nm.

A change in probe wavelength correlates with a strong change in intensity modulation at the front of the wakefield and the lack of a strong signal in the 450 nm case correlates with the simple theory of spectral dependence described in **Fig. 29** of this work, see **Chapter 7**. Potential diffraction rings, i.e., the half-ring signal, are also visible in front of the wakefield, primarily in the 600 nm case.

Appendix D – Cited Figures

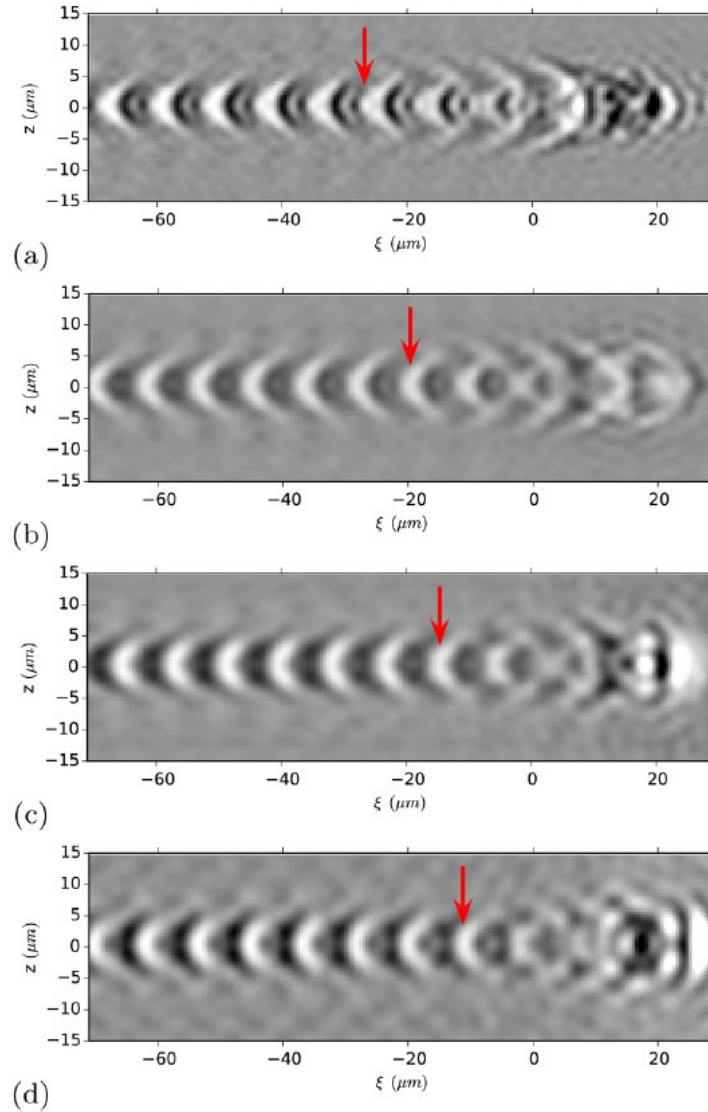


Figure 14. Effect of introducing a bandpass filter after the $\tau_{pr} = 30$ fs chirped pulse of figure 13(b) has propagated through the wake. The filters allow transmission of wavelengths (a) $0.6 \pm 0.01 \mu\text{m}$, (b) $0.7 \pm 0.01 \mu\text{m}$, (c) $0.8 \pm 0.01 \mu\text{m}$, (d) $0.9 \pm 0.01 \mu\text{m}$. The red arrow indicates the position of the intensity maximum that we track in order to deduce the phase velocity of the wake.

Figure 14 from Siminos et al. [27]: Further examples of a change in the visualization of the front of the wakefield with varying central wavelength of the probe beam. Can be compared to **Figs. 6d** and **11** of [27]. Potential diffraction rings, i.e., the half-ring motion, are also visible in front of the wakefields. Red arrows were used in the cited reference to indicate motion of the wakefield with temporal filtering due to the intended temporal chirped of the probe beam.

Appendix D – Cited Figures

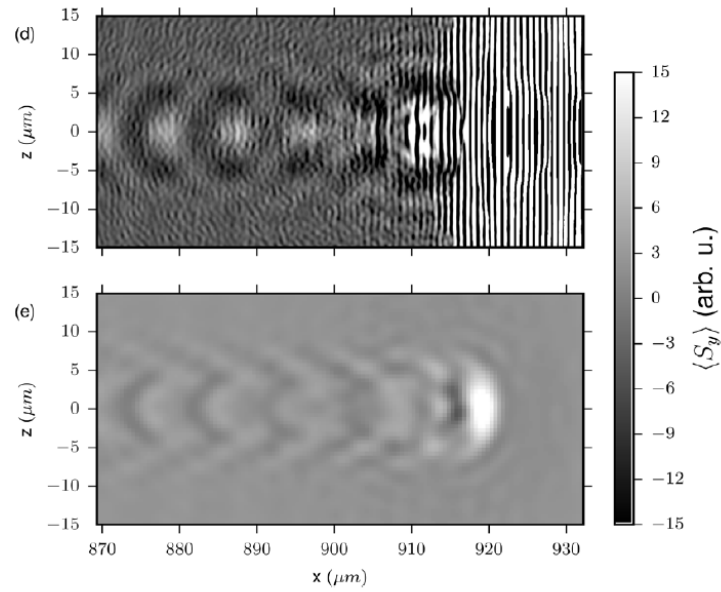


Figure 2. Probe pulse propagation across the wake. Panels (a)–(c): three snapshots from the PIC simulation showing the probe electric field envelope squared $|\mathcal{E}_x^{\text{probe}}|^2$ and contours of the plasma density corresponding to $n = 2n_0$. (d) Image obtained by recording the time-integrated Poynting flux $\langle S_y \rangle$ passing through the plane $y_S = -20 \mu\text{m}$ (e) Time-integrated Poynting flux $\langle S_y \rangle$ after adjusting for focusing optics, assuming the object plane is at $y_o = 0$.

Figure 2d and 2e from Siminos et al. [27]: Faint diffraction rings, i.e., the half-ring signal, can be seen at the front of the wakefield.

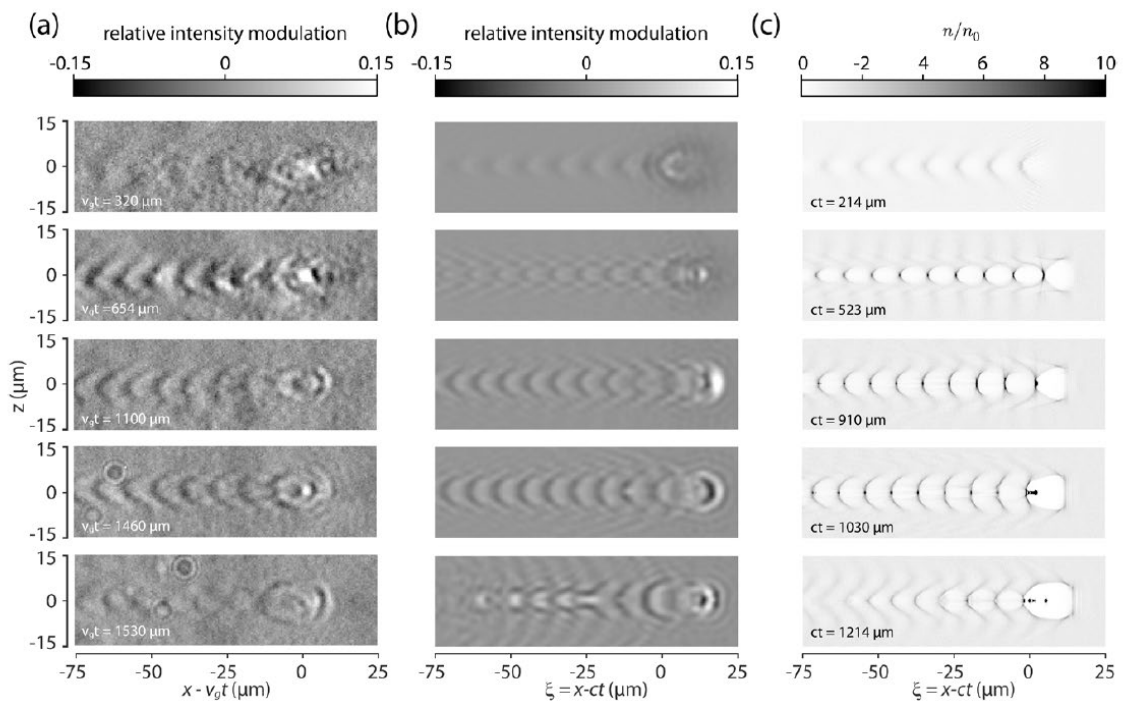


Figure 8. (a) Experimental shadowgrams (b) computed shadowgrams, (c) density cross-sections from the simulation.

Figure 8 from Siminos et al. [27]: Appearance of the half-ring signal at the front of the wakefield first becomes visible after $\sim 900 \mu\text{m}$ propagation of the pump laser in plasma (lowest three mini-plots of subplots a and b) due to the necessary self-steepening of the pump pulse as described in Chapter 7.

Appendix D – Cited Figures

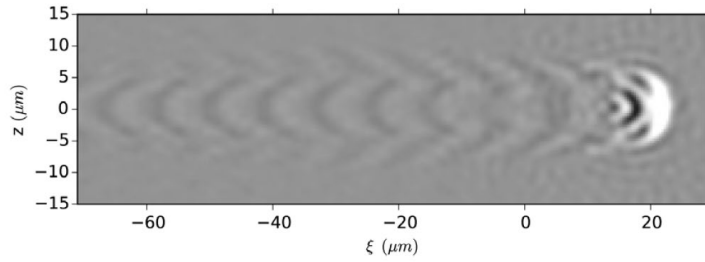


Figure 12. Same as figure 6(d) but with $NA = 0.35$.

Figure 12 from Siminos et al. [27]: A decrease in the visibility of the diffraction rings, i.e., half-ring signal, is seen for an increase in the optical system's NA as expected from coherent imaging theory

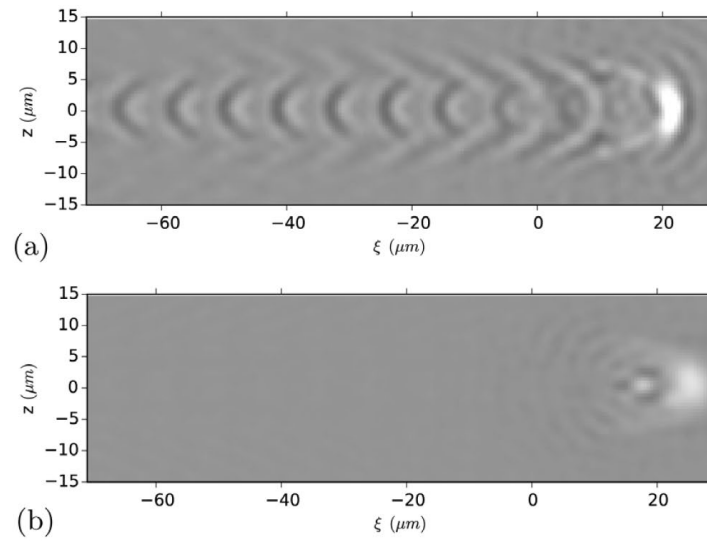


Figure 13. Effect of varying the probe pulse duration through the introduction of a linear chirp. (a) Fourier limited probe pulse duration $\tau_{pr} = 4.4$ fs, (b) $\tau_{pr} = 30$ fs. To be compared to figure 6(d) where $\tau_{pr} = 12$ fs. All images have been obtained for the same delay and the object plane position is fixed to $y_o = 0$.

Figure 13 from Siminos et al. [27]: An improvement in the half-ring signal's visibility is seen for a decrease in the probe beam's pulse duration as seen in subplot (a), compared to a drastic decrease in visibility for longer pulse duration as seen in subplot (b). Temporal averaging of the shadowgram is so extreme in (b), even the train of plasma oscillations behind the wakefield's head is no longer visible.

Appendix D – Cited Figures

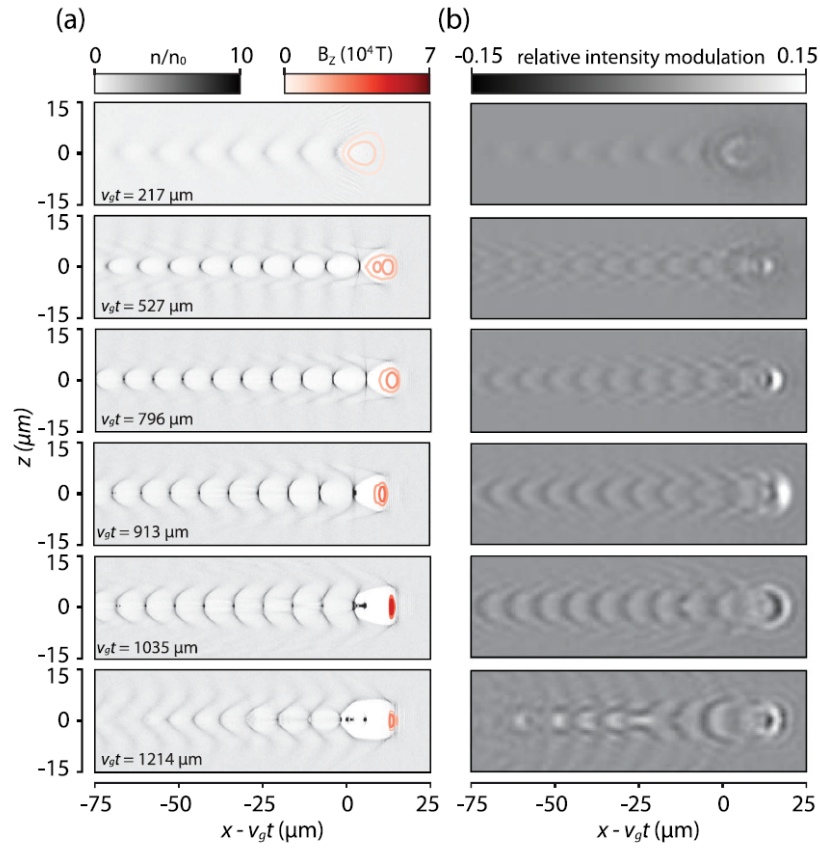


FIG. 3 (color online). (a) Electron density maps (gray) from the simulations at various positions and contours of the envelope of pump magnetic field B_z (red or solid lines) corresponding to 50% and 75% of the peak. (b) Shadowgrams simulated from the images in Fig. 3(a).

Figure 3 from Sävert et al. [26]: Similar to **Fig. 8** from [27]; however, with the addition of the contour lines of the pump's magnetic field, the correlation between the onset of the pump's self-steepening and the appearance of the half-ring signal can be observed. This onset begins around a propagation distance of $913 \mu\text{m}$.

9. References

- [1] A. P. Chernyaev and S. M. Varzar, “Particle accelerators in modern world,” *Phys. At. Nucl.*, vol. 77, no. 10, pp. 1203–1215, 2014.
- [2] V. Shiltsev, “A phenomenological cost model for high energy particle accelerators,” *J. Instrum.*, vol. 9, no. 7, 2014.
- [3] M. Florio, A. Bastianin, and P. Castelnovo, “The socio-economic impact of a breakthrough in the particle accelerators’ technology: A research agenda,” *Nucl. Instruments Methods Phys. Res.*, vol. 909, no. January, pp. 21–26, 2018.
- [4] L. Evans and P. Bryant, “LHC Machine,” *J. Instrum.*, vol. 3, no. 8, 2008.
- [5] “SLAC Website.” <https://www6.slac.stanford.edu/> (accessed Sep. 27, 2021).
- [6] “KEK Website.” <https://www.kek.jp/en/> (accessed Sep. 27, 2021).
- [7] A. J. Gonsalves *et al.*, “Petawatt Laser Guiding and Electron Beam Acceleration to 8 GeV in a Laser-Heated Capillary Discharge Waveguide,” *Phys. Rev. Lett.*, vol. 122, no. 8, 2019.
- [8] M. Litos *et al.*, “High-efficiency acceleration of an electron beam in a plasma wakefield accelerator,” *Nature*, vol. 515, pp. 92–95, 2014.
- [9] E. Adli *et al.*, “Acceleration of electrons in the plasma wakefield of a proton bunch,” *Nature*, vol. 561, pp. 363–367, 2018.
- [10] T. Kurz *et al.*, “Demonstration of a compact plasma accelerator powered by laser-accelerated electron beams,” *Nat. Commun.*, vol. 12, pp. 1–9, 2021.
- [11] F. Albert *et al.*, “2020 Roadmap on Plasma Accelerators,” *New J. Phys.*, vol. 23, no. 3, 2021.
- [12] T. Tajima and J. M. Dawson, “Laser Electron Accelerator,” *Phys. Rev. Lett.*, vol. 43, no. 4, pp. 267–270, 1979.
- [13] P. Chen, J. M. Dawson, R. W. Huff, and T. Katsouleas, “Acceleration of electrons by the interaction of a bunched electron beam with a plasma,” *Phys. Rev. Lett.*, vol. 54, no. 7, pp. 693–696, 1985.
- [14] P. Chen, J. J. Su, J. M. Dawson, K. L. F. Bane, and P. B. Wilson, “Energy Transfer in the Plasma Wake-Field Accelerator,” *Phys. Rev. Lett.*, vol. 56, no. 12, pp. 1252–1255, 1986.
- [15] F. Grüner *et al.*, “Design considerations for table-top, laser-based VUV and X-ray free electron lasers,” *Appl. Phys. B Lasers Opt.*, vol. 86, no. 3, pp. 431–435, 2007.
- [16] K. Nakajima, “Towards a table-top free-electron laser,” *Nat. Phys.*, vol. 4, no. February, pp. 92–93, 2008.
- [17] A. R. Maier, A. Meseck, S. Reiche, C. B. Schroeder, T. Seggebrock, and F. Grüner, “Demonstration scheme for a laser-plasma-driven free-electron laser,” *Phys. Rev. X*, vol. 2, no. 3, pp. 1–7, 2012.
- [18] J. M. Cole *et al.*, “Tomography of human trabecular bone with a laser-wakefield driven x-ray source,” *Plasma Phys. Control. Fusion*, vol. 58, 2016.
- [19] K. W. D. Ledingham, P. R. Bolton, N. Shikazono, and C. M. C. Ma, “Towards laser driven hadron cancer radiotherapy: A review of progress,” *Appl. Sci.*, vol. 4, no. 3, pp. 402–443, 2014.
- [20] S. Steinke *et al.*, “Multistage coupling of independent laser-plasma accelerators,” *Nature*, vol. 000, pp. 190–193, 2016.
- [21] P. Forck, “Lecture Notes on Beam Instrumentation and Diagnostics,” *Joint University Accelerator School*. pp. 0–152, 2019.
- [22] N. H. Matlis *et al.*, “Snapshots of laser wakefields,” *Nat. Phys.*, vol. 2, no. 11, pp. 749–753, 2006.
- [23] M. C. Kaluza *et al.*, “Measurement of Magnetic-Field Structures in a Laser-Wakefield Accelerator,” *Phys. Rev. Lett.*, vol. 105, no. 11, 2010.
- [24] A. Buck *et al.*, “Real-time observation of laser-driven electron acceleration,” *Nat. Phys.*, vol. 7, no. 7, pp. 543–548, 2011.
- [25] M. B. Schwab *et al.*, “Few-cycle optical probe-pulse for investigation of relativistic laser-plasma interactions,” *Appl. Phys. Lett.*, vol. 103, no. 19, pp. 1–5, 2013.
- [26] A. Sävert *et al.*, “Direct Observation of the Injection Dynamics of a Laser Wakefield Accelerator Using Few-Femtosecond Shadowgraphy,” *Phys. Rev. Lett.*, vol. 115, no. 5, pp. 1–5, 2015.
- [27] E. Siminos, S. Skupin, A. Sävert, J. M. Cole, S. P. D. Mangles, and M. C. Kaluza, “Modeling

9. References

- ultrafast shadowgraphy in laser-plasma interaction experiments,” *Plasma Phys. Control. Fusion*, vol. 58, no. 6, 2016.
- [28] C. J. Zhang *et al.*, “Femtosecond Probing of Plasma Wakefields and Observation of the Plasma Wake Reversal Using a Relativistic Electron Bunch,” *Phys. Rev. Lett.*, vol. 119, no. 6, pp. 1–6, 2017.
- [29] M. F. Gilljohann *et al.*, “Direct Observation of Plasma Waves and Dynamics Induced by Laser-Accelerated Electron Beams,” *Phys. Rev. X*, vol. 9, no. 1, 2019.
- [30] K. Nakagawa *et al.*, “Sequentially timed all-optical mapping photography (STAMP) utilizing spectral filtering,” *Nat. Photonics*, vol. 23, no. 23, 2015.
- [31] J. P. Geindre *et al.*, “Frequency-domain interferometer for measuring the phase and amplitude of a femtosecond pulse probing a laser-produced plasma,” *Opt. Lett.*, vol. 19, no. 23, pp. 1997–9, 1994.
- [32] J.-P. Geindre, P. Audebert, S. Rebibo, and J.-C. Gauthier, “Single-shot spectral interferometry with chirped pulses,” *Opt. Lett.*, vol. 26, no. 20, 2001.
- [33] E. Esarey, C. B. Schroeder, and W. P. Leemans, “Physics of laser-driven plasma-based electron accelerators,” *Rev. Mod. Phys.*, vol. 81, no. 3, pp. 1229–1285, 2009.
- [34] S. Akturk, X. Gu, P. Bowlan, and R. Trebino, “Spatio-temporal couplings in ultrashort laser pulses,” *J. Opt.*, vol. 12, no. 9, 2010.
- [35] R. Weingartner *et al.*, “Ultralow emittance electron beams from a laser-wakefield accelerator,” *Phys. Rev. Spec. Top. - Accel. Beams*, vol. 15, no. 11, pp. 1–5, 2012.
- [36] S. V. Bulanov, T. Z. Esirkepov, N. M. Naumova, F. Pegoraro, and V. A. Vshivkov, “Solitonlike Electromagnetic Waves behind a Superintense Laser Pulse in a Plasma,” *Phys. Rev. Lett.*, vol. 82, no. 17, pp. 3440–3443, 1999.
- [37] D. A. Gurnett and A. Bhattacharjee, *Introduction to Plasma Physics: with Space, Laboratory and Astrophysical Applications*, 2nd ed. Cambridge University Press, 2017.
- [38] F. F. Chen, *Introduction to Plasma Physics and Controlled Fusion*, 3rd ed. Springer Verlag, 2018.
- [39] J. A. Bittencourt, *Fundamentals of Plasma Physics*, 3rd ed. Springer Verlag, 2004.
- [40] F. V. Hartemann, *High-Field Electrodynamics*. CRC Press, 2002.
- [41] I. H. Hutchinson, *Principles of Plasma Diagnostics*, 2nd ed. Cambridge University Press, 2002.
- [42] J. A. Stamper and B. H. Ripin, “Faraday-rotation measurements of megagauss magnetic fields in laser-produced plasmas,” *Phys. Rev. Lett.*, vol. 34, no. 3, pp. 138–141, 1975.
- [43] S. A. Colgate, H. Li, and V. Pariev, “The origin of the magnetic fields of the universe: The plasma astrophysics of the free energy of the universe,” *Phys. Plasmas*, vol. 8, no. 5, pp. 2425–2431, 2001.
- [44] G. B. Taylor and R. A. Perley, “Magnetic Fields in the Hydra A Cluster,” *Astrophys. J.*, vol. 416, pp. 554–562, 1993.
- [45] R. W. Boyd, *Nonlinear Optics*, 2nd ed. Academic Press, 2003.
- [46] E. Hecht, *Optics*, 4th ed. Addison Wesley, 2002.
- [47] C. Rulliere, *Femtosecond Laser Pulses*, 2nd ed. Springer, 2005.
- [48] A. M. Weiner, *Ultrafast Optics*. John Wiley & Sons, Inc., 2009.
- [49] J. C. Diels and W. Rudolph, *Ultrashort Laser Pulse Phenomena*, 2nd ed. Academic Press, 2006.
- [50] J. W. Goodman, *Introduction to Fourier Optics*, 2nd ed. The McGraw-Hill Companies, Inc., 1996.
- [51] G. G. Paulus *et al.*, “Absolute-phase phenomena in photoionization with few-cycle laser pulses,” *Nature*, vol. 414, pp. 182–184, 2001.
- [52] T. Rathje *et al.*, “Review of attosecond resolved measurement and control via carrier-envelope phase tagging with above-threshold ionization,” *J. Phys. B At. Mol. Opt. Phys.*, vol. 45, no. 7, 2012.
- [53] S. Keppeler *et al.*, “The generation of amplified spontaneous emission in high-power CPA laser systems,” *Laser Photonics Rev.*, vol. 10, no. 2, pp. 264–277, 2016.
- [54] M. Hornung *et al.*, “High-intensity, high-contrast laser pulses generated from the fully diode-pumped Yb:glass laser system POLARIS,” *Opt. Lett.*, vol. 38, no. 5, pp. 718–720, 2013.

9. References

- [55] D. N. Payne and W. A. Gambling, “Zero Material Dispersion in Optical Fibres,” *Electron. Lett.*, vol. 11, no. 8, 1975.
- [56] I. H. Malitson, “Interspecimen Comparison of Refractive Index of Fused Silica,” *J. Opt. Soc. Am.*, vol. 55, no. 10, 1965.
- [57] G. S. Settles, *Schlieren and Shadowgraph Techniques: Visualizing Phenomena in Transparent Media*. Heidelberg: Springer, 2001.
- [58] P. K. Panigrahi and K. Muralidhar, *Schlieren and Shadowgraph Methods in Heat and Mass Transfer*. New York: Springer, 2012.
- [59] R. W. Lewis, R. E. Teets, J. A. Sell, and T. A. Seder, “Gas By Quantitative Shadowgraphy,” vol. 26, no. 17, pp. 3695–3704, 1987.
- [60] G. De Izarra and C. De Izarra, “Quantitative shadowgraphy made easy,” *Eur. J. Phys.*, vol. 33, no. 6, pp. 1821–1842, 2012.
- [61] A. Gopal, S. Minardi, and M. Tatarakis, “Under-Critical Laser Plasmas,” vol. 32, no. 10, pp. 1238–1240, 2007.
- [62] M. F. Kasim *et al.*, “Quantitative shadowgraphy and proton radiography for large intensity modulations,” *Phys. Rev. E*, vol. 95, no. 2, pp. 1–8, 2017.
- [63] A. Zangwill, *Modern Electrodynamics*. Cambridge University Press, 2013.
- [64] R. B. Palmer, “A LASER-DRIVEN GRATINGS LINAC,” *Part. Accel.*, vol. 11, pp. 81–90, 1980.
- [65] L. C. Steinhauer and W. D. Kimura, “A new approach for laser particle acceleration in vacuum,” *J. Appl. Phys.*, vol. 72, no. 8, pp. 3237–3245, 1992.
- [66] J. H. Yang, R. S. Craxton, and M. G. Haines, “Explicit general solutions to relativistic electron dynamics in plane-wave electromagnetic fields and simulations of ponderomotive acceleration,” *Plasma Phys. Control. Fusion*, vol. 53, no. 12, pp. 1–25, 2011.
- [67] B. Quesnel and P. Mora, “Theory and simulation of the interaction of ultraintense laser pulses with electrons in vacuum,” *Phys. Rev. E*, vol. 58, no. 3, pp. 3719–3732, 1998.
- [68] C. E. Clayton *et al.*, “Ultrahigh-Gradient Acceleration of Injected Electrons by Laser-Excited Relativistic Electron Plasma Waves,” *Phys. Rev. Lett.*, vol. 70, no. 1, 1993.
- [69] A. Modena *et al.*, “Electron acceleration from the breaking of relativistic plasma waves,” *Nature*, vol. 377, pp. 606–608, 1995.
- [70] V. Malka, “Charged particle source produced by laser–plasma interaction in the relativistic regime,” *Laser Part. Beams*, vol. 20, pp. 217–221, 2002.
- [71] C. Gahn *et al.*, “Multi-MeV Electron Beam Generation by Direct Laser Acceleration in High-Density Plasma Channels,” *Phys. Rev. Lett.*, vol. 83, no. 23, pp. 4772–4775, 1999.
- [72] J. Faure *et al.*, “A laser-plasma accelerator producing monoenergetic electron beams,” *Nature*, vol. 431, pp. 541–544, 2004.
- [73] C. G. R. Geddes *et al.*, “High-quality electron beams from a laser wakefield accelerator using plasma-channel guiding,” *Nature*, vol. 431, no. September, pp. 538–541, 2004.
- [74] S. P. D. Mangles *et al.*, “Monoenergetic beams of relativistic electrons from intense laser – plasma interactions,” *Nature*, vol. 431, no. September, pp. 535–538, 2004.
- [75] E. Esarey, P. Sprangle, S. Member, J. Krall, and A. Ting, “Overview of Plasma-Based Accelerator Concepts,” *IEEE Trans. Plasma Sci.*, vol. 24, no. 2, pp. 252–288, 1996.
- [76] J. Wenz and S. Karsch, “Physics of Laser-Wakefield Accelerators (LWFA),” *Proc. 2019 Cern.*, 2020.
- [77] W. B. Mori, “The physics of the nonlinear optics of plasmas at relativistic intensities for short-pulse lasers,” *IEEE J. Quantum Electron.*, vol. 33, no. 11, pp. 1942–1953, 1997.
- [78] P. Sprangle, E. Esarey, and A. Ting, “Nonlinear Theory of Intense Laser-Plasma Interactions,” *Phys. Rev. Lett.*, vol. 64, no. 17, pp. 2011–2014, 1990.
- [79] B. E. A. Saleh and M. C. Teich, *Fundamentals of Photonics*. John Wiley & Sons, Inc., 1991.
- [80] S. Kneip *et al.*, “Near-GeV acceleration of electrons by a nonlinear plasma wave driven by a self-guided laser pulse,” *Phys. Rev. Lett.*, vol. 103, no. 3, 2009.
- [81] J. Faure *et al.*, “Observation of laser-pulse shortening in nonlinear plasma waves,” *Phys. Rev. Lett.*, vol. 95, no. 20, pp. 1–4, 2005.
- [82] J. Schreiber *et al.*, “Complete temporal characterization of asymmetric pulse compression in a

9. References

- laser wakefield,” *Phys. Rev. Lett.*, vol. 105, no. 23, pp. 1–4, 2010.
- [83] X. L. Chen and R. N. Sudan, “Two-dimensional self-focusing of short intense laser pulse in underdense plasma,” *Phys. Fluids B*, vol. 5, no. 4, pp. 1336–1348, 1993.
- [84] P. Mora and T. M. Antonsen, “Kinetic modeling of intense, short laser pulses propagating in tenuous plasmas,” *Phys. Plasmas*, vol. 4, no. 1, pp. 217–229, 1997.
- [85] W. Lu, C. Huang, M. Zhou, W. B. Mori, and T. Katsouleas, “Nonlinear theory for relativistic plasma wakefields in the blowout regime,” *Phys. Rev. Lett.*, vol. 96, no. 16, pp. 1–4, 2006.
- [86] W. Lu, C. Huang, M. M. Zhou, W. B. Mori, and T. Katsouleas, “Limits of linear plasma wakefield theory for electron or positron beams,” *Phys. Plasmas*, vol. 12, no. 6, pp. 1–8, 2005.
- [87] W. Lu *et al.*, “A nonlinear theory for multidimensional relativistic plasma wave wakefields,” *Phys. Plasmas*, vol. 13, no. 5, pp. 1–13, 2006.
- [88] E. Esarey, P. Sprangle, J. Krall, and A. Ting, “Self-focusing and guiding of short laser pulses in ionizing gases and plasmas,” *IEEE J. Quantum Electron.*, vol. 33, no. 11, pp. 1879–1914, 1997.
- [89] S. Gordienko and A. Pukhov, “Scalings for ultrarelativistic laser plasmas and quasimonoenergetic electrons,” *Phys. Plasmas*, vol. 12, no. 4, pp. 1–11, 2005.
- [90] W. Lu *et al.*, “Generating multi-GeV electron bunches using single stage laser wakefield acceleration in a 3D nonlinear regime,” *Phys. Rev. Spec. Top. - Accel. Beams*, vol. 10, no. 6, pp. 1–12, 2007.
- [91] H. Ding *et al.*, “Nonlinear plasma wavelength scalings in a laser wakefield accelerator,” *Phys. Rev. E*, vol. 101, no. 2, pp. 1–10, 2020.
- [92] S. V. Bulanov, F. Pegoraro, A. M. Pukhov, and A. S. Sakharov, “Transverse-Wake Wave Breaking,” *Phys. Rev. Lett.*, vol. 78, no. 22, pp. 4205–4208, 1997.
- [93] S. Kalmykov, S. A. Yi, V. Khudik, and G. Shvets, “Electron self-injection and trapping into an evolving plasma bubble,” *Phys. Rev. Lett.*, vol. 103, no. 13, pp. 1–4, 2009.
- [94] I. Kostyukov, E. Nerush, A. Pukhov, and V. Seredov, “Electron self-Injection in multidimensional relativistic-plasma wake fields,” *Phys. Rev. Lett.*, vol. 103, no. 17, pp. 1–4, 2009.
- [95] S. Corde *et al.*, “Observation of longitudinal and transverse self-injections in laser-plasma accelerators,” *Nat. Commun.*, vol. 4, pp. 1–7, 2013.
- [96] S. P. D. Mangles *et al.*, “Self-injection threshold in self-guided laser wakefield accelerators,” *Phys. Rev. Spec. Top. - Accel. Beams*, vol. 15, no. 1, pp. 2–7, 2012.
- [97] J. Osterhoff *et al.*, “Generation of stable, low-divergence electron beams by laser-wakefield acceleration in a steady-state-flow gas cell,” *Phys. Rev. Lett.*, vol. 101, no. 8, pp. 1–4, 2008.
- [98] S. Bulanov, N. Naumova, F. Pegoraro, and J. Sakai, “Particle injection into the wave acceleration phase due to nonlinear wake wave breaking,” *Phys. Rev. E*, vol. 58, no. 5, pp. 5257–5260, 1998.
- [99] C. G. R. Geddes *et al.*, “Plasma-density-gradient injection of low absolute-momentum-spread electron bunches,” *Phys. Rev. Lett.*, vol. 100, no. 21, pp. 1–4, 2008.
- [100] J. Faure, C. Rechatin, O. Lundh, L. Ammoura, and V. Malka, “Injection and acceleration of quasimonoenergetic relativistic electron beams using density gradients at the edges of a plasma channel,” *Phys. Plasmas*, vol. 17, no. 8, 2010.
- [101] A. J. Gonsalves *et al.*, “Tunable laser plasma accelerator based on longitudinal density tailoring,” *Nat. Phys.*, vol. 7, no. 11, pp. 862–866, 2011.
- [102] H. Suk, N. Barov, J. B. Rosenzweig, and E. Esarey, “Plasma electron trapping and acceleration in a plasma wake field using a density transition,” *Phys. Rev. Lett.*, vol. 86, no. 6, pp. 1011–1014, 2001.
- [103] A. V. Brantov, T. Z. Esirkepov, M. Kando, H. Kotaki, V. Y. Bychenkov, and S. V. Bulanov, “Controlled electron injection into the wake wave using plasma density inhomogeneity,” *Phys. Plasmas*, vol. 15, no. 7, 2008.
- [104] K. Schmid *et al.*, “Density-transition based electron injector for laser driven wakefield accelerators,” *Phys. Rev. Spec. Top. - Accel. Beams*, vol. 13, no. 9, pp. 1–5, 2010.
- [105] A. Buck *et al.*, “Shock-front injector for high-quality laser-plasma acceleration,” *Phys. Rev.*

9. References

- Lett.*, vol. 110, no. 18, pp. 1–5, 2013.
- [106] D. Umstadter, J. K. Kim, and E. Dodd, “Laser injection of ultrashort electron pulses into wakefield plasma waves,” *Phys. Rev. Lett.*, vol. 76, no. 12, pp. 2073–2076, 1996.
- [107] G. Fubiani, E. Esarey, C. B. Schroeder, and W. P. Leemans, “Beat wave injection of electrons into plasma waves using two interfering laser pulses,” *Phys. Rev. E - Stat. Physics, Plasmas, Fluids, Relat. Interdiscip. Top.*, vol. 70, no. 1, pp. 1–12, 2004.
- [108] C. Rechatin, J. Faure, A. Lifschitz, V. Malka, and E. Lefebvre, “Plasma wake inhibition at the collision of two laser pulses in an underdense plasma,” *Phys. Plasmas*, vol. 14, no. 6, 2007.
- [109] X. Davoine, E. Lefebvre, J. Faure, C. Rechatin, A. Lifschitz, and V. Malka, “Simulation of quasimonoenergetic electron beams produced by colliding pulse wakefield acceleration,” *Phys. Plasmas*, vol. 15, no. 11, 2008.
- [110] J. Faure, C. Rechatin, A. Norlin, A. Lifschitz, Y. Glinec, and V. Malka, “Controlled injection and acceleration of electrons in plasma wakefields by colliding laser pulses,” *Nature*, vol. 444, no. 7120, pp. 737–9, 2006.
- [111] J. Wenz *et al.*, “Dual-energy electron beams from a compact laser-driven accelerator,” *Nat. Photonics*, vol. 13, no. April, pp. 263–270, 2019.
- [112] R. Jung, “Ph.D. Thesis: Laser-plasma interaction with ultra-short laser pulses,” 2007.
- [113] A. Pak, K. A. Marsh, S. F. Martins, W. Lu, W. B. Mori, and C. Joshi, “Injection and trapping of tunnel-ionized electrons into laser-produced wakes,” *Phys. Rev. Lett.*, vol. 104, no. 2, pp. 1–4, 2010.
- [114] M. Chen, E. Esarey, C. B. Schroeder, C. G. R. Geddes, and W. P. Leemans, “Theory of ionization-induced trapping in laser-plasma accelerators,” *Phys. Plasmas*, vol. 19, no. 3, 2012.
- [115] C. McGuffey *et al.*, “Ionization induced trapping in a laser wakefield accelerator,” *Phys. Rev. Lett.*, vol. 104, no. 2, pp. 1–4, 2010.
- [116] B. B. Pollock *et al.*, “Demonstration of a narrow energy spread, ~ 0.5 GeV electron beam from a two-stage laser wakefield accelerator,” *Phys. Rev. Lett.*, vol. 107, no. 4, pp. 1–4, 2011.
- [117] J. P. Verboncoeur, “Particle simulation of plasmas: Review and advances,” *Plasma Phys. Control. Fusion*, vol. 47, pp. 231–260, 2005.
- [118] T. D. Arber *et al.*, “Contemporary particle-in-cell approach to laser-plasma modelling,” *Plasma Phys. Control. Fusion*, vol. 57, no. 11, 2015.
- [119] A. Marcowith, G. Ferrand, M. Grech, Z. Meliani, I. Plotnikov, and R. Walder, *Multi-scale simulations of particle acceleration in astrophysical systems*, vol. 6, no. 1. Springer International Publishing, 2020.
- [120] J.P. Berenger, “A Perfectly Matched Layer for the Absorption of Electromagnetic Waves,” *Journal of Computational Physics*, vol. 114, pp. 185–200, 1994.
- [121] E. Michel *et al.*, “Accurate modeling of laser-plasma accelerators with particle-in-cell codes,” *AIP Conf. Proc.*, vol. 877, pp. 213–219, 2006.
- [122] E. Cormier-Michel, B. A. Shadwick, C. G. R. Geddes, E. Esarey, C. B. Schroeder, and W. P. Leemans, “Unphysical kinetic effects in particle-in-cell modeling of laser wakefield accelerators,” *Phys. Rev. E - Stat. Nonlinear, Soft Matter Phys.*, vol. 78, no. 1, pp. 1–17, 2008.
- [123] K. S. Yee, “Numerical Solution of Initial Boundary Value Problems Involving Maxwell’s Equations in Isotropic Media,” *IEEE Trans. Antennas Propag.*, vol. 14, no. 3, pp. 302–307, 1966.
- [124] J. P. Boris, “No Title,” *Proc. 4th Conf. Numer. Simul. Plasmas*, pp. 3–67, 1970.
- [125] H. Qin, S. Zhang, J. Xiao, J. Liu, Y. Sun, and W. M. Tang, “Why is Boris algorithm so good?,” *Phys. Plasmas*, vol. 20, no. 8, 2013.
- [126] T. Z. Esirkepov, “Exact charge conservation scheme for Particle-in-Cell simulation with an arbitrary form-factor,” *Comput. Phys. Commun.*, vol. 135, no. 2, pp. 144–153, 2001.
- [127] S. F. Martins, R. A. Fonseca, W. Lu, W. B. Mori, and L. O. Silva, “Exploring laser-wakefield-accelerator regimes for near-term lasers using particle-in-cell simulation in Lorentz-boosted frames,” *Nat. Phys.*, vol. 6, no. 4, pp. 311–316, 2010.
- [128] M. E. Jones, D. S. Lemons, R. J. Mason, V. A. Thomas, and D. Winske, “A grid-based coulomb collision model for PIC codes,” *J. Comput. Phys.*, vol. 123, no. 1, pp. 169–181, 1996.
- [129] T. Takizuka and H. Abe, “A binary collision model for plasma simulation with a particle

9. References

- code,” *J. Comput. Phys.*, vol. 25, no. 3, pp. 205–219, 1977.
- [130] C. P. Ridgers *et al.*, “Modelling gamma-ray photon emission and pair production in high-intensity laser-matter interactions,” *J. Comput. Phys.*, vol. 260, pp. 273–285, 2014.
- [131] L. V. Keldysh, “Ionization in the field of a strong electromagnetic wave,” *Sov. Phys. JETP*, vol. 20, no. 5, pp. 1307–1314, 1965.
- [132] N. B. Delone and V. P. Krainov, *Multiphoton Processes in Atoms*, 2nd ed. Springer-Verlag Berlin Heidelberg, 2000.
- [133] M. V. Ammosov, N. B. Delone, and V. P. Krainov, “Tunnel ionization of complex atoms and of atomic ions in an alternating electromagnetic field,” *Sov. Phys. JETP*, vol. 64, no. December, pp. 1191–1194, 1986.
- [134] J. Posthumus, M. Thompson, L. Frasinski, and K. Codling, “Molecular dissociative ionisation using a classical over-the-barrier approach,” in *7th International Conference on Multiphoton Processes*, 1996, pp. 298–307.
- [135] D. Strickland and G. Mourou, “Compression of Amplified Chirped Optical Pulses,” *Opt. Commun.*, vol. 56, no. 3, pp. 219–221, 1985.
- [136] O. Jaeckel, J. Polz, S. M. Pfotenhauer, H.-P. Schlenvoigt, H. Schworer, and M. C. Kaluza, “All-optical measurement of the hot electron sheath driving laser ion acceleration from thin foils,” *New J. Phys.*, vol. 12, no. 10, 2010.
- [137] M. Yeung *et al.*, “Noncollinear Polarization Gating of Attosecond Pulse Trains in the Relativistic Regime,” *Phys. Rev. Lett.*, vol. 115, no. 19, pp. 1–5, 2015.
- [138] B. Landgraf *et al.*, “Generation of multi-millijoule red-shifted pulses for seeding stimulated Raman backscattering amplifiers,” *Opt. Express*, vol. 23, no. 6, 2015.
- [139] A. Gopal *et al.*, “Observation of gigawatt-class THz pulses from a compact laser-driven particle accelerator,” *Phys. Rev. Lett.*, vol. 111, no. 7, pp. 1–5, 2013.
- [140] S. Herzer *et al.*, “An investigation on THz yield from laser-produced solid density plasmas at relativistic laser intensities,” *New J. Phys.*, vol. 20, no. 6, 2018.
- [141] S. Kuschel *et al.*, “Demonstration of passive plasma lensing of a laser wakefield accelerated electron bunch,” *Phys. Rev. Accel. Beams*, vol. 19, no. 7, pp. 1–9, 2016.
- [142] A. G. R. Thomas, S. P. D. Mangles, Z. Najmudin, M. C. Kaluza, C. D. Murphy, and K. Krushelnick, “Measurements of wave-breaking radiation from a laser-wakefield accelerator,” *Phys. Rev. Lett.*, vol. 98, no. 5, pp. 2–5, 2007.
- [143] B. Miao *et al.*, “Coherent ultra-broadband laser-assisted injection radiation from a laser plasma accelerator,” *Phys. Rev. E*, vol. 98, no. 4, pp. 1–8, 2018.
- [144] B. Landgraf, “Diplomarbeit: Charakterisierung von Überschalldüsen zur Elektronenbeschleunigung,” Friedrich-Schiller University Jena, 2010.
- [145] S. Kuschel *et al.*, “Controlling the Self-Injection Threshold in Laser Wakefield Accelerators,” *Phys. Rev. Lett.*, vol. 121, no. 15, 2018.
- [146] H. Hamster, A. Sullivan, S. Gordon, W. White, and R. W. Falcone, “Subpicosecond, electromagnetic pulses from intense laser-plasma interaction,” *Phys. Rev. Lett.*, vol. 71, no. 17, pp. 2725–2728, 1993.
- [147] M. J. Mead, D. Neely, J. Gauvain, R. Heathcote, and P. Patel, “Electromagnetic pulse generation within a petawatt laser target chamber,” *Rev. Sci. Instrum.*, vol. 75, no. 10, pp. 4225–4227, 2004.
- [148] M. De Marco *et al.*, “Basic features of electromagnetic pulse generated in a laser-target chamber at 3-TW laser facility PALS,” *J. Phys. Conf. Ser.*, vol. 508, no. 1, pp. 12–16, 2014.
- [149] J. Cikhardt *et al.*, “Measurement of the target current by inductive probe during laser interaction on terawatt laser system PALS,” *Rev. Sci. Instrum.*, vol. 85, no. 10, 2014.
- [150] D. Ullmann, “Master’s Thesis: Optical Diagnostics for LWFA Experiments,” Friedrich-Schiller University Jena, 2016.
- [151] S. Kuschel, “Doktorarbeit: Erzeugung dichter Elektronenpulse mit Laser-Plasma-Beschleunigern für QED Experimente in hohen Feldern,” Friedrich-Schiller University Jena, 2018.
- [152] A. A. Babin, D. V. Kartashov, A. M. Kiselev, V. V. Lozhkarev, A. N. Stepanov, and A. M. Sergeev, “Ionization spectrum broadening and frequency blue-shift of high-intensity

9. References

- femtosecond laser pulses in gas-filled capillary tubes,” *Appl. Phys. B Lasers Opt.*, vol. 75, no. 4–5, pp. 509–514, 2002.
- [153] K. Kosma, S. A. Trushin, W. Fuß, and W. E. Schmid, “Characterization of the supercontinuum radiation generated by self-focusing of few-cycle 800 nm pulses in argon,” *J. Mod. Opt.*, vol. 55, no. 13, pp. 2141–2177, 2008.
- [154] A. M. Sayler, T. Rathje, W. Müller, K. Rühle, R. Kienberger, and G. G. Paulus, “Precise, real-time, every-single-shot, carrier-envelope phase measurement of ultrashort laser pulses,” *Opt. Lett.*, vol. 36, no. 1, pp. 1–3, 2011.
- [155] D. Adolph *et al.*, “Real-time, single-shot, carrier-envelope-phase measurement of a multi-terawatt laser,” *Appl. Phys. Lett.*, vol. 110, no. 081105, pp. 1–4, 2017.
- [156] V. Neef, “Bachelorarbeit: Charakterisierung eines Mikroskops zum Zweck der Untersuchung von am Jeti-100-Lasersystem,” Friedrich-Schiller University Jena, 2018.
- [157] D. Polli, D. Brida, S. Mukamel, G. Lanzani, and G. Cerullo, “Effective temporal resolution in pump-probe spectroscopy with strongly chirped pulses,” *Phys. Rev. A - At. Mol. Opt. Phys.*, vol. 82, no. 5, pp. 1–8, 2010.
- [158] E. Esarey, S. K. Ride, and P. Sprangle, “Nonlinear Thomson scattering of intense laser pulses from beams and plasmas,” *Phys. Rev. E*, vol. 48, no. 4, 1993.
- [159] A. Boboc, L. Zabeo, and A. Murari, “Simultaneous Cotton-Mouton and Faraday rotation angle measurements on JET,” *Rev. Sci. Instrum.*, vol. 77, no. 10, pp. 14–17, 2006.
- [160] A. S. Joshi, P. A. Naik, S. Barnwal, Y. B. S. R. Prasad, and P. D. Gupta, “A novel technique for measurement of self-generated magnetic fields and the plasma density in laser produced plasmas from the Faraday rotation using two color probes,” *Opt. Commun.*, vol. 283, no. 23, pp. 4713–4716, 2010.
- [161] H. Soltwisch and H. R. Koslowski, “Observation of magnetic field perturbations during sawtooth activity in tokamak plasmas,” *Plasma Phys. Control. Fusion*, vol. 39, no. 5, pp. 341–349, 1997.
- [162] J. Chen *et al.*, “Faraday-effect polarimeter diagnostic for internal magnetic field fluctuation measurements in DIII-D,” *Rev. Sci. Instrum.*, vol. 87, no. 11, pp. 34–36, 2016.
- [163] A. Sävert, “Few-cycle microscopy of a laser wakefield accelerator,” Friedrich-Schiller-Universität Jena, 2016.
- [164] J. Götzfried *et al.*, “Physics of High-Charge Electron Beams in Laser-Plasma Wakefields,” *Phys. Rev. X*, vol. 10, no. 4, 2020.
- [165] H. Unz, “Relativistic Magneto-Ionic Theory for Drifting Plasma in Longitudinal Direction,” *Phys. Rev.*, vol. 146, no. 1, pp. 1–4, 1966.
- [166] U. E. Schroeder, *Spezielle Relativitätstheorie*. Harri Deutsch, 1994.
- [167] M. Bornatici, “Theory of electron cyclotron absorption of magnetized plasmas,” *Plasma Phys.*, vol. 24, no. 6, pp. 629–638, 1982.
- [168] V. Erckmann and U. Gasparino, “Electron cyclotron resonance heating and current drive in toroidal fusion plasmas,” *Plasma Phys. Control. Fusion*, vol. 36, pp. 1869–1962, 1994.
- [169] C. Thaury *et al.*, “Plasma mirrors for ultrahigh-intensity optics,” *Nat. Phys.*, vol. 3, no. 6, pp. 424–429, 2007.
- [170] M. B. Schwab *et al.*, “Visualization of relativistic laser pulses in underdense plasma,” *Phys. Rev. Accel. Beams*, vol. 23, no. 3, 2020.
- [171] G. A. Becker *et al.*, “Characterization of laser-driven proton acceleration from water microdroplets,” *Sci. Rep.*, vol. 9, no. 1, pp. 1–8, 2019.
- [172] F. Hinterberger, *Physik der Teilchenbeschleuniger und Ionenoptik*, 2nd ed. Springer Verlag, 2008.
- [173] M. Göppert-Mayer, “Über elementarakte mit zwei Quantensprüngen,” *Ann. Phys.*, vol. 401, pp. 273–294, 1931.
- [174] P. Agostini, F. Fabre, G. Mainfray, G. Petite, and N. K. Rahman, “Free-free transitions following six-photon ionization of xenon atoms,” *Phys. Rev. Lett.*, vol. 42, no. 17, pp. 1127–1130, 1979.
- [175] H. B. Bebb and A. Gold, “Multiphoton ionization of hydrogen and rare-gas atoms,” *Phys. Rev.*, vol. 143, no. 1, pp. 1–24, 1966.

9. References

- [176] G. Baravian and G. Sultan, “Determination of multiphoton ionization cross sections in focused laser experiments,” *Phys. B+C*, vol. 128, no. 3, pp. 343–352, 1985.
- [177] R. R. Freeman, P. H. Bucksbaum, H. Milchberg, S. Darack, D. Schumacher, and M. E. Geusic, “Above-threshold ionization with subpicosecond laser pulses,” *Phys. Rev. Lett.*, vol. 59, no. 10, pp. 1092–1095, 1987.
- [178] P. B. Corkum, N. H. Burnett, and F. Brunel, “Above-threshold ionization in the long-wavelength limit,” *Phys. Rev. Lett.*, vol. 62, no. 11, pp. 1259–1262, 1989.
- [179] P. B. Corkum, “Plasma perspective on strong-field multiphoton ionization,” *Phys. Rev. Lett.*, vol. 71, no. 13, pp. 1994–1997, 1993.
- [180] U. Mohideen *et al.*, “High Intensity Above-Threshold Ionization of He,” *Phys. Rev. Lett.*, vol. 71, no. 4, pp. 509–512, 1993.
- [181] S. C. Rae and K. Burnett, “Possible production of cold plasmas through optical-field-induced ionization,” *Phys. Rev. A*, vol. 46, no. 4, pp. 2077–2083, 1992.
- [182] Y. Ma *et al.*, “Polarization-Dependent Self-Injection by Above Threshold Ionization Heating in a Laser Wakefield Accelerator,” *Phys. Rev. Lett.*, vol. 124, no. 11, pp. 1–7, 2020.
- [183] H. A. Bethe and E. E. Salpeter, *Quantum Mechanics of One- and Two-Electron Atoms*. New York: Plenum, 1977.
- [184] X. M. Tong and C. D. Lin, “Empirical formula for static field ionization rates of atoms and molecules by lasers in the barrier-suppression regime,” *J. Phys. B At. Mol. Opt. Phys.*, vol. 38, no. 15, pp. 2593–2600, 2005.
- [185] S. F. Zhao, L. Liu, and X. X. Zhou, “Multiphoton and tunneling ionization probability of atoms and molecules in an intense laser field,” *Opt. Commun.*, vol. 313, pp. 74–79, 2014.
- [186] M. Nisoli, S. De Silvestri, and O. Svelto, “Generation of high energy 10 fs pulses by a new pulse compression technique,” *Appl. Phys. Lett.*, vol. 68, no. 20, pp. 2793–2795, 1996.
- [187] B. J. Eggleton *et al.*, “Integrated Tunable Fiber Gratings for Dispersion Management in High-Bit Rate Systems,” *J. Light. Technol.*, vol. 18, no. 11, pp. 1418–1432, 2000.
- [188] R. L. Fork, O. E. Martinez, and J. P. Gordon, “Negative dispersion using pairs of prisms,” *Opt. Lett.*, vol. 9, no. 5, pp. 150–152, May 1984.
- [189] L. Walmsley, L. Waxer, and C. Dorrer, “The role of dispersion in ultrafast optics,” *Rev. Sci. Instrum.*, vol. 72, no. 1, pp. 1–29, 2001.
- [190] R. Szipocs, K. Ferencz, C. Spielmann, and F. Krausz, “Chirped multilayer coatings for broadband dispersion control in femtosecond lasers,” *Opt. Lett.*, vol. 19, no. 3, pp. 201–203, 1994.
- [191] I. A. Walmsley and C. Dorrer, “Characterization of ultrashort electromagnetic pulses,” *Adv. Opt. Photonics*, vol. 1, no. 2, pp. 308–437, 2009.
- [192] A. Monmayrant, S. Weber, and B. Chatel, “A newcomer’s guide to ultrashort pulse shaping and characterization,” *J. Phys. B At. Mol. Opt. Phys.*, vol. 43, no. 10, 2010.
- [193] R. Trebino *et al.*, “Measuring ultrashort laser pulses in the time-frequency domain using frequency-resolved optical gating,” *Rev. Sci. Instrum.*, vol. 68, no. 9, pp. 3277–3295, 1997.
- [194] C. Iaconis and I. A. Walmsley, “Spectral phase interferometry for direct electric-field reconstruction of ultrashort optical pulses,” *Opt. Lett.*, vol. 23, no. 10, pp. 792–794, 1998.
- [195] L. Lepetit, G. Chériaux, and M. Joffre, “Linear techniques of phase measurement by femtosecond spectral interferometry for applications in spectroscopy,” *J. Opt. Soc. Am. B*, vol. 12, no. 12, pp. 2467–2474, 1995.
- [196] G. Stibenz and G. Steinmeyer, “Optimizing spectral phase interferometry for direct electric-field reconstruction,” *Rev. Sci. Instrum.*, vol. 77, no. 7, pp. 1–9, 2006.
- [197] T. Oksenhendler *et al.*, “Self-referenced spectral interferometry,” *Appl. Phys. B Lasers Opt.*, vol. 99, pp. 7–12, 2010.
- [198] A. Trabattori *et al.*, “Self-referenced spectral interferometry for single-shot measurement of sub-5-fs pulses,” *Rev. Sci. Instrum.*, vol. 86, no. 11, pp. 1–5, 2015.
- [199] T. Rathje *et al.*, “Review of attosecond resolved measurement and control via carrier-envelope phase tagging with above-threshold ionization,” *J. Phys. B At. Mol. Opt. Phys.*, vol. 45, no. 7, 2012.
- [200] “Sequoia HD.” <https://amplitude-laser.com/module/sequoia-hd/> (accessed Jul. 01, 2020).

9. References

- [201] S. Keppler, R. Bödefeld, M. Hornung, A. Sävert, J. Hein, and M. C. Kaluza, “Prepulse suppression in a multi-10-TW diode-pumped Yb:glass laser,” *Appl. Phys. B*, vol. 104, no. 1, pp. 11–16, 2011.
- [202] D. Meshulach, D. Yelin, and Y. Silberberg, “Real-time spatial–spectral interference measurements of ultrashort optical pulses,” *J. Opt. Soc. Am. B*, vol. 14, no. 8, pp. 2095–2098, 1997.

10. Ehrenwörtliche Erklärung

10. Ehrenwörtliche Erklärung

Ich erkläre hiermit ehrenwörtlich, dass ich die vorliegende Arbeit selbständig, ohne unzulässige Hilfe Dritter und ohne Benutzung anderer als der angegebenen Hilfsmittel und Literatur angefertigt habe. Die aus anderen Quellen direkt oder indirekt übernommenen Daten und Konzepte sind unter Angabe der Quelle gekennzeichnet.

Bei der Auswahl und Auswertung folgenden Materials haben mir die nachstehend aufgeführten Personen in der jeweils beschriebenen Weise entgeltlich/unentgeltlich geholfen:

1. Dr. Evangelos Siminos – Durchführung einer Simulation mit EPOCH (siehe **Abschnitt 5.3**) und Erstellung von der **Abbildung 32**. Wie im Text beschrieben (siehe **Abschnitt 6.1.2** und **6.2.2**) stammen einige zitierten Abbildungen aus seiner Arbeit. Die Abbildungen selbst sind im **Anhang D** zu finden.
2. Dr. Daniel Ullmann und Thomas Heinemann – Durchführung Simulationen mit VSim (siehe **Abschnitt 5.2**)
3. Dr. Alexander Sävert – wie im Text beschrieben (siehe **Abschnitt 6.2.2**) stammt eine zitierte Abbildung aus seiner Arbeit. Die Abbildung selbst ist im **Anhang D** zu finden.

Weitere Personen waren an der inhaltlich-materiellen Erstellung der vorliegenden Arbeit nicht beteiligt. Insbesondere habe ich hierfür nicht die entgeltliche Hilfe von Vermittlungs- bzw. Beratungsdiensten (Promotionsberater oder andere Personen) in Anspruch genommen.

Niemand hat von mir unmittelbar oder mittelbar geldwerte Leistungen für Arbeiten erhalten, die im Zusammenhang mit dem Inhalt der vorgelegten Dissertation stehen.

Die Arbeit wurde bisher weder im In- noch im Ausland in gleicher oder ähnlicher Form einer anderen Prüfungsbehörde vorgelegt.

Die geltende Promotionsordnung der Physikalisch-Astronomischen Fakultät ist mir bekannt.

Ich versichere ehrenwörtlich, dass ich nach bestem Wissen die reine Wahrheit gesagt und nichts verschwiegen habe.

Ort, Datum

Unterschrift d. Verfassers

11. Chronological List of Publications

11. Chronological List of Publications

1. M. B. Schwab *et al.*, “Visualization of relativistic laser pulses in underdense plasma,” *Phys. Rev. Accel. Beams*, vol. 23, no 3, p. 32801, 2020.
2. P. Niknejadi *et al.*, “Status of the Transverse Diagnostics at FLASHForward,” *J. Phys. Conf. Ser.*, vol. 1067, no. 4, 2018.
3. G. A. Becker, M. B. Schwab *et al.*, „Characterization of laser-driven proton acceleration from water microdroplets,” *Sci. Reports*, vol. 9, 2019.
4. S. Kuschel, M. B. Schwab *et al.*, “Controlling the Self-Injection Threshold in Laser Wakefield Accelerators,” *Phys. Rev. Lett.*, vol. 121, no. 15, p. 154801, 2018.
5. G. A. Becker *et al.*, “Ring-like spatial distribution of laser accelerated protons in the ultra-high-contrast TNSA-regime,” *Plasma Phys. Control. Fusion*, vol. 60, no. 5, 2018.
6. A. K. Arunachalam, M. B. Schwab *et al.*, “Observation of non-symmetric side-scattering during high-intensity laser-plasma interactions,” *New J. Phys.*, vol. 20, 2018.
7. D. Adolph *et al.*, “Real-time, single-shot, carrier-envelope-phase measurement of a multi-terawatt laser,” *Appl. Phys. Lett.*, vol. 110, 2017.
8. S. Kuschel *et al.*, “Demonstration of passive plasma lensing of a laser wakefield accelerated electron bunch,” *Phys. Rev. Accel. Beams*, vol. 19, no.7, pp. 1-9, 2016.
9. A. Sävert *et al.*, “Direct Observation of the Injection Dynamics of a Laser Wakefield Accelerator Using Few-Femtosecond Shadowgraphy,” *Phys. Rev. Lett.*, vol. 115, no. 5, pp. 1-5, 2015.
10. M. B. Schwab *et al.*, “Few-cycle optical probe pulse for investigation of relativistic laser-plasma interactions,” *Appl. Phys. Lett.*, vol. 103, no. 19, pp. 1-5, 2013.

12. Chronological List of Presentations and Posters

1. European Advanced Accelerator Concepts Workshop 2017
 - a. Poster – LWFA: Electron Cyclotron Resonance Imaging
2. Advanced Accelerator Concepts Workshop 2016
 - a. Presentation – Few-Cycle Optical Probing of LWFA Experiments
3. Accelerator Research and Development Workshop 2016
 - a. Presentation – Few-Cycle Probing for Laser-Plasma Accelerators
4. European Advanced Accelerator Concepts Workshop 2015
 - a. Poster – Few-Cycle Optical Probing of LWFA
5. LAOLA Workshop, Wismar 2015
 - a. Presentation – Optical Probing of Laser Wakefield Acceleration Experiments
6. 35th International workshop on Physics of High Energy Density in Matter, Hirschegg 2015
 - a. Presentation – Optical Probing of Laser Wakefield Acceleration Experiments
7. Abbe School of Photonics Seminar 2014
 - a. Presentation – Few-Cycle Optical Probing of LWFA Experiments
8. Deutsche Physikalische Gesellschaft e. V., Tagung Berlin 2014
 - a. Presentation – Few-Cycle Optical Probe-Pulse for Investigation of Relativistic Laser-Plasma Interactions